UNIVERSIDAD DE CHILE
FACULTAD DE CIENCIAS FÍSICAS Y MATEMÁTICAS
ESCUELA DE POSTGRADO

SEDIMENT TRANSPORT IN AREAS OF FLOW OBSTRUCTION DUE TO A PILE. EXPERIMENTAL STUDY OF INCIPIENT SEDIMENT TRANSPORT IN FRONT OF A PILE AND MODELING OF SCOUR IN TRANSIENT AND OSCILLATORY FLOW REGIME

TESIS PARA OPTAR AL GRADO DE DOCTOR EN CIENCIAS DE LA INGENIERÍA MENCIÓN FLUIDODINÁMICA

MATÍAS FERNANDO QUEZADA LABRA

PROFESOR GUÍA
DR. YARKO NIÑO CAMPOS

MIEMBROS DE LA COMISIÓN:
DR. ALDO TAMBURRINO TAVANTZIS
DR. WERNHER BREVIS VERGARA
DR. OSCAR LINK LAZO
DR. ÁLVARO VALENCIA MUSALEM

Esta tesis ha sido parcialmente financiada por CONICYT
Beca de Doctorado Nacional N° 21140091

SANTIAGO DE CHILE
2020

RESUMEN

RESUMEN DE TESIS PARA OPTAR AL
GRADO DE DOCTOR EN CIENCIAS DE LA
INGENIERÍA MENCIÓN FLUIDODINÁMICA
POR: MATÍAS QUEZADA LABRA
PROF. GUÍA: DR. YARKO NIÑO CAMPOS

SEDIMENT TRANSPORT IN AREAS OF FLOW OBSTRUCTION DUE TO A PILE. EXPERIMENTAL STUDY OF INCIPIENT SEDIMENT TRANSPORT IN FRONT OF A PILE AND MODELING OF SCOUR IN TRANSIENT AND OSCILLATORY FLOW REGIME

El transporte de sedimentos en zonas de obstrucción de flujo debido a una pila, fue estudiado experimental y numéricamente. El trabajo experimental se desarrolló en el laboratorio de Hidrodinámica de la Universidad de Sheffield, aplicando la técnica de Particle Image Velocimetry (PIV) para registrar los campos bidimensionales de velocidad frente de una pila circular, para un total de 15 ensayos, los que permitieron caracterizar efectos en el flujo debido a cambios en el caudal y en la obstrucción. Las series de tiempo de velocidades fueron analizadas mediante la Proper Orthogonal Decomposition y análisis de cuadrantes. Los modos dominantes se asociaron a la dinámica del flujo descendente vinculado con la capa límite incidente y al vórtice de herradura. Estas estructuras turbulentas fueron correlacionadas con el transporte incipiente de los sedimentos, obteniendo una correlación entre 80% y 87%, siendo concordante con el análisis de cuadrantes.

El estudio numérico se desarrolló mediante un modelo basado en la Dinámica Computacional de Fluidos llamado REEF3D, basado en las ecuaciones promediadas de Navier-Stokes según Reynolds (RANS) y la ecuación de evolución morfodinámica propuesta por Exner. Como primer trabajo, se analizó la socavación por flujo impermanente y oscilatorio, mientras que en el segundo se estudió la hidrodinámica de olas y corrientes (codirecionales y opuestas) y la socavación en pilas. En el caso del primer estudio, con la calibraciónse definió el modelo de cierre turbulento y un coeficiente de relajación en la ecuación de gasto sólido de fondo, con el propósito de incrementar la movilidad de los sedimentos en las cercanías de la pila. Posteriormente, un set de casos fueron ejecutados utilizando diferentes hidrogramas y olas. Se detectó una gran concordancia entre los datos simulados y los obtenidos en laboratorio por terceros. Una conclusión del estudio fue la necesidad de mejorar la descripción del transporte de sedimentos, para evitar el uso del coeficiente de relajación.

En el segundo estudio y posterior a la calibración, la hidrodinámica y socavación entorno de una pila fue estudiada para un set de casos definidos mediante la velocidad relativa de la corriente (U_{cw}). Los resultados mostraron que la hidrodinámica para olas y corrientes codireccionales u opuestas, no varía significativamente en sus velocidades, vorticidades y tensión de corte media, debido a que las corrientes fueron más relevantes para el flujo neto. La estimación de la socavación de equilibrio, obtuvo valores cercanos a los descritos en la literatura y a partir de esto, se verificó que ésta es menor cuando las olas y corrientes actúan en direcciones opuestas. Debido a esto, U_{cw} fue modificado para representar adecuadamente la socavación por olas y corrientes codireccional u opuestas.

Como conclusión general, el coeficiente de relajación permite simplificar el proceso de socavación alrededor de pilas, habilitando el uso de las RANS en problemas de ingeniería, sin la necesidad de simular la hidrodinámica de los pequeños vórtices y de esta manera usar los recursos computacionales de una manera más eficiente.

ABSTRACT

RESUMEN DE TESIS PARA OPTAR AL
GRADO DE DOCTOR EN CIENCIAS DE LA
INGENIERÍA MENCIÓN FLUIDODINÁMICA
POR: MATÍAS QUEZADA LABRA
PROF. GUÍA: DR. YARKO NIÑO CAMPOS

SEDIMENT TRANSPORT IN AREAS OF FLOW OBSTRUCTION DUE TO A PILE. EXPERIMENTAL STUDY OF INCIPIENT SEDIMENT TRANSPORT IN FRONT OF A PILE AND MODELING OF SCOUR IN TRANSIENT AND OSCILLATORY FLOW REGIME

Sediment transport in areas of flow obstruction due to a pile was studied by means of experimental and numerical techniques. The experimental work was carried out in the Hydrodynamics Laboratory of the University of Sheffield, applying the Particle Image Velocimetry (PIV) technique to register the two-dimensional velocity field in front of a circular pile, in a total of 15 tests, which allowed to characterize the effects of changes in flow and obstruction, on the hydrodynamic behavior of the fluid. The velocities time series were analyzed by the Proper Orthogonal Decomposition and Quadrant Analysis. The dominant modes describe the dynamics of the down-flow associated with the incoming boundary layer and the dynamics of the primary horseshoe vortex. These structures were correlated with the incipient sediment transport, which shows a correlation from 80% to 87% of the total grain movements events, which is in agreement with the Quadrant Analysis.

The numerical studies were carried out by applying a model based on Computational Fluid Dynamics software called REEF 3D, which through the application of the Reynols Averaged Navier-Stokes Equations (RANS) and the Exner equation for the morphological evolution of the bed, allowed to characterize the hydrodynamics around circular piles for various flow conditions. As the first work, the numerical simulation of scour around circular piles due to unsteady currents and oscillatory flow was analyzed, while the second work was the numerical study of the hydrodynamics of waves and currents (codirectional and opposite) and their effects in pier scouring. In the case of the first study, from calibration process it was possible to define the turbulence closure model to be used and a relaxation coefficient in the bed load equation necessary to increase the sediment mobility in the vicinity of the pile. After that, a set of numerical simulations was performed using different hydrographs and wave conditions. There is a strong agreement between simulated data and experimental data reported by other authors for unsteady flow. In the case of scour due to oscillatory flow, the numerical results showed the same behavior as the experimental data previously published by others. A conclusion of the study is the need to improve the description of sediment transport, to avoid the use of a relaxation coefficient that reduces the threshold condition of the incipient transport.

In the second numerical study and after the calibration process, the hydrodynamics and pile scour were studied for a set of scenarios, which were defined by the relative velocity of the current (U_{cw}). The results showed that the hydrodynamics for codirectional or opposite waves and currents does not have significant differences when analyzed in terms of their velocities, vorticities and mean shear stresses, since the currents proved to be more relevant compared to the net flow. The equilibrium scour estimation, enabled us to estimate values close to those described in the literature and from this, it was verified that the dimensionless scour would be less when the waves and currents are from opposite directions. Due to those results, U_{cw} was modified to represent adequately the pile scour for waves and currents acting both codirectional and opposite.

As a main conclusion, the relaxation coefficient allows to simplify the process of pile scour, allowing the use of RANS in engineering problems, without the need to simulate in detail the hydrodynamics of the small vortices and employ computational resources more efficiently.

Para mi hermosa hija Agustina Quezada y mi amada mujer Ximena Vásquez, mis pilares fundamentales en la construcción de este sueño.

A mis padres, Fernando Quezada y Anabel Labra†, quien partió a la eternidad antes de ver concretado este sueño.

AGRADECIMIENTOS

Agradecer, es un acto de nobleza humana y prácticamente un requisito cuando se llega a la meta de una inmensa travesía, en la cual muchas manos, aveces invisibles, colaboran para el cumplimiento del propósito.

Mis agradecimientos a CONICYT quien mediante su beca de doctorado nacional N° 21140091, financió el desarrollo de mis estudios de postgrado.

Agradecer también a mis compañeros del programa de doctorado que colaboraron inmensamente en mis primeros pasos, Alfredo Aranda y Benjamin Herrmann muchas gracias!.

Quiero expresar mis más sinceros agradecimientos a Ecotecnos S.A. por el apoyo brindado durante estos años de estudio, en especial al Dr. Humberto Díaz y al Sr. Mario Herrera, por sus palabras de aliento, apoyo y contención durante este camino. Así mismo, quiero agradecer a mi equipo por sus colaboraciones y recomendaciones, José Ribba, Felipe Galaz, Felipe Rifo, Ricardo Castillo, Ariel González y Pia Monreal, muchas gracias.

Especial mención quiero hacer a mi querida Pia Monreal, por su paciencia, apoyo, comprensión, silencio y aveces simplemente por escuchar mientras pensaba en voz alta!...gracias por todo.

Quiero agradecer a mi gran amigo Eduardo Cosio Toledo, por siempre darme una palabra de apoyo e incentivarme en cada paso dado, eres sin dudas unos de los amigos que cada persona debe tener.

Quisiera agradecer profundamente a mis estimados Profesores, que han hecho posible recorrer este camino de una manera exitosa, lleno de nuevos conocimientos y paciencia para enfrentar las dificultades que se presentan en el proceso. Al Profesor Dr. Yarko Niño y Profesor Dr. Aldo Tamburrino, muchas gracias de corazón... a los maestros con cariño.

Gracias al Profesor Wernher Brevis por recibirme en la Universidad de Sheffield y colaborar intensamente en el desarrollo de los trabajos experimentales, que permitieron obtener y desarrollar parte importante de esta investigación. Gracias también a Daniel Mella, quien colaboró en mi trabajo durante mi estadía en el Laboratorio de Hidrodinámica de la Universidad de Sheffield.

Finalmente quiero agradecer a mi familia, por el apoyo incondicional, la paciencia y compartir mis tiempos con este desafío...a mi hija Agustina, mi mujer Ximena, mi padre Fernando, mi madre Anabel†....muchas gracias.

El orden de los factores, no altera el producto....

Contents

List of Figures

List of Tables

Chapter 1

Introduction

1.1 General Features

Fluid motion has been studied for more than 200 years, being one of the major contributions the progress made by Claude-Louis Navier and George Gabriel Stokes, who proposed fundamental equations of a flowing fluid, nowadays known as Navier Stokes equations (Navier, 1823; Stokes, 1845).

By using Navier - Stokes equations it has been possible to describe the flow characteristics for a set of typical scenarios such as: flow around a sphere (Stokes Law), flow between rotating cylinders, oscillatory movement of a viscous flow, damping of gravity waves, among others.

Varied exact solutions of Navier Stokes equations may be found in specialized literature (Landau and Lifshits, 1959; Batchelor, 1997; Kundu et al., 2015), nevertheless, in most cases no such solutions exist, and therefore, the study is generally based on experimental work and/or numerical models. This is the case of flow around a cylindrical pile.

An exact approach of the flow around a pile may be found by means of potential flow or ideal fluid solution, as referenced in Guyon et al. (2001), which enables to assess the general behavior of velocities and pressure of the flow around a pile, nevertheless, further progress has been achieved through experimental work.

Greatest advances in knowledge regarding the flow around a cylindrical pile have been developed by several investigators which according to Breusers et al. (1977) have proposed the experimental analysis since 1932 (Keutner, 1932), and according to our investigation have continued to develop up to present. In this respect, the evolution of the horseshoe vortex system in front a vertical circular cylinder in open channel have been described by Particle Image Velocimetry (PIV) measurements, based on the investigation conducted by Chen et al. (2019). Some of the leading studies in the flow around a circular pile analysis have been previously presented by Tritton (1959), Roshko (1961), Baker (1979, 1980), Dargahi (1987, 1989), Devenport and Simpson (1990), Graf and Yulistiyanto (1998), Ahmed and Rajaratnam (1998), Ataie-Ashtiani and Aslani-Kordkandi (2013) and Apsilidis et al. (2015). Nevertheless, a solid overview of the progress achieved up to 1997 regarding flows and forces around cylindrical structures for both. steady current and oscillatory flow (waves), is presented by Sumer and Fredsøe (1997) and subsequently updated by the same authors in Sumer and Fredsøe (2006).

In addition to the hydrodynamic charanterization around cylindrical piles, studies are usually developed aiming to estimate the expected scour. To date, there exist several studies available for steady current flow. For example in the literature it is possible to find works of Laursen and Toch (1956), Hjorth (1975), Melville (1975), Ettema (1976), Breusers et al. (1977), Ettema (1980), Dargahi (1987), Chiew and Melville (1987), Dargahi (1990), Kobayashi

and Oda (1994), Whitehouse (1998), Melville and Coleman (2000), Link (2006), Link et al. (2008b), Melville (2008), Zanke et al. (2011), among others. In oscillatory flow case, the number of publications decreases standing out the following: Sumer et al. (1992), Sumer et al. (1993), Kobayashi and Oda (1994), Sumer et al. (1997), Zanke et al. (2011) and Sumer et al. (2012). In the case of combined action of waves and currents, the investigation development is limited to a small number of scientific publications, including Eadie and Herbich (1986), Kawata and Tsuchiya (1988), Raaijmakers and Rudolph (2008), Rudolph et al. (2008), Zanke et al. (2011), Ong et al. (2013), Sumer and Fredsøe (2001), Qi and Gao (2014a), and Qi and Gao (2014b).

Nevertheless, most of the publications indicated above, base their experimental studies in the linkage of the problem characteristic scales, such as pile diameter (D), flow mean velocity (U), water depth (h), with maximum or equilibrium scour (S), failing to directly focus on the description of the physics of the flow around the pile and the triggering mechanisms of the sediment incipient motion, which later triggers the scour hole development.

The effect of the sediments into the pile scour mainly allow to define if the scour occurs under the regime of clear water or live bed. However, some studies can be found regarding to sediment gradiation (geometric standar of sediment distribution) and his effects over the scour depths (Ettema, 1976).

One of the tools that several authors have used to improve the understanding of the scour process around cylindrical piles, corresponds to numerical modeling, which enables to robustly describe flow, sediments transport and scour. Some of the studies available in literature oriented to the numerical representation of the scour process were presented by several authors, among which the following stand out: Kobayashi (1992), Olsen and Melaaen (1993), Roulund et al. (2005), Paik et al. (2007), Liu and García (2008), Bihs (2011), Baykal et al. (2015), Schanderl and Manhart (2016), Baykal et al. (2017), Schanderl et al. (2017), and the recently conducted for the purposes of this doctoral thesis: Quezada et al. (2018), and Quezada et al. (2019).

Although numerous advances are being made in numerical modeling of scour around cylindrical piles, sediments transport in flow obstruction areas have failed to be entirely described and equations for bed load are usually used for the determination of sediment transport in alluvial channels, such as Meyer-Peter and Müller (1948), Engelund and Fredsøe (1976) or Van Rijn (1984a). Maybe among the most relevant numerical studies in the estimation of scour around piles are those developed by Liu and García (2008) and Escauriaza and Sotiropoulos (2011a,b), who analyzed the need of using flexible mesh in scour estimation (Liu and García, 2008) and the relevance of lagrangian representation of the sediments transport (Escauriaza and Sotiropoulos, 2011a,b) and Link et al. (2012). Nevertheless, the mentioned works demand large computational costs in order to obtain a solution, which regarding scientific knowledge are relevant, although for engineering studies are complex to be applied.

This thesis has been developed based on the above, whose purpose is to study the sediments transport in flow obstructed areas in accordance with two views. The first view is scientific, aiming to describe the incipient motion based on the coherent turbulent structures of the flow, while the second is the engineering view, and that through the application of the relaxation coefficient, the scour around cylindrical piles can be estimated using Reynolds Averaged Navier - Stokes equations (RANS) computationally efficient.

1.2 Objetives

The general purpose of the doctoral thesis was to study the sediment transport in areas of flow obstructed due to a pile using experimental and numerical techniques.

To achieve the intended general objective, the specific objectives below were established:

- Study through experimental work the coherent structures of the flow upstream of a pile and determine their role in the incipient movement of sediments.
- Model numerically the scour around cylindrical piles due to unsteady current and oscillatory flow, applying Eulerian techniques to define the sediment transport and regular grids for the numerical solution of the hydrodynamics around the structure, in order to verify the capacity of the Reynolds Averaged Navier Stokes Equations (RANS) to determine the scour.
- Study through numerical models the scour around piles, in environments with waves and currents acting codirectional and opposite, to verify the capacity of the Reynolds Averaged Navier Stokes Equations (RANS) to determine the scour.

Each specific objective was addressed through the development of papers in scientific journals.

1.3 Organizacional structure of the thesis

This doctoral thesis has been elaborated based on papers. As of the date of submission of this document, two articles have been published, while a third is under review by an international journal. Scientific publications in chronological order are listed below:

- **Numerical simulation of scour around circular piles due to unsteady currents and oscillatory flows**, published in the international Journal Engineering Applications of Computational Fluid, available since March 2018.
- **Numerical study of the hydrodynamics of waves and currents and their effects in pier scouring**, published in the international Journal Water, in a special issue on Experimental, Numerical and Field Approaches to Scour Research, available for reading from October 2019.
- **Coherent turbulent structures in front of a circular pile embedded on a granular bed and its relationship with the sediment incipient motion**, prepared for the international journal Experiments in Fluids, and submitted in March 2020.

This thesis has been organized into four chapters, including introduction and conclusions.

Chapter 2 describes the hydrodynamics and sediment transport around cylindrical structures, developing purely theoretical aspect such as an extended bibliographical review, and which allow complementing what is presented in the scientific article called **Coherent turbulent structures in front of a circular pile embedded on a granular bed and its relationship with the sediment incipient motion**, included in section 2.4 and which is an experimental work developed during the doctoral investigation.

In chapter 3, general aspects relevant to hydrodynamic numerical modeling are presented, such as the problem governing equations, the existing approximations for the simulation of turbulence and the basic aspects of representation of the interaction of the flow with the structures placed in the flow. This chapter includes two scientific publications that were developed as part of the doctoral investigation and address specific topics regarding scour around circular piles and are titled as follows: **Numerical simulation of scour around circular**

piles due to unsteady currents and oscillatory flows and **Numerical study of the hydrodynamics of waves and currents and their effects in pier scouring**.

Finally, conclusions obtained from the study conducted are presented in chapter 4, where a general conclusion of the doctoral thesis has been included and specific conclusions also obtained in each of the scientific publications prepared as part of the investigation.

Chapter 2

Hydrodynamics and sediment transport around cylindrical structures

2.1 General hydrodynamics aspects

2.1.1 A brief history of fluid mechanics

The study of fluids in motion has historically drawn the attention of world's leading thinkers, philosophers and even prophets, such is the case of Deborah, to whom is ascribed the phrase: "mountains flow before the Lord", which inspired the scientist Marku Reiner to propose the dimensionless number called the Deborah Number ($D = t_{re}/t_{ob}$) (Reiner, 1964), which compare the time of relaxation (t_{re}) with the time of observation (t_{ob}). The latter allows to establish when a body behaves as solid or fluid.

Perhaps the first approach to fluids in motion studies was raised by the philosopher Heraclitus, with his phrase: πάντα ῥεῖ (everything flows) around 500 BC. Subsequently, Hippocrates and Aristotle mention aspects related to fluid dynamics, in the field of medicine and the natural sciences, correspondingly.

Archimedes, Greek noted engineer, physicist, inventor, astronomer and mathematician, was one of the first scientists to propose a law regarding hydrostatics. Because of the relevance of his work, the vertical force acting on submerged bodies is called Archimedes Principle.

All contributions by Heraclitus, Hippocrates and Archimedes occurred before Christ. It took nearly a millennium to find significant developments in the understanding of fluid mechanics field, being Leonardo Da Vinci the most outstanding author. According history, the book titled "Del moto e misura dell'aqua" may be considered his master piece in terms of fluid mechanics; book consulted by the author of the present thesis, in English language version, and published under the reference da Vinci (1958).

Subsequent the meaningful developments made by Da Vinci; Blaise Pascal in the understanding of the fluid behavior incorporates the pressure acting on them. Such variable enables to obtain constituent laws. Isaac Newton works are, nonetheless, those who start shaping the fluid mechanics as it is known today, since he is the creator of a large part of the mathematical tools (differential and integral calculus, for example) which enable formal writing of physics describing the fluids, even proposing a stress-deformation relation to describe the so-called Newtonians fluids.

After Newton works, many had been the contributions of distinguished authors such as

Daniel Bernoulli, Leonhard Euler, Claude Louis Marie Henry Navier, George Gabriel Stokes, and Osborne Reynolds, to name a few. However, at present scientific advances continued to develop in the understanding of fluids in motion, through both experimental techniques and numerical models. The aim of this thesis is to contribute with the specific understanding of the flow behavior in areas obstructed by a pile.

Next, a summary of some general and specific aspects of the fluid mechanics necessary to understand the results of the conducted investigation is presented.

2.1.2 General hydrodynamics equations

The mechanical description of fluids, related to their field of velocities and pressures, is approached through the concepts of conservation of their essential properties:

- Mass
- Momentum
- Energy

Based on this laws of conservation the equations of fluid mechanics are proposed, which are known as the Navier-Stokes equations, in honor of their authors (Claude-Louis Navier and George Gabriel Stokes), who in the 18th century (Navier, 1823; Stokes, 1845) propose them considering a viscous and incompressible fluid. These are the fundamental starting point for the solution of problems in environmental fluid mechanics, which depending on the appropriate boundary conditions, are capable of representing the physics of various processes.

Equation of Continuity: mass conservation

Consider a fluid medium composed of a single phase, contained in a control volume (V) moving with $\vec{u}$ velocity and located at a distance $\vec{r}$ of the reference axis, as illustrated in Figure 2.1.

The mass contained in a control volume (M_V) can be mathematically expressed according to the equation 2.1.1, where $\rho(\vec{r}, t)$ is the fluid density in a given spatial location ($\vec{r}$) and time (t). If conservation is imposed, the rate of change equal to zero should be obtained, in such way that can be described according to equation 2.1.2.

$$M_V = \int_V \rho(\vec{r}, t) dV \tag{2.1.1}$$

$$\frac{\partial M_V}{\partial t} = \frac{\partial}{\partial t} \left(\int_V \rho(\vec{r}, t) dV \right) \tag{2.1.2}$$

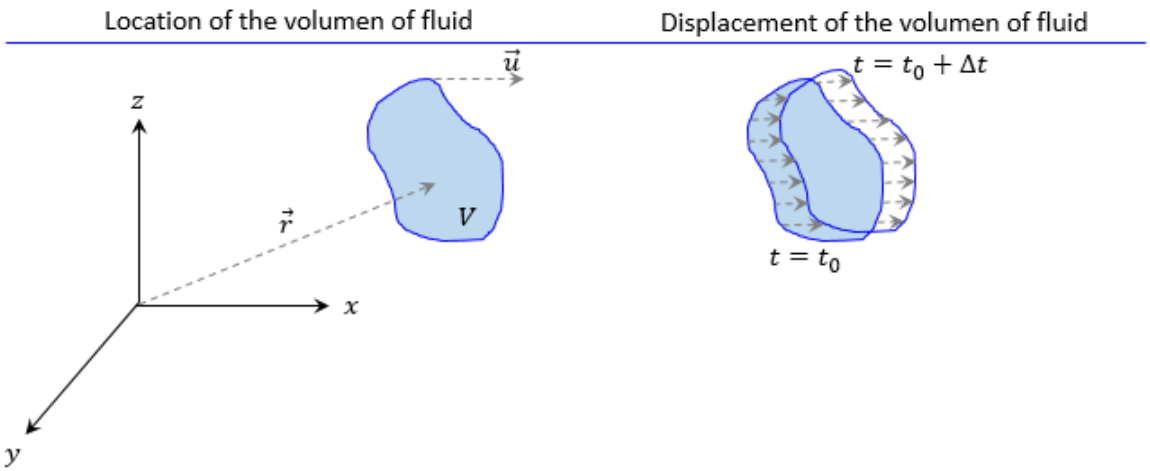

Figure 2.1: Control Volume and the associated displacement considered for the analysis of the mass conservation.

By applying the Reynols transport theorem in the equation 2.1.2, the rate of change of the mass can be decomposed according to the variation associated with the pass of time (or local) and the associated with the displacement of the control volume (mass advection). In this way, the equation 2.1.2 can be expressed as:

$$\frac{\partial M_V}{\partial t} = \int_V \frac{\partial}{\partial t}\rho(\vec{r},t)dV + \int_S \frac{\partial}{\partial t}\rho(\vec{r},t)\vec{u}\cdot\vec{n}dS \tag{2.1.3}$$

where $\vec{n}$ is the unit vector of the surface S that defines the volumen V. The equation 2.1.3 can be treated by the divergence theorem, obtaining the expression 2.1.4. If it is imposed that the mass change rate is null and it is fulfilled for the whole volume, the so-called continuity equation is obtained according to the equation 2.1.5.

$$\frac{\partial M_V}{\partial t} = \int_V \frac{\partial}{\partial t}\rho(\vec{r},t)dV + \int_V \nabla\cdot(\rho\vec{u})\,dV = 0 \tag{2.1.4}$$

$$\frac{\partial}{\partial t}\rho(\vec{r},t) + \nabla\cdot(\rho\vec{u}) = 0 \tag{2.1.5}$$

When the fluid in the control volume that is studied corresponds to an incompressible material, with isotropic characteristics in its density, it is easy to observe that the equation 2.1.5 can be simply written as:

$$\nabla\cdot\vec{u} = 0 \tag{2.1.6}$$

The equation 2.1.6 can also written in index notation (equation 2.1.7), where u_i is the velocity and x_i is the space, where $i = 1$, 2 and 3 (vector components).

$$\frac{\partial u_i}{\partial x_i} = 0 \tag{2.1.7}$$

Momentum Conservation Equation

Suppose that a body with some mass is moving at some velocity, it is known that, by Newton's Law, the product of mass and velocity is called momentum.

The momentum variations are necessarily produced by the action of external forces, in such a way that the momentum conservation approach is a balance of forces, and in the case of a fluid medium this balance is developed over a control volume.

For a control volume V that moves at a speed $\vec{u}$, the momentum can be defined $\vec{P}(t)$ according to the equation 2.1.8, and whose exchange rate can be expressed according to 2.1.9.

$$\vec{P}(t) = \int_V \rho(\vec{r},t)\ \vec{u} dV \tag{2.1.8}$$

$$\frac{\partial \vec{P}(t)}{\partial t} = \frac{\partial}{\partial t}\left(\int_V \rho(\vec{r},t)\ \vec{u} dV\right) \tag{2.1.9}$$

To expand the equation 2.1.9, the Reynolds transport theorem is applied, and consequently, the divergence theorem for the treatment of the surface integral. In this way, it can be obtained the equation 2.1.10.

$$\frac{\partial \vec{P}(t)}{\partial t} = \int_V \frac{\partial}{\partial t}\left(\rho(\vec{r},t)\ \vec{u}\right)\ dV + \int_S \left(\rho(\vec{r},t)\vec{u}\right)\left(\vec{u}\cdot\vec{n}\right) ds \tag{2.1.10}$$

According to Newton's second law, the variation of momentum equals the external forces. In this way, it is possible to define, in an auxiliary way, the balance of the external forces that act on the fluid, being these mainly the gravity and those associated with the surface of the control volume.

$$\sum \vec{F}_{externas} = \int_V \rho(\vec{r},t)\ \vec{g}\, dV + \int_S \vec{\tau}\cdot\vec{n} ds \tag{2.1.11}$$

where τ are the surface forces per unit area (stress). By applying the divergence theorem and equating the action of external forces with the variation of momentum, we obtain the equation 2.1.12, which considered as valid for any volume of control, is reduced to the equation 2.1.13.

$$\int_V \frac{\partial \rho(\vec{r},t)\vec{u}}{\partial t} dV + \int_V \nabla\cdot\left(\rho(\vec{r},t)\vec{u}\vec{u}\right) dV = \int_V \rho(\vec{r},t)\vec{g} dV + \int_V \nabla\cdot\vec{\tau} dV \tag{2.1.12}$$

$$\frac{\partial \rho(\vec{r},t)\vec{u}}{\partial t} + \nabla\cdot\left(\rho(\vec{r},t)\vec{u}\vec{u}\right) = \rho(\vec{r},t)\vec{g} + \nabla\cdot\vec{\tau} \tag{2.1.13}$$

The equation 2.1.13 can be rewritten in tensor notation (index notation) according to the expression 2.1.14, where the term τ_{ij} allows describing the deformation rate-stress relation of the fluid.

$$\frac{\partial\left(\rho u_i\right)}{\partial t} + \frac{\partial\left(\rho u_i u_j\right)}{\partial x_j} = \rho g_i + \frac{\partial \tau_{ij}}{\partial x_j} \tag{2.1.14}$$

Constitutive equation for a Newtonian fluid

Stress-deformation rate relation (τ_{ij}) defined in the momentum conservation equation 2.1.14, has some mathematical properties, as well as according its definition, enables to incorporate the type of fluid to be represented through the conservation equation.

Mathematically, the first index of τ_{ij} denotes the direction normal to the surface, while the second describes the direction in which the stress is acting, being considered as symmetrical, that is $\tau_{ij} = \tau_{ji}$ (Kundu et al., 2015).

As in the case of solid materials, in order to describe the physics of fluids, the relation between stress (τ_{ij}) and deformation rate ($\frac{\partial u_i}{\partial x_j}$) is named constitutive equation, and in classic fluid mechanics, the simpler lineal relation known is the so-called Newtonian (Kundu et al., 2015).

Stresses developed in a fluid may be denoted through a fraction associated to the fluid at rest and the other to the flowing fluid. In the case of the fluid at rest, stresses to which is subjected are mainly developed by the range of working pressures (p), while in the case of flowing fluids, additional stresses develop (σ_{ij}). In this way, a simple approximation to total stresses of a fluid may be expressed according equation 2.1.15, where δ_{ij} corresponds to a Kronecker delta.

$$\tau_{ij} = -p\delta_{ij} + \sigma_{ij} \tag{2.1.15}$$

Considering the following assumptions in equation 2.1.15:

- Isotropy: Fluid properties are isotropic.
- Incompressibility: The fluid is incompressible.

Subsequent to mathematical development, the constitutive law of a Newtonian fluid may be obtained according to the presented in equation 2.1.16. For further antecedents of the development of governing equations, it is suggested an in-depth review (Kundu et al., 2015, Chapter 4).

$$\tau_{ij} = -p\delta_{ij} + 2\mu S_{ij} + \lambda S_{mm}\delta_{ij} \tag{2.1.16}$$

Where μ is dynamic viscosity of the fluid, S_{ij} is the antisymmetric tensor of the spatial gradient of velocity ($\frac{\partial u_i}{\partial x_j}$), $S_{mm} = \frac{\partial u_i}{\partial x_i}$, and μ_v is the coefficient of bulk viscosity.

The Navier - Stokes momentum equation

The Navier-Stokes momentum equation is obtained incorporating the equation 2.1.16 in the equation 2.1.14, which shapes according equation 2.1.17.

$$\frac{\partial (\rho u_i)}{\partial t} + \frac{\partial (\rho u_i u_j)}{\partial x_j} = \rho g_i + \frac{\partial}{\partial x_j}\left(-p\delta_{ij} + 2\mu S_{ij} + \lambda S_{mm}\delta_{ij}\right) \tag{2.1.17}$$

On the previous equation, several algebraic simplifications may be applied, as well as vector properties. For example, pressure derived and Kronecker delta may be simplified according to $\frac{\partial p}{\partial x_j}\delta_{ij} = \frac{\partial p}{\partial x_i}$, and expressing S_{ij} based on spatial gradient of velocities, the Navier-Stokes momentum equation may be rewritten in a general manner according equation 2.1.18.

$$\frac{\partial (\rho u_i)}{\partial t} + \frac{\partial (\rho u_i u_j)}{\partial x_j} = -\frac{\partial p}{\partial x_i} + \rho g_i + \frac{\partial}{\partial x_j}\left[\mu\left(\frac{\partial u_j}{\partial x_i} + \frac{\partial u_i}{\partial x_j}\right)\right] \tag{2.1.18}$$

This way, terms constituting the Navier - Stokes momentum equation are the inertia forces (terms on the equation left), forces due to the range of working pressures, external forces acting on the fluid (as gravity) and viscous forces.

2.1.3 A potential flow solution for a boundary layer of fluid past a cylindrical structure

In the mathematical description of fluids there are different approaches to determine their dynamics. One of its most recognized simplifications is the so-called potential flow or ideal fluid, which is based on that the fluid can be considered as inviscid and incompressible, meanwhile the flow can be considered as irrotational.

Under the conditions of irrotationality, incompressibility and inviscidity, the equations of mass conservation and momentum can be expressed as 2.1.19 and 2.1.20, respectively. Notice that the equation 2.1.19 is equal to the equation 2.1.6, a sole change to tensor notation has been incorporated.

$$\frac{\partial u_i}{\partial x_i} = 0 \tag{2.1.19}$$

$$\frac{\partial u_i}{\partial t} + u_j \frac{\partial u_i}{\partial x_j} = -\frac{1}{\rho}\frac{\partial \widehat{p}}{\partial x_i} \tag{2.1.20}$$

The condition of irrotationality is fulfilled in such a way that there is a scalar function, ϕ, that describes the velocity field according to the equation 2.1.21 and that additionally satisfies the condition of continuity according to the equation 2.1.22.

$$u_i = \frac{\partial \phi}{\partial x_i} \tag{2.1.21}$$

$$\frac{\partial^2 \phi}{\partial x_i^2} = 0 \tag{2.1.22}$$

Potential flow solutions can be applied to various conditions, even in those where the viscosity of the fluid is not strictly equal to zero. For example, it can be applied when the disturbance to the flow velocity field induced by the viscosity does not have enough time to propagate through the diffusion mechanism (Guyon et al., 2001).

From the potential flow equations, solutions of general problems in fluid mechanics can be obtained, such as the uniform flow in a channel, the velocity field that is produced from a source/sink, flow around a sphere, flow around a cylinder, among other solutions, as can be seen in Guyon et al. (2001) or Kundu et al. (2015).

The potential flow around a cylinder without considering circulation (Γ), results from the superposition of the uniform flow and the dipole. Usually, this analytical solution is presented in two dimensions and is solved in polar coordinates. According to the development presented in Guyon et al. (2001), for an approach velocity U which is disturbed by the presence of a cylinder with radius R, the potential flow can be written according to the equation 2.1.23.

$$\phi = \phi_{uniform} + \phi_{dipole} \tag{2.1.23}$$

The potential flow described in equation 2.1.23 is not for a cylinder in a channel, but a cylinder in an infinity media. In that case, when the boundary conditions at infinity and in the radius are imposed on the equation 2.1.23, so that the velocity is equal to U and zero in the case of the radial velocity, respectively, the polar velocity field can be written according to the equation 2.1.24 and 2.1.25 for the radial and tangential velocity, respectively.

$$u_r = U\left(1 - \frac{R^2}{r^2}\right) cos\theta \tag{2.1.24}$$

$$u_\theta = -U\left(1 + \frac{R^2}{r^2}\right) sin\theta \tag{2.1.25}$$

The total flow velocity around the cylinder (u_T) can be obtained from the vector composition of the radial velocity (u_r) and angular (u_θ). An example of its spatial distribution, obtained by the author, considering the axis of symmetry of the cylinder is illustrated in Figure 2.2.

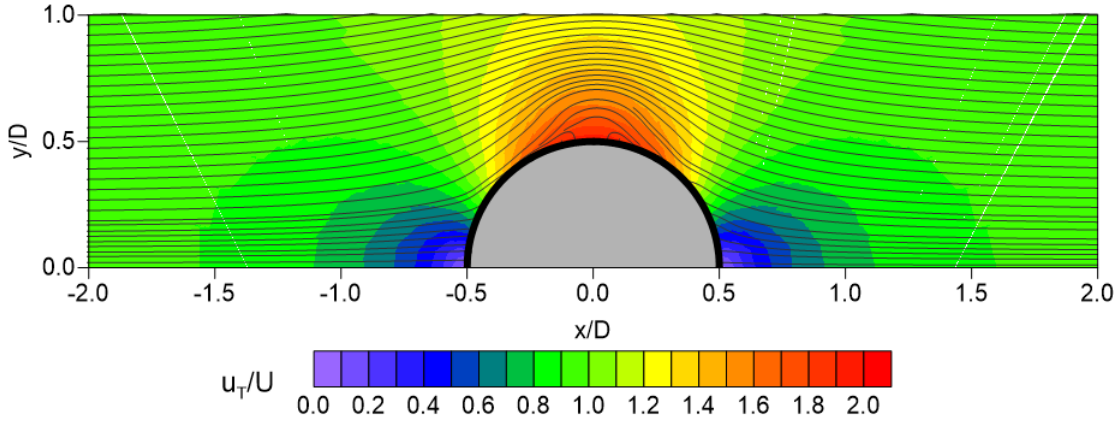

Figure 2.2: Potential flow around a cylinder, adapted from Hoffman et al. (2016).

According to the solution of the potential flow around a cylinder, there are two stagnation points: one in the upstream sector and another downstream. Additionally, two zones of flow intensification are produced on the side faces of the cylinder, which are generated by the narrowing of the flow lines.

By analyzing in detail the total dimensionless velocity (u_T/U) on the face of the cylinder ($r = R$), it can be seen that for $\theta = 90°$ the highest intensifications are obtained, doubling the approach speed (U), which, consequently, will produce an increase in the shear stresses in the bed (see Figure 2.3).

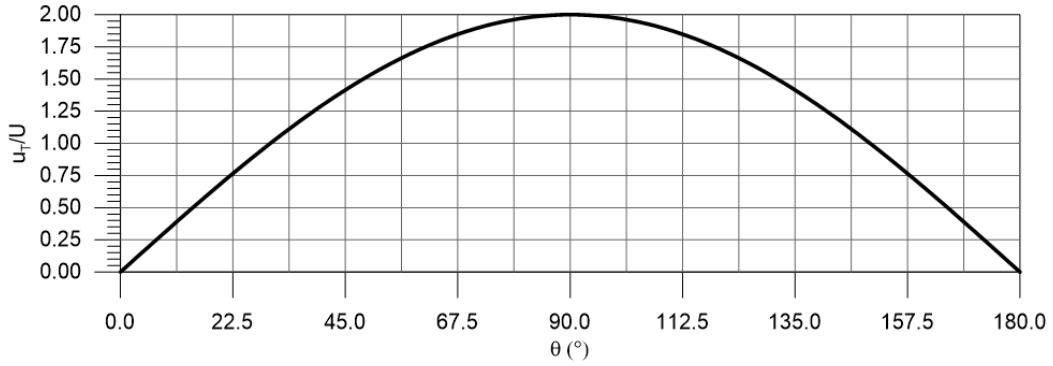

Figure 2.3: Total dimensionless speed on the face of the cylinder ($r = R$), adapted from Hoffman et al. (2016).

2.1.4 Experimental studies of flow around a cylinder in steady current

In addition to the description of the potential flow around a circular pile, several authors have carried out their investigations to characterize the flow based on a fluid that has viscosity and therefore, the simplification of irrotationality no longer applies.

In this section experimental aspect of the of the hydrodynamic behavior of flow past a cylinder are presented.

Experimental studies

The hydrodynamic behavior of a flow interaction with a cylindrical pile, has been widely characterized for permanent uniform flow through experimental work by many authors (Tritton, 1959; Roshko, 1961; Baker, 1979, 1980; Dargahi, 1987, 1989; Sumer and Fredsøe, 1997; Hamill, 1998; Ahmed and Rajaratnam, 1998; Graf and Yulistiyanto, 1998; Sumer and Fredsøe, 2006; Dey and Raikar, 2007; Chen et al., 2019).

When a vertical pile is incorporated in an alluvial channel flow with a bed of sediment, it corresponds to an obstruction to the free flow and produces significant effects in the natural hydrodynamic of the flow. In Figure 2.4 the main effects produced on the flow are presented (modified from Hamill, 1998). Additionally, a scour hole generation is identified.

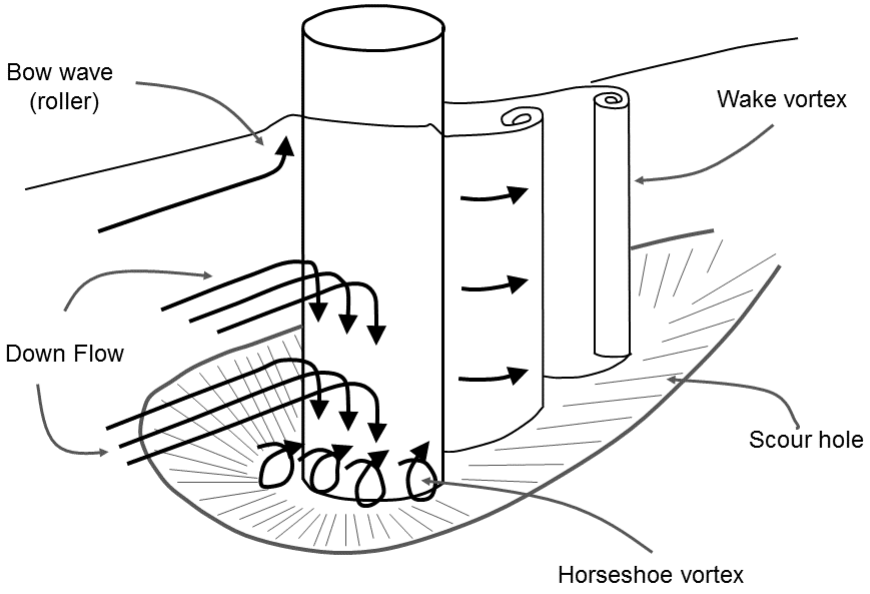

Figure 2.4: Hydrodynamic behavior of flow interaction with a cylindrical pile and the bed expected reaction (modified from Hamill, 1998).

The obstruction interact with the flow and produces a stagnation point, meaning, the velocity in the flow direction is unable to penetrate the object, reach an equal to zero magnitude, which produce a momentum imbalance. In response to that, the fluid pressure increases, producing two main effects:

- Fluid surface: A superelevation of the flow level in the upstream part of the obstruction is produced (Baker, 1979, 1980; Dargahi, 1987, 1989; Hamill, 1998; Ahmed and Rajaratnam, 1998; Unger and Hager, 2007; Muzzammil and Gangadhariah, 2003).

- Water column: Downflow is produced in the vertical, which interacts directly with the bed and the inccoming boundary layer (Baker, 1979, 1980; Dargahi, 1987, 1989; Hamill, 1998; Ahmed and Rajaratnam, 1998; Unger and Hager, 2007; Muzzammil and Gangadhariah, 2003).

These two pressure effects produce the so-called horseshoe and wake vortices, which are the main responsible of the bed scour, together with the flow lines contraction on the obstruction sides (Melville, 1975; Ettema, 1980; Chiew and Melville, 1987; Dargahi, 1987, 1990; Melville and Coleman, 2000; Sumer and Fredsøe, 2002; Sheppard et al., 2004).

In order to hydrodynamically describe the vortices produced in flow-structure interaction, dimensionless numbers dominating the studied situation are used. They are described below.

Sumer and Fredsøe (2002) states that the following dimensionless numbers are relevant in the horseshoe vortex analysis:

- $\frac{\delta}{D}$: Proportion between boundary layer thickness and pile diameter.

- Re_D or Re_δ : Reynolds Number of the pile or the boundary layer.

- Pile Geometry.

Several authors have linked the proportion between the boundary layer thickness (δ) and the pile diameter (D) to the existence of the horseshoe vortices or the absence of them, as well as to the determination of its eventual starting point (Baker, 1979, and Sumer et al., 1997 in Sumer and Fredsøe, 2002), as shown in Figure 2.5. From this figure, it can be noted that a proportion $\frac{\delta}{D}$ tending to low values, will reduce the horseshoe vortex magnitude.

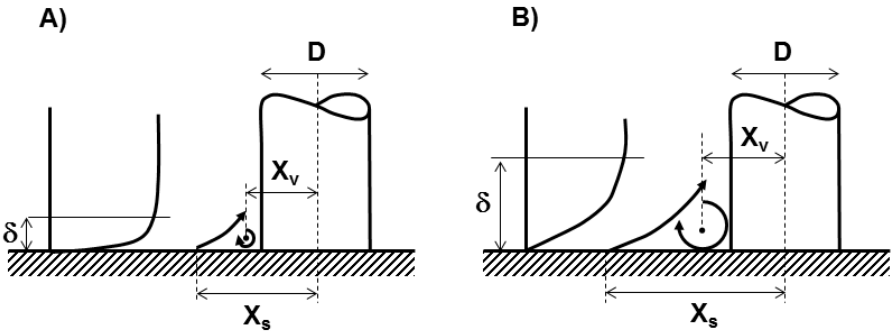

Figure 2.5: Effects of $\frac{\delta}{D}$ in the horseshoe vortices development (Sumer and Fredsøe, 2002). A) Vortex absence and B) Vortex generation.

Reynolds number is also an indicator of the horseshoe vortex generation or absence, since when values are low the effects of the boundary layer does not allow its separation and subsequent development of the vorticity (Sumer and Fredsøe, 2002).

Baker (1979) based on the pile Reynolds number (Re_D) assessed the location of the horseshoe vortex (x_v) for the case of the laminar boundary layer, concluding that the smaller Re_D

the smaller the value of $\frac{x_v}{D}$. But, for the case of turbulent boundary layer, the role of the Reynolds number of the pile may be reversed, that is, the size of the horseshoe vortex ($\frac{x_v}{D}$) may decreased with increasing Re_D.

The behavior of the turbulent horseshoe vortex was explained by Baker (1980), who said that the increment of the momentum exchange due to the turbulent behavior of the boundary layer, produce a delay of the boundary layer separation and due to this is one of the main source flow that produce the horseshoe vortex (the other one is the downflow), decrease the vortex size ($\frac{x_v}{D}$).

In the case of the wake vortex (see Figure 2.4), the main dimensionless numbers that describe the behavior is the Reynolds number of the pile (Re_D) according to Sumer and Fredsøe (1997).

A detailed description of the Reynolds number influence in the wake vortices formation is presented in Figure 2.6, which has been adapted by Sumer and Fredsøe (1997). According to the hydrodynamic behavior, five stages of the flow/pile interaction can be described:

- Subcritcal: Occurs when in both sides of the pile, a laminar boundary layers separation is produced.
- Critical (lower transition): Occurs when one side of the pile have a laminar boundary layer separation, meanwhile the other one is a turbulent boundary layer separation, but the incomming boundary layer are laminar.
- Supercritical: Occurs when in both sides of the pile, a turbulent boundary layer separation is produced, but the incomming boundary layer are laminar.
- Upper transition: Occurs when one side of the pile have a turbulent boundary layer separation, but the incomming boundary layer are laminar; meanwhile the other one is completely turbulent.
- Transcritical: Ocurrs when in both sides of the pile, a boundary layer completely turbulent is produced.

In Figure 2.6 instants are noticed which are typical of the flow interaction with a cylindrical obstruction. Box A) corresponds to the reaction obtained for a flow with $Re_D < 5$, where no boundary layer separation exists. Nevertheless, when the velocity increases and the Reynolds Number goes around 5 and 40 ($5 < Re_D < 40$), the first wake vortices start developing with symmetrical and laminar features (box B).

In box C, development of wake vortices of laminar characteristics are shown. Condition presented in case of Reynolds between 40 and 200 ($40 < Re_D < 200$). The beginning of the transition to turbulent regimen is produced in box D, where a higher flow velocity is presented ($200 < Re_D < 300$).

The development of the wake vortices in completely turbulent regimen is presented for Reynolds numbers between 300 and 3×10^5 ($300 < Re_D < 3\times10^5$), nevertheless, the separation of the cylinder boundary layer (points **a** in box E) is laminar. This condition of flow is classified by Sumer and Fredsøe (1997) as subcritical.

When the Reynolds number slightly increases ($3 \times 10^5 < Re_D < 3.5\times10^5$), it is produced the boundary layer separation in a turbulent manner (point **b** in box F) only in one side of the cylinder, while the other remains with its laminar characteristics. This situation is called the critical flow with low transition (Sumer and Fredsøe, 1997).

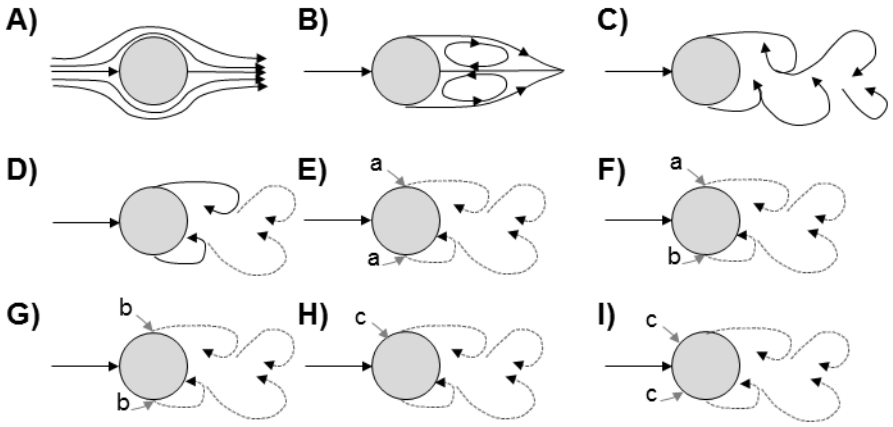

Figure 2.6: Description of wake vortices development around the cylindrical obstructions (adapted from Sumer and Fredsøe, 1997), where **a** is the laminar boundary separation, **b** the turbulent boundary layer separation, and **c** the boundary layer completely turbulent.

Turbulent separation of the boundary layer in both sides is produced for a range of Reynolds number given by $3.5 \times 10^5 < Re_D < 1.5 \times 10^6$, which is commonly classified as super-critical condition, nevertheless, the boundary layer around the cylinder (upstream) behaves laminar (see box G).

Transition to boundary layer and its completely turbulent separation begins for a Reynolds range given by $1.5 \times 10^6 < Re_D < 4.0 \times 10^6$, solely developing in one of the cylinder edges (see point **c** in box H). This situation is classified as transition and reaches full development for $Re_D > 4.0 \times 10^6$, where both sides of the cylinder are governed by the turbulence (box I).

2.2 General aspects about sediment transport

The hydrodynamics forces acting over the bed of an alluvial channel, a beach, or any other water body, develops shear stresses, friction, and turbulence. When these act on the sediment particles that constitute the bottom, the probability that they are mobilized begins to exist.

There are several criteria for the incipient motion initiation. However, the one developed around the work of Shields (1936) holds the greatest connotation worldwide. Shields proposes, for a free flow, a dimensionless relationship between its mobility parameter $\theta_{cr} = \frac{\tau_{cr}}{(\rho_s - \rho)gd}$ and the Reynolds number of the particle $Re*_d = \frac{u*d}{\nu}$, where τ_{cr} is the critical bed shear stress, ρ_s is the sediment density, ρ is the water density, g is the gravity, d is the sediment diameter, $u*$ is the frictional velocity at the bed, and ν is the kinematic viscosity.

In the case of free surface flows with the presence of obstructions or solid bodies, there are some approximations to movement initiation criteria such as the one proposed by Dargahi (1990) or Hager and Oliveto (2002), both for sediment particles that begin to move near a pile.

Some overall aspects of the movement initiation are outlined next.

2.2.1 Incipient motion due to free flow

Determining the hydrodynamic conditions for which the movement of the sediment particles that compose the bed initiates its motion corresponds to a major problem of the sediment transport studies.

Due to the incipient motion occurs in a small spatial scales, their experimental record becomes more complicated since the velocity sensors modify the free flow behavior on the bed and linked to this, modifed the hydrodynamics around the sediments particles too.

Based on the previous paragraph, is common to use a physical approach to define the forces that are needed to initiate the motions of the sediments by applying a force equilibrium system.

In uniform flow there are two main branches for the description of the initiation of movement or incipient motion of the sediments. One is based on the physical concept of balance of forces, while the other is based on stochastic characteristics of the process.

The incipient motion approach according to Van Rijn (1993b) was studied first by Brahms (1757), who proposed a potential relationship between the flow velocity and particles required weight in order to be stable, and subsequently by Du Buat (1816), who introduces the critical shear stress term for the first time in the description of the process.

However, for uniform flow, the mostly spread criterion for the motion initiation is presented by Shields (1936) in his doctoral thesis. Shields linked information of shear stress on the bed with the mobility ($\theta_{cr} = \frac{\tau_{cr}}{(\rho_s - \rho)gd}$) of the grains for different Reynolds numbers ($Re*_d = \frac{u_* d}{\nu}$) (consequently, different flow regimes), gathered from experimental tests. His main result is illustrated in Figure 2.7.

Shields (1936) proposed as a result of his research, a band in which the experimental data for different Reynolds numbers based on frictional velocity and the particle diameter, developed movement or incipient motion for the hydrodynamic conditions tested.

It is important to highlight that Shields (1936) determines the Reynolds number as a function of the frictional velocity, that is, the so-called u_*, which is widely used to describe the hydraulic resistance of alluvial channels.

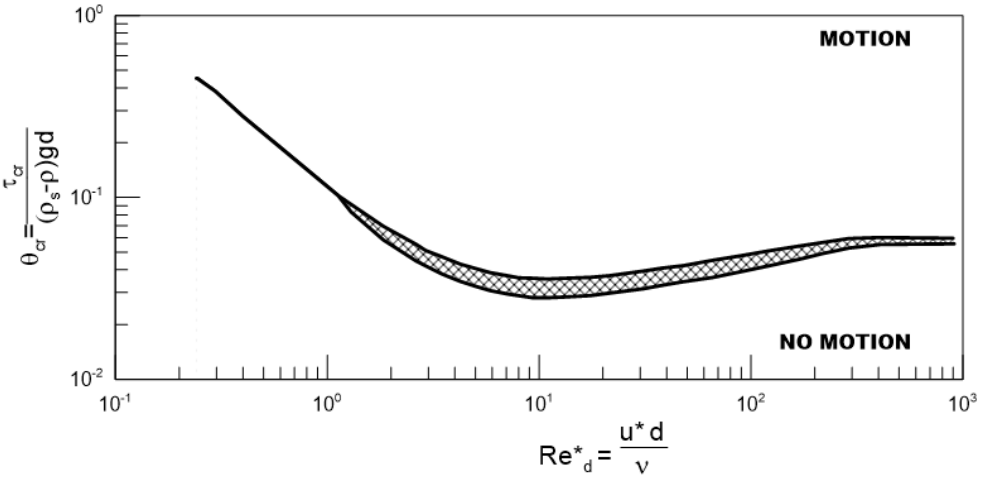

Figure 2.7: Incipient transport for uniform flow on a flat bottom, Shields (1936).

Grass (1970) introduces in the scientific debate, the concept of incipient transport from a stochastic approach, establishing that both the fluid by its turbulent behavior and the sediments by its granulometric composition, have, in fact, a probability distribution of shear

stress and that movement will occur not only when the average value is exceeded, but also when both distributions overlap.

In Figure 2.8 the concept of the incipient motion of sediments under the stochastic approach is illustrated using the τ_b nomenclature for the stress in the bed exerted by the fluid, considering the average velocity and τ_c for sediment critical stress provided by its average diameter and the relative position of the particle.

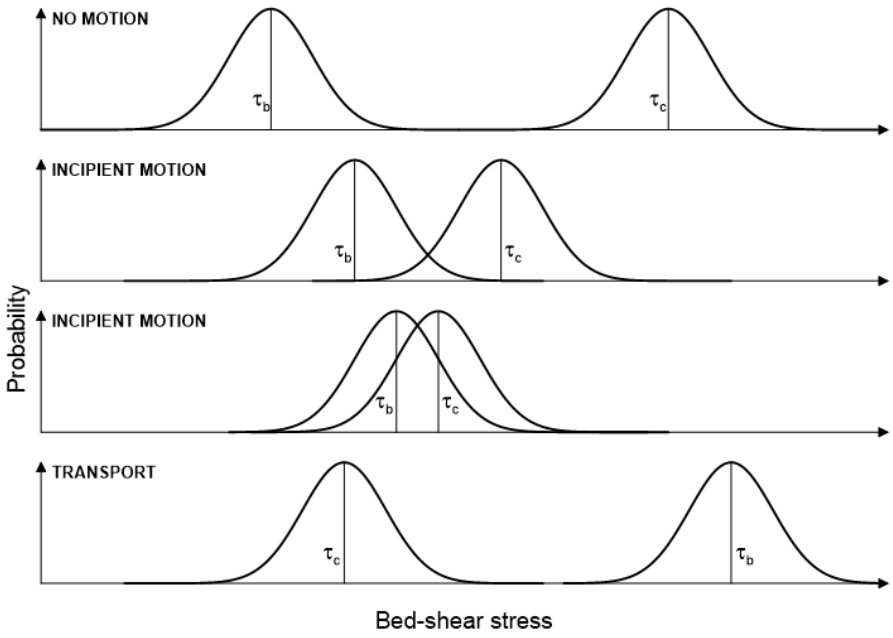

Figure 2.8: Incipient transport for uniform flow on a flat bottom, according to the stochastic approach proposed by Grass (1970).

Dey and Papanicolaou (2008) indicate that the investigation of incipient transport under the stochastic approach continued its development over time, highlighting the works of Mingmin and Qiwei (1982) and Wu and Chou (2003). In the case of the Mingmin and Qiwei (1982), they proposed a probabilistic model expressing both the behaviour of velocities near the bottom and the sediments that compose it.

On their part, Wu and Chou (2003) studied the probability distributions associated with the rolling and suspension of the sediment particles, which are incorporated into the flow due to its turbulent fluctuations. These were associated by two criteria of incipient transport and critical entraiment threshold, which was linked to the Reynolds number.

Most of the work conducted to obtain incipient motion conditions has mainly considered an experimental approach. Nonetheless, there are some recent publications that incorporate governing equations to determine the incipient sediment transport conditions based on two-phase equations, such as the study proposed by Meruane et al. (2015), who develops a physical mathematical representation of the sediment drag for a bed of homogeneous granular material, validating its results with the curve of Shields (1936).

The main results obtained by Meruane et al. (2015), indicate that there is a proper adjustment between the calculated values and those indicated by Shields (1936) for low Reynolds numbers. However, as the turbulence becomes more important in the flow, a divergence between the set of data and the mathematical model occurs, attributing this to the drag force

and the closing model used for the turbulence simulation ($K-\epsilon$, which will be described in the next chapter of this thesis), which are linked by the work done on the particle.

Experimental investigations for the determination of the threshold of incipient motion under oscillatory flow begin with the study carried out by Bagnold and Taylor (1946), who analysed the formations of *ripples*, both from a morphodynamic point of view and the flows near the bed.

Bagnold and Taylor (1946), as an additional result of the study of *ripples* formations for oscillatory flow, presented an approximation for the determination of the velocity threshold on the bed for which the grains begin to move and rearrange, being accepted as the first criterion of incipient transport in oscillatory flow.

Following Bagnold and Taylor (1946) work, several authors made proposals to determine the threshold of incipient movement under oscillatory flow considering both laminar and turbulent regime in laboratory tests. The main results were compiled by Silvester and Mogridge (1970), highlighting that all of them are based on the maximum orbital velocity in the bed, which is defined according to equation 2.2.1, where H is the wave height, T_w the wave period, k_L the wave number and h is the water depth.

$$U_m = \frac{H\pi}{T_w sin(k_L h)} \tag{2.2.1}$$

Komar and Miller (1973) are the first authors to propose an incipient transport criterion based on the number of Shields (1936), applying results obtained from previous studies: Bagnold and Taylor (1946) and Manohar (1955), and considering that the maximum horizontal velocity of the oscillatory flow on the bed is responsible for mobilizing the particles.

Following the Shields (1936) research, Naheer (1978) develops an experimental study to obtain an empirical relationship that describes for which conditions the superficial rocks of a seabed are set in motion, when the forcing action of a solitary wave is considered.

One of the first field experiments aimed at determining the sediments incipient movement threshold due to the action of irregular waves was the one executed by Davies (1985) on the beach of Blackpool Sands, Start Bays, Devon, England. The measurements were made with an experimental assembly based on video cameras that obtained the particles movement in real time. The currents were recorded using flow meters located on the beach, from which the frequency spectrum of the incident wave was obtained, and pressures on the bed were measured with a transducer.

Davies (1985) uses, as a comparison base, the criteria for incipient motion proposed by Bagnold and Taylor (1946), Manohar (1955) and Komar and Miller (1973), concluding that there is a difference with field data (movement registered in video) of an order of magnitude. This is an evidence that the complexity of determine the incipient motion of the sediment.

Similar work to the one developed by Komar and Miller (1973) is carried out by Van Rijn (1993a), who re-analyzing experimental data from other authors, proposes an expression of the Shields type, considering that the critical tension must be estimated with the information of the friction factor of the oscillatory flow on the bed.

Although, the work of Van Rijn (1993a) establishes that the criterion of Shields (1936) can be used in the definition of the threshold under an oscillatory flow (which is sufficient for practical purposes), several investigations continued to analyze this problem and new authors proposed their own equations. Beheshti and Ataie-Ashtiani (2008) present a summary of the main criteria of incipient transport under oscillatory flow.

2.2.2 Incipient motion near to flow obstruction

The criteria for the beginning of motion, outlined in the previous section, consider, as the main characteristic, that the environment where the incipient motion will occur contains only sediments and a flowing fluid. However, there exist several approaches and investigations that describe this process when obstacles, or opaque bodies, are immersed in the flow, modifying the flow and thus modulating in different ways the incipient motion of sediments.

In this section, various criteria and studies of the incipient motion are described, when obstructions on a spatial scale of the grain size (vegetation effect) or scale of the flow (pile effect) exist.

Rigid vegetation effect over incipient motion

One of the first approaches to the study of the critical shear stress in vegetation beds was developed by Nagy and Watanabe (2000), who based on experimental data conclude that the critical shear stress increases depending on the vegetation density present during the test. Subsequently, Watanabe et al. (2002) through experimental work analyses the threshold motion using results obtained from 53 tests, considering textural ranges of the sediments that covered diameters equal to 0.335, 0.701, 0.987 and 1.29 mm, for an approximate range of Reynolds numbers of particles ($Re*_d$) from 10^1 to 10^2.

When comparing the results previously published by Shields (1936) with those obtained by Watanabe et al. (2002), they describe that in the presence of vegetation on the bed, the incipient motion requires higher shear stresses, as can be seen in Figure 2.9.

Figure 2.9 shows the relationship between the Reynolds numbers of particles ($Re*_d$) and the mobility parameter (θ_{cr}) for two diferents cases, the first one obtained by Shields (1936) (black line in Figure 2.9) for a free stream case and the second one obtained by Watanabe et al. (2002) (black dots in Figure 2.9) for a flow with vegetation beds.

As can be seen from Figure 2.9, Watanabe et al. (2002) data needs greater mobility parameter for the incipiente motion at same Reynolds numbers of particle as Shields (1936) data. That is to say, that for a vegetated bed the flow require greater bed shear stress to produce the incipient motion of the sediments particles, in comparison with a non-vegetated bed.

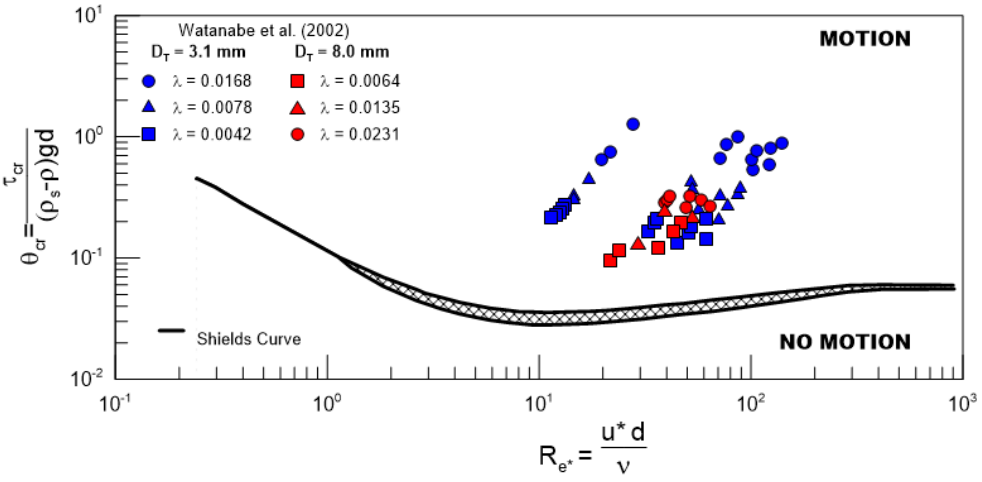

Figure 2.9: Comparison between the data obtained by Watanabe et al. (2002) and Shields (1936) curve for the movement threshold.

The key results obtained by Watanabe et al. (2002) showed that shear stress was influenced by the density of plants (λ) and the ratio of the number of plant along a cross-sectional distribution to trunk diameter (D_T).

Although, the works of Nagy and Watanabe (2000) and Watanabe et al. (2002) provide approximations to the critical shear stress that initiates the movement of sediments based on experimental data, it is not until the work of Hongwu et al. (2013) where a theoretical development that tries to describe the critical velocity of sediments incipient motion is proposed.

Hongwu et al. (2013) using a momentum balance based on the drag force (F_D), lift force (F_L) and buoyant weight of sediments (W'), establish that the critical velocity can be estimated with an equation similar to the expression 2.2.2.

$$u_{pc} = f\left(\frac{h}{D_s}, \frac{d_{50}}{D_s}, \lambda\right) u_c \tag{2.2.2}$$

where u_{pc} is the spatially averaged critical velocity including the vegetation, h flow depth, D_s stem diameter, d_{50} mean sediment grain size, λ area concentration of stems and u_c critical velocity of sediment according to Kramer (1935) which produce the incipient motion.

The effect of vegetation on the incipient transport of sediments proposed by Hongwu et al. (2013) is presented in the equation 2.2.3 and although it has been obtained through experimental work, all the tests were conducted for values of λ <0.1, in such a way that the results proposed by Hongwu et al. (2013) require more research to cover a greater range of stems concentration area.

$$f\left(\frac{h}{D_s}, \frac{d_{50}}{D_s}, \lambda\right) = 0.316 \left(\frac{D_s\sqrt{\frac{\frac{\pi}{4}-\lambda}{\lambda}}}{\sqrt{h d_{50}}}\right)^{0.319} \tag{2.2.3}$$

Continuing with the theoretical development to determine an expression capable of representing the incipient motion, incorporating the presence of rigid vegetation, Wang et al. (2014) develop an experimental study to investigate the bed resistance with vegetation using circular cylinders to represent plant stems and the incipient motion of the sediment without the presence of vegetation.

Wang et al. (2014) focused the analysis on the determination of the shear stresses that act on the bed in presense of vegetation. In this way, they established relationships for the incipient motion, based mainly on hydraulic definitions of the flow. Wang et al. (2014) define the streamwise component of the water weight per unit of bed area (τ_w) according to equation 2.2.4, where J is the energy slope and all the other variables have been previously defined.

$$\tau_w = \rho g J h (1 - \lambda) \tag{2.2.4}$$

The shear stress associated with the hydraulic resistance imposed by the vegatation on the bed, suggested by Wang et al. (2014) is determined according to the equation 2.2.5, where C_{dv} is the vegetation drag coefficient defined according to equation 2.2.6, N is the number of stems per unit plant area of the bed, and all the other variables have been defined previously.

$$\tau_v = \frac{1}{2}\rho C_{dv} N D_S h u^2 \tag{2.2.5}$$

$$C_{dv} = \frac{90}{\sqrt{R_v}} + 4.5\frac{D_s}{h} - 0.303\ln(\lambda) - 0.9 \tag{2.2.6}$$

$$R_v = \frac{(1-\lambda)uh}{\nu} \tag{2.2.7}$$

where R_v is the vegetation Reynolds number.

Based on these definitions, Wang et al. (2014) establishes that the shear stress necessary to produce the incipient motion can be estimated as $\tau_{bc} = \tau_w$ - τ_v.

As a key result of his research, Wang et al. (2014) compare the necessary shear stress to initiate the movement (τ_{bc}) and the shear stress associated with the vegetation (τ_{vc}), as well as the shear stress necessary to initiate the movement (τ_{bc}) and the critical shear stress with the sediments without vegetation (τ_{gc}), determined according to the criterion of Shields (1936), for differents area concentration of stems (λ), which are presented below in Figure 2.10.

From the analysis of the Figure 2.10, it can be noticed that in all the cases that Wang et al. (2014) analized, the proportion $\frac{\tau_{bc}}{\tau_{vc}}$ was less than one. Thats mean that the bed shear stress associated to the hydraulic resistance imposed by the vegetation on bed (τ_{vc}), was greather than the bed shear stress needed to produce the incipient motion of sediment particles (τ_{bc}).

Additionaly, from Figure 2.10 the proportion $\frac{\tau_{bc}}{\tau_{gc}}$ was greather than one in all the cases studied by Wang et al. (2014), that is to say that the bed shear stress necesary to produce the incipient motion of sediment particles in a vegetated bed (τ_{bc}) must be greather than an non-vegetated bed for the same sediment particles (τ_{gc}). These results are concordant with the presented by Watanabe et al. (2002) and Hongwu et al. (2013), and with the previusly showed in Figure 2.9.

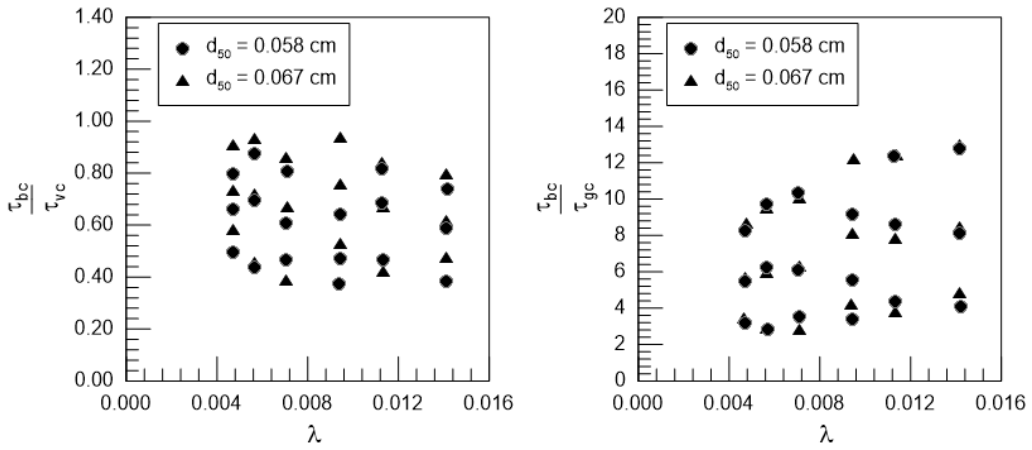

Figure 2.10: Comparison of shear stress associated with incipient motion, vegetated resistance and grain shear stress, adapted from Wang et al. (2014).

Pile effect over incipient motion

The determination of the sediment incipient transport due to the action of permanent flow without obstructions in alluvial channels has been previously studied by Shields (1936), which is widely accepted and applied (Hager and Oliveto, 2002).

One of the complications presented by Shields (1936) work is its direct application to the determination of incipient transport, because in both axes of its abacus the frictional critical velocity is present (u^*). However, these difficulties have been addressed by different authors, by including the dimensionless diameter of the sediments (D_*) defined by equation 2.2.14; such is the case of Bonnefille (1963) and Yalin (1972), which are described in Van Rijn (1993b).

Although, the critical values proposed by Shields (1936) are currently applied to the estimation of incipient motion around a pile, theoretically its application is not correct given that the threshold values of movement were obtained for a flow free from obstruction.

Dargahi (1990), through experimental analysis, suggests that the scour at the bottom of the pile in the upstream section would be the result of the following factors:

1. The vorticity system.
2. The impact of high-momentum flow during the in-rush phase on the bed.
3. The high turbulence level and a periodical motion associated with the horseshoe vortex.

According to Dargahi (1990), the influence of turbulence intensity on the movement of sediment particles can be demonstrated by means of a simple stability analysis, which includes the root mean squares of the turbulent fluctuations velocities (u') within the definition of the drag force.

The free body diagram proposed by Dargahi (1990) is illustrated in Figure 2.11, while the acting forces are described in the equations 2.2.8 for the drag force and equation 2.2.9 for buoyant weight. Where C_d is the drag coefficient, A is the projected sediment area, $\bar{U}$ the mean velocity, and all the other parameter have been defined previously.

$$F_D = C_d A \rho \left(\bar{U} + u'\right)^2 \tag{2.2.8}$$

$$F_W - F_B = g\left(\rho_s - \rho\right)\left(\frac{\pi}{6}\right) d_{50}^3 \tag{2.2.9}$$

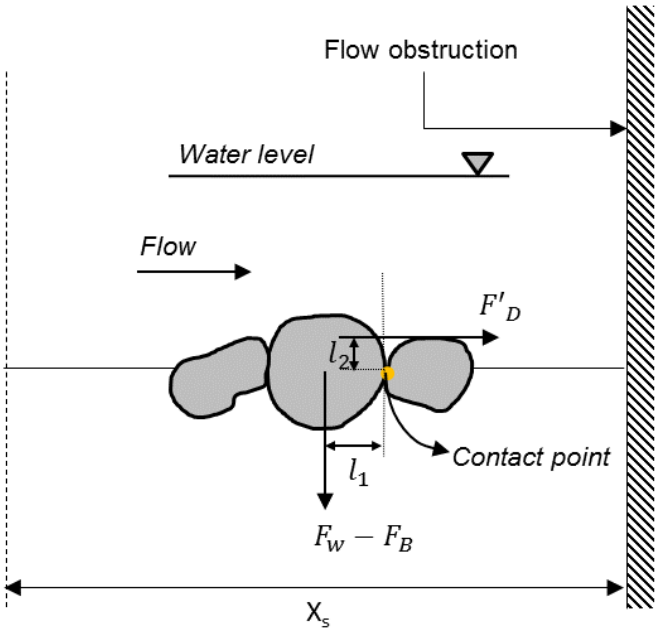

Figure 2.11: Diagram of acting forces, considering the presence of flow obstruction and turbulent fluctuations according to the proposal by Dargahi (1990).

Considering the equations 2.2.8 and 2.2.9, expanding them and taking moment with respect to the point of contact (see Figure 2.11), the critical mean velocity is obtained according to

equation 2.2.10, where $r = u'/\bar{U}$ is the relative turbulence intensity and $S = \rho_s/\rho$, α is the angle of repose.

$$\bar{U_c} = \left(\frac{1}{1+r}\right)\left[\frac{4g(S-1)}{6C_d} d_{50}\ tan\alpha\right] \tag{2.2.10}$$

The equation 2.2.10 state that the higher the turbulence intensity, the lower the critical velocity for the particle movement.

Although, the work of Dargahi (1990) has been used by different authors (Olsen and Melaaen, 1993; Dey et al., 1995; Olsen and Kjellesvig, 1998; Brørs, 1999; Ali and Karim, 2002; Ettema et al., 2006; Kirkil et al., 2008; Escauriaza and Sotiropoulos, 2011b) to describe the flow around circular piles, their incipient transport criteria has been less used in the estimation of scour in piles.

Later Kothyari et al. (1992) based on experimental results of other authors, proposed an equation for the determination of the critical velocity of the sediment movement initiation, as a function of the diameter of the pile (D), sediments diameter (d_{50}), specific weight of sediments (γ_s) and the fluid (γ), fluid density (ρ) and flow depth (h), as shown in the equation 2.2.11.

$$\frac{U_c^2}{\frac{\gamma_s-\gamma}{\gamma} g d_{50}} = 1.2\left(\frac{D}{d_{50}}\right)^{-0.11}\left(\frac{h}{d_{50}}\right)^{0.16} \tag{2.2.11}$$

An approach based on the modification of Shields number to incorporate the effects of the pile on the sediments incipient transport was proposed by Hager and Oliveto (2002) who based on laboratory tests and classic dimensionless numbers of hydraulics, such as Froude number, proposes criteria for the mobility of sediments at the toe of a pile.

As previously commented, one of the complexities presented in Shields (1936) work is its direct application to the incipient motion, due to in both axes of his abacus the frictional critical velocity (u^*) is present. However, Hager and Del Giudice (2000) presents a parametrization of the Shields curve split in three intervals, according to what is shown in the equation 2.2.12.

$$T_i = \begin{cases} 0.120 D_*^{-1/2} & D_* \leq 10 \\ 0.026 D_*^{1/6} & 10 < D_* < 150 \\ 0.060 & D_* \geq 150 \end{cases} \tag{2.2.12}$$

where Ti corresponds to the critical Shields number defined according to the expression 2.2.13, while the dimensionless diameter (D_*) through the expression 2.2.14.

$$T_i = \frac{\tau_{50i}}{(\rho_s - \rho) g d_{50}} \tag{2.2.13}$$

$$D* = \left(\frac{g'}{\nu^2}\right)^{1/3} d_{50} \tag{2.2.14}$$

with g' equal to the reduced gravity determined according to the expression 2.2.15.

$$g' = \left(\frac{\rho_s - \rho}{\rho}\right) g = \rho' g \tag{2.2.15}$$

From the previous expressions, Hager and Del Giudice (2000) develop a transformation of the number of Shields based on the incorporation of the Froude number, whose analytical development is presented below.

Considering that the stress on the bed can be determined by using characteristic parameters of the channel ($\tau = \rho g R_h S_0$) as the hydraulic radius (R_h) and the slope (S_0), the equation 2.2.16 can be obtained.

$$T_i = \frac{R_h S_0}{\rho' g d_{50}} \tag{2.2.16}$$

To separate the energy slope and incorporate the Froude number in the Shields number, the so-called Manning-Strickler equation is used to compute the streamflow velocity according to the following equation 2.2.17, which allows rewriting the number of Shields according to the equation 2.2.18.

$$V_i = \left(\frac{1}{n}\right) S_0^{1/2} R_h^{2/3} \tag{2.2.17}$$

$$T_i = \left(\frac{V_i n}{R_h^{2/3}}\right)^2 \left(\frac{R_h}{\rho' d_{50}}\right) \tag{2.2.18}$$

The Froude number used by Hager and Del Giudice (2000) is the densimetric particle Froude number defined according to equation 2.2.19.

$$F_{di} = \frac{V_i}{\sqrt{g' d_{50}}} \tag{2.2.19}$$

Considering the equations 2.2.17, 2.2.18 and 2.2.19, it is easy to see that the Froude number can be rewritten according to the equation 2.2.20, where equation 2.2.22 can be obtained if the approximation of the Manning coefficient is incorporated as a function of the diameter of the sediments (equation 2.2.21).

$$F_{di} = T_i^{1/2} \left(\frac{\rho'}{g'}\right)^{1/2} R_h^{1/6} \left(\frac{1}{n}\right) \tag{2.2.20}$$

$$\left(\frac{1}{n}\right) = 6.75 g^{1/2} d_{50}^{-1/6} \tag{2.2.21}$$

$$F_{di} = T_i^{1/2} \left(\frac{\rho'}{g'}\right)^{1/2} R_h^{1/6} 6.75 g^{1/2} d_{50}^{-1/6} \tag{2.2.22}$$

Algebraically simplifying the equation 2.2.22, the following expression is obtained, which determines the Froude number according to a sedimentological (T_i) and hydraulic variable $\left(\frac{R_h}{d_{50}}\right)$.

$$F_{di} = 6.75 T_i^{1/2} \left(\frac{R_h}{d_{50}}\right)^{1/6} \tag{2.2.23}$$

Eventually, the expression 2.2.23 can be incorporated in the incipient transport criterion, parameterized by Hager and Del Giudice (2000), obtaining what is shown in the equation 2.2.24.

$$F_{di} = \begin{cases} 2.34 D_*^{-1/4} \left(\frac{R_h}{d_{50}}\right)^{1/6} & D_* \leq 10 \\ 1.09 D_*^{1/12} \left(\frac{R_h}{d_{50}}\right)^{1/6} & 10 < D_* < 150 \\ 1.65 \left(\frac{R_h}{d_{50}}\right)^{1/6} & D_* \geq 150 \end{cases} \tag{2.2.24}$$

The parameterization shown in the equation 2.2.24 corresponds to an approximation for the determination of incipient transport, applying characteristic parameters of the sediments that compose the bottom and, additionally, characteristics of the stream flow through the hydraulic radius. However, it is not able to represent the effect of obstructions in the flow, as would be the case of a pile.

To incorporate the presence of an obstruction in the incipient transport, Hager and Oliveto (2002) propose the incorporation of the proportion of the densimetric Froude number (equation 2.2.19, with the cross-sectional velocity) and the incipient one (equation 2.2.19), according to the equation 2.2.25.

$$\phi_B = \frac{F_d}{F_{di}} \tag{2.2.25}$$

The form adopted by ϕ_B depends on the type of obstruction that is being evaluated, however, it can be written in a general manner according to the equation 2.2.26.

$$\phi_B = 1 - \frac{2}{3}\Sigma\beta^{\Sigma/4} \tag{2.2.26}$$

Where Σ corresponds to the shape factor that, for circular piles is equal to 1, while for an abutment is equal to 5/4. β is the coefficient of contraction, which is defined as the ratio of the pile diameter or width of the abutment, with the width of the channel.

From the equation 2.2.26, it is easy to see that when there is no pile or abutment, $\phi_B = 1$ and, therefore, from the equation 2.2.25 is obtained that the critical Froude can be estimated according to Shields criteria.

One of the biggest differences between the work of Dargahi (1990) and Hager and Oliveto (2002), is based on the fact that the first one considers that the obstruction is relevant in the incipient transport due to the turbulence induced in the flow, while the second, summarizes these effects in a proportion coefficient that simulates physics, but does not explain it.

2.2.3 Experimental studies of sediment transport near to a pile

The sediment transport near a pile or other solid structure immersed in the flow is usually determined by the use of formulations obtained for flows without obstructions as the classical equations of Meyer-Peter and Müller (1948) or Engelund and Fredsøe (1976), and the characterization of the flow through hydraulic parameters (average velocity or shear stress).

Currently, the solution of hydrodynamics around the cylindrical body is usually estimated by the numerical solution of the Reynolds Averaged Navies Stokes Equations (RANS), Large Eddy Simulation (LES) or Direct Numerical Simulations (DNS). Numerous applications are available in the literature, such as Liu and García (2008), Baranya et al. (2012), Baykal et al. (2015), Quezada et al. (2018), among others.

However, there are some studies aimed at improving or proposing new methodologies for the computation of sediment transport, which allows explicitly incorporate the effects of flow obstruction, which have been developed experimentally and also numerically; some basic aspects from just for the experimentally approach are presented below.

Sediment transport in the vicinity of flow obstructions has been addressed through studies related to scour around piles or in an abutment. However, to date there are no studies aimed at determining the equations that can model the dynamics of particle movement.

An approximation to the description of the dynamics of sediments motion around the flow obstructions is presented by Dargahi (1990) who, through extensive laboratory work, describes

in a conceptual manner the development of the vortices and additionally the scouring process that occurs.

Based on experimental results, Dargahi (1990) describes that the behavior of the horseshoe vortex produces quasi-periodic forces with a complex turbulent behavior, due to the variability of scales that control the process. Additionally, the author states that the scour does not begin until the vorticity is fully developed.

According to Dargahi (1990) the system of vortices that develops around the flow obstructions is responsible for mobilizing the sediments and the beginning of the scouring process.

From the measurement of scour profiles, Dargahi (1990) proposes a solid discharge equation across the upstream plane symmetry as a function of the time, according to the equation 2.2.27 (valid for $\frac{t_s}{t_f} > 0$) in which t is the scour time, t_f is the final scour time, q_s and $q_{s,f}$ rates of local transport per unit length at t and t_f, respectively.

$$\frac{q_s}{q_{s,f}} = A + B \cdot log\left(\frac{t}{t_f}\right) \tag{2.2.27}$$

Three main aspects of the equation 2.2.27 are described by Dargahi (1990) and are summarized below:

- The maximum rate occurs at about $\frac{t_s}{t_f} \approx 0.02$
- The rate fluctuates in the time interval $0.1 < \frac{t_s}{t_f} < 0.5$
- A more or less steady state is approached as $\frac{t_s}{t_f} \to 1$

The coefficients A and B of the equation 2.2.27 adopt values in terms of describing the area of scour or deposit. When there is scour $A = 0.37$ and $B = 0.20$, while in the deposit sector $A = 0.90$ and $B = 0.44$.

Dou and Jones (2000) on the basis that there is no extensive literature available in formulas for the transport of sediments in areas close to obstructions such as piles or abutment, proposes a new equation using previous results (Dou, 1974) and suggesting a new definition called the effective sediment transport capacity.

According to Dou and Jones (2000), the sediment transport capacity (STC) can be obtained by the application of the equation 2.2.28, where U is the depth-averaged velocity, h the flow depth, ω is the fall velocity of the sediment, g is the gravitational acceleration and f_0 is a coefficient depended on the Chezy number, sediment and water densities (for more details, see Dou and Jones, 2000).

$$STC = f_0 \frac{U^3}{gh\omega} \tag{2.2.28}$$

The equation 2.2.28 can not be applied to the estimation of the scour in piles, because it does not include in its formulation the mechanisms that produce it and, therefore, according to Dou and Jones (2000), must be adapted for that purpose, as expressed in the equation 2.2.29, which corresponds to the effective sediment transport capacity ($ESTC$).

$$ESTC = f_0 \frac{U^3}{gh\omega} + f_1 \chi \left[e^{-k\frac{y_s}{b}} + f_2\left(1 - e^{-k\frac{y_s}{b}}\right)\right] \tag{2.2.29}$$

$ESTC$ is a function of STC and a term that incorporates the effects of the pile acting on sediment transport, where f_1, f_2 and k are coefficients that must be experimentally determined. χ is a distribution parameter constructed by a linear average among three normalized

parameters which come directly from the magnitude of downflow, the strength of vortices and the turbulence intensity induced by the presence of a structure, y_s is the socur depth and b is the characteristic length.

Although, χ is a parameter that would vary between 0 (without obstruction) and 1 (total obstruction), its computation is complex and can be consulted in greater detail in Dou and Jones (2000), who suggests a methodology based on numerical models.

A methodology based on hydraulic parameters to determine sediment transport around a circular pile, corresponds to that proposed by Mia and Nago (2003), who based on a set of experimental data introduced a new equation, which is briefly described below.

Mia and Nago (2003) proposed the a parameter and the excess dimensionless tractive force at time t (s_t), both given by equation 2.2.30 and 2.2.31, respectively. Where $\theta_{cr} = \frac{\tau_{cr}}{(\rho_s - \rho)gd}$ is the critical mobility number, u_{*c} is the critical Shields bed-shear velocity computed by equation 2.2.32, and u_{*t} is the bed-shear velocity at the nose of pier at time t, computed accordding to equation 2.2.33.

$$a = 2.45 \frac{\sqrt{\theta_{cr}}}{\left(\frac{\rho_s}{\rho}\right)^{0.4}} \tag{2.2.30}$$

$$s_t = \frac{u_{*t}}{u_{*c}} - 1 \tag{2.2.31}$$

$$u_{*c} = \sqrt{\frac{\tau_c}{\rho}} \tag{2.2.32}$$

$$u_{*t} = \sqrt{\frac{\tau_t}{\rho}} \tag{2.2.33}$$

where τ_c is the critical shear stress of bed material and τ_t is bed-shear stress at the pier nose at time t.

From the equations 2.2.30 and 2.2.31, Mia and Nago (2003) propose the equation 2.2.34 to determine the solid flow rate as a function of time.

$$q_{st} = 1.80\ d_{50}\ u_{*t}\ s_t \left[1 - \frac{1}{as_t} ln\left(1 + as_t\right)\right] \tag{2.2.34}$$

The equation 2.2.34 compared to the equation 2.2.29, allows obtaining an estimate of solid flows based on classic hydraulic parameters, which are simpler to estimate with the characteristic scales of the experiment or project under analysis.

Recent investigations using Particle Image Velocimetry (PIV) have evaluated the influence of horseshoe vortex on the sediment transport and shear stress in front of a pile, as is the case of the investigation of Li et al. (2018), who by means of a statistical treatment of the turbulent fluctuations of the velocity, propose a formulation for the bed load estimation.

Li et al. (2018) proposed as a statistical indicator the relative magnitude of the shear stress (I_r), according to the equation 2.2.35 and where τ_{rms} corresponds to the root mean squares (RMS) value of turbulent shear stress on the bed and τ_m is the shear stress associated with the average velocity.

$$I_r = \left|\frac{\tau_{rms}}{\tau_m}\right| \tag{2.2.35}$$

Thus, Li et al. (2018) suggests that the instantaneous normalized sediment transport (q_n) can be estimated according to the equation 2.2.36, where q is the dimensionless instantaneous

sediment transport rates, q_m is the mean sediment transport rate, considering that q_n is obtained with a shear stress difference equation, according to the expression 2.2.37, where m is a function of the Reynolds number of the pile ($Re_D = \frac{U_m D}{\nu}$, which is estimated by the average velocity of the approaching flow) according to the expression 2.2.38.

$$q_n = \frac{q}{q_m} \tag{2.2.36}$$

$$q_n = exp\left[m\left(I_r - 0.44\right)\right] \tag{2.2.37}$$

$$m = 6.969 \cdot exp\left(-1.172 \times 10^{-4} Re_D\right) \tag{2.2.38}$$

To determine the transport associated with the average flow velocity (q_m), Li et al. (2018) propose to use the equation 2.2.39, where U_m is the depth average flow velocity, ρ the density of the fluid and τ_c is the incipient motion critical shear stress, which can be determined by the Shields criterion.

$$q_m = \frac{1}{U_m^3 \rho^{3/2}} \left(\tau_m - \tau_c\right)^{3/2} \tag{2.2.39}$$

2.3 Brief conclusion and research needs

After this extended literature review, it could be noticed that there are a large number of experimental studies that have allowed characterizing the flow around a circular piles, identifying the main mechanisms of horseshoe vortex generation and vortex shedding.

For the most part, the authors who have studied the flow around circular piles have placed a major emphasis on parameterizing the behavior of the horseshoe vortex and vortex sheeding using dimensionless numbers. However, there is a gap in the knowledge of the turbulent structures that occur in the section upstream of the pile, their ordering and categorization according to the decomposition of coherent structures that are possible to estimate using Proper Orthogonal Decomposition (POD) or other modal decomposition techniques.

On the other hand, historically, the incipient motion of sediments due to the action of the flow has been estimated by the criterion of Shields (1936) even in cases where there are obstructions to the flow.

While there are some formulations to describe the incipient motion for cases where there is a blockage of flow (Dargahi, 1990; Hager and Oliveto, 2002) or in the presence of vegetation in the bed (Watanabe et al., 2002; Hongwu et al., 2013), they are mainly based on hydraulic parameters, such as average flow velocity, bed shear stress, or Froude number.

However, the turbulent coherent structures that develop around a pile, although they have been characterized by experimentally data, they have not been directly linked to the incipient motion, neither has been identify which turbulent structures are the most relevant and binding with the movement of the sediments.

In consideration of this knowledge gap detected, both into the coherent turbulent structures and the incipient motion associated, the experimental research described in the next section, has been developed.

2.4 Article: Coherent turbulent structures in front of a circular pile embedded on a granular bed and its relationship with the sediments incipient motion.

This paper was submitted to the journal Experiments in Fluids, and actually is under review.

2.4.1 Abstract

The unsteady turbulent structures developed in front of a circular pile and its relationship with the incipient transport of the sediments were analysed from experimental laboratory measurements. Horizontal and vertical two-dimensional Particle Image Velocimetry measurements were performed and the obtained velocity time series analysed by means of the Proper Orthogonal Decomposition and Quadrant Analysis. The obtained dominant modes described the dynamics of the downflow associated to the incoming boundary layer and to the dynamics of the primary horseshoe vortex. These structures were correlated with the incipient transport of sediments showing that dominant modes were responsible of 80 to 87% of the total movements events of the grains, results in agreement with the Quadrant Analysis.

2.4.2 Introduction

The incorporation of a circular pile in a natural flow produce several effects acting in both hydrodynamics (vortex formation, adverse pressure gradient, down-flow, among others) and morphodynamics (pile scour). Currently, many research papers which study, describe, and propose methodologies in order to estimate hydrodynamics around a pile and scour are available. However, researches are less concerned with the coherent turbulent structures produced due to the flow interaction with the pile; in fact no many articles have been published on this issue.

Flow around a circular pile has been studied by many researchers, such as Tritton (1959), Roshko (1961), Baker (1979, 1980), Dargahi (1987, 1989), Graf and Yulistiyanto (1998), Ahmed and Rajaratnam (1998), Sumer and Fredsøe (2006) y Ataie-Ashtiani and Aslani-Kordkandi (2013), among others.

Flow around a wall mounted cylindrical pile located in the center of a uniform flow is characterized by a horseshoe vortex system resulting from the interaction of the incoming boundary layer and the adverse pressure gradient induced by the presence of the pile, Unger and Hager (2007). This vortex system can be found under several flow conditions, such as those developed during unsteady flow, oscillatory flow (waves), and steady currents (Quezada et al., 2018). Many researchers have studied the behavior and formation of the horseshoe vortex system. Baker (1979) pointed out that two governing parameters define the horseshoe vortex characteristics, which are the ratio between the height of the boundary layer and the pile diameter (δ/D) and the pile Reynolds number $Re_D = UD/\nu$, where U is the mean horizontal velocity, D pile diameter and ν cinematic viscosity.

The first parameter (δ/D) describes the initial mechanism of the horseshoe vortex formation and its location. This will be delayed if δ/D is small due to the separation of the bed boudary, which will also imply a small-size horseshoe vortex. On the contrary, if δ/D is very small, the boundary layer may not even separate, and the horseshoe vortex shall not form.

The effect of Re_D over the horseshoe vortex is similar to that previously described for δ/D, which will be delayed due to the boundary layer separation if the Reynolds number is small, reason is that the viscosity effect is greater than the flow/pile interaction. Cleary, for a

very small Re_D (laminar flow), the boundary layer shall not separate from the bed and the horseshoe vortex may not occur.

A more detailed explanation of the effect of δ/D and δ/D, effect over the hydrodynamic behavior of the horseshoe vortex can be found in the work of Sumer and Fredsøe (2002).

The adverse pressure gradient triggers a flow pattern termed as downflow, which is characterized as a current driven towards the bed. The work of Ahmed and Rajaratnam (1998), who analyzed the hydrodynamics behavior over smooth, rigid rough bed, and mobile bed, showed that the downflow can reach up to 75% of U magnitude. These observations agree with Sarker (1998), who studied horizontal and vertical velocities profiles for steady and unsteady currents with different pile diameters over a fine sediment bed with a mean particle diameter $d_{50} = 0.80$ mm. Meanwhile, working with a semi-circular cylinder attached to the side wall, the work of Unger and Hager (2007) presents a detailed quantitative study of the downflow by means of the analysis of velocity profiles obtained with Particle Image Velocimetry (PIV). It was concluded that downflow has not a significant temporal variation and its speed is dominated by the approach flow.

Many researchers have study the coherent turbulent structures of the flow around a circular pile. Most research to date is based on the analysis of results obtained by numerical models. For example Kirkil et al. (2005) using Large Eddy Simulations (LES) studied the horseshoe vortex behavior around a circular pile in a flat bed. Some of the results reported by Kirkil et al. (2005) indicate that the entrainment of the sediments close to the pile is produced by the horseshoe vortex which increases the turbulent fluctuations (velocity and preassure), and consequently, the bed shear stresses and turbulent kinetic energy increases as well.

Kirkil et al. (2008) studies the coherent turbulent structure around a circular pile in an equilibrium scoured bed, through both a LES numerical simulation and laboratory test, considering a $Re_D = 16.000$ and in order to visualize the flow, the experimental technique called Large Particle Image Velocimetry (LPIV) was applied. Kirkil et al. (2008) main result was that the turbulent fluctuations (velocity and preassures) are the responsible for the sediment entrainment in front of the pile, similar to the results previously reported by Kirkil et al. (2005).

Escauriaza and Sotiropoulos (2011c) studied the effects of Reynolds number over the coherent turbulent structures dynamics using detached eddy simulation (DES), and validated the results comparing them with experimental data. As a main conclusion, Escauriaza and Sotiropoulos (2011c) established that the vorticity developed due to the pile/flow interaction increases together with the Reynolds number, and consequently, significant variations occur in the turbulent behavior near the bed.

Results obtained by Escauriaza and Sotiropoulos (2011c) where later used by Link et al. (2012) who additionally introduces the movement of the sediment particles around a circular pile over a previously scoured bed which has not reached the equilibrium scour depth yet. The main results presented by Link et al. (2012) regarding the bed shear stress shows that the horseshoe vortex is the main turbulent structure that induces the fluctuations of the bed shear stress and, as a consequence, governs the sediment transport around the pile. Results of Link et al. (2012) highlight the intermittent characteristics of sediment motion and also that the load bed slowly but progressively distributes in accordance with the scour depth.

Experimental results of the coherent turbulent structures behavior in front a circular pile was presented by Apsilidis et al. (2016). Using a Proper Orthogonal Decomposition (POD) of the flow field, determined the dominant flow structures for a smooth and rough bed. Results of Apsilidis et al. (2016) provide information concerning the horseshoe vortex formation for both types of bed used. Regarding the energy content of the POD modes, Apsilidis et al. (2016)

demonstrated that the first two modes were the most energetic ones both in a smooth bed and rough bed, however, to reconstruct half of the total kinetic energy, 10 modes are required for a smooth bed meanwhile for a rough bed just 4 modes are required.

The analysis of the first four POD modes for smooth and rough bed developed by Apsilidis et al. (2016) differs significantly between the two type of bed used. For the first mode in a smooth bed, four structures were clearly detected; contrary to the rough bed where there were no structures detected. For the second POD mode, the smooth bed showed one structure associated to a main vortex topology placed near the bed; meanwhile for a rough bed one structure was detected, but its spatial scale was larger than the scale detected for the same mode but in a smooth bed. The third and fourth modes for smooth bed were composed of a complex topology of structures (four and three vortexes, respectively), but in the case of a rough bed, it was detected only in two structures of each mode.

The studies described above have focused their efforts on determining the behavior of the turbulent coherent structures of the flow around a circular pile. However, they do not provide information about the relationship between the coherent turbulent structures and the incipient motion of the sediments.

The turbulence effects on sediment transport have been addressed by several authors. Sumer et al. (2003) developed an experimental study to evaluate the turbulence influence over the sediment transport that occur in a open channel. The size of the sediments used in their experimental work corresponds to a range of sands, while the turbulence is generated by rigid structures, such as a horizontal pile and metal filament grids.

The turbulence velocity fluctuation produces a significant increase in the incipient motion, as stated by the main findings of Sumer et al. (2003). For example, an increase of 20% in the level of turbulence ($\sqrt{\overline{u'^2}}$) induces six-fold increase in the shear stress. Additionally, they conclude that the Shields parameter plus the Root Mean Squares (RMS) of the longitudinal velocity component satisfactorily correlates with the incipient motion. Hence it is proposed as an indicator for said purposes.

Also, in the context of the use of the Shield criterion for the estimation of particles entrainment, Vollmer and Kleinhans (2007) proposes a modification of the Shields parameter considering the effects of the exposure of the sediment to the flow and the fluctuating pressure field on spheres. For this purpose, Vollmer and Kleinhans (2007) incorporate both: the average lift force (conventional Shields approach) and the fluctuating lift force.

The theoretical approach developed by Vollmer and Kleinhans (2007) concludes tthat the proposed analytical solution of the Shields parameter is a good indicator of the incipient motion over rough and smooth beds. Additionally, Vollmer and Kleinhans (2007) state that with their analytical solution it is possible to improve the understanding of the process of dislodgement of sediments in a bed.

According to Diplas et al. (2008) the Shields criterion does not adequately capture the turbulent flow and its natural fluctuations, which are relevant and elemental in the process of incipient motion. Diplas et al. (2008) propose that not only the magnitude of the velocity fluctuations ($\overline{u'^2}$) due to the turbulence is relevant in the movement, but also the time in which this magnitude is sustained (impulse).

In order to verify that the impulse is the responsible of the incipient motion of sediments, Diplas et al. (2008) developed an experimental study based on a totally controlled environment in which the turbulent fluctuations of the flow was simulated by using a electromagnetic force acting over a steel sphere placed on teflon spheres.

From its experimental results, Diplas et al. (2008) establishes that, compared to the Shields criterion, the combined effect of the magnitude and duration of turbulent kinetic energy near

the bed is a better indicator of the incipient motion of the grains.

The results obtained by Diplas et al. (2008) were subsequently confirmed by hydraulic channel tests by Celik et al. (2010), which in addition to the impulse concept proposed by Diplas et al. (2008), not only obtains a probability distribution associated to the impulse but also links it with the incipient motion of the grains.

Although the previously described criteria of incipient motion tried to incorporate the effects of the turbulence, all of them are based on the concept of the bed shear stress and did not link it to a turbulent structure.

Techniques for modal decomposition offer a practical alternative to identify important flow structures from turbulent time series in order to analyze a fluid flow. Several techniques exist to achieve the aforementioned, such as the Dynamic Mode Decomposition (DMD), Proper Othogonal Decomposition (POD) and Balanced Proper Othogonal Decomposition (BPOD) (Taira et al., 2017). For the purpose of this article, the POD technique was applied; a brief description is presented below.

The POD algorithm was introduced to fluid dynamic analysis by Lumley (1967) as a mathematical method to extract coherent structures from a turbulent flow field. Since this technique has been independently derived from other research areas, it is known by many different names. For example, in applied mathematics it is known as Singular Value Decomposition (SVD) and his theoretical development can be found in the work of Golub and Reinsch (1970).

POD is a linear method meaning that the temporal behaviour spatial modes can be superimposed to reconstruct the original signal. With this technique, the mode decomposition is obtained in an orderly manner from higher to lower contribution to the total turbulent kinetic energy.

The detection of the turbulent structures due to flow obstruction has been applied both numerically (Kirkil et al., 2008; Escauriaza and Sotiropoulos, 2011c; Chang et al., 2011; Link et al., 2012) and experimentally (Keshavarzi et al., 2014; Apsilidis et al., 2016; Higham and Brevis, 2018). However, no experimental studies have been presented that, by using proper orthogonal decomposition, identify and categorize the turbulent coherent structures of the flow in front of a pile (prior to scouring) and associate them to both the downflow and the horseshoe vortex.

The general objective of this article is to analyze the behavior of the turbulent structures that occur at the upstream part of a circular pile and to describe their role on the entrainment of bed sediment.

2.4.3 Experiments

Facilities, physical model and experiments developed

The experiments were carried out in the Hydrodynamics Laboratory of the University of Sheffield, United Kingdom. The section of the flume was 18 m (length) $\times$ 0.5 m (width) $\times$ 0.5 m (height) and slope (S) of 0.001, with bottom and side glass walls, thus allowing full optical access. At the beginning of the channel there is a reservoir in which the water is supplied by means of a computer controlled pump that connects to the recirculation tank (see Figure 2.12).

Silicon glass spheres were used at the flume bed as an analogous granular material. The density of the particles (ρ_s) was 2220 (kg/m^3) and diameter (d_{50}) equal to 2.5 mm. From the inlet, the first 2 meters remained unchanged with the original glass bottom, this was followed by a transition of 5 m of length in which a false acrylic bottom of 10 mm thickness was built.

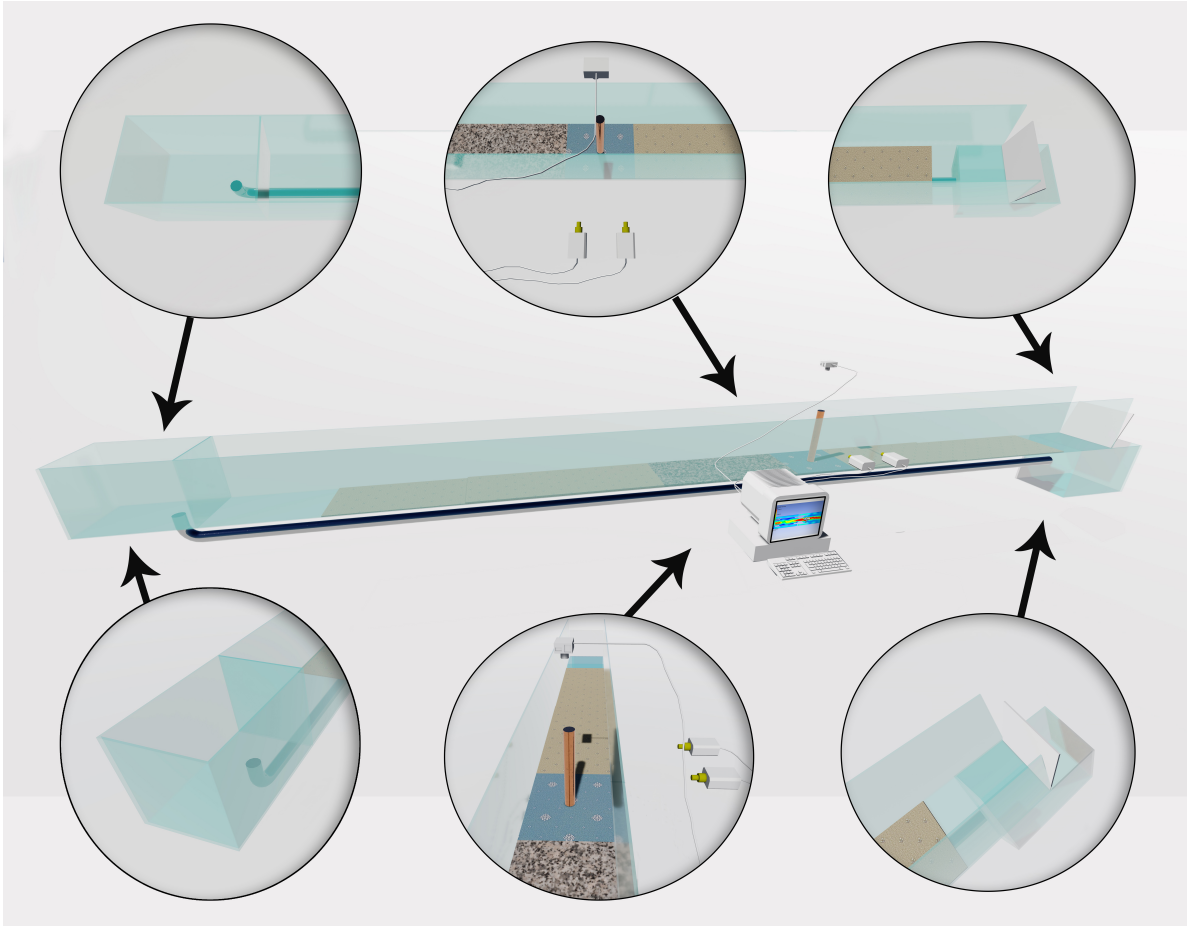

Figure 2.12: Flume configuration for the developed experiments.

The following 2 m were composed by the same acrylic layer with glued fixed spheres on its surface. This flume section reproduced the roughness conditions associated to the spheres, thus it was placed, and its length verified, to ensure the presence of a fully developed velocity profile upstream the cylinder. After this, a lentgh of 60 cm were left without the false bed, i.e. glass bottom, which was filled with particles. The cylinder was located at the center of this section, 9.3 m from the inlet. This section was followed by the same false bottom used upstream but for a 3 m length. The rest of the flume bottom downstream was not modified. An schematic representation of the experimental setup is presented in Figure 2.12.

A total of 15 experiments were developed, in which different pile diameters (D) and flow rates (Q) were tested. In Table 2.2 the details of the laboratory tests are presented, such as water depth (h), the mean horizontal velocity (U_m), the frictional velocity (u_*), the Reynolds number of the pile ($Re_D = \frac{U_m D}{\nu}$, where ν is the water viscosity), the Froude number ($F_r = \frac{U_m}{\sqrt{gh}}$) and the total time registered for each test (T). All the tested cases were in clear water condition, however, when the incipient motion in front the pile was observed, a label I was added to the test name to identify the case.

The velocity field was measured using two-dimensional Particle Image Velocimetry (PIV) in two synchronized planes. Two 4Mpix cameras recorded the upstream and dowsntream regions of the flow. Polyamide 12 particles of 100 μm was used as flow tracer and their movement was recorded with frequencies in the 60-240 Hz range. The characteristics of the illumination and

Table 2.1: Characteristics of the equipment used for the PIV measurements.

Component		Specification
Seeding	Type	Polymide powder
	Specific gravity	1.016 gmc^{-1}
	Diameter	100 μm
Light sheet	Laser type	Double pulsed Nd:YAG
	Maximum energy	200 mJ
	Wave length	532 nm
	Thickness	2 mm
Camera	Type	Imager MX 4M
	Resolution	2048 x 2048 px
	Pixel size	0.21 mm
	Lens focal area	24 mm

optical system are summarized in Table 2.1, while the specific acquisition frequencies for each of the cases is detailed in in Table 2.2

The image series were analysed using PIVLab (Thielicke and Stamhuis, 2014a,b; Thielicke, 2014). A multipass interrogation window of sizes 129 to 32 pixel with an overlap of 75 % were used for the analysis. The image deformation technique was selected for the analysis and the subpixel estimator was approximated with a Gauss 2 x 3 point technique. All results were filtered using an in-house implementation of the normalised median filter proposed by Westerweel and Scarano (2005).

2.4.4 Data analysis

From the PIV analysis, synoptical time series of the streamwise and vertical velocities (u and v) were obtained in a vertical plane placed at the centerline of the pile. Each velocity field was described as a function of time (t), streamwise (x) and vertical (y) coordinates. From each velocity snapshot, the turbulent fluctuations (u' and v') were determined according to the Reynolds decomposition, i.e., by subtracting their time averaged $\bar{u}$ and $\bar{v}$. All length were made dimensionaless using D, while velocities were made dimensionless using the frictional velocity (u_*) which was approximated according to equation 2.4.1, where g is the gravitational acceleration and R_h the hydraulic radius of the flume.

$$u_* = \sqrt{gR_hS} \tag{2.4.1}$$

For all test cases, the origin of the dimensionless vertical coordinate, ($y/D = 0$), was located at the top of the sediment bed, because it seeks to identify the average speed conditions that act on the grains.

Proper Orthogonal Decomposition

The flow dynamics is commonly analysed by means of the characterisation of physically important flow patterns or modes. For this, there are several techniques available, such as Dynamic Mode Decomposition (DMD), Proper Orthogonal Decomposition (POD) and Balanced Proper Orthogonal Decomposition (BPOD) (Taira et al., 2017). The POD was introduced to fluid dynamics analysis by Lumley (1967), as a mathematical method to extract coherent structures

Table 2.2: Parametric description of experiments

Test	Q (L/S)	h (m)	U_m (m/s)	u_* (m/s)	D (m)	Re_D	F_r	f (Hz)	T (s)	Condition
D01	5.211	0.256	0.042	0.0350	0.060	2513	0.026	80	90	Clear water
D02	10.130	0.262	0.080	0.0351	0.060	4773	0.050	80	90	Clear water
D03	15.030	0.258	0.120	0.0350	0.060	7192	0.075	80	90	Clear water
D04	19.990	0.262	0.157	0.0351	0.060	9419	0.098	80	90	Clear water
I01	27.000	0.251	0.221	0.0348	0.060	13280	0.141	70	240	Incipient motion
D05	5.340	0.252	0.044	0.0348	0.040	1744	0.028	80	90	Clear water
D06	10.310	0.254	0.084	0.0349	0.040	3341	0.053	80	90	Clear water
D07	15.270	0.253	0.124	0.0349	0.040	4968	0.079	80	90	Clear water
D08	20.060	0.255	0.162	0.0349	0.040	6475	0.102	80	90	Clear water
I02	27.000	0.251	0.221	0.0348	0.040	8853	0.141	70	240	Incipient motion
D09	5.130	0.260	0.041	0.0351	0.028	1137	0.025	80	90	Clear water
D10	10.120	0.256	0.081	0.0350	0.028	2278	0.051	80	90	Clear water
D11	15.240	0.254	0.123	0.0349	0.028	3457	0.078	80	90	Clear water
D12	20.400	0.257	0.163	0.0350	0.028	4573	0.103	80	90	Clear water
I03	27.000	0.251	0.221	0.0348	0.028	6197	0.141	60	240	Incipient motion

from a turbulent velocity field. This technique receives different names, depending on the area where it is applied, such as Singular Value Decomposition (SVD) in linear algebra (Golub and Reinsch, 1970). The DMD technique is able to extract spatial modes which are temporally orthogonal with a unique frequency (Higham et al., 2018). The BPOD method is based on the balanced truncation technique proposed by Moore (1981). Although is quite similar to POD, there are some important differences because BPOD provides two sets of modes, the balancing and adjoint modes, and the POD only provides one (Taira et al., 2017). To apply the BPOD algorithm, special datasets are needed: the linear and impulsive response of the system, due to that, the applicability to experimental data is usually not possible (Taira et al., 2017). In this work the POD technique is used for the data analysis. Even though, the POD is a linear technique, its main advantage over the non-linear DMD is the ability to rank the obtained modes according to the variance of the signal, or in case of velocity time series to the Turbulent Kinetic Energy (TKE). This characteristics enable a direct physicial description of the modes.

After Reynolds decomposition of the instantaneous velocity field, the fluctuating velocity field was computed for the recording period (T), i.e. $u'(x, y, t_i)$, $v'(x, y, t_i)$, where $t_i = i \times \Delta t$, $\Delta t = T/N_T$, $i = 1, 2, ...N_T$, with N_T the number of time steps.

This information was used to build a matrix W, where the fluctuating velocity field are ordered in columns to form a matrix that has a dimension of $N \times N_T$, where N is the total number of points in where the velocity field was computed from the PIV analysis, and has a dimension equal to $N = nx \times ny$, with nx the streamwise number of points and ny vertical number of points.

Following a SVD to perform de analysis, W can be expressed as a fuction of S, a diagonal matrix containing the energy contribution of the modes, Φ, which contains the spatial structure of each mode C which describes the time evolution of each mode:

$$W \equiv \Phi \cdot S \cdot C^* \tag{2.4.2}$$

The notation $(\cdot)^*$ represents the conjugate transpose matrix, Φ is a matrix of $N \times \Omega$, S and C are matrix of $\Omega \times \Omega$, where Ω is the number of modes obtained from the decomposition.

The curl of the first four mode obtained from the POD of the velocity field, (ω), was derived to understand the vortex system developed in front the pile, therefore it was used to identify the horseshoe vortex and other topologycal structures.

Observation of the incipient motion

During the experiments visual observation of incipient motion was carried out and captured with the camera system. With this information two different analysis were performed. The first analysis was to correlate the time evolution of the modes obtained from the coherent turbulence structure with the time series of occurrences of incipient motion.

To determinated the cross correlatio (R_{XY}), the equation 2.4.3 was applied. Where X and Y are random vectors, the notation $(\cdot)^*$ are the conjugate, and E is the expected value.

$$R_{XY} = E\{XY^*\} \tag{2.4.3}$$

The second analysis was to define the turbulent field over the particle in the same time step in which the incipient motion occurs. For this task, the ejections and sweeps was determinated using the turbulence velocity fluctuations (u' and v') in concordance with Kaftori et al. (1995), Niño and García (1996) and Lee and Hong (2019).

It should be taking into account that the turbulence velocity fluctuations defined to perform the incipient motion analysis were obtained for each location where the particles move.

In order to compare our results with those previously obtained from other researchers, the Stokes Number (S_t) analysis was carried out. To determinate S_t the equation 2.4.4 was applied, where τ_p is the particle time response computed according to equation 2.4.5 and τ_η is the dissipative time defined as the equation 2.4.6. Where μ is the dynamic viscosity, ϵ dissipation rate and ν kinematic viscosity.

$$S_t = \frac{\tau_p}{\tau_\eta} \tag{2.4.4}$$

$$\tau_p = \frac{\rho_p d_{50}^2}{18\mu} \tag{2.4.5}$$

$$\tau_\eta = \sqrt{\frac{\epsilon}{\nu}} \tag{2.4.6}$$

Also the particle Reynolds number was determined according to equation 2.4.7. A summary of the Stokes Number, the particle response time, the disipative time and the particle Reynolds number, can be found in Table 2.3.

$$Re_p = \frac{U_m d_{50}}{\nu} \tag{2.4.7}$$

2.4.5 Results

Vertical distribution of the mean streamwise velocity

The results obtained for the mean velocity profiles (solid black line) are shown in Figures 2.13, 2.14 and 2.15, for the pile diameter 0.060, 0.040 and 0.028 m, respectively. Additionaly a gray fill have been added to each figure and this corresponds to the standard deviation of the data.

Table 2.3: Stokes number analysis.

Test	τ_p (s)	τ_η (s)	S_t	Re_p
I01	$6.762 \cdot 10^{-1}$	$5.137 \cdot 10^{-3}$	131.628	485.388
I02	$6.762 \cdot 10^{-1}$	$4.597 \cdot 10^{-3}$	147.077	485.388
I03	$6.762 \cdot 10^{-1}$	$5.137 \cdot 10^{-3}$	131.628	485.388

The vertical distribution of the dimensionless mean horizontal velocity ($\bar{u}/u_*$) shows a characteristic behavior associated with both the distance to the pile, and the increase in the Reynolds number of the pile. Regardless of the Reynolds number of the pile, it is determined that the average velocity profile develops higher magnitudes when it is further away upstream from the pile. For a fixed location (x/D), it is possible to visualize that the average velocity profile increases its magnitude as a function of the Reynolds number of the pile.

A relevant aspect of the dimensionless velocity profiles was detected for a dimensionless distance of $x/D = 0.2$, regarding to two items: its relationship with the Reynolds number of the pile and the incipient motion detection. When no motion of the sediment was produced, the dimensionless velocity profile at $y/D = 0$, was equal to zero; however, when Re_D increase and the sediment reach the incipient motion in front the pile, $\bar{u}/u_*$ was greater than zero.

The results described in the last paragraph are an indicator of the increase in sediment transport capacity that occurs when Re_D increase.

The behavior of the standard deviation for each velocity profile (gray fill in Figures 2.13, 2.14 and 2.15) was influenced for both the dimensionless distance (x/D) and for Re_D.

When analising the standard deviation according to the dimensionless distance (x/D), it is obtained that with a higher value of x/D, that is, farther from the pile, the standard deviation of the mean velocity profile decreases.

On the other hand, when the standard deviation is analyzed as a function of the Re_D, for a fixed location x/D, it can be seen that with a greater Re_D, the standard deviation of the average velocity profile was greater; situation that once again reflects the importance of turbulent fluctuations.

The mechanisms responsible for the turbulence at greater distance upstream from the pile would be those imposed by the flow, while for the fluctuations near the pile, the effect of the horseshoe vortex would be added.

Proper Orthogonal Decomposition

The first 4 vorticity modes obtained from the POD are shown in Figures 2.16, 2.17 and 2.18, for the pile diameter 0.006 m, 0.040 m and 0.028 m, respectively.

When the most energetic turbulent mode (Φ_1) in front the pile is analyzed , it was observed that for none of the laboratory tests carried out a vortex was detected either in the bed or in the pile.

The spacial behavior for the turbulent mode 1 (Φ_1), could be the result of the down-flow triggered by the adverse pressure gradient developed by the presence of the obstacle, wich manifests as an intensification of the vorticity in front of the pile. On the other hand, the increase of vorticity in the bed would be linked to the development of the boundary layer of the incident flow. The down-flow detected in the first turbulent mode (Φ_1) correspond to one of the flows that produce the horseshoe vortex.

The second turbulent mode (Φ_2) shows for all the experiments, the presence of one vortex,

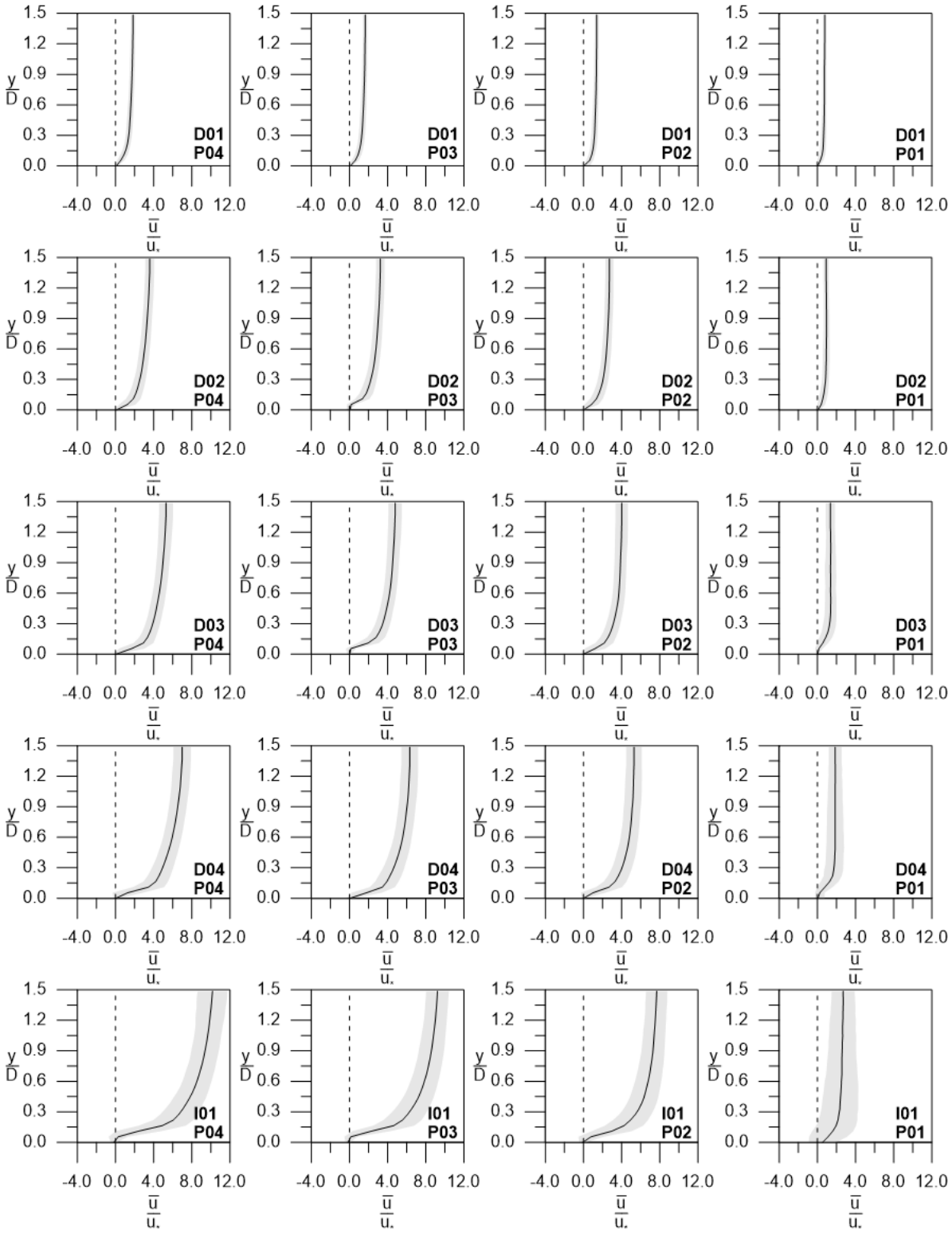

Figure 2.13: Mean velocity profiles for each x/D location studied, associated to a pile diameter equal to 0.060 meters. The gray area represents the standard deviation of the data.

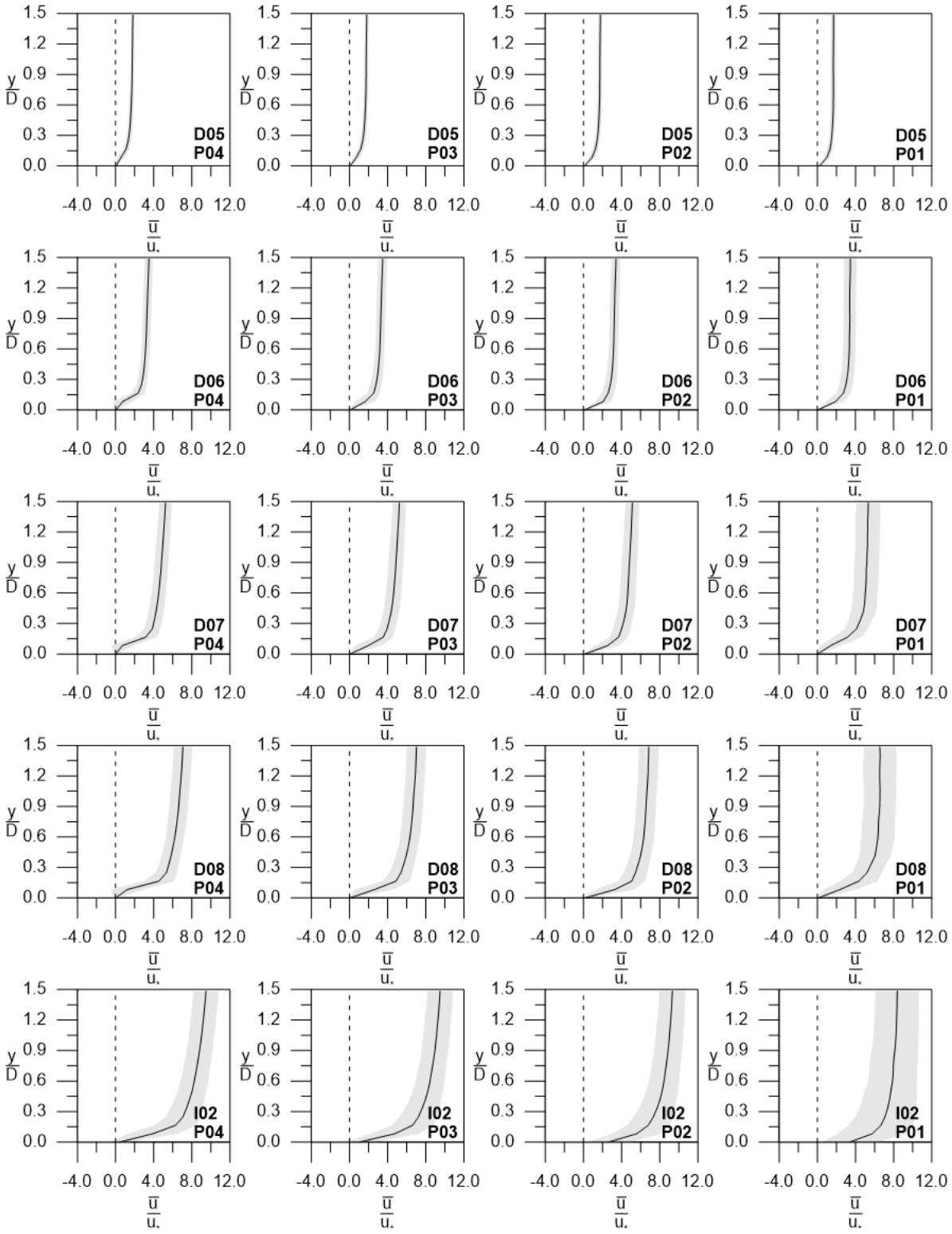

Figure 2.14: Mean velocity profiles for each x/D location studied, associated to a pile diameter equal to 0.040 meters. The gray area represents the standard deviation of the data.

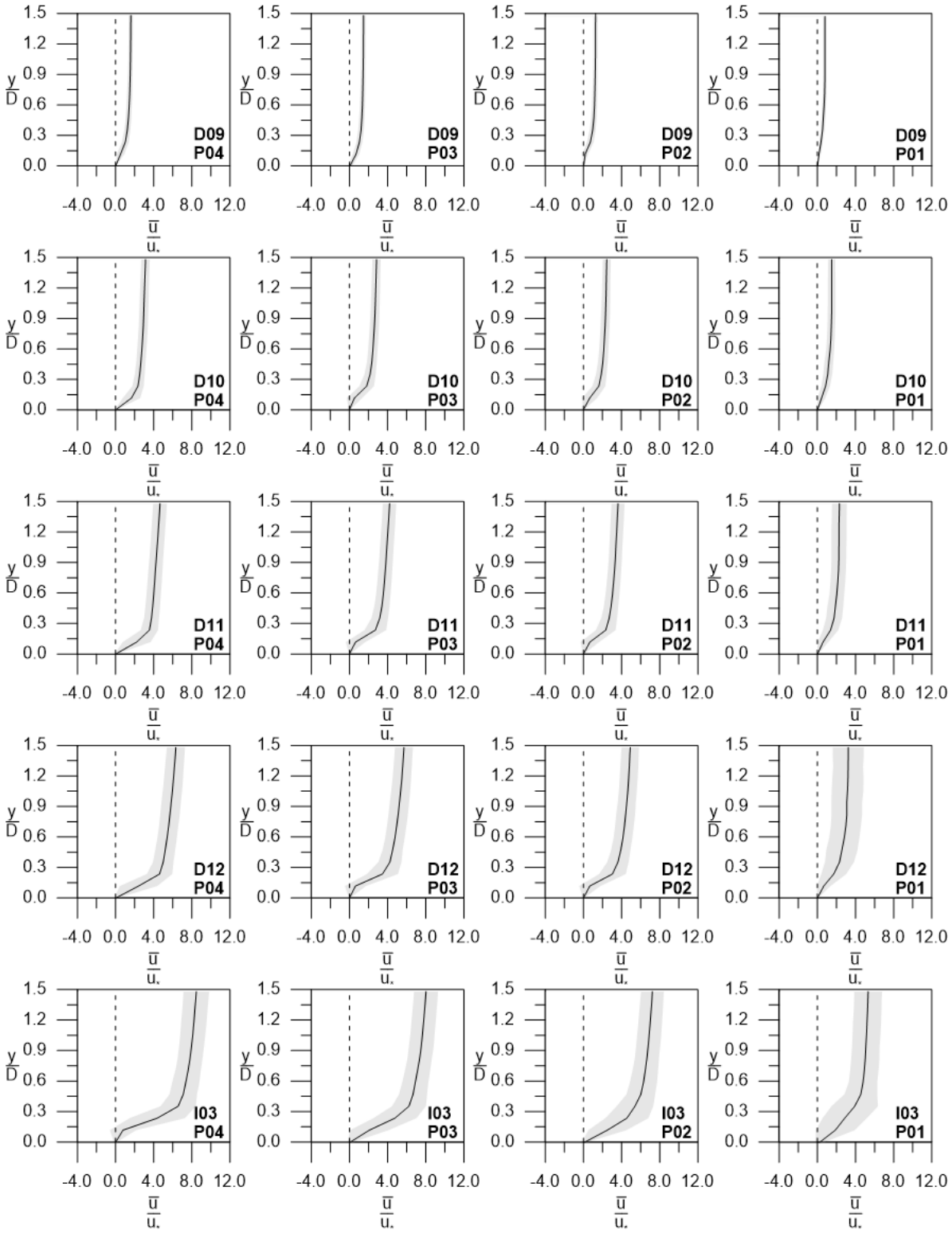

Figure 2.15: Mean velocity profiles for each x/D location studied, associated to a pile diameter equal to 0.028 meters. The gray area represents the standard deviation of the data.

whose center was located approximatly between 0.6 to 0.9 x/D. In some of the cases that were analyzed (D01 to D04, D09 to D12, I01 and I02) it is verified that the vortex was accompanied by two intensifications of the vorticity (one in the bed and another in the face of the pile), presumably showing a link between the main mode (Φ_1) and the second one (Φ_2).

The spatial behavior of mode 1 (Φ_1) and mode 2 (Φ_2), did not shown a clear relationship with Re_D. The above may be due to the fact that all the laboratory trials were developed for high Re_D.

Greater spatial variability shows the third turbulent mode (Φ_3). There were cases in which only one vortex was developed (D01, D05, D07, D08, D09, D10, D11, I02 and I03), in others two vortices (D02, D03, D04, I01, D06 and D12).

The presence of one or two vortices in the spatial field of the third turbulent mode, does not show a clear coincidence with the increase or decrease of Re_D. In the case of tests D01 and I01 (all for a pile of 0.060 m in diameter), as the Reynolds number in the pile increased, the double vorticity is developed. However, this trend was lost in the remaining tests.

It is important to mention that in the third turbulent mode for cases in which two vortices occurred (cases D02, D03, D04, I01, D06 and D12), it is possible to appreciate that when one adopted negative magnitudes, the other was positive. Although in the POD decomposition the turbulent modes Φ only present their real sign when multiplied with its time evolution (C), it can be shown that, regardless of the sign they have, it will be in the presence of two systems of circulation with opposite rotation.

The behavior of the fourth mode (Φ_4) was similar to the third turbulent mode, because the results were also obtained without presence of vortices (D04, I01, D05, D06 and D12), with one vortex (D03, D07, D08, I02, D09, D10 and I03) and with two vortices (D01, D02 and D11). This detected behavior, again, does not present a relationship with the increase or decrease of Re_D.

In the case of tests carried out for a pile of 0.060 m in diameter, for the lowest Re_D (D01 a D03, Figure 2.16), a rotation of the streamlines is developed, which then disappears for the case D04 and I01. On the other hand, in all the tests performed on a 0.040 m diameter pile (Figure 2.17), in all cases (D05 al I02) a vortex is developed. In the test with the pile of 0.028 m in diameter, only the case D12 does not developed a vortex.

An important aspect to be highlighted is presented in the behavior of the second and third turbulent mode (Φ_2 and Φ_3), as it was clearly shown in cases D01 to I01; in the vicinity of the bed and the pile are vorticity intensifications, similar to those determined in the first mode (Φ_1). This would be an indicator that for this cases, the first three turbulent modes would be linked in their formation, a situation that can be confirmed with the analysis of the POD relative energy content shown in the Figure 2.19.

The POD relative energy contents has been defined as the fraction between the kinetic energy for each mode regarding to the total kinetic energy of all modes detected.

The energy content of the first three modes is greater than 10% of the total energy contained in the first 10 main turbulent modes, while from the fourth to the higher modes, the energy content decreases. This energy content would be an indicator that the first three modes are linked.

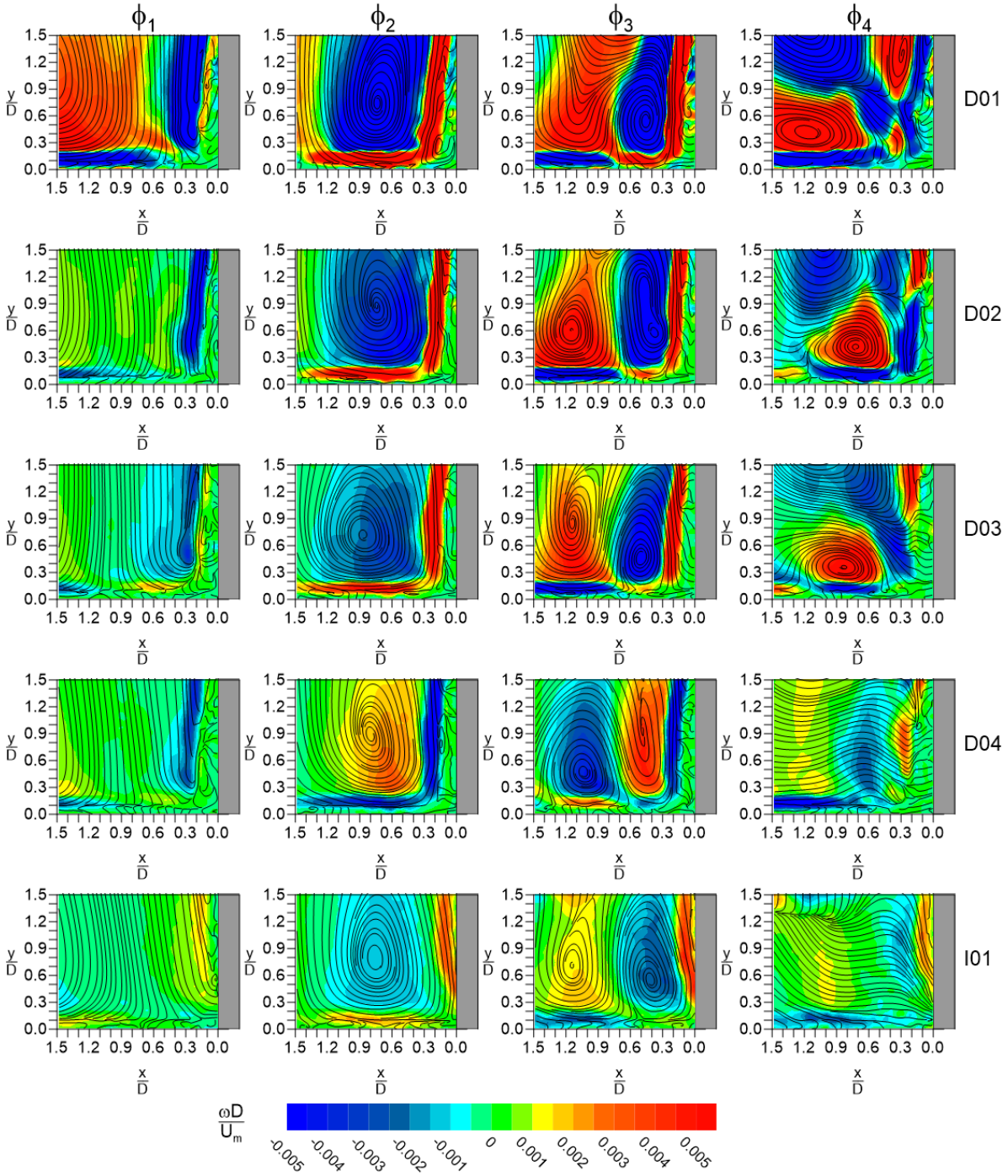

Figure 2.16: Voricity and streamlines POD modes obtained for a pile diameter equal to 0.060 meters.

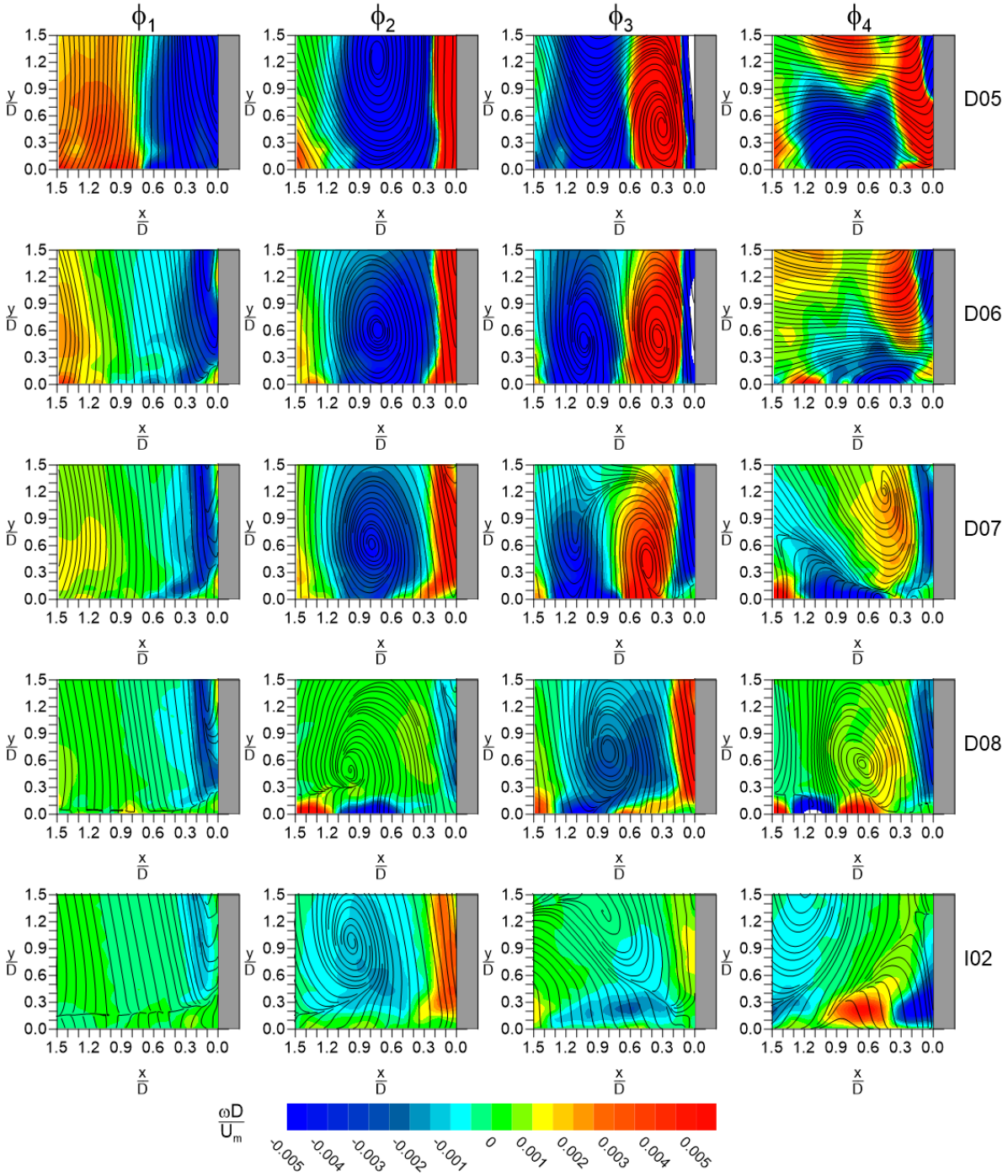

Figure 2.17: Voricity and streamlines POD modes obtained for a pile diameter equal to 0.040 meters.

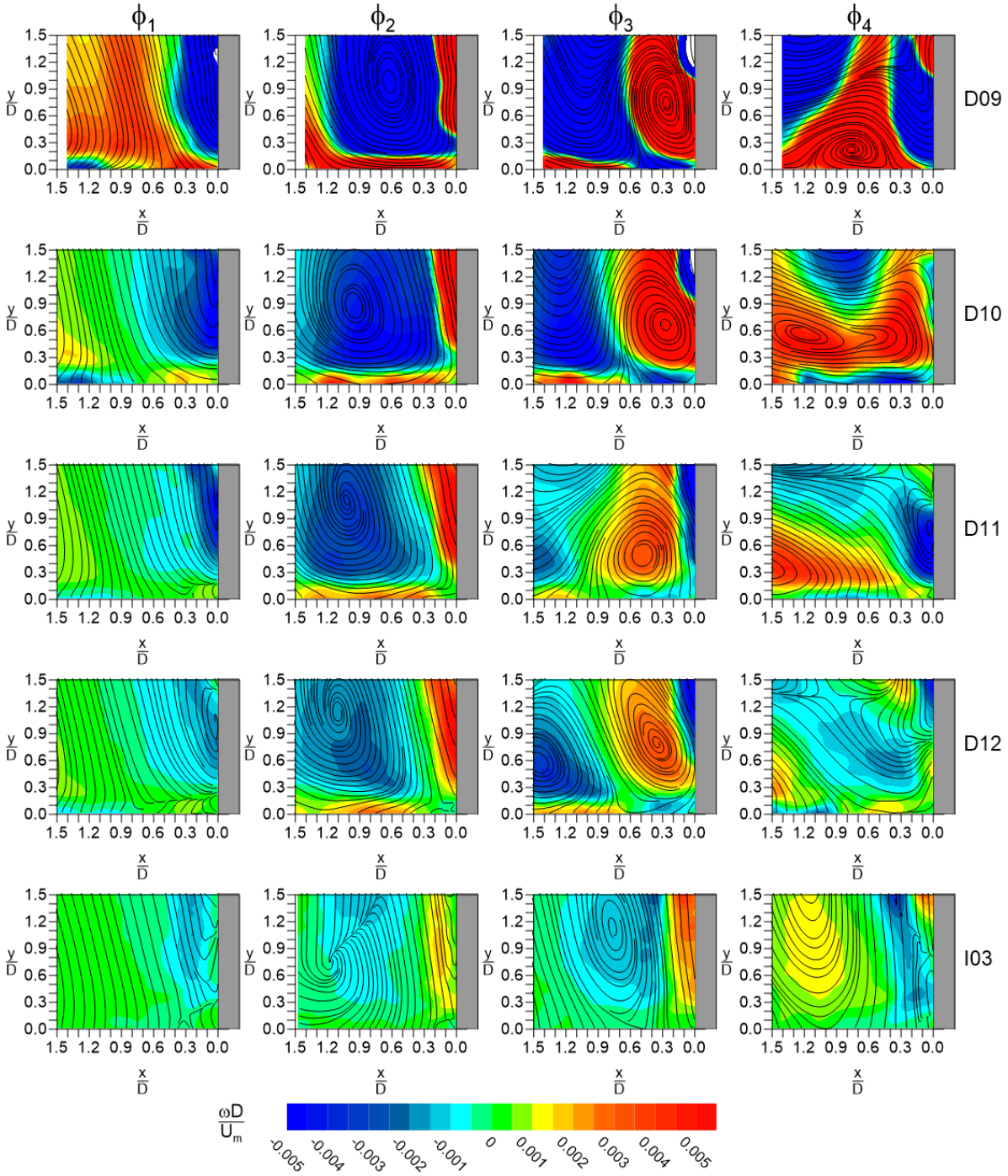

Figure 2.18: Voricity and streamlines POD modes obtained for a pile diameter equal to 0.028 meters.

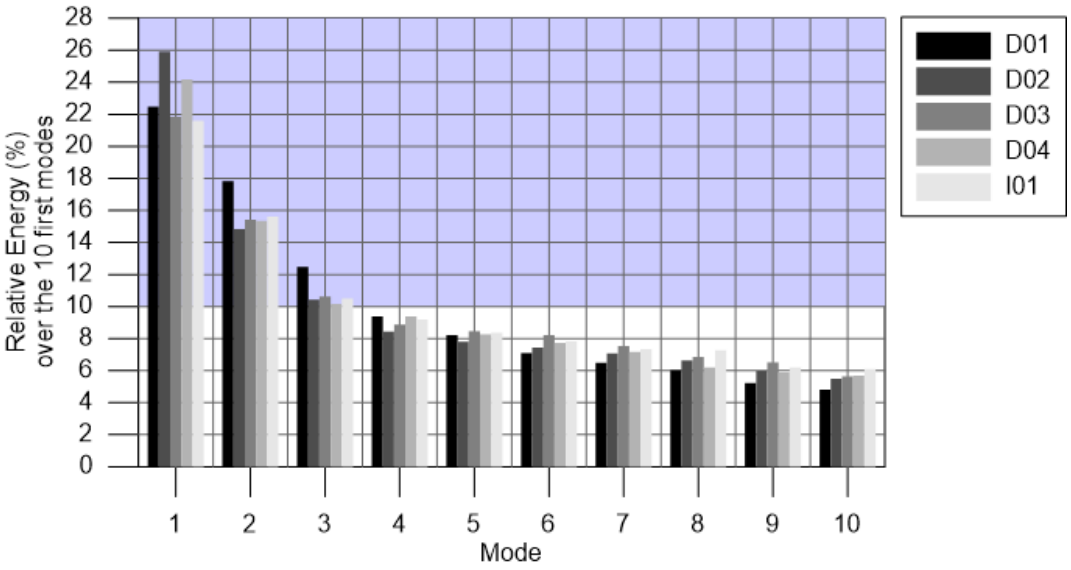

Figure 2.19: Relative POD energy associated with the first ten modes.

According to the spatial behavior of the first three turbulent modes detected from the POD decomposition, Φ_1 can be relate to the down-flow and boundary layer, Φ_2 to the primary horseshoe vortex and Φ_3 to the secondary vortex system.

Observations of the incipient motion

The time evolution of the first four turbulent modes obtained for the I01 test (black line) and the movements of the recorded sediment (vertical gray lines), is shown in Figure 2.20.

The temporal evolution of the main mode of the I01 test (C_1 in Figure 2.20), shows significant coincidences between peak values of the time series (negative or positive) and the movements of the sediments. For example, the first recorded movement of the sediments was detected around second 13 of recording, it can be seen that the time evolution of the first turbulent mode has a peak of the order of -0.015. Similar coincidences are also clearly repeated for the recording times equal to 52, 82, 103, 166, 170, 210 and 216 seconds, approximately.

Movements of the sediments that do not coincide with the peaks of the temporal evolution of the first turbulent mode, are peaks associated with the time series of the second turbulent mode as it is seen for 29, 158 and 160 second in the graph for C_2 in Figure 2.20.

In the case of the third and fourth turbulent modes, it can be seen that the comparison of the time series does not show an obvious relationship between the peaks of the turbulent mode's temporal evolution and the movement of the sediments.

Results similar to those obtained for the I01 test, are found for the I02 and I03 cases, and then plots are not shown.

When considering the joint action of the first and second turbulent mode in relation to its temporal evolution, and with it to determine the cross-correlation with respect to the movements of the sediments, the results shown in Figure 2.21 were obtained, for the three incipient transport tests studied.

For all the incipient transport tests (I01, I02 and I03), the maximum cross-correlation between the time evolution of the first two turbulent modes ($C_1 + C_2$) and the movements of the grains, is reached for a lag of 0 seconds, with magnitudes of 0.87 (I01) and 0.80 (I02, I03).

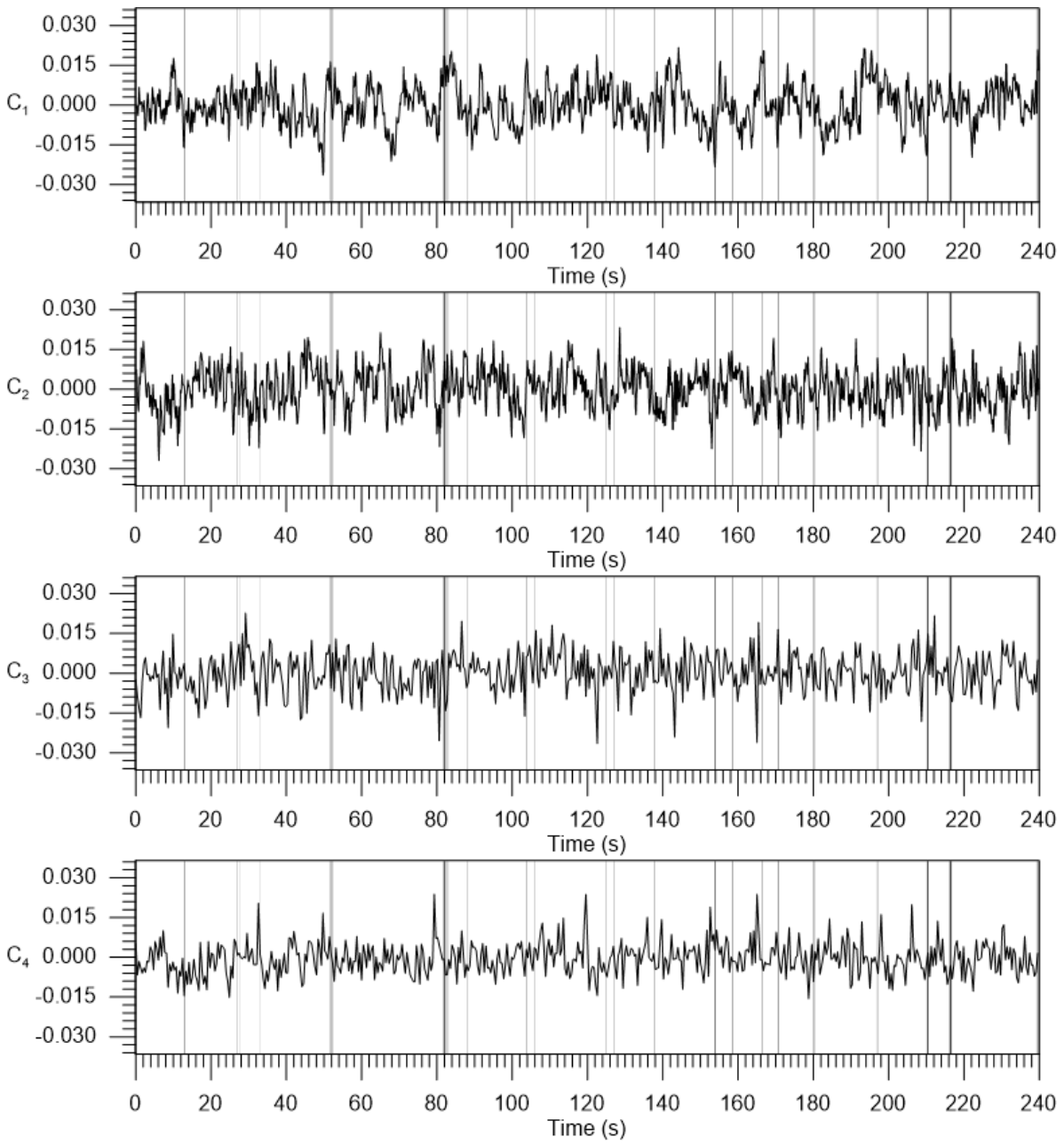

Figure 2.20: Time series of the time evolution coefficient associates to the first four modes (black lines) of the test I01 and the movement of the sediment (vertical gray lines).

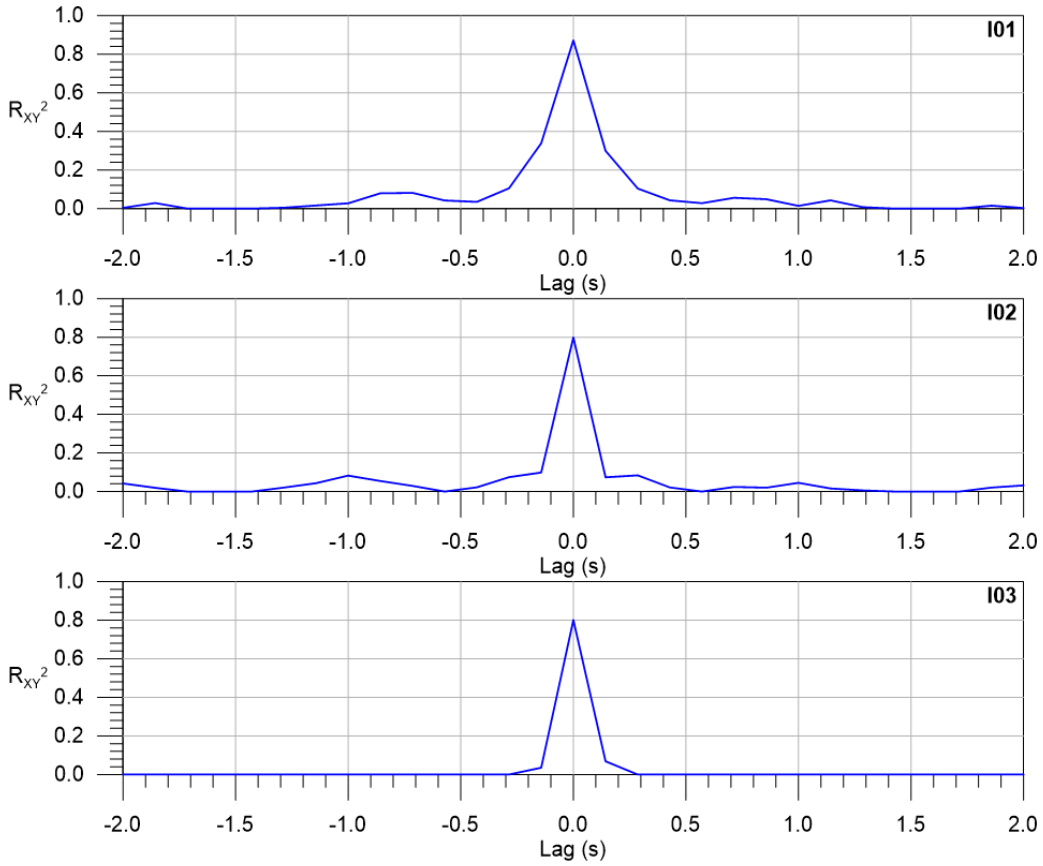

Figure 2.21: Cross-correlation between the time evolution coefficient associated to the first two turbulent modes and the movement of the sediment.

The results obtained from the cross-correlation analysis indicate two important aspects: the first is related to the identification of sediment transport mechanisms, which is discussed in detail below, and the second, with the time scale that acts in the sediment movement, which, according to the maximum cross-correlation obtained at zero seconds of delay, indicates that the incipient movement of the sediments is instantaneously related to the dynamics that drives them.

The time lag equal to zero obtained in our cross-correlation analysis are in concordance with the results previously obtained by Nelson et al. (1995) and Keshavarzy and Ball (1999) and when all of this experimental results are compared according to the Stokes and Reynolds particle numbers (see Figure 2.22), can be note that all the tests were developed in a a high Stokes and Reynolds number regime.

Since the first two turbulent modes are those that, in their temporal evolution, would explain the incipient transport of the sediments in front of the pile, and given the results previously discussed in section 3.2, the forcing responsible for the beginning of the sediment movement would be the down-flow identified in the first mode (Φ_1) and the horseshoe vortex identified in the second mode (Φ_2), which, as a whole, would explain 80% of incipient transport events.

The general flow pattern near the bed can associated with the quadrant behavior of instant turbulent fluctuations (u' & v') that produce the incipient motion of sediments, in wich the outward interaction occurs when $u' > 0$ and $v' > 0$, sweep when $u' > 0$ and $v' < 0$, inward

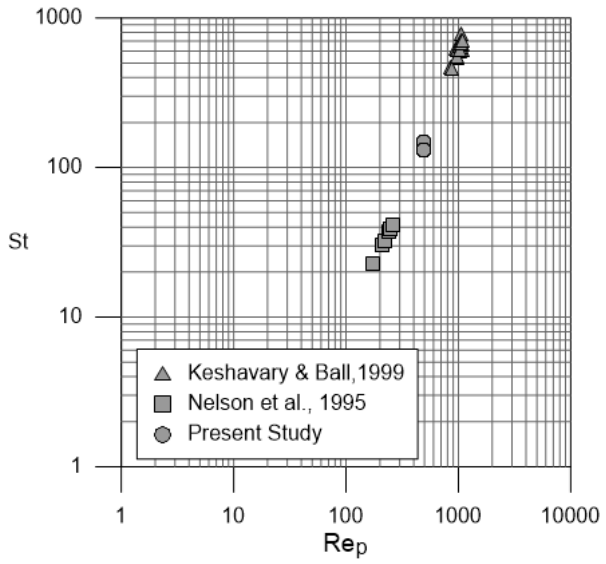

Figure 2.22: Comparison between our results and those obtained by Nelson et al. (1995) and Keshavarzy and Ball (1999).

interaction when $u' < 0$ and $v' < 0$ and ejection when $u' < 0$ and $v' > 0$.

Based on what has been described in the previous paragraphs and when analyzing the turbulent fluctuations according to what is described in section 2.2.3, the results obtained are shown in Figure 2.23. In each quadrant of the figure the main mechanism that acts is indicated (i.e. ejection) and the fraction (f) that represents the total of cases in which incipient transport was produced for the respective test, being $f = 1$, the whole.

In the test I01 (upper frame of Figure 2.23) it can be observed that the dominant mechanisms in the incipient transport would be the processes of sweep, outward interaction and ejection, since they are the ones with the highest fraction of occurence (0.31, 0.28 and 0.24, respectively), representing a total of 0.83 (83%). The remaining cases of incipient transport would be explained by the inward interaction ($f = 0.17$).

When the results obtained for the I02 test are analyzed (central box of Figure 2.23), a greater dispersion of the data can be observed in comparison with the results of the I01 test, since a dominant fraction can not be observed in the incipient transport mechanism, since f is practically equal to 0.25 in all quadrants. In a similar way to that obtained for the I01 test, the incipient transport associated with outward interaction, sweeps and ejection represent a fraction of 0.76.

For the I03 test (lower box of Figure 2.23) results were obtained with a greater tendency towards the movements driven by ejections ($f = 0.38$) and sweeps ($f = 0.34$), in comparison to the previous cases. The total fraction of cases that showed incipient movement of the sediments due to ejection, sweeps and outward interaction, was equal to 0.89.

In general terms, the results of the quadrant analysis of incipient transport cases show that the ejections, outward interaction and sweeps (the three most important mechanisms detected in the analysis) reached a fraction close to 0.8, which is equivalent to the magnitude of the cross-correlation determined in the time series of C_1 and C_2 for each of the tests (I01, I02 and I03), that amounted to approximately 80%. This agreement could be due to the fact that the mechanisms of ejections, outward interaction and sweeps would be related to the turbulent mechanisms detected in the first two modes (Φ_1 and Φ_2).

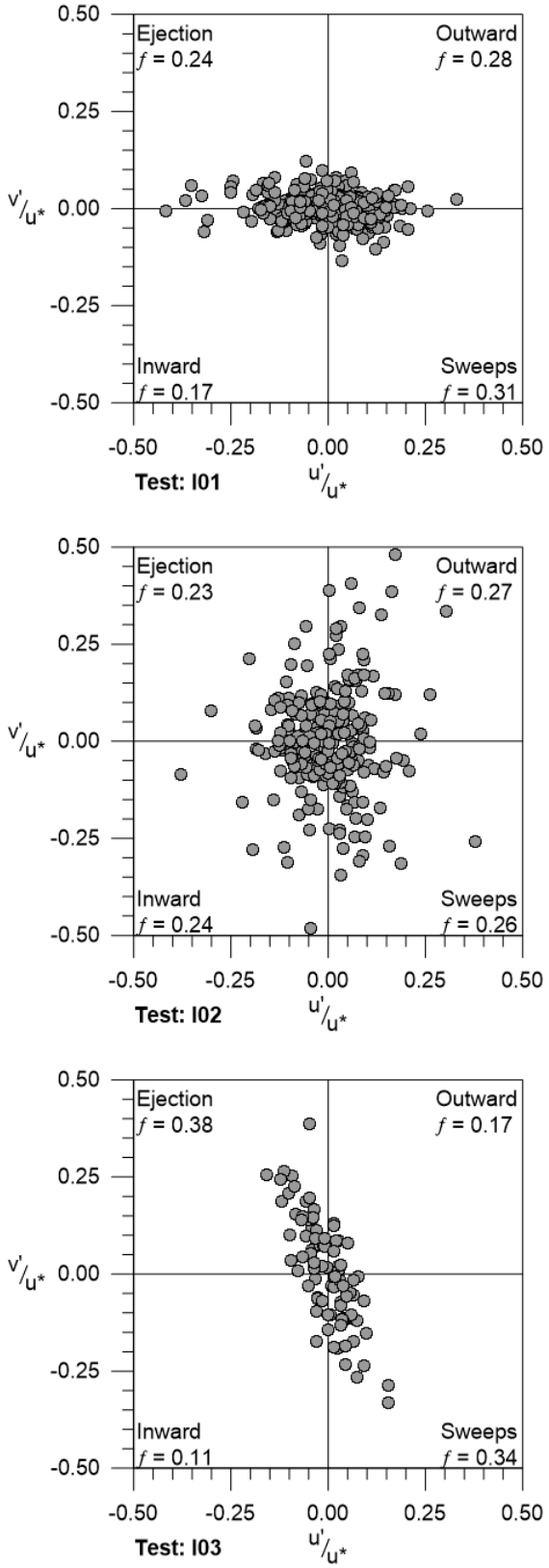

Figure 2.23: Turbulent velocity fluctuations associated to each incipient motion detected.

2.4.6 Discussion

The velocity profiles upstream to a pile were previously studied by Ahmed and Rajaratnam (1998), considering smooth and rough bed, for glued and mobile sediment. Ahmed and Rajaratnam (1998) showed that the velocity profile gradually decreased as it approached the cylinder. This result is confirmed in this research.

Regarding the decrease in the magnitudes of the velocity profile, both towards the bed and in the vicinity of the pile, Graf and Yulistiyanto (1998) and Sarker (1998) presented similar results. However, both Graf and Yulistiyanto (1998) and Sarker (1998) carried out the experiments in a fixed bed, assigning the decrease in magnitude to the effects to the reversal flow.

Also, the experiments developed by Chen et al. (2017) for greater R_{eD} than those tested in this article, obtained similar results for the velocity profiles. Chen et al. (2017) showed, for a smooth bed, that the velocity profile decreases in magnitude when going from a dimensionally longitudinal distance $x/D = 3.3$ to $x/D = 0.7$, associating the decrease to the presence of the pile and horseshoe vortex.

The results of the present investigation showed that the mean velocity profiles near the bottom, for a relative distance of $x/D = 0.2$, increased when incipient sediment transport occurred, which is equivalent to what was Ahmed and Rajaratnam (1998) previously described.

The spatial behavior of the first four turbulent modes of vorticity detected in the present investigation, was found to be in agreetment with what was previously described by Apsilidis et al. (2016), who for bed sediment similar to that used in this research ($d_{50} = 3.6$ mm), detected that the main mode of the turbulent coherent structures (Φ_1) is not associated with flow lines that describe the rotation and rather behave parallel to both the bed and the pile.

Apsilidis et al. (2016) associate the behavior of the turbulent modes with the roughness of the bottom, however, Guan et al. (2018), by means of measurements with the PIV technique for a bed composed of sediments with a smaller diameter ($d_{50} = 0.56mm$) that those of Apsilidis et al. (2016) and those in this article, indicate that, for a bed before starting the scour (that is flat bed), a down-flow is clearly visible on the upstream face of the pier, but no obvious vortex is generated at the upstream base of the pier. Additionally, the maximum vorticity occurs in the regions near the bed.

The results presented by Guan et al. (2018) agree with the categorization of the turbulent modes that in the present article has determined for a bed in the state previous to the scour, identifying the down-flow as the main mechanism of the flow. Guan et al. (2018) link their results to the Reynolds number of the pile used in their experiments ($R_{eD} = 13680$), but in the present investigation the same behavior was obtained for smaller R_{eD}, which would be an indicator of the general behavior of the flow in the initial stages of the scouring process.

Chen et al. (2017), through laboratory tests carried on in a flume with a smooth bed and a pile of 3.2 cm of diameter, studied the behavior of the horseshoe vortex using PIV measurements. In order to produce the horseshoe vortex in their experiments, Chen et al. (2017) use a bimodal probability distribution of the turbulent velocity fluctuations (u' & v') and from their experiments, they determined that a certain times the typical circulation of the vortex does not develop and the streamlines tend to be parallel to the bed in some sections, and parallel to the pile in others. Based on the results of Chen et al. (2017), the statement regarding to the down-flow as a most energetic mode before the scour start, suggested in this article, would be confirmed.

Equivalent results to those obtained by Unger and Hager (2007) are found in this article. Even though, the tests of Unger and Hager (2007) were developed to evaluate the evolution

of the down-flow, as a function of the scour depth, and, turbulent structures were not studied from a study of their PIV data, Unger and Hager (2007) showed that in the initial stages of the scouring process, the mean velocity field did not robustly show the presence of the horseshoes vortex and the streamlines being mainly parallel to the bed and the pile.

As is well known, the presence of a pile modifies the hydrodynamic behavior in comparison with the free stream case, forming the so-called horseshoe vortex in front of the pile, which have been historically described by Baker (1979) for the laminar case and Baker (1980) for the turbulent one, among others.

Dargahi (1989) describes in detail the formation of horseshoe vortices due to turbulent flows that interact with a circular pile embedded in a granular bed, indicating the main mechanisms that occur in this process, which in the opinion of the authors of this article, can be linked to the turbulent modes detected in this article.

The first dynamic characteristic described by Dargahi (1989) is the downward flow wich, combined with the boundary layer over the bed generates a small vortex which also has been mentioned by other authors (Ahmed and Rajaratnam, 1998; Sarker, 1998; Unger and Hager, 2007).

In our experiments, the phenomenon described by Dargahi (1989) is represented basically by the first turbulent mode (Φ_1) determined by the POD analysis.

Further Dargahi (1989) describes the formation of a larger vortex that rotates clockwise with a large spatial development which is identified by the second turbulent mode (Φ_2) in the present investigation, this structure corresponds to the primary horseshoe vortex.

What is described in the previous paragraph can also be based on the results obtained in the analysis of the cross-correlation between the time evolution of the turbulent modes and the time series of sediment movement, which was presented previously in Figure 2.21 was shown that the joint action of C_1 and C_2 is related by approximately 80 % with the incipient movement of the sediments. Historically diverse authors have linked the scouring process in front of the pile to the horseshoe vortex, among which it can mentioned are those made by Breusers et al. (1977), Keutner (1932), Tison (1940), Posey (1949), Laursen and Toch (1956), Roper et al. (1967) and Melville (1975); or one of the most recent authors such as Unger and Hager (2007), Dey and Raikar (2007) or Das et al. (2013), among others.

The third turbulent mode (Φ_3) corresponds to a system of double vorticity, where each of the vortex rotates in the opposite directions. This structure is also consistent with that described in detail by Dargahi (1989), Simpson (2001), Kirkil and Constantinescu (2015) and Apsilidis et al. (2016).

The results associated to the cross-correlation analysis between the incipient motion and the turbulent modes Φ_1 and Φ_2, has shown that the maximum correlation is obtained for a zero lag, this being consistent with what was previously presented by Nelson et al. (1995) and Keshavarzy and Ball (1999). However, the Stokes number was greater than one which theoretically would be an indicator that the response time of the particle is greater than the time that the flow mobilizes it and therefore the inertia would dominate the incipient transport, which would not be concordant with a lag equal to zero.

Lucci et al. (2011) based on experiments and numerical results about spheres moving in a fluid, concludes that the Stokes number can be applied when $Re_p < 0.5$ with an excellent agreement. An acceptable agreement is wating when $0.5 < Re_p < 1.0$ and it is not recomended is application when $Re_p > 1.0$, such as is the case of the present investigation and of what previously developed by Nelson et al. (1995) and Keshavarzy and Ball (1999). Lucci et al. (2011) concludes that the Stokes number should not be used as an indicator of turbulence modulation by large particles.

As a complement to which was described by Lucci et al. (2011), Bourgoin et al. (2011) comment that the particle response time to turbulent forcing remains essentially of the order of carrier flow dissipation time rather than any particle dependent time (as Stokes time for instance). These observations are in contrast with usual predictions from Stokesian models for point particles. In the case of the expimental test carried on in this research, the turbulent processes into the incipient motion, was more important that the stokesian ones and due to that, the Stokes number can be used to compare the obtained results with other ones, but not as a motion indicator.

The relevance of the turbulence on the incipient transport of the sediments in the vicinity of a pile was incorporated and discussed by Dargahi (1990), who based on experimental data, described in detail how the scouring process occurs. Dargahi (1990) proposes a modification of the critical velocity for the incipient transport of the sediments, incorporating the effects of turbulence, not as a physical process in the flow, but through a coefficient associated with the relative intensity of the turbulence. Dargahi (1990) recognizes the importance of the vortex at the base of the pi in the local scour and stablished the deficit of the shear stress on the bed as a descriptor of the incipient transport.

Similar approach to that described by Dargahi (1990), was developed by Hager and Oliveto (2002), who proposed a modification of the beginning of the sediment transport, incorporating a coefficient to the critical velocity equation associated with the geometry of the pile.

Both Dargahi (1990) and Hager and Oliveto (2002) recognize the need to improve the description of the incipient transport of sediments at the bottom of the pile. However, the derivation of their respective thresholds of initiation of sediment transport, continue to be based mainly on the mean flow. However according to the results found in the present investigation, the incipient transport of the sediments in front of the pile, would be strongly linked to turbulent fluctuations and not only to the average approximating flow.

The above can be verified by observing the time series of the coefficients C_1 and C_2 (which are associated with the turbulent modes Φ_1 and Φ_2, respectively) shown in Figure 2.20 and whose cross-correlation with the movement identification would reach magnitudes of about 80% in all tests developed.

Experimentally and despite the fact that their tests were developed for a flume without the presence of a pile, Nelson et al. (1995), Kaftori et al. (1995) and Niño and García (1996) highlight the role of turbulence in the beginning of the particle movement. In the case of the Nelson et al. (1995) research, they mention that in the uniform steady flow condition, the bed shear stress scale with the turbulent fluctuations, but when a non-uniform flow or unsteady flows is developed, the bed shear stress not necessarily scale with the turbulent fluctuations, and obviously in those cases the bed shear stress can not be used as a sediment transport indicator, due to this flow parameter loses representativity.

The aforementioned by Nelson et al. (1995) was recently confirmed by Lee and Hong (2019) for a flow in presence of a pile, establishing that the mean flow variable is not enough to explain complex turbulent flow field and the pile scour.

Nelson et al. (1995) in his research indicates that sediment movements can be associated with the behavior of horizontal and vertical turbulent fluctuations, both for sweepig ($u' > 0$, $v' < 0$) and bursting ($u' < 0$, $v' > 0$), being the same pattern detected in the present investigation, situation that it would describe that, independent of the mechanism of production of turbulence (a pile in this investigation or a step in the case of Nelson et al., 1995), has a relevant role in the incipient transport of sediments.

The results obtained in this research, regarding to the quadrant analysis, are concordant with those obtained by Lee and Hong (2019). Because this research establish that the ejection

and sweeps are relevant for the incipient motion, while Lee and Hong (2019) demostrated that the scour hole upstream of a pile are dominated by two primary forcing: ejection and sweep.

In the case of the investigation by Kaftori et al. (1995), they establish the importance of the vortex that are formed in the flow due to particle streaks near the wall and particle motion. In this investigation the link between primary vortex and incipient transport seems to follow the patterns of Kaftori et al. (1995).

Numerically, there are some studies that suggest the need to describe the sediment transport with techniques complementary to those currently used in the flow without obstructions or modify the mobility of sediments to facilitate their transport. Such is the case of the work developed by Escauriaza and Sotiropoulos (2011a) and Quezada et al. (2018).

Escauriaza and Sotiropoulos (2011a), based on experimental evidence, developed a numerical methodology to represent the initial stages in the sediment transport around a pile, providing a novel sediment transport model for fine sand in order to take into account the effects related to the horseshoe vortex, according to the previous research of Dargahi (1990). Escauriaza and Sotiropoulos (2011a) establish the importance of correctly representing, by means of hydrodynamic simulation, the vorticity in the bottom of the pile, since it is the main responsible for the sediment transport in their initial stages. This is in agreement with the results of the pesent investigation, since it has been determined that the first two turbulent flow modes (down-flow and horseshoe vortex) are those that explain in greater correlation the movements of the sediments in front of the pile.

Additional indications of the need to reevaluate the sediment transport computation in areas where the turbulence fluctuations are greater than the scale that establishes the bed shear stress was developed by Cheng et al. (2018), who proposed an approximate methodology to incorporate in the Reynolds Average Navier Stokes equations (RANS) the effect of the coherent structures on the sediment entrainment and then they are applied to the scour in piles.

Quezada et al. (2018), based on RANS model, develop the numerical simulation of the scour in piles for different types of flows. By using a coefficient that increases the mobility of the sediments, they manage to represent with greater precision the maximum magnitudes of sediment scouring of several experimental studies.

Given the above, the results found in the present investigation provide information on the mechanisms of incipient motion, according the experimental and numerical evidence that has been previously developed.

2.4.7 Conclusions

Using velocity fields registered with the PIV technique, the average behavior of the velocity profiles, the turbulent flow structures and the characteristics of the incipient transport in the vicinity of the pile were analyzed.

The average velocity profiles determined from the experimental data indicated that, when the incipient transport are reached the average magnitude of the velocity near the bottom are not equal to zero. This situation that would be due to the intensification of turbulent fluctuations and would be responsible for moving the sediments in front of the pile.

Through the analysis of Proper Orthogonal Decomposition, it was possible to characterize the behavior of the turbulent structures in front of the pile and classify them in the different types of flows and vorticities that ocurr. The hydrodynamic mechanism of higher energy corresponds to the down-flow and the incoming boundary layer (Φ_1), followed by the primary horseshoe vortex (Φ_2) and the secondary vorticity system (Φ_3).

The analysis of the incipient transport of the sediments showed that the temporal evolution

of the turbulent structure associated with mode 1 (Φ_1) and mode 2 (Φ_2), corresponding to the down-flow/incoming boundary layer and the primary horseshoe vortex, respectively, match significantly with the events of movements of the sediments registered for the I01, I02 and I03 tests, as shown by the high values of the cross-corelation of $C_1 + C_2$ with the incipient motion events.

The quadrant analysis of the turbulent fluctuations showed that ejection, sweeps and outward interaction mechanisms represent the 80% of the fraction of events in which incipient transport occurs. The results were concordant with the analysis of the turbulent modes in the incipient transport, in such a way that it can be concluded that both the down-flow/incoming boundary layer and the primary horseshoe vortex, are the hydrodynamic mechanisms responsible for incipient motion in front of the pile.

Chapter 3

Numerical modelling of pile scour

3.1 Numerical representation of hydrodynamics around a pile

Currently, general equations of hydrodynamics obtained from the Navier-Stokes do not possess a general analytical solution and only some exact solutions for particular cases can be found in specialized literature.

Given the absence of a general solution of the Navier-Stokes equations, it is necessary to implement numerical approximations that allow to determine the hydrodynamics for different boundary conditions, numerical domains and forcings.

Reynolds (1895) included the effects of turbulence in the Navier-Stokes equations, considering the temporal average (and later extended to ensemble averages, Tucker, 2012) of the velocity field, these are called the *Reynolds Averaged Navier-Stokes Equations* (RANS), which are described in more detail in the section 2.2.

Alternatively, there are other approaches to the description of turbulence in the flow besides the RANS; those are the *Direct Numerical Simulation* (DNS) and the *Large Eddy Simulation* (LES).

The DNS model corresponds to a technique that seeks to solve the primitive Navier-Stokes equations, with no more approximations than those made in the numerical schemes used. In other words, it does not include simplifications or sub-models becausethe grid sizeshould be smaller than the smaller eddy present in flow. Its main disadvantage compared to RANS and LES, is the high computational cost to solve the eddies since it requires high resolution spatial discretizations.

The LES model is based on a filter of the governing equations of the fluid, focusing on large-scale eddies which are solved, while the smaller are approximated by the so-called sub-models, some of which are indicated below:

- Smagorinsky's sub-model (Smagorinsky, 1963).
- Scale similarity sub-model (Bardina et al., 1980).

All of these methodologies for determining flow behavior have associated ranges of applicability in the process of energy transfer along the turbulence spectrum, which has been described by Kolmogorov (1941). Main aspects of using RANS, DNS and LES are illustrated in Figure 3.1, where $E(\kappa)$ is the energy spectrum and κ is the wave number.

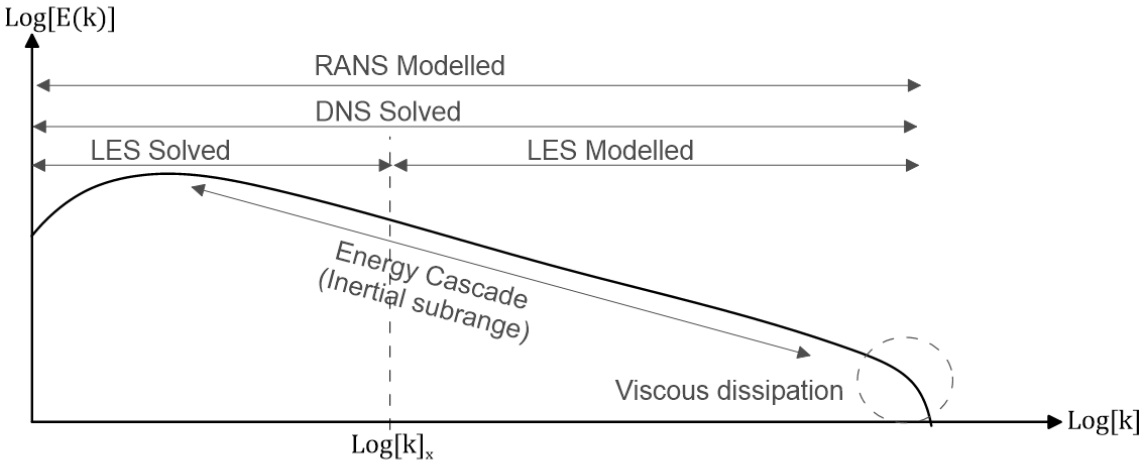

Figure 3.1: Applicability of RANS, DNS and LES according to the Kolmogorov's turbulence spectrum.

3.1.1 Reynolds Averaged Navier-Stokes Equations: RANS

Statistics and some properties of the turbulent flow

Previously to development of the *Reynolds Averaged Navier-Stokes Equations*, some properties of the turbulent flow must to be analyzed, in orden to have a better understanding of the Reynolds decomposition.

According to Kundu et al. (2015), there are five basic features of turbulence, that can be summarized according to:

- Fluctuations: The turbulent fluctuations (e.g. velocity, pressure, temperature), appear to be irregular, chaotic, and unpredictable.
- Nonlinearity: The turbulence occurs when the relevant nonlinearity parameter, say Reynolds number (Re), exceeds a critical value. When this critical value is reached, small perturbation of the flow can grow spontaneously. However, this state become unstable and reaches a nonrepeating unpredictable state. The nonlinearity is clearly evident in the vortex stretching, which is a key process by which three-dimensional turbulent flows maintain their fluctuations.
- Vorticity: In a turbulent flow, some indentifiable structures are present, particularly those that spin and are called *eddies*, which involve a range of eddy sizes, according to the Reynolds number.
- Dissipation: The vortex stretching mechanism transfers fluctuation energy and vorticity to smaller and smaller scales via nonlinear interaction, until the viscosity convert the energý into heat.
- Diffusivity: Due to the high agitation and overturning motions, the turbulent flows are characterized by a rapid rate of mixing and diffusion of the species, momentum, and heat.

Previously to developed the averaged equations of the fluid motion, it is necessary to remember some statistical properties of turbulent flows, which according to Tennekes and Lumley (1972), does not need to be sophisticated, because a simple decomposition of all quantities into mean values and fluctuations with zero mean suffice.

The determination of the average of a random time series that results from a stochastic process, requires the incorporation of specific terminology (Kundu et al., 2015):

- Ensemble: is a collection of independent realizations (N) of a random variable, obtained under identical conditions.
- Ensemble average: Ordinary arithmetic average over the collection (denoted by an over bar).
- Expected value: is the ensemble average applied over a ensemble with a large number of realizations ($N \longrightarrow \infty$) and is denoted with angle brackets.

Considering the previous definitions and taking a random variable defined as $a(t)$, the expected value can be defined according to the equation 3.1.1:

$$\langle a(t) \rangle = \lim_{N \to \infty} \overline{a(t)} = \lim_{N \to \infty} \frac{1}{N} \sum_{n=1}^{N} a(t) \tag{3.1.1}$$

It is evident that both in experimentation and in numerical modeling, performing infinite tests ($N \longrightarrow \infty$) is impracticable. However, in stationary time processes, its statistics do not depend on time and therefore the average value can be described by the use of the ensemble average, which is estimated from the equation 3.1.2.

$$\overline{a} = \lim_{T \to \infty} \frac{1}{T} \int_0^T a(t) dt \tag{3.1.2}$$

This impossibility of making an infinite number of test, leads to the need to establish that the process to be stationary in time requires that ergodicity be fulfilled, because statistically when the time average of a series of random values is independent of time. This necessarily implies that any assembly that is taken in an inertial window of the process, reports the same statistics regardless if it is captured at the beginning, middle or end of the time series.

As mentioned by Kundu et al. (2015), there are some relevant averaged ensemble properties to remember before obtaining the averaged motion equations. These properties are indicated below:

- Commutative: The ensemble averaging commutes with the addition, multiplication by a constant, time integration, spatial differentiation and spatial integration.
- The ensemble average of an average, is just the average.
- The emsemble average of a product of random variables (e. g. a and b), is not necessarily the product of the ensemble average ($\overline{ab} \neq \overline{a}\overline{b}$).

The avegared equations of motion

Equations 3.1.3 and 3.1.4 are the Navier-Stokes equations for a homogeneous, incompressible and Newtonian fluid, which include the momentum and the continuity conservation by the use of both fluid and flow properties.

Flow properties are associated with u_i and $\widehat{p}$, that correspond to the three-dimensional velocity field (u_1, u_2 and u_3) and piezometric pressure ($\widehat{p}$), respectively. Fluid properties are the density and kinematic viscosity of the fluid, ρ and ν accordingly.

The piezometric pressure is defined according to equation 3.1.5, where p is the thermodynamic pressure, g denotes the gravity acceleration and x_3 is a vertical axis defined positive upwrads, against the direction of gravity.

Additionally, the spatial dimension (x_i) is included into the Navier-Stokes equations, and correspond to a three-dimensional field (x_1, x_2 and x_3).

$$\frac{\partial u_i}{\partial x_i} = 0 \tag{3.1.3}$$

$$\frac{\partial u_i}{\partial t} + u_j \frac{\partial u_i}{\partial x_j} = -\frac{1}{\rho}\frac{\partial \widehat{p}}{\partial x_i} + \nu \frac{\partial^2 u_i}{\partial x_j \partial x_j} \tag{3.1.4}$$

$$\widehat{p} = p + \rho g z \tag{3.1.5}$$

A turbulent flow instantaneously satisfies the Navier-Stokes equations (Kundu et al., 2015), however, for high Reynolds number it is virtually imposible to predict the flow due to the enormous range of lenght and time scales present in the flow.

Reynolds (1895) incorporated an approximation to the turbulent flow behaviour. Although the Navier-Stokes native equations are valid with numerical models unless the vortices were larger than the Kolmogorov scale, they present quasi random characteristics over time, even in a permanent flow condition (Niño, 2013).

The Reynolds proposal was based on the decomposition of the velocity field and the pressure, following a scheme similar to that shown in Figure 3.2. Assuming that turbulence produces perturbations (fluctuations), which can be statistically treated as ergodic process, velocity and pressure can be described according to the equations 3.1.6 and 3.1.7.

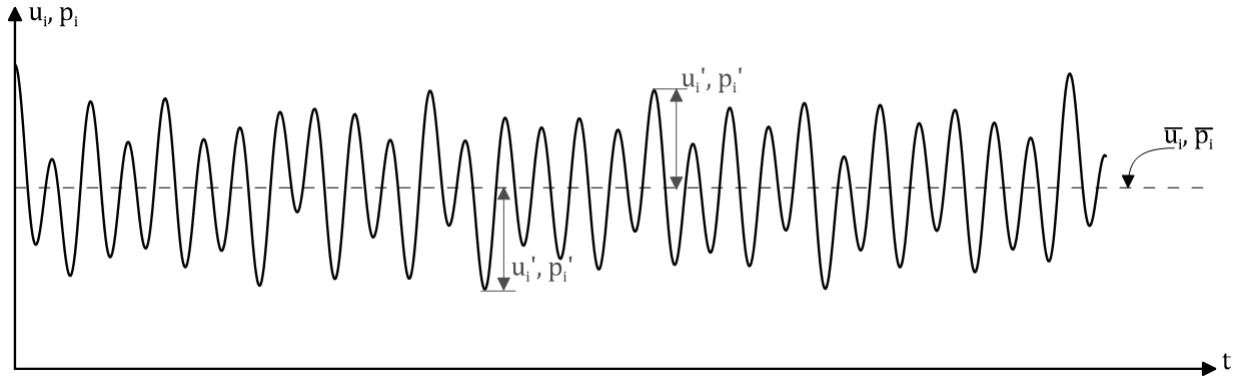

Figure 3.2: Reynolds decomposition for velocities and pressures, depending on the mean value and turbulent fluctuations.

$$u_i = \overline{u_i} + u_i' \tag{3.1.6}$$

$$\widehat{p} = \overline{\widehat{p}} + p' \tag{3.1.7}$$

Incorporating this decomposition into the Navier-Stokes equations (Reynolds decomposition), and taking a temporal average over them, considering that $\overline{\overline{a_i}} = \overline{a_i}$ and $\overline{a_i'} = 0$, where a corresponds to the velocity or pressure, the RANS are obtained according to the equations 3.1.8 and 3.1.9.

$$\frac{\partial \overline{u_j}}{\partial x_j} = 0 \tag{3.1.8}$$

$$\frac{\partial \overline{u_i}}{\partial t} + \overline{u_j}\frac{\partial \overline{u_i}}{\partial x_j} = -\frac{1}{\rho}\frac{\partial \overline{\widehat{p}}}{\partial x_i} + \nu\frac{\partial^2 \overline{u_i}}{\partial x_j \partial x_j} - \frac{\partial \overline{u_i' u_j'}}{\partial x_j} \tag{3.1.9}$$

The appearance of an additional term linked to the velocity fluctuations is noticed from 3.1.9, which is denominated the turbulent tensor of Reynolds ($\tau_{tij} = -\rho\overline{u_i' u_j'}$). This new term can be incorporated into the law of Newtonian fluids according to the expression 3.1.10.

$$\tau_{i,j} = \tau_{vij} + \tau_{tij} = \mu\left(\frac{\partial \overline{u_i}}{\partial x_j} + \frac{\partial \overline{u_j}}{\partial x_i}\right) - \rho\overline{u_i' u_j'} \tag{3.1.10}$$

Although, the development of Reynolds (1895) allows to identify, in mean terms, the effect of turbulence in the hydrodynamic governing equations, this does not solve the problem, since it incorporates new unknowns. To achieve a solution, it is first necessary to model the turbulent tensor of Reynolds and subsequently propose a closure equation for it. The mathematical representation of τ_{tij} is conducted in a similar manner to a Newtonian fluid, assuming that it can be described according to the expression 3.1.11.

$$\tau_{tij} = 2\mu_t\left(\frac{\partial \overline{u_i}}{\partial x_j} + \frac{\partial \overline{u_j}}{\partial x_i}\right) \tag{3.1.11}$$

It is important to note from the equation 3.1.11 that μ_t is referred to as *eddy dynamic viscosity* and it can be interpreted as a property of the flow, since it depends on the velocity.

In order to estimate the magnitude of the eddy viscosity, the turbulent closure equations are applied. Some of them are presented below.

A extended demonstration of the averaged equation can be found in Tennekes and Lumley (1972), Pope (2000), Durbin and Reif (2011), (Kundu et al., 2015), among others.

3.1.2 Turbulence closure modelling

Obtaining applied solutions out of the RANS requires the definition of a turbulence closure equation for the determination of the eddy viscosity, and afterwards the Reynolds tensor. Currently, there exist several proposals to fulfil this purpose, which according to Rodi (1980) and García (1996) can be categorized into:

- Algebraic or zero equation models.
- One-equation models.
- Two-equation models.
- Higher order models.

Following, each category of the turbulent closure equations are broadly described.

Zero equations models

The zero equation models correspond to the most simplified vision of representing the *eddy viscosity*, since it approximates it as a proportion of the product of the fluctuation velocity ($\frac{\partial u}{\partial x}$) and a characteristic length (l, Prandtl's mixing length), its largest degree of application is in engineering problems García (1996). Due to the low computational cost of implementation and execution, García (1996) establishes that these can be sub-classified in the following categories:

- Constant turbulent viscosity.
- Mixing length models.
- Prandtl model for confined flows.

However, according to García (1996), its applicability is restricted to a limited set of two-dimensional cases.

One equation models

Development of one equation models begins as an alternative and improved form of the zero equation, including an auxiliary differential equations that allows to estimate turbulent viscosity. According to García (1996) this type of model provide a direct link between the scale of velocity fluctuations and the average velocity gradients, through differential equations of transport.

For the numerical simulation of fire propagation, Capote et al. (2008) indicates that the models of one equation of Baldwin and Barth (1990), Spalart and Allmaras (1992) or Kolmogorov - Prandtl (described in Wilcox et al., 1998) are usually used. However, for problems associated with environmental fluid mechanics, García (1996) and Niño (2013) agree that Kolmogorov - Prandtl is the most commonly used approach.

The Kolmogorov - Prandtl model links the turbulent viscosity (ν_t) with the turbulent kinetic energy (K) that is contained in the large scales (L), by an empirical constant (c'_μ) according to the equation 3.1.12.

$$\nu_t = c'_\mu \sqrt{K} L \tag{3.1.12}$$

To obtain turbulent kinetic energy included in the Kolmogorov - Prandtl eddy viscosity, Tennekes and Lumley (1972) propose a transport equation considering dissipation according to the expression 3.1.13.

$$\frac{\partial K}{\partial t} + \overline{u_i}\frac{\partial K}{\partial x_i} = \frac{\partial}{\partial x_i}\left(\frac{\nu_t}{\sigma_K}\frac{\partial K}{\partial x_i}\right) + \nu_t\left(\frac{\partial \overline{u_i}}{\partial x_j} + \frac{\partial \overline{u_j}}{\partial x_i}\right)\frac{\partial \overline{u_i}}{\partial x_j} + \beta g_i \frac{\nu_t}{\sigma_t}\frac{\partial \overline{\phi}}{\partial x_i} - c_D \frac{K^3/2}{L} \tag{3.1.13}$$

Where ϕ corresponds to a variable that represents the variation in density, β is a constant of transformation and σ_K is a constant of diffusion. The last two terms on the right side of the equation 3.1.13 correspond to buoyancy and dissipation (ϵ), respectively.

It is important to note that the Kolmogorov - Prandtl model pre-conditions the value of the dissipation, because it assigns a proportional form to constan value of the model (c_ϵ) and the length scale of the great vortices (L), accoridng to equation 3.1.14. This situation

becomes more flexible in the case of models with two equations, proposing an expression of transportation for these purposes, as analyzed in the next section.

$$\epsilon = c_\epsilon \frac{K^{3/2}}{L} \tag{3.1.14}$$

Two equation models

In the case of the two-equation models, the main assumption is that the characteristic length of the large scales (L) can be estimated from a transport differential equation, assuming that the size of the vortices associated with L conditions the turbulent eddies, their dissipation and the processes related to the energy cascade (García, 1996).

Within this classification of turbulence closure models, there are three schemes widely applied to engineering problems (Menter, 1994):

- $K - \epsilon$ model
- $K - \omega$ model
- SST model

The $K - \epsilon$ model is based on the solution of transport differential equations for turbulent kinetic energy (K) and the dissipation rate (ϵ) which together determine the eddy viscosity value according to the expression 3.1.15.

$$\nu_t = c'_\mu \frac{K^2}{\epsilon} \tag{3.1.15}$$

The transport equations of the turbulent kinetic energy and the dissipation rate are shown in the expressions 3.1.16 and 3.1.17, respectively.

$$\frac{\partial K}{\partial t} + \overline{u_i}\frac{\partial K}{\partial x_i} = \frac{\partial}{\partial x_i}\left(\frac{\nu_t}{\sigma_K}\frac{\partial K}{\partial x_i}\right) + \nu_t\left(\frac{\partial \overline{u_i}}{\partial x_j} + \frac{\partial \overline{u_j}}{\partial x_i}\right)\frac{\partial \overline{u_i}}{\partial x_j} + \beta g_i \frac{\nu_t}{\sigma_t}\frac{\partial \overline{\phi}}{\partial x_i} - \epsilon \tag{3.1.16}$$

$$\frac{\partial \epsilon}{\partial t} + \overline{u_i}\frac{\partial \epsilon}{\partial x_i} = \frac{\partial}{\partial x_i}\left(\frac{\nu_t}{\sigma_\epsilon}\frac{\partial \epsilon}{\partial x_i}\right) + c_{1\epsilon}\frac{\epsilon}{K}\left(P + G\right)\left(1 + c_{3\epsilon}R_f\right) - c_{2\epsilon}\frac{\epsilon^2}{K} \tag{3.1.17}$$

From the equation 3.1.17 σ_ϵ, $c_{1\epsilon}$, $c_{2\epsilon}$ and $c_{3\epsilon}$, are empirical constants, while R_f is Richardson number defined according to equation 3.1.20. The terms P and G correspond to expressions 3.1.18 and 3.1.19, respectively, and that have been presented summarized in formulation 3.1.17.

$$P = \nu_t\left(\frac{\partial \overline{u_i}}{\partial x_j} + \frac{\partial \overline{u_j}}{\partial x_i}\right)\frac{\partial \overline{u_i}}{\partial x_j} \tag{3.1.18}$$

$$G = \beta g_i \frac{\nu_t}{\sigma_t}\frac{\partial \overline{\phi}}{\partial x_i} \tag{3.1.19}$$

$$R_f = -\frac{G}{P + G} \tag{3.1.20}$$

Although, the $K - \epsilon$ is one of the most common models, it presents difficulties in the representation of large negative pressure gradients (Wilcox et al., 1998). Additionally Menter (1994)

establishes that variations from 5% to 10% of the constants involved, produce improvements or increase the error, significantly.

The $K-\omega$ model is based on the determination of two transport equations additional to the RANS problem, one associated with turbulent kinetic energy (K) and the other to the specific dissipation (ω). The primitive form for this turbulent closure is presented by Wilcox (1988) and establishes that the eddy viscosity can be estimated from the equation 3.1.21.

$$\nu_t = \frac{K}{\omega} \tag{3.1.21}$$

To determine the turbulent kinetic energy and the specific dissipation values, transport equations are applied for each of them according to the expressions 3.1.22 and 3.1.23, where β^*, σ^*, α, β and σ, are constants of the model.

$$\frac{\partial K}{\partial t} + \overline{u_i}\frac{\partial K}{\partial x_i} = \tau_{ij}\frac{\partial u_i}{\partial x_j} - \beta^* K\omega + \frac{\partial}{\partial x_j}\left[(\nu + \sigma^*\nu_t)\frac{\partial K}{\partial x_j}\right] \tag{3.1.22}$$

$$\frac{\partial \omega}{\partial t} + \overline{u_i}\frac{\partial \omega}{\partial x_i} = \alpha\frac{\omega}{K}\tau_{ij}\frac{\partial u_i}{\partial x_j} - \beta\omega^2 + \frac{\partial}{\partial x_j}\left[(\nu + \sigma\nu_t)\frac{\partial \omega}{\partial x_j}\right] \tag{3.1.23}$$

The model $K-\epsilon$ presents difficulties in representing large adverse pressure gradients, same as model $K-\omega$. In addition, it does not represent well the asymptotic behavior of turbulence in the vicinity of the wall (Menter, 1994).

In order to improve the deficiencies of the models $K-\epsilon$ and $K-\omega$, Menter (1994) proposes the so-called *shear stress transport model* (SST), based on the structure of $K-\omega$, but incorporating aspects of both $K-\epsilon$, and the technique called *Reynolds stress model* (RSM).

In essence, the SST model considers the following:

- In the viscous sub-layer, a *Low-Re turbulence model* type is applied, which allows to solve directly what happens in the vicinity of the wall.
- On the free surface, the model $K-\epsilon$ is applied, which has shown to have better results in this area of the flow (Menter, 1994).

The transport equations that Menter (1994) proposed to construct the closure model of the SST turbulence are presented in the expressions 3.1.24, 3.1.25 and 3.1.26, where a_1 is a constant of the model, S is the absolute value of the vorticity, $F1$ and $F2$ are specific fuction of the model defined according to equations 3.1.27 and 3.1.28, respectively, where y is the distance to the next surface, $CD_{k\omega}$ is the positive portion of the cross-diffusion. The term P_K is defined according to equation 3.1.29 Further information on this calculation methodology can be consulted directly in Menter (1994).

$$\nu_t = \frac{a_1 K}{max(a_1\omega, SF_2)} \tag{3.1.24}$$

$$\frac{\partial K}{\partial t} + \overline{u_i}\frac{\partial K}{\partial x_i} = P_K - \beta^* K\omega + \frac{\partial}{\partial x_j}\left[(\nu + \sigma_K\nu_t)\frac{\partial K}{\partial x_j}\right] \tag{3.1.25}$$

$$\frac{\partial \omega}{\partial t} + \overline{u_i}\frac{\partial \omega}{\partial x_i} = \alpha S^2 - \beta\omega^2 + \frac{\partial}{\partial x_j}\left[(\nu + \sigma_\omega\nu_t)\frac{\partial \omega}{\partial x_j}\right] + 2(1-F_1)\sigma_{\omega 2}\frac{1}{\omega}\frac{\partial K}{\partial x_i}\frac{\partial \omega}{\partial x_i} \tag{3.1.26}$$

$$F_1 = \tanh\left[\left(min\left[max\left(\frac{\sqrt{k}}{0.09\omega y};\frac{500\nu}{y^2\omega}\right);\frac{4\rho\sigma\omega 2}{y^2 CD_{k\omega}}\right]\right)^4\right] \tag{3.1.27}$$

$$F_2 = \tanh\left[\left[max\left(\frac{\sqrt{k}}{0.09\omega y};\frac{500\nu}{y^2\omega}\right)\right]^2\right] \tag{3.1.28}$$

$$P_K = \tau_{ij}\frac{\partial u_i}{\partial x_j} \tag{3.1.29}$$

Higher order models

Higher-order models correspond to those that use more than two equations to determine the eddy viscosity. According to García (1996) this approach is based on the derivation of an exact form of the turbulent shear streeses.

Some of the available methods are presented in Capote et al. (2008), highlighting the following:

- Four-equation models.
- *Reynolds stress model* (RSM).

The four-equation models are based mainly on the scheme developed by $K-\epsilon$, however, local effects of pressure rate of strain tensor are incorporated, in such a way that they allow to simulate more accurately the effects that occur in the vicinity of the walls. More information for this type of approach, can be consulted in Durbin (1995) and Popovac and Hanjalic (2007).

The *Reynolds stress model* uses seven transport equations for the determination of the eddy viscosity, using each of them for the definition of Reynolds stresses. However, its computational cost is high and its application to practical engineering problems is limited. The theoretical development of this technique can be reviewed in Launder et al. (1975).

3.2 Numerical representation of fluid/structure interaction

The numerical treatment of the governing equations of hydrodynamics interacting with rigid or mobile structures is one of the areas of development of fluid mechanics that is currently fully investigated, proposing new methodologies for the representation of this biphasic flow. The first approximations to the solution of the Navier - Stokes equations go back to the XX Century when Chorin (1968), using the method of finite differences, proposed a time dependent solution for the velocity and pressure fields for biphasic incompressible fluids.

Nakayama and Romero (1971) presented their proposal for obtaining the aforementioned variables of interest, considering quasi-three-dimensional characteristics of the flow, for an incompressible fluid and with the presence of a simple solid obstacle within the domain.

In the same line of research, Hirt and Cook (1972) present a technique to solve the Navier Stokes equations by finite differences, considering the temporal variation of the system and the three-dimensional components of the velocity field. Specifically, the authors apply the method called *Marked and Cell method* (MAC) in a confined space. The obstacles are treated as grid cells where there is no possibility of flow or movement, mentioning that the thermal characteristics in the interaction are important to include in numerical modeling.

Based on the results of Hirt and Cook (1972), the authors Nichols and Hirt (1973) incorporate the effects of considering a free surface (without confinement), evaluating both submerged and emerged obstacles. In both cases, it is considered as a static body, meaning it does not move under the action of the flow. Until 1973, the solutions of the proposed Navier - Stokes equations have been addressed considering a flat bottom, a situation that in general terms constitutes a limitation. In order to overcome this limitation, Gal-Chen and Somerville (1975) propose a numerical approach incorporating bathymetry using finite difference techniques.

The work of Gal-Chen and Somerville (1975) proposes the use of a staggered grid for the solution of the fluid equations (2D) around the area with bathymetry, considering its action as an irregular boundary condition, which has the particularity of representing both the concept of non-slip and slip.

By incorporating additional physical processes in the equations of fluids, Fornberg (1977) performs a numerical study of two-dimensional turbulence for a periodic boundary condition in the Navier-Stokes equations applying Fourier series. As a general recommendation Fornberg (1977) establishes the need to propose the Navier - Stokes as a function of vorticity. Additionally, he comments that the viscosity becomes relevant in the energy dissipation scale of the turbulence spectrum.

The incorporation of turbulence in the Navier - Stokes equations and an alternative solution is presented by Chen et al. (1990), considering the model $K - \epsilon$ as the closure equation for incompressible fluids. On the other hand Bassi and Rebay (1997) by using the finite element method in its discontinuous form (incorporating numerical concepts typical of finite volumes and *Riemann solvers*), propose a numerical approximation to the Navier - Stokes equations for compressible fluids.

From the nineties onwards, the numerical solutions of the Navier - Stokes equations continued to be developed, focusing mainly on increasing the accuracy in the methods. Some of the authors who continued in this line of research are highlighted below:

- Brown et al. (2001): Propose the application of the numerical projection method[1] for the solution of an incompressible fluid.
- Quarteroni and Rozza (2007): Propose a numerical method of reduction[2] to obtain the solution of the velocity field of the fluid, also incorporating parametrization of non-linear components.
- Hokpunna and Manhart (2010): Using the method of finite volumes, propose a solution for the Navier - Stokes equations, considering a staggered grid.
- Zhang (2014): Develops the semi-implicit method with fourth order approximation, considering periodic boundary conditions in incompressible fluids.

When studying scouring in piles, in addition to the determination of the velocity and pressure field, at least the following interactions must be also studied:

- Fluid - Free surface interaction

[1]The projection method is an effective numerical method to solve time-dependent incompressible fluid-flow problems firstly proposed by Chorin (1968). This method is based on the decoupuled treatment of the velocity and pressure fields. Sometimes, this method is also called Helmholtz-Hodge decomposition.

[2]According to Maday and Rønquist (2002), the method of reduction or also called the reduced-basis element method is a numerical approach to diminish the number of degrees of freedom associated with the numerical approximation to a set of partial differential equations.

- Fluid - Mobile bed interaction
- Fluid - Rigid body interaction

In the Figure 3.3 each of the points of interest is illustrated, which are described in a general manner below.

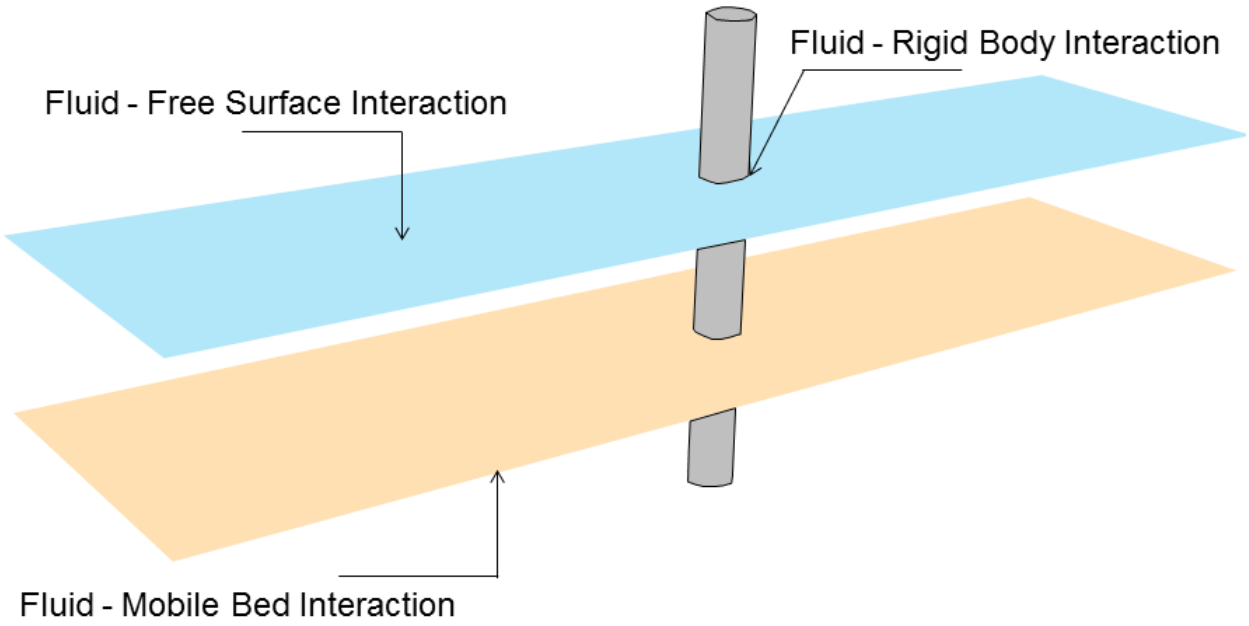

Figure 3.3: Identification of the fluid - structure interaction, of greater relevance for the study of undermining in piles.

3.2.1 Fluid - free surface interaction

From a numerical point of view, a free surface corresponds to another phase within the fluid and, in such a way, must be treated as a fluid-structure interaction, since it has the characteristic of developing movements linked to fluid dynamics and its numerical values, the representation becomes complex. However, this can be addressed through a discretization in the Eulerian or Lagrangian coordinate systems, where the first corresponds to a mesh with nodes in a fixed position, while the second allows the movements of these, adapting and densifying in those areas that require a higher resolution.

Pracht (1975) establishes that the main disadvantage of the Eulerian grids is their low capacity to adequately represent and solve free surfaces or mobile boundary conditions, aspects that are addressed by Lagrangian coordinates, which, however, do not adjust to flows with high distortions. Nonetheless, considering the strengths of each of the approaches, Pracht (1975) proposes the method known as Lagrangian-Eulerian arbitrary (ALE).

Solving the Navier–Stokes equation using the ALE method, provides several advantages according to the established by Pracht (1975), because it can be applied to all velocity ranges (laminar and/or turbulent regime), as well as for incompressible or compressible fluids. Additionally, highly curved areas, such as free surfaces, can be resolved.

Although, the ALE method provides a robust alternative for the solution of the fluid free surfaces. The adaptation of the grid in each step of time produces a high computational expense

and, eventually, high information storage requirements for prolonged simulations. Based on the latter, other approaches were developed, which can be classified into:

- Height Functions.
- Line and Segment.
- Tracers.

Height functions are based on the pre-definition of the behavior of the fluid free surface, through the kinematic equation 3.2.1:

$$\frac{\partial h}{\partial t} + u\frac{\partial h}{\partial x} = v \tag{3.2.1}$$

where h is the water depth, t the time, u the fluid flow velocity at h, and x the spatial coordinates.

On the other hand, line and segment concept corresponds to an extension of the height functions, which has greater flexibility, although it can pose problems of convergence and stability as a result of the representation of surface movements in time.

The tracers correspond to the use of particles that directly describe the free surface, which according to the amount used, it can increase the computational expense.

Hirt and Nichols (1981) raise for the first time the use of a methodology based on the volume of fluid (VOF), with the aim of representing the free boundaries within a domain. This method defines an auxiliary function F, that adopts a value between 1 and 0 for each cell, to indicate the fraction of it that contains fluid, being 1 its totality and 0 its absence. This allows the information to be stored more efficiently reducing the necessary storage.

Hirt and Nichols (1981) successfully applied the VOF method to the breakage of dams, propagation of a hydraulic jump, a breaking *bore* and the instability of Rayleigh-Taylor. All these examples being associated with mobile borders.

Smith (1988) introduce the concept of *Implict Continuous Eulerian (ICE) Hydrodynamics*, which requires a special treatment of boundary conditions, being careful to adequately define the conservation of the mass and momentum equation. Although developed for the hydrodynamic simulations in the presence of ice, their concepts are general and compatible to extrapolate to other disciplines.

Osher and Sethian (1988) develop the method called Level Set Method, which is based on the monitoring of motion interface, defining for this purpose an auxiliary function that identifies the phases of the fluid that is being modelled ($\phi(\vec{x}, t)$).

It can be established that if $\phi(\vec{x}, t) > 0$, the fluid is in the presence of phase 1, while if $\phi(\vec{x}, t) < 0$, is in phase 2, finally if $\phi(\vec{x}, t) = 0$ this corresponds to the interface.

The interface moves according to the fluid in such away that to obtain $\phi(\vec{x}, t)$, an additional advective characteristic equation can be proposed, as shown in expression 3.2.2.

$$\frac{\partial \phi}{\partial t} + \overline{u_j}\frac{\partial \phi}{\partial x_j} = 0 \tag{3.2.2}$$

With this method systems of governing equations for each of the phases can be build, since $\phi(\vec{x}, t)$ according to its sign will indicate in which of them the movement must be resolved. Nevertheless, Osher and Sethian (1988) indicate that in the interface a density and viscosity must be re-defined, because the change of these properties is not instantaneous, proposing for its characterization a differential thickness defined as 2ε in which area the equations 3.2.3 and 3.2.4 can be applied to quantify them.

$$\rho(\phi) = \rho_1 H(\phi) + \rho_2(1 - H(\phi)) \tag{3.2.3}$$

$$\nu(\phi) = \nu_1 H(\phi) + \nu_2(1 - H(\phi)) \tag{3.2.4}$$

where $H(\phi)$ is a function of the Hamilton-Jacobi type, ρ_1 and ρ_2 are the density of phase 1 and 2 respectively; ν_1 and ν_2 are the viscosity of phase 1 and 2 following the previous order.

Strictly speaking, the equations 3.2.3 and 3.2.4 correspond to a smoothing in the change of the properties of the flow phases, since when recognizing a thickness in which the interface is developed, both the density and the viscosity gradually vary.

The smoothing proposed by the *Level Set Method*, decreases the instabilities that can be achieved in numerical simulations (Saud, 2013).

Both the VOF method and the *Level Set Method* are based on the capture of the waterfront formed on the free surface, that is, they identify the geometric configuration of the interface. However, there are other approaches that allow fulfilling this purpose, one of them developed by Unverdi and Tryggvason (1992).

Unverdi and Tryggvason (1992) propose a methodology based on the monitoring of the interface, in which a curve is used to define the limits between the two phases under analysis, which is included within the numerical domain and advected in a lagrangian way to determine its evolution in time.

Kang et al. (2011) proposes a numerical method for the treatment of free surface called *Curvilinear immersed boundary* (CURVIB), based in the configuration of an unstructured grid, which can be adapted to complex forms of the interface.

An additional method for the representation of the free surface is the one named as *Smoothed Particle Hydrodynamics* (SPH) which is based on the description of the fluid as a set of distributed particles, which are displaced according to the hydrodynamic conditions in such a way that the trajectories of each of them can be traced in time, thus describing the interface. Originally this method was developed by Gingold and Monaghan (1977).

3.2.2 Fluid - mobile bed interaction

The description of the interaction of the fluid with the moving bed corresponds to a particular application of the methodologies previously described for the free surface. That is, the VOF, *Level Set Method*, CURVIB or SPH are equally applicable, however, given the granular nature of the phase that needs to be solved, some authors have proposed other approaches.

Liu and García (2008) propose a method for the description of the scour, considering an automatic deformation in the numerical mesh on which the equations are solved, based on the numerical method previously developed by Liu and García (2006).

The numerical method proposed by Liu and García (2006) establishes that, in order to perform the movements of the nodes of the mesh used to solve the bed evolution problem, it must be conducted according to the equation 3.2.5, in which γ is a diffusion coefficient that defines the movement of the nodes and v is the speed at which it moves.

$$\bigtriangledown \cdot(\gamma \bigtriangledown v) = 0 \tag{3.2.5}$$

Through the equation 3.2.5, the velocity fields are obtained for the movements of the mesh, which displaces its nodes according to the expression 3.2.6.

$$x^{k+1} = x^k + \triangle t \cdot v \tag{3.2.6}$$

The method developed by Liu and García (2006) can be classified as a Lagrangian technique, since it adapts to the movement of the interface to be solved.

Continuing with the Lagrangian approach, but focusing on the sediment grains that compose the moving bed, Escauriaza and Sotiropoulos (2011b) develop a computational study considering a rectangular channel with the presence of a circular cylinder. The grains of sediments are defined by a system of equations that describe the trajectory and momentum, integrating them with the equations of fluid movement, assuming that the sediments are a passive agent, meaning that their dimensions are of smaller scale than the last vortex solved by the fluid equations, thus not affecting the flow.

Escauriaza and Sotiropoulos (2011b) establish that, although the proposed Lagrangian model is simple, it manages to consistently represent the dynamics of the particles in the bed and provides fundamental information to study the start of sediment movement.

The Lagrangian equations of the sediment particles are basically two, which can be written according to the expressions 3.2.7 and 3.2.8.

$$\frac{\partial x_i}{\partial t} = v_i \tag{3.2.7}$$

$$m\frac{\partial v_i}{\partial t} = f_i \tag{3.2.8}$$

where x_i is the position of each grain, t is time, v_i the movement velocity of each particle, m is the particle mass and f_i the forces that act on the grains, which, according to Escauriaza and Sotiropoulos (2011b), are constituted of:

- Drag force.
- Gravitational force.
- Lift force.
- Added mass force.
- Force associated with fluid stresses.

Although the methodology proposed by Escauriaza and Sotiropoulos (2011b) allows a realistic approximation to the change of the bed due to the interaction of the fluid with it, the computational expense is high because the flow conditions must be solved hydrodynamically and the rearrangement of sediment particles that make up the bed before updating it.

3.2.3 Fluid - rigid body interaction

The fluid - rigid body interaction corresponds to one of the most studied fluid mechanics problems with the objective of determining both the forces that develop and the field of velocities.

A body that is interposed to the flow, numerically represents a boundary condition that must be described correctly because in its vicinity significant changes occur in the field of pressures and forces, generating as a response disturbances to the flow velocities, which, of course, will be mostly affected as the Reynolds number growths.

To solve numerically the fluid structure interaction, there are some general methodologies that have monopolized throughout history the majority of the application cases, being these indicated below:

- *Immersed boundary method*
- *Singularity method*
- *Immersed interface method*
- *Ghost cell method*

For each of these methodologies, a brief description is presented below.

Immersed boundary method

One of the first approaches to the interaction of the fluid with a rigid body corresponds to that developed by Peskin (1972), who applies this concept to the numerical simulation of blood flow in the cardiac system, using the term *immersed boundary method* for the first time.

The main feature of the method proposed by Peskin (1972) was its application to simple cartesian grids. Although the shape of the simulated body (heart) does not fit well, the results of its simulation were represented correctly.

From the proposal of Peskin (1972), some authors proposed modifications to the methodology based always on Cartesian grids, highlighting the following works:

- Clarke et al. (1986): Extend the method proposed by Peskin (1972), in a discretization of finite volumes.
- DeZeeuw and Powell (1993): Propose a methodology complementary to that of Peskin (1972), incorporating a refinement of the grid around the rigid body, depending on its curvature.
- Berger and Aftosmis (1998): Incorporate a methodology to reduce the number of cells in the representation of rigid bodies immersed in the fluid.

Singularity method

Thames et al. (1977) propose a numerical method for the solution of the incompressible Navier - Stokes equations, time-dependent and in whose domain there is a two-dimensional body of arbitrary geometry, considering two coordinate systems one Cartesian (for the areas separated from the two-dimensional body) and another curvilinear (to represent the two dimensional body), ensuring that in the construction of the grid, each of the curvilinear nodes coincide with the Cartesian ones. This simulation strategy is called by the authors as *Body-fitted curvilinear coordinate system.*

Following the same line of research, Krieg and Hailfinger (1980) develop the method called as Singularity Method or that is also known as Panel Method. The authors emphasize that their proposal is capable of representing any three-dimensional geometry and that their boundary conditions are based on the field of pressures and/or accelerations of the flow.

Immersed interface method

The *Immersed interface method* was developed by Leveque and Li (1994) and it was initially applied to the solution of elliptical problems with discontinuities. Essentially, it is created to provide an improvement to the approximations in conventional finite differences, because

when dealing with discontinuities, the expansions of Taylor series are not valid, however, it proposes additional terms to the numerical discretization which seek to represent them.

From the work of Leveque and Li (1994), other authors have proposed modifications to the method, among which can be named: Leveque and Li (1997), Li and Lai (2001), Berthelsen (2004), among others.

More information can be directly consulted in the references.

Ghost cell method

The phantom cell method (*Ghost cell method*), corresponds to an alternative way of imposing the necessary boundary conditions for the numerical modeling of obstacles submerged in the fluid medium.

In theory, this approach corresponds to the use of fictitious cells that are incorporated within the numerical domain, specifically in the obstacle that is being simulated, on which the boundary conditions apply.

The formal mathematical formulation of this methodology can be consulted directly in Tseng and Ferziger (2003), which, from a numerical point of view, consists of a particular case of the *Immersed boundary method* technique.

Berthelsen and Faltinsen (2008) propose an approximation based on this technique, which was successfully applied to the simulation of fluid interaction with circular and square piles, both for permanent and impermanent flow.

Currently, its applicability has been extended to the SPH technique, through the work carried out by Marrone et al. (2013), who use the phantom cell to a set of standard cases of fluid mechanics, in order to compare their results with the established theoretical values.

3.3 Brief conclusion and research needs

The numerical solution of RANS equations allows to obtain a robust description of the flow velocities field under various runoff conditions and geometric configurations of the domain of interest. In the particular case of flow around circular piles, several authors have studied the general behavior of flow velocities using RANS, both for steady current (Olsen and Melaaen, 1993; Roulund et al., 2005) and for oscillatory flow (Kamath et al., 2015; Ahmad et al., 2015; Bihs et al., 2017).

Several authors have studied the maximum pile scour for steady flows (as will be reviewed in the following sections of this chapter), however, achieving equilibrium scour requires large time scales (on the order of days) in which must be kept constant the flow that acts, so that for large flows (floods, for example) this definition of equilibrium scour corresponds to the theoretical maximum.

Castillo and Link (2015) and Link et al. (2017) present experimental results of the pile scour due to the action of floods, which were subsequently used by Quezada et al. (2018), with the purpose of studying the capacities of the RANS equations in the estimation of hydrodynamics, sediment transport and bed change, based on the research gap detected for these types of scenarios. This research work corresponds to the first publication associated with this doctoral thesis.

As will be seen in the next section, Quezada et al. (2018) demonstrated that the use of a relaxation coefficient in the critical shear stress for the incipient motion of non-cohesive sediments manages to adequately represent the equilibrium scour associated with steady currents, as well as in unsteady flow and oscillatory flow scenarios.

Considering the results obtained by Quezada et al. (2018) and the knowledge gap in the pile scour studies in environments where waves and currents interact together, both co-directional and in the opposite direction, is that a numerical investigation was developed that had the main objective of describing the hydrodynamics and pile scour in mixed environments, with the results presented in Quezada et al. (2019).

3.4 Article: Numerical simulation of scour around circular piles due to unsteady currents and oscillatory flows

This paper was published by the Journal Engineering Applications of Computational Fluid Mechanics on March 13th, 2018.

The manuscript can be downloaded from https://doi.org/10.1080/19942060.2018.1438924 and can be cited as Quezada et al. (2018). A plain version is included in this section.

3.4.1 Abstract

Numerical modeling of pile scour is performed due to the action of unsteady currents and oscillatory flow greens, using 3D Reynolds averaged Navier–Stokes (RANS) equations for the hydrodynamic description and the Exner equation for the morphological evolution of the bed, all of them incorporated into the computational fluid dynamics tool called REEF3D. As a first task, the numerical model was calibrated by comparing its results of scour against two sets of data, the first one obtained from numerical simulations and the second one from experimental tests. From these results it was possible to define the closure model of turbulence and a relaxation coefficient on the bed load equation necessary to increase the mobility of the sediments in the vicinity of the pile. Once the model was calibrated, a set of numerical simulations of pile scour under unsteady flow and oscillatory flow was performed using different hydrographs and wave conditions. There is a strong agreement between the simulated data and the experimental data reported by other authors for unsteady flow. In the case of scour associated with oscillatory flow, the numerical results showed the same statistical behavior as the experimental data previously published by others. When the numerical results are analyzed according to the Keulegan-Carpenter number, they represent the scour phenomenon in the same order of magnitude of the experiments. A conclusion of the study is the necessity to improve the sediment transport description, in order to avoid the use of a dedicated relaxation coefficient that reduces the threshold condition of the incipient transport.

3.4.2 Introduction

The scour process around a cylindrical pile founded on a riverbed composed of non-cohesive granular material, corresponds to a mechanism in which the hydrodynamics behaviour of the fluid and sediment transport are highly influenced by the presence of the obstacle, changing the bottom bed shear stresses near the pile and causing the scour of the bed.

In pile scour studies, two different terms are commonly used: clear-water condition and live bed condition. The first of them refers to the condition in which the flow velocity near the bed is less than the incipient threshold and the sediment transport are just developed in the vecinity of the pile. On the other hand, the live-bed regime is the condition in which the flow velocity (shear stress) near the bed is greater than the incipient threshold.

It is a fact that a grain of sediment needs a higher bed shear stress to suspend than to move as a bed load (Van Rijn, 1984b), thus, in a pile scour study, a clear water condition is

not able to produce suspended load, due to the fact that in this kind of regimen the bed shear stress is less than the critical value associated to the sediment.

The pile obstructs the flow and modifies the hydrodynamic behavior in comparison with the free stream case, forming the so called horseshoe vortex and vortex shedding in the neighborhood of the pile, which have been historically described by Baker (1979) for the laminar case, and Baker (1980) and Sumer and Fredsøe (2002) for the turbulent one. In oscillatory flows something analogous happens, which is described by Sumer et al. (1992) and Sumer et al. (1997).

The vortex system that develops around cylindrical piles, is the hydrodynamic mechanism that produces the scour near a pile. This has been observed previously by many authors, for example Breusers et al. (1977) describes in his state-of-art research that since 1932 the scour has been associated to the horseshoe vortex according to Keutner (1932), which is concordant with the work carried out by Tison (1940), Posey (1949), Laursen and Toch (1956), Roper et al. (1967) and Melville (1975), among others.

The horseshoe vortex and its relationship with the scour hole are still under research, both experimentally (Unger and Hager, 2007; Dey and Raikar, 2007; Das et al., 2013) and numerically (Link et al., 2008a; Roulund et al., 2005; Baykal et al., 2015).

The numerical modelling of cylindrical pile scour due to steady and oscillatory flows has been previously studied by several authors, focusing their efforts both in the correct description of the horseshoe vortex and vortex shedding, and in the quantification of the bed level change around the structure, because experimentally it has been demonstrated that these two vortices are responsible for pile scour. Sumer and Fredsøe (2002), based on the compilation of previous works on numerical modelling of fluid-pile interactions, indicate that one of the most important aspects in the representation of the scouring is the hydrodynamic description of the horseshoe vortex and vortex shedding, which generally come from the solution of RANS equations with a turbulence model for closure or another more complex approximation, like Direct Numerical Simulations (DES), Large-eddy Simulations (LES) or Detached-Eddy Simulation (DES).

For steady flows, Olsen and Melaaen (1993) developed a three-dimensional numerical model to solve the hydrodynamic and the bed level change around the cylindrical pile, incorporating as turbulence closure the $K - \epsilon$ model, while the sediment transport was determined by an advection-diffusion approximation of the sediment continuity equation. Olsen and Melaaen (1993)'s numerical results were compared with data obtained in laboratory experiments, showing agreement between both of them (Sumer and Fredsøe, 2002).

Complementary to the Olsen and Melaaen (1993) work, Roulund et al. (2005) proposed a three-dimensional numerical model to solve RANS equations for a pile scour with a turbulence closure model given by the $K - \omega$ equations, and compared their hydrodynamic and scour results against experimental data obtained in the laboratory. The results show that the numerical simulation developed captures all the main features of the scour process, including the equilibrium scour depth, that agree well with the experiments for the upstream scour hole, but some discrepancy was observed at the downstream (30% of differences between the modeled scour and the measurements, according to Roulund et al. (2005) estimations).

The Lagrangian approach to estimate the scour around cylindrical piles due to steady flow is applied by Liu and García (2008) and Escauriaza and Sotiropoulos (2011b). The former, orientates this technique on the definition of a grid which adapts to the variations of the river-bed, whilst the latter focused in the determination of movement particle by particle.

The Lagrangian techniques have also been applied to the simulation of non-Newtonian flows, in order to estimate its rheology. One of the recent applications of this technique was the one presented by Xie and Jin (2016).

In the case of oscillatory flows, Kobayashi (1992) developed a three-dimensional numerical model to explain the flow around cylindrical piles. However, the model solely reviewed the generation of vortex sheddings, but no horseshoe vortex, without further explaining on how to determine the bed level change. Later, the excluded aspects by Kobayashi (1992) were incorporated by Yuhi et al. (2000).

In what is related to sediment transport and its modelling, Sumer (2007) in his review describes some of the key aspects indicated by Roulund et al. (2005) who acknowledges the existence of three fundamental aspects to incorporate to the numerical models of pile scour: sediment transport as a bed load, sand slide and the conservation of sediment. With respect to bed load, Roulund et al. (2005) in Sumer (2007) comments that it is usual to employ bidimensional conventional equations, which are also used for sediment avalanches. The conservation of sediment is usually approached by the vectorization of Exner's equation (x and y directions), which shows bed variations over time. In the mean time, for the turbulence closure, the use of the $K-\omega$ model is recommended based on the results presented by Menter (1994). However Olsen and Kjellesvig (1998) obtained good agreement with empirical equations by employing the $K-\epsilon$ closure model into the RANS equations to estimate the maximum scour depth.

An additional sediment transport mechanism that can be present in the pile scour is the backfilling. This corresponds to the sedimentation in the downstrem region of the pile. However, the description is still underdeveloped. Very few studies regarding this phenomenon have been written, e.g. Sumer et al. (2013) (experimental) and Baykal et al. (2017) (numerical). In both cases the live bed regimen is considered.

Recently, a numerical study of flow around circular piers using the $K-\epsilon$ closure model in the RANS equations was carried out by Baranya et al. (2012). In this study, three pier arrangements were simulated: flow around a single pier, and flows around two piers placed in two different layouts. The hydrodynamical results were validated using measurements obtained from an Acoustic Doppler Velocimeter (ADV). Baranya et al. (2012) highlight results which indicate that for a single pier simulation the vertical velocity profiles have a good agreement with the ADV data. However, a slight underestimation of the velocities is expected in the downstream region.

Nowadays, several open access numerical tools for computational fluid dynamics (CFD) are available, such is the case of OpenFoam®, SPHysics, Fluidity or REEF3D, among others.

CFD models have been applied by many author to different cases. For example, OpenFoam has been applied to simulate pile scour (Liu and García, 2008), flow structure interaction (Doolan, 2010; Haque et al., 2016) or particle tracking applied to study the particle-laden flows (Greifzu et al., 2016), among other applications.

SPHysics is a model based on Smoothed Particle Hydrodynamics (SPH) developed jointly by researchers at the Johns Hopkins University, the University of Vigo , the University of Manchester and the University of Rome La Sapienza. This model has been applied to simulate water waves (Dalrymple and Rogers, 2006; Altomare et al., 2015), sedimentation, resuspension and scour (Saghatchi et al., 2014; Fourtakas and Rogers, 2016), among other applications.

Fluidity is a CFD model developed by The Imperial College, which has been applied to simulate multiphase flows (Jacobs et al., 2015), tsunami propagation (Oishi et al., 2013) and geodynamics Davies et al. (2011), among others.

The REEF3D numerical model resulted from the doctoral research work by Bihs (2011). In its first version it was capable of determining the hydrodynamic, sediment transport and bed changes, under steady flow. Bihs (2011) applied the model to simulate the scour around cylindrical piles under steady flow. Later versions of the numerical model include the capability

to simulate oscillatory flow (Saud, 2013).

An application of the REEF3D model to simulate the pile scour under oscillatory flow was performed by Ahmad et al. (2015) who considered monopile and pile group in his simulation. Another application to sediment transport was the study developed by Afzal et al. (2015) who applied the model to simulate the pile scour under current and waves.

There are several numerical models, both commercial and in-house developed, which have been applied to simulate various phenomena, such hydrodynamics (Brevis et al., 2014; Ulloa et al., 2015), water quality (Chau and Jiang, 2001, 2004; Wu and Chau, 2006), non-Newtonian flow (Trewhela et al., 2014; Özkan et al., 2016; Xie and Jin, 2016; Greifzu et al., 2016). However, it is not the aim of this article to describe each application of the numerical models and we just are focused in the applications to the pile scour simulation.

A review of the last 20 years of literature of pile scour shows that the clear water condition (such that the scour reaches it is maximum value according to Melville (2008)) has been used for the numerical estimations of the scour around piles. That is to say, the flow condition corresponds to the threshold for sediment transport.

The time scales involved in the scouring process to reach equilibrium due to steady flow, may vary from days to weeks (Melville and Chiew, 1999; Oliveto and Hager, 2002); whilst for the oscillatory flows the time for equilibrium should be about 1000 times the wave period (Kobayashi and Oda, 1994). In both cases (steady flow and oscillatory flow) the requirement for reaching the scour equilibrium is that the flow remains constant during the whole period (time scale). However, as is well known, the river discharge or waves in a beach, associated with a flood or extreme climate, have a limited duration and due to this, some authors have begun to develop experimental work to measure the temporal distribution influence in the scour around piles.

In order to analyze the time dependence of the bed change around of a pile due to unsteady flows, most of the research has approached the study experimentally testing the effect of hydrographs on the local scour (Melville and Chiew, 1999; Kothyari et al., 1992; Oliveto and Hager, 2002; Mia and Nago, 2004; Chang et al., 2004; Gjunsburgs et al., 2010; Link et al., 2017). In the case of oscillatory flows, studies on the determination of scour are scarce and the inclusion of the temporal scale is reduced to a couple of experimental works (Kobayashi and Oda, 1994; Sumer and Fredsøe, 2002).

The main objective of this paper is to model numerically the scour around cylindrical piles due to unsteady current and oscillatory flow, by applying Eulerian techniques when defining sediment transport and regular grids for the numerical solution of the hydrodynamics around the structure.

In order to achieve that objective, a series of specific activities were followed, oriented to obtaining numerical results. At first task, REEF3D was compared against numerical and experimental results obtained by other authors, in order to verify the numerical tool capability to represent the scour around circular piles under steady flow. The second task was developed to verify the numerical tool capability to represent the scour around circular piles under unsteady flow, against experimental results obtained by other authors. The last one was to compare the numerical results from the scour due to oscillatory flow against experimental data in the available literature.

With the present article, the authors intend to provide a numerical background related to studies of scour around circular piles, for temporary scales smaller than those necessary to reach the equilibrium scour.

3.4.3 Materials and methods

REEF3D numerical model

REEF3D v15.12 (Bihs, 2011; Saud, 2013) was employed in order to run the numerical simulation. It is a CFD model and has been developed with the capability to study hydraulic, coastal and estuarine phenomena, for both compressible and incompressible fluids.

The model solves the RANS three-dimensional equations (Reynolds, 1895) by applying the finite differences method on a squared-element grid, with turbulence closure models: $K-\epsilon$ (Launder and Sharma, 1974) and $K-\omega$ (Wilcox et al., 1998).

The RANS three-dimentional equations solved by REEF3D are then showed. The equation 3.4.1 corresponds to the continuity for an incompressible flow and equation 3.4.2 to the momentum conservation:

$$\frac{\partial u_j}{\partial x_j} = 0 \tag{3.4.1}$$

$$\frac{\partial u_i}{\partial t} + u_j \frac{\partial u_i}{\partial x_j} = -\frac{1}{\rho}\frac{\partial p}{\partial x_i} + \frac{\partial}{\partial x_j}\left((\nu + \nu_t)\frac{\partial u_i}{\partial x_j}\right) + g_i \tag{3.4.2}$$

where $i, j = 1, 2, 3$, u_i is the mean velocity vectorial component, x_i is the spatial vectorial component, t is the time, ρ is the water density, p is the pressure, ν is the kinematic viscosity, ν_t is the kinematic eddy viscosity and g is the gravity.

The closure models for ν_t used ($K-\epsilon$ and $K-\omega$) are described in the next equations. The $K-\epsilon$ cloure model defines the turbulent viscosity (ν_t) according to the equation 3.4.3 in wich c_μ is a constant value equal to 0.09 (Launder and Spalding, 1974), k is the turbulent kinetic energy, and ϵ is the turbulent dissipation.

$$\nu_t = c_\mu \frac{k^2}{\epsilon} \tag{3.4.3}$$

Both the turbulent kinetic energy and the turbulent dissipation are determined with a transport equation according to the equations 3.4.4 and 3.4.5. Where σ_k, σ_ϵ, $c_{\epsilon 1}$ and $c_{\epsilon 2}$ are constant values equal to: 1, 1.3, 1.44 and 1.92, respectively, according to Launder and Spalding (1974). P_k is the turbulent production rate given by equation 3.4.6.

$$\frac{\partial k}{\partial t} + u_j \frac{\partial k}{\partial x_j} = \frac{\partial}{\partial x_j}\left[\left(\nu + \frac{\nu_t}{\sigma_k}\right)\frac{\partial k}{\partial x_j}\right] + P_k - \epsilon \tag{3.4.4}$$

$$\frac{\partial \epsilon}{\partial t} + u_j \frac{\partial \epsilon}{\partial x_j} = \frac{\partial}{\partial x_j}\left[\left(\nu + \frac{\nu_t}{\sigma_\epsilon}\right)\frac{\partial \epsilon}{\partial x_j}\right] + c_{\epsilon 1}\frac{\epsilon}{k}P_k - c_{\epsilon 2}\frac{\epsilon^2}{k} \tag{3.4.5}$$

$$P_k = \nu_t \frac{\partial u_i}{\partial x_j}\left[\frac{\partial u_i}{\partial x_j} + \frac{\partial u_j}{\partial x_i}\right] \tag{3.4.6}$$

In the case of the $K-\omega$ closure model, the turbulent viscosity (ν_t) is defined according to the equation 3.4.3, and both the turbulent kinetic energy (k) and the specific turbulent dissipation (ω) are determined with a transport equation, according to expressions 3.4.8 and 3.4.9, where $\beta_k = 9/100$, $\alpha = 5/9$, $\beta = 3/40$, $\sigma_\omega = 1/2$ and P_k is the turbulent production rate given by equation 3.4.6.

$$\nu_t = \frac{k}{\omega} \tag{3.4.7}$$

$$\frac{\partial k}{\partial t} + u_j \frac{\partial k}{\partial x_j} = \frac{\partial}{\partial x_j}\left[\left(\nu + \frac{\nu_t}{\sigma_k}\right)\frac{\partial k}{\partial x_j}\right] + P_k - \beta_k k\omega \tag{3.4.8}$$

$$\frac{\partial \omega}{\partial t} + u_j \frac{\partial \omega}{\partial x_j} = \frac{\partial}{\partial x_j}\left[\left(\nu + \frac{\nu_t}{\sigma_\omega}\right)\frac{\partial \omega}{\partial x_j}\right] + \frac{\omega}{k}\alpha P_k - \beta\omega^2 \tag{3.4.9}$$

Due to the model use of the cartesian grid, a special treatment is used to solve the flow around complex structures and geometries. This is called the ghost cell method (Tseng and Ferziger, 2003; Berthelsen, 2004). This corresponds to a method for imposing the boundary conditions necessary for the numerical simulation of obstacles submerged in the fluid. This approach uses fictional cells, that is incorporated in the domain (specifically on the obstacles) and corresponds to a particular case of the known immerse boundary method (Leveque and Li, 1994).

Since this method extrapolates the solution into the immersed obstacle, the boundary condition are implicity incorporated into the numerical discretization and due to that, does not need to be accounted for explicitly in the grid cell definition.

The temporal discretization of the governing equations was solved by applying the Runge-Kutta method (second order). For the convective terms, the WENO (Weighted Essentially Non-Oscillatory) scheme was implemented (Jiang and Shu, 1996). The velocities and pressure are worked under a staggered grid, and applies the SIMPLE (Patankar and Spalding, 1972) or PISO method (Issa, 1986) when incorporating the pressure gradients in the problem governing equations. For this application the SIMPLE method was used as pressure algorithm.

Additional information regarding the boundary condition and initialization, used as a general definition for REEF3D configuration are showed in Table 3.1.

Table 3.1: Complementary information for the REEF3D general configuration for the hydrodynamics simulation.

Configuration	Definition
Boundary Condition	Non-slip for velocities
	Non-slip for k, ω and ϵ
	Logarithmic profile for inlet flow
	Fix pressure at inlet
	Zero-gradient outflow
Initialization	Potential flow for velocities
	Hydrostatic for pressure

REEF3D has the capability to calculate sediment transport as bed load, suspended load and sandslide. For the bed load it is possible to employ Meyer-Peter and Müller (1948), Engelund and Fredsøe (1976) or Van Rijn (1984a) equations. The suspended solids are estimated from the advection-diffusion equation of the sediment concentration. The sandslide correspond to a mechanism of sediment transport regarding to the slope instability of the bed and is determinated according to Burkow (2010).

In this study only the bed load is considered, due to the grain size of the sediment, and was determined using the Meyer-Peter and Müller (1948) equation:

$$q_b^* = 8(\tau^* - \tau_c^*)^{3/2} \tag{3.4.10}$$

where q_b^* is the dimensionless bed load, τ^* is the dimensionless shear stress on the bed, τ_c^* is the dimensionless critical shear stress and the dimensionless magnitudes are:

$$\tau^* = \frac{\tau}{(\rho_s - \rho)\, gd} \tag{3.4.11}$$

$$\tau_c^* = \frac{\tau_c}{(\rho_s - \rho)\, gd} \tag{3.4.12}$$

$$q_b^* = \frac{q_b}{\sqrt{\frac{(\rho_s - \rho)\, g}{\rho} d^3}} \tag{3.4.13}$$

where τ and τ_c are the shear stress and the critical shear stress, q_b is the bed load, ρ_s is the sediment density, ρ is the fluid density, d is the sediment diameter and g is gravity acceleration.

The critical shear stress is computed from Shields (1936) diagram for flat bed parameterized by Yalin (1972), incorporating the slope corrections proposed by Dey (2001). Moreover, as an additional sediment transport mechanism, the sandslide effect was considered according to the Burkow (2010) (in Saud (2013)).

The reduction of the incipient shear stress due to the bed slope proposed by Dey (2001), is based on taking the Shields critical shear stress for flat horizontal bed (τ_c') and using a coefficient (r), according to the following expressions:

$$\tau_c = r\tau_c' \tag{3.4.14}$$

$$r = 0.954 \left(1 - \frac{\theta}{\phi}\right)^{0.745} \left(1 - \frac{\alpha}{\phi}\right)^{0.372} \tag{3.4.15}$$

where θ and α are the longitudinal and transversal angles of slope, respectively, and ϕ is the angle of repose. It is important to note that this incipient shear stress reduction must be applied when the bed has a slope, otherwise $r = 1$.

Additionally, a relaxation coefficient (K_r) is incorporated over the bed, which allows to regulate the particles behaviour due to the hydrodynamics action. In that sense, it increases the sediment mobility in particular zones within the numerical domain, as it was presented and developed by Bihs (2011).

The relaxation coefficient is implemented numerically in REEF3D, affecting the dimensionless critical shear stress (τ_c^*) according to the following expression:

$$\tau_c^* = \begin{cases} K_r \tau_c^* & \text{if } x_j \in A_r \\ \\ \tau_c^* & \text{if } x_j \notin A_r \end{cases} \tag{3.4.16}$$

where A_r corresponds to the area in which the relaxation coefficient $K_r < 1$ wants to be applied.

To define the area in which the relaxation coefficient must to be applied, a preliminary estimation of the equilibrium scour hole was made according to Link et al. (2008b) and Diab et al. (2010).

To determine the bed level change due to the hydrodynamics and the sediment transport, the conservation of sediment equation is applied. It was initially proposed by Exner (1925) and later generalized by Paola and Voller (2005) in accordance to the following equation:

$$(1 - n)\frac{\partial z_b}{\partial t} + \left(\frac{\partial q_{b,x}}{\partial x} + \frac{\partial q_{b,y}}{\partial y}\right) = 0 \tag{3.4.17}$$

where n is the porosity of the bed, z_b is the bed elevation, $q_{b,x}$ and $q_{b,y}$ are the sediment transport as bed load in the x and y directions, respectively, which are determined according to:

$$q_{b,x} = q_b \frac{\tau_{bx}}{|\tau_b|} \tag{3.4.18}$$

$$q_{b,y} = q_b \frac{\tau_{by}}{|\tau_b|} \tag{3.4.19}$$

$$|\tau_b|^2 = \tau_{bx}^2 + \tau_{by}^2 \tag{3.4.20}$$

$$\tau_{bx} = \frac{1}{2}\rho\sqrt{c_\mu}\left(\sqrt{u_b^2 + v_b^2 + w_b^2}\right) u_b \tag{3.4.21}$$

$$\tau_{by} = \frac{1}{2}\rho\sqrt{c_\mu}\left(\sqrt{u_b^2 + v_b^2 + w_b^2}\right) v_b \tag{3.4.22}$$

where τ_{bx} and τ_{by} are the x and y components of the total shear stress (τ_b), $\sqrt{c_\mu}$ is a constant coefficient related to friction (equal to 0.3 according to Saud, 2013) and u_b, v_b and w_b are the flow velocities components in x, y and z directions near the bed (frictional velocities).

Once the bed morphology has been updated according to the bed load action (solution of Exner equation), the sandslide is verified. This is an iterative processes in which the local slope is compared with the repose angle of sediment (ϕ) according to:

$$\begin{aligned} z_{b(i,j)} - z_{b(i+1,j)} &> tan(\phi)\Delta x \\ z_{b(i,j)} - z_{b(i,j+1)} &> tan(\phi)\Delta y \end{aligned} \tag{3.4.23}$$

If the condition 3.4.23 is true then the model make the sediment surface distribution in both directions, longitudinal and lateral, according to Burkow (2010) methodology. While 3.4.23 still is fulfilled, the sediment surface distribution continued to deform until the local slope (longitudinal and lateral) becomes equal to the repose angle.

The bed level and the free surface locations are treated as fluid-sediment or fluid-atmosphere interfaces, through one of the following methods: Level Set Method (Osher and Sethian, 1988) or Particle Level Set Method (Enright et al., 2002), the first of them being the one used in this application.

The level set method is a moving boundary solution both for the free surface and for the bed and due to that, it incorporates or eliminates cells for the flow calculation, according to whether the surface becomes wavy or the bed begins to scour.

To solve the oscillatory flows, REEF3D incorporates the following wave theories: Cnoidal Wave for 1^{st} and 5^{th} order, Solitary Wave for 1^{st} and 3^{th} order, Stokes Waves for 2^{nd} and 5^{th} order and Linear Theory. Any of these wave theories can be used to define the boundary condition at the inlet of the numerical domain.

Methodology

In this research a total of 17 numerical test of pile scour were made. Two of them (CAL01 and CAL02) were calibration test, and five tests (H01 to H05) were simulated under unsteady currents and the last ten cases (C01 to C10) were defined to represent the pile scour under oscillatory flow.

The general numerical setting of REEF3D model has been summarized in Table 3.2. In this table the domain length (L), width (W), depth (h), grid element size (Δx, Δy, Δz), cells

number (N° Cells), simulated time (t_{test}) and computational time ($t_{computation}$), have been included.

It is important to mention that the cell numbers indicated in Table 3.2 are defined as the total cells included in the whole numerical domain. That includes sediment bed, the water column and the air above the water. This way, at each time interval, the computed number of cells can be less than the total cell number. This will vary according to the free surface and bed movements along time.

The simulated time (t_{test}) corresponds to the total time to resolve in the model, meanwhile the computational time ($t_{computation}$) is the real time employed to solve any case in the used computer (Intel (r) Core (TM) i7-5930k CPU 3.5 GHz, 64.0 GB, 6 cores).

Table 3.2: Summary of the numerical configuration of REEF3D model, applied to each simulated cases.

Case	L (m)	W (m)	h (m)	Δx,Δy,Δz (m)	N° Cells	t_{test} (min)	$t_{computation}$(days)
CAL01	0.8	0.6	0.2	0.005	$7.68{\cdot}10^5$	2	1.1
CAL02	4.0	2.0	0.8	0.025	$4.10{\cdot}10^5$	1,260	62.3
H01	4.0	1.5	1.0	0.010	$6.60{\cdot}10^6$	90	5.6
H02	4.0	1.5	1.0	0.010	$6.60{\cdot}10^6$	47	3.6
H03	4.0	1.5	1.0	0.010	$6.60{\cdot}10^6$	27	2.1
H04	4.0	1.5	1.0	0.010	$6.60{\cdot}10^6$	21	2.1
H05	4.0	1.5	1.0	0.010	$6.60{\cdot}10^6$	360	15.2
C01	15.0	2.0	1.0	0.010	$3.00{\cdot}10^7$	50	3.4
C02	15.0	2.0	1.0	0.010	$3.00{\cdot}10^7$	67	4.4
C03	15.0	2.0	1.0	0.010	$3.00{\cdot}10^7$	50	3.7
C04	15.0	2.0	1.0	0.010	$3.00{\cdot}10^7$	67	4.6
C05	15.0	2.0	1.0	0.010	$3.00{\cdot}10^7$	50	3.7
C06	15.0	2.0	1.0	0.010	$3.00{\cdot}10^7$	67	4.6
C07	15.0	2.0	1.0	0.010	$3.00{\cdot}10^7$	50	3.8
C08	15.0	2.0	1.0	0.010	$3.00{\cdot}10^7$	67	4.7
C09	15.0	2.0	2.0	0.010	$6.00{\cdot}10^7$	84	6.7
C10	15.0	2.0	2.0	0.010	$6.00{\cdot}10^7$	167	12.4

Model configuration - calibration test for steady flow To define a base configuration for the REEF3D model oriented to pile scour simulation, two kind of calibration tests were performed. The first one was oriented to compare with another numerical simulation (Baykal et al., 2015), meanwhile the second one was oriented to compare with experimental data (Link, 2006). In both cases steady flow was used to simulate the discharge.

Numerical behavior The data obtained from the numerical simulation of pile scour corresponds to Baykal et al. (2015) research. The reported results corresponds to a numerical study about scour around cylindrical piles founded on a bed of uniform sediment, under the action of a steady flow. The tubulence closure used for was the $K-\omega$ SST model.

Baykal et al. (2015) study provides the temporal evolution information about the maximum scour produced for a uniform flow, made dimensionless by the pile diameter, S/D, for a period of 120 seconds of simulation, both for the upstream and downstream zones. These time series were compared with the REEF3D generated data.

The numerical simulations in REEF3D were performed considering a rectangular channel 0.8, 0.6 and 0.2 (m) long, wide and deep, respectively; being those dimensions in agreement with the Baykal et al. (2015) recommendations.

The spacial discretization was determined using Hirt and Cook (1972) criterion, which relates the cell size ($\Delta x = \Delta y = \Delta z$) with the pile Reynolds number. The timestep (Δt) was automatically determined by the Courant criterion in the REEF3D model.

Hirt and Cook (1972) present a technique to solve the Navier-Stokes equations by finite differences, considering the temporal variation of the system and the three-dimensional components of the velocity field. Specifically, the authors apply the method called Marked and Cell method (MAC) in a confined space.

In order to define the optimal cell size to solve the RANS equations, they recommend defining the Reynolds number associated to the pile (R_{ePile}) and the number of points must be greater than the square root of R_{ePile} ($N_p > \sqrt{R_{ePile}}$).

The water depth in the test channel was 0.08 (m), placed over a 0.12 (m) uniform sediment layer ($d_{50} = 0.17$ (mm)). The pile diameter was 0.04 (m), while the discharge remained constant and equal to 0.02 (m^3/s) during the whole modelling period as an inlet boundary condition.

To solve the advective terms from the governing equations, the WENO method was employed, while for the pressure incorporation a projection algorithm was used according to the Chorin (1968) methodology. To determine the free surface, the level set method was used, with a temporal discretization by the Runge-Kutta's 3^{rd} order approximation, whilst a Runge-Kutta's 2^{nd} order for the momentum equations was used. This model configuration was used for all the pile scour simulations contained in this research.

The turbulence closure model for the RANS equations was selected between the $K-\epsilon$ and $K-\omega$, in order to define which of them have the best agreement with the Baykal et al. (2015) data.

The main objective of this calibrating test by comparing numerical data, was to verify that the REEF3D model responds similarly to other numerical tools available, as well as to determine the relaxation coefficient (K_r) magnitude of the sediment transport and the turbulence closure model to employ.

Comparison with experimental data Tha data obtained by Link (2006) correspond to experimental results for a clear water condition scour under steady flow, running in a flume with 37 (m) long, 2 (m) wide and 1 (m) deep.

In the middle of the flume a pile of 0.2 (m) of diameter was placed over a bed composed of a uniform sediment ($d_{50} = 0.97$ (mm)). The water depth tested was 0.3 (m) and a discharge of 0.18 (m^3/s) acting for 21 hours, in order to reach the equilibrium scour.

To represent numerically the experimental data obtained previously by Link (2006), REEF3D model was set at considering a numerical flume with 4 (m) length, 2 (m) wide and 0.8 (m) depth. The cell size was 0.025 (m) with a time step automatically defined by the model, according to Courant criterion.

The turbulence closure model for the RANS equations was selected according to the one that showed the best agreement in the previous calibration test, that is, section 2.2.1.1.

The main objective of this test is to calibrate the numerical model, to verify that the results obtained from REEF3D present a good agreement with the experimental data.

A summary of the calibration test is shown in Table 3.3 in which the scour regimen is also indicated. The live bed condition was obtained for the numerical comparison and the clear water condition was obtained for the experimental comparison.

Table 3.3: Summary of the calibration test for REEF3D.

Case	Calibration Test	Duration (min)	$\tau*$	d_{50} (mm)	ρ_s (Kg/m^3)	ϕ (°)	$\tau*_c$	$\frac{\tau*}{\tau*_c}$	Regimen
CAL01	Numerical	2.00	0.13	0.18	2650	30	0.06	2.85	Live Bed
CAL02	Experimental	1,260	0.02	0.97	2650	30	0.03	0.66	Clear water

Pile scour simulation for unsteady current and oscillatory flow The scour was studied with two kinds of flow conditions. The first of them corresponded to unsteady current defined through hydrographs, while the second corresponded to oscillatory flow generated by regular gravitational waves.

To study the scour around cylindrical piles due the action of unsteady current, five hydrographs previously tested in laboratory by Link et al. (2017) were considered. They provide information about the temporal evolution of the maximum scour for the different length trials. The test performed by Link et al. (2017) took place in the hydraulic laboratory of Universidad de Concepción (Chile), in a rectangular channel of 26, 1.5 and 0.74 (m) of long, wide and deep, respectively. The employed pile had 0.15 (m) of diameter made out of plexiglass. An Electronic Distance Measurement (EDM) laser allowed to measure the scour around the pile with a precision of ± 0.4 mm. The bed was composed of a $d_{50} = 0.36$ (mm) diameter sand with a geometrical standard deviation of 1.45 and a density of 2650 (kg/m^3).

According to Link et al. (2017) for the sediment used in his experiments, the incipient motion occurs at a velocity of 0.32 (m/s). The experiment was conducted under clear water condition, with a maximum discharge of 91% of that associated to the incipient motion condition. In Link et al. (2017), seven different hydrographs were tested. However, in the present research, just five of them were considered. They were named tests A, B, C, D and E, and are illustrated in Figure 3.4.

The test A corresponds to a staggered hydrograph of 90 minutes of duration, in which the maximum discharge is reached 40 minutes after the test started and remains constant for another 20 minutes to decrease for another 20 minutes. The test B also corresponds to a staggered hydrograph, but with just one growing phase, reaching the maximum discharge 19 minutes after the test started, remaining constant for another 20 minutes. The total duration of the experiment was about 49 minutes, approximately. The test C corresponds to a triangular hydrograph lasting around 28 minutes, with a maximum discharge reached 12 minutes after the test started. The hydrograph corresponding to the test D has a smooth triangular distribution, where the maximum discharge is reached 3 minutes after the experiment started, lasting 21 minutes. Finally, the test E corresponds to a pulsating flow, composed by three peaks within the temporal development, all three of them of the same magnitude, with a period of 110 minutes.

The numerical tests made in REEF3D were performed considering a rectangular channel of 4.0 (m) long, 1.5 (m) wide and 1.0 (m) deep. A sediment layer of 0.5 (m) was placed over the bottom of the channel, with a water height of 0.17 (m) over this sediment layer. The pile diameter was 0.15 (m).

The spacial discretization of the domain realized was based on the criterion proposed by Hirt and Cook (1972), associated to the Reynolds number of the pile, which resulted in $\Delta x = \Delta y = \Delta z = 0.01(m)$, while the timestep was automatically determined in agreement with Courant number limits.

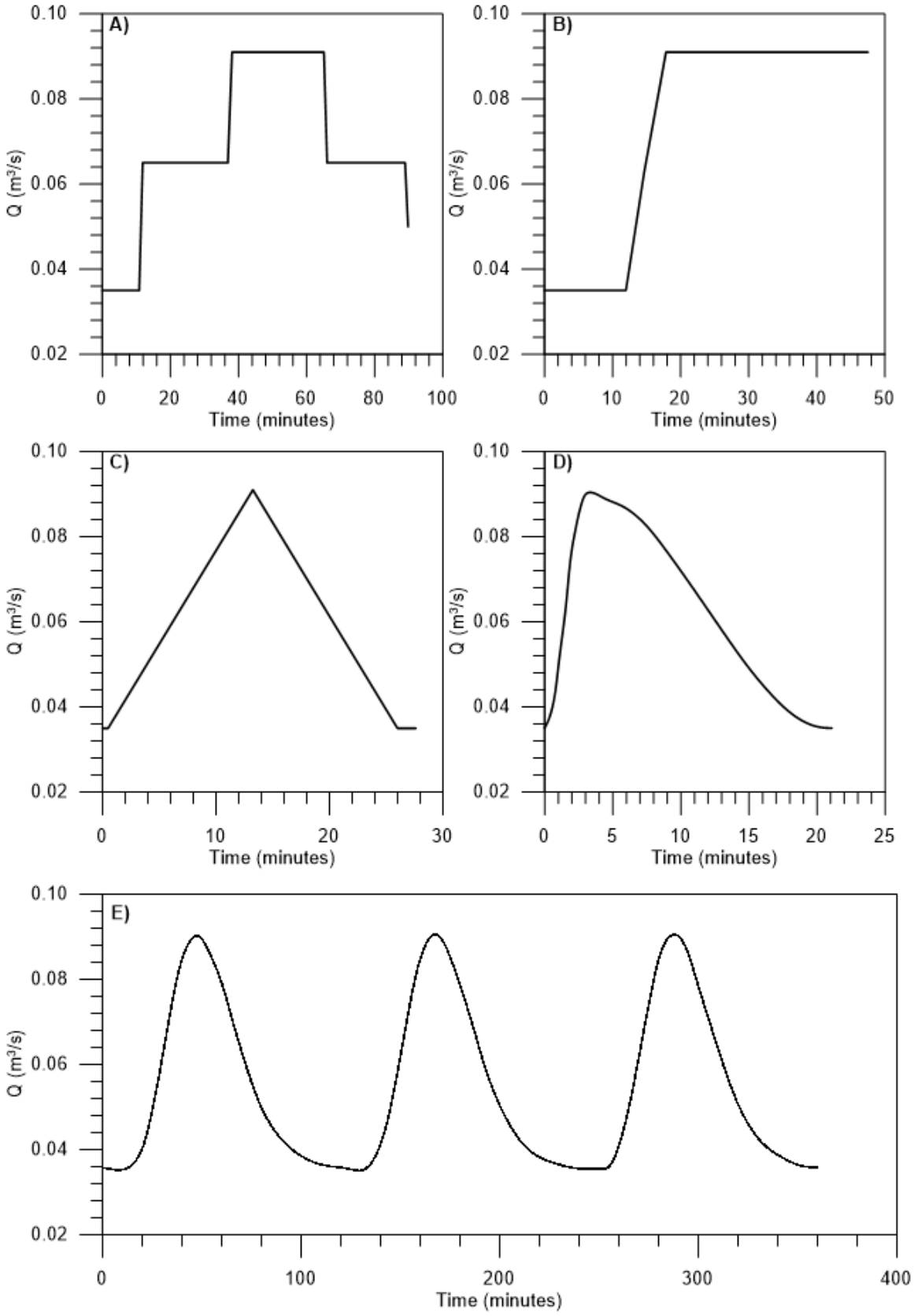

Figure 3.4: Hydrographs used for the pile scouring simulation under the action of unsteady flow.

A summary of the flow, test duration and sediment transport characteristics is shown in Table 3.4.

Table 3.4: Summary of the unsteady current simulated cases in REEF3D to estimate pile scour.

Case	Flow	Duration (min)	$\tau*$	d_{50} (mm)	ρ_s (Kg/m^3)	ϕ (°)	$\tau*_c$	$\frac{\tau*}{\tau*_c}$	Regimen
H01	Hydroghaph A	90.00	0.03	0.36	2,650	30	0.04	0.82	Clear water
H02	Hydroghaph B	47.00	0.03	0.36	2,650	30	0.04	0.82	Clear water
H03	Hydroghaph C	27.00	0.03	0.36	2,650	30	0.04	0.82	Clear water
H04	Hydroghaph D	21.00	0.03	0.36	2,650	30	0.04	0.82	Clear water
H05	Hydroghaph E	360.00	0.03	0.36	2,650	30	0.04	0.82	Clear water

The evaluation of the scour around piles due to oscillatory flow was performed by the simulation of 10 cases with Keulegan-Carpenter number (KC) ranging from 6.98 to 91.63. A summary of the parameters used are presented in Table 3.5.

The Keulegan-Carpenter number is used to describe the hydrodynamic behavior of bodies in oscillatory flows and it is defined as (Sumer and Fredsøe, 2002):

$$KC = \frac{U_m T_w}{D} \tag{3.4.24}$$

where U_m is the maximum oscillatory velocity, T_w the wave period and D the pile diameter. The KC number is a comparison of the distance traveled by a fluid particle and the pile diameter. U_m could be determinated according to equation 3.4.25.

$$U_m = \frac{H\pi}{T_w sin(k_L h)} \tag{3.4.25}$$

In order to know which scour regimen will be simulated, an estimation of Shields number has been made employing equation 3.4.26 and an approximation to the wave boundary layer velocity (U_{fm}) using the equation 3.4.27.

The friction factor (f_w) including in equation 3.4.27 was determined according to Fredsøe and Deigaard (1992, p. 25).

$$\theta_w = \frac{U_{fm}^2}{(\rho_s - \rho)\, gd} \tag{3.4.26}$$

$$U_{fm} = \sqrt{\frac{f_w}{2}} U_m \tag{3.4.27}$$

To estimate the critical Shields number under oscillatory flow, the Komar and Miller (1975) criterion was applied according to the equation 3.4.28. Additionally, whether the pile scour simulation was under clear water or live bed conditions is defined.

$$\theta_{cr,w} = 0.21 \left(\frac{U_{cr} T_w}{\pi d} \right)^{0.5} \tag{3.4.28}$$

In order to avoid wave breaking along the flume, two different water depth in the channel was used. For the cases 1 to 8, water depth was set at 1 (m) and for the cases 9 and 10, 2 (m) was considered. In all the cases the flume length was 15 (m) with a width of 2 (m).

A summary of waves condition and sediment transport characteristics is shown in Table 3.5 and it is noted that all cases are simulated in clear water conditions.

Table 3.5: Oscillatory flow cases simulated with REEF3D to estimate pile scour.

Case	T_w (s)	H (m)	KC	θ_w	$d_{50}(mm)$	$\rho_s(Kg/m^3)$	ϕ (°)	$\theta_{cr,w}$	$\frac{\theta_w}{\theta_{cr,w}}$	Regimen
C01	3.0	0.15	6.98	0.06	0.36	2,650	30	0.24	0.50	Clear water
C02	4.0	0.15	9.57	0.06	0.36	2,650	30	0.33	0.36	Clear water
C03	3.0	0.20	9.31	0.10	0.36	2,650	30	0.29	0.42	Clear water
C04	4.0	0.20	12.76	0.10	0.36	2,650	30	0.34	0.35	Clear water
C05	3.0	0.30	13.96	0.20	0.36	2,650	30	0.30	0.40	Clear water
C06	4.0	0.30	19.13	0.20	0.36	2,650	30	0.35	0.34	Clear water
C07	3.0	0.35	16.29	0.26	0.36	2,650	30	0.30	0.40	Clear water
C08	4.0	0.35	22.32	0.26	0.36	2,650	30	0.35	0.34	Clear water
C09	5.0	0.89	43.93	0.54	0.36	2,650	30	0.58	0.21	Clear water
C10	10.0	0.89	91.63	0.52	0.36	2,650	30	0.60	0.20	Clear water

The sediment used in all the cases was uniform with a diameter (d_{50}) equal to 0.36 (mm) and density 2650 (kg/m^3). The pile used had the same dimensions than the ones used in the case of unsteady flow.

As in the previous cases, the grid size was determined according to Hirt and Cook (1972) criterion, resulting in $\Delta x = \Delta y = \Delta z = 0.01(m)$ and the timestep was automatically determined by the REEF3D model in accordance with the Courant number limits.

To describe the water waves mechanics (e.g the flow velocities, orbital velocity, phase velocity, pressure distribution, among other properties), many mathematical solutions for the wave problem exist in the literature. One of the most common is the Airy waves, developed by Airy (1841)who simplified the wave problem by conserving just the linear term into the governing equation (Laplace problem) and due to this, it is commonly called the linear wave theory. After the Airy's wave, many other authors have included additional terms and different boundary conditions into the governing equation of the wave problem, to obtain more complex and nonlinear solutions. Each wave theory has limitations for his application and to know if one specific wave theory can be applied to a specific problem, many parameters must be previously defined. Le Mehaute (1976) proposes a graphical solution to know where a wave theory can be applied as a function of wave mean height (H), wave period (T_w), aceleration of gravity (g) and water depth (h).

To represent the oscillatory flow in the test channel, it was necessary to adopt two different theories: Cnoidal (Cases 1 to 4) and Solitary Wave (Cases 5 to 10). Is important to say that in the case of the solitary wave the period are regarding to the apparent wave period defined has a proportion of the wavelength and the wave celerity.

The wave theories applied to each case were determined in accordance with Le Mehaute (1976, ch. 15, p. 205) criterion, who elaborated a graphical representation, in agreement with the valid range of each of them. Figure 3.5 presents an adaptation to Le Mehaute (1976) graph, incorporating the simulated cases, which were previously described in Table 3.5.

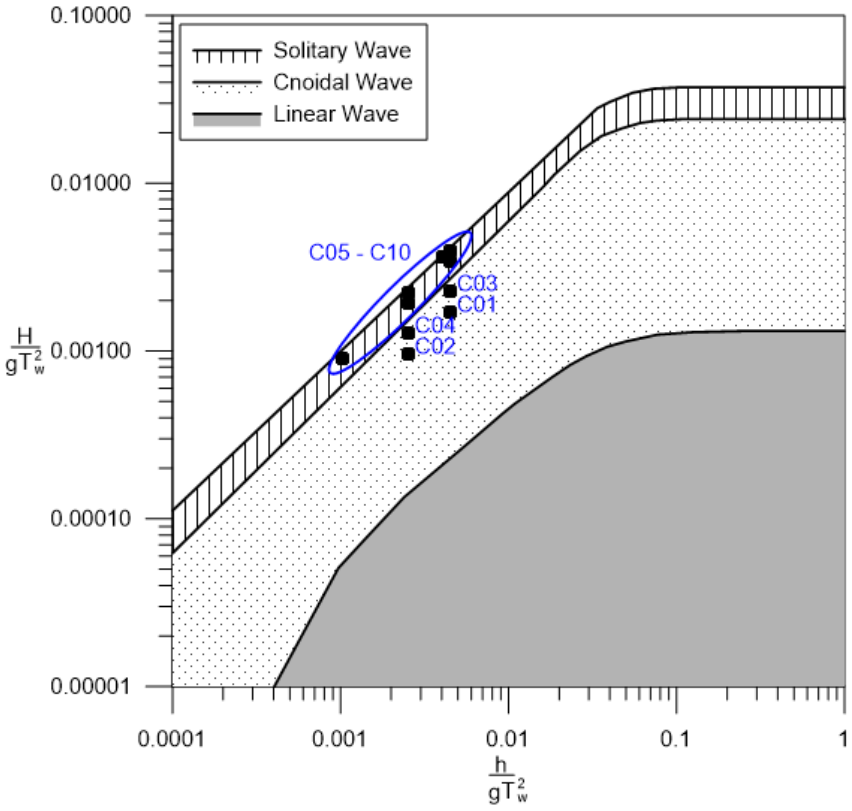

Figure 3.5: Identification of the dominion of the wave theories applied to each of the oscillatory flow simulated cases, according to Le Mehaute (1976) criterion

REEF3D models are able to simulate wave propagation via the implementation of a numerical wave tank. To capture the surface movements, the Level Set Method (Osher and Sethian, 1988) is applied. At the inlet, the waves are generated according to Mayer et al. (1998), and are adapted to CFD models according to Jacobsen et al. (2012).

The cnoidal waves are imposed at the inlet according to the Korteweg and De Vries (1895) theory, while the solitary waves are imposed according to Munk (1949) theory.

The time duration for each numerical simulation was adopted based on the recommendation of Kobayashi and Oda (1994).

The maximum scour obtained from the numerical simulation was made dimensionless with the pile diameter (S/D) and were expressed as a function of Keulegan-Carpenter number with the purpose of enabling the comparison of these magnitudes with the laboratory test performed by Sumer et al. (1992) and Sumer and Fredsøe (2001).

3.4.4 Results

Model configuration - calibration test

Numerical behavior The results obtained from the calibration process of the REEF3D numerical model to represent the scour around a cylindrical pile in a steady flow, are presented in Figure 3.6. Therein, a comparison between the time series of the maximum dimensionless scour at the upstream region (Figure 3.6A) and at the downstream region (Figure 3.6B),

obtained for each turbulence closure model employed, are shown.

The scour shown in Figures 3.6A-B have been obtained using a relaxation coefficient K_r, with magnitudes equal to 1.0 and 0.8. This relaxation of the incipient sediment transport was only applied in a sub-area contained in the vicinity of the pile and whose width was equal to the channel width, while in the axial axis the distance was twice the pile diameter (2D), in both directions, upstream and downstream.

The REEF3D maximum scour obtained with the $K-\epsilon$ turbulent closure model is higher than the one determined by $K-\omega$.

Likewise, the maximum scour obtained with the value of the relaxation coefficient, K_r, equal to 0.8 is higher than the one determined when this coefficient is equal to 1, that is to say, when the incipient shear stress is applied just with the slope corrections proposed by Dey (2001).

The REEF3D simulation with $K_r = 0.8$ is more or less equal to those reported by Baykal et al. (2015) for the upstream and downstream region (Figure 3.6). The REEF3D dimensionless scour S/D was 0.98 for the upstream region and 0.73 for the downstream region, while those values were 0.91 and 0.73 for Baykal et al. (2015). In general, the results obtained with REEF3D and $K-\epsilon$ model show similarities with the temporal behavior of S/D when they compare with the reported values by Baykal et al. (2015), being adequately represented both upstream and downstream zones of the pile. So the relaxation coefficient $K_r = 0.8$, and the $K-\epsilon$ turbulent closure made the REEF3D a similar numerical model as the one of Baykal et al. (2015). In the next section the calibrated REEF3D is compared with experimental data.

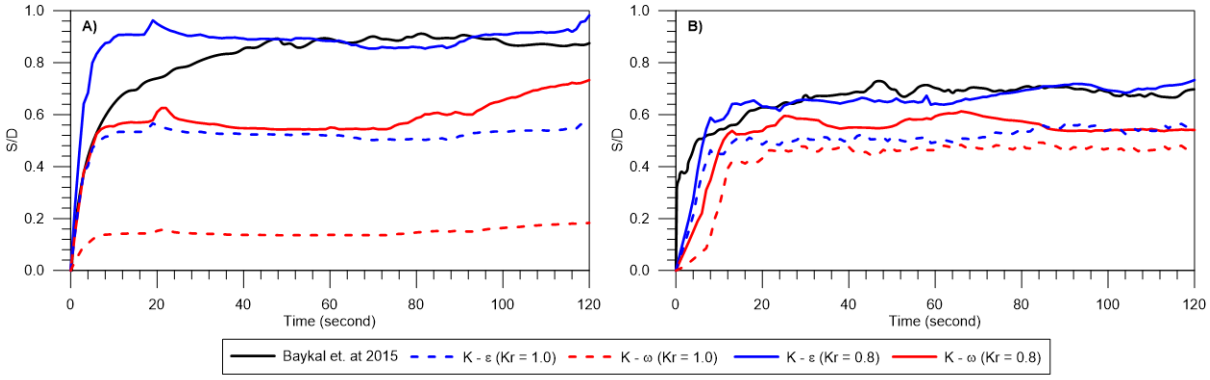

Figure 3.6: S/D time series comparison. a) Upstream pile zone and b) Donwstream pile zone.

Comparison with experimental data The time series of pile scour evolution obtained from the REEF3D simulations of the experiment by Link (2006), are shown in Figure 3.7. Three different times are illustrated, a) initial bed response (5 minutes after the beginning of the simulation) due to a constant discharge, b) bed response after 2.1 hours, or 10% of the total time of the simulation and c) bed response after 21 hour, or the final time of the simulation.

The results obtained from the comparison of the turbulent closures models and their ability to better represent the scour around a pile, turn out to be expected according to what was previously reported by Kato (1993), Baranya et al. (2012) and Hamidi and Siadatmousavi (2018), given that according to these authors, this turbulent closure is capable of producing greater turbulence in the upper region of the flow separation. This added to the bed shear

stress that we are using (based on the turbulence, according to equations 3.4.21 and 3.4.22) produces the results obtained and illustrated in Figure 3.6.

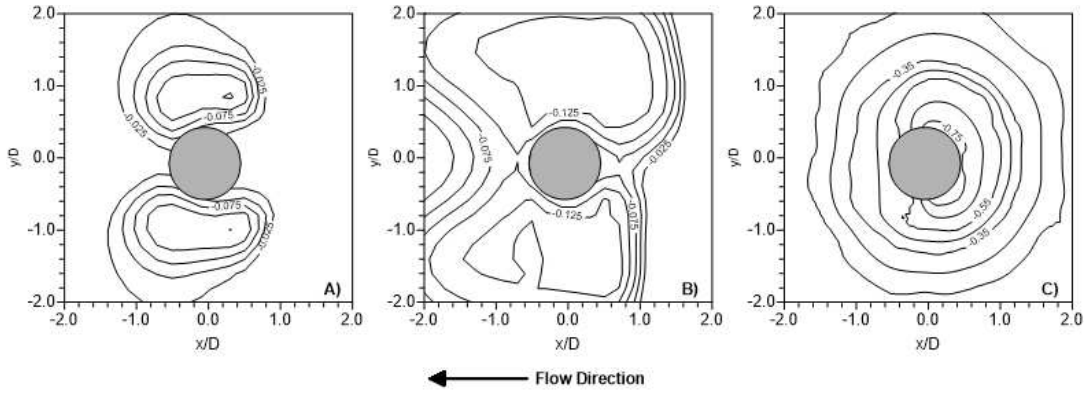

Figure 3.7: Time series of scour around a pile obtained from REEF3D Simulation. a) 5 minutes after initiated the test, b) 2.1 hour after initiated the test and c) 21 hour after initiated the test.

In the downstream, the results obtained are concordant with the expectations, given that the RANS coupled with the turbulent closure model $K - \epsilon$, has a slight tendency to underestimate speeds near the bottom (Baranya et al., 2012) and in this way the TKE decreases and therefore the shear stress and consequent the sediment transport decrease as well.

Figure 3.7A shows that the initial scour starts at the sides of the pile. This bed response is due to the streamline contraction induced by the presence of the pile in the flow, which amplifies the bed shear stress, reaching a maximum over the incipient shear stress. The scour increased in time, both in area and depth (Figure 3.7B). Bed response at this time is developed around the pile.

Finally, Figure 3.7C shows the contour lines to the pile scour after 21 hours of simulation, where the scour is fully developed and it is at equilibrium. The maximum scour depth is reached in front of the pile with a magnitud of 0.15 meters ($S/D = 0.75$).

In general terms the results shown at Figure 3.7 are concordant with the time evolution of scour described previously by Melville and Chiew (1999) and Link et al. (2008b). Figure 3.8 presents the laboratory experiment of Link (2006) at 21 hours and the REEF3D simulation for the same 21 hours. It is shown that in both cases the maximum scour have the same value (0.15 meters), however, this location differs slightly.

The scour hole geometry determined by REEF3D has a larger area than that measured by Link (2006) in laboratory and that is due to the relaxation coefficient area. However, both results (numerical and experimental) have similar magnitudes with differences between -0.01 ($S_{dif}/D = 0.05$) to +0.03 meters ($S_{dif}/D = 0.15$), according to Figure 3.9. The mean value of the differences found between numerical and experimental data, has a magnitude of +0.01 meters ($S_{dif}/D = 0.05$). That is, REEF3D showed a greater sensitivity to the bed response due to the forcing action of the uniform flow and, consequently, induced a greater scour.

According to the results obtained, the REEF3D simulations were able to adequately reproduce the pile scour evolution and its maximum value, with a good agreement with the scour hole geometry.

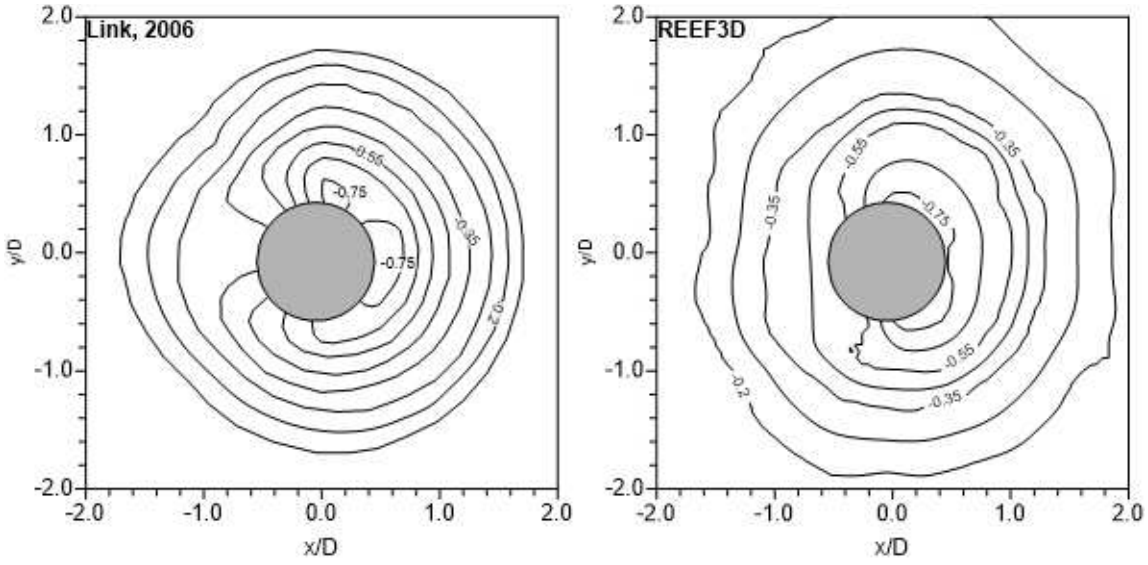

Figure 3.8: Scour contour lines comparison between experimental (Link, 2006) and numerical data, for 21 hour of simulation.

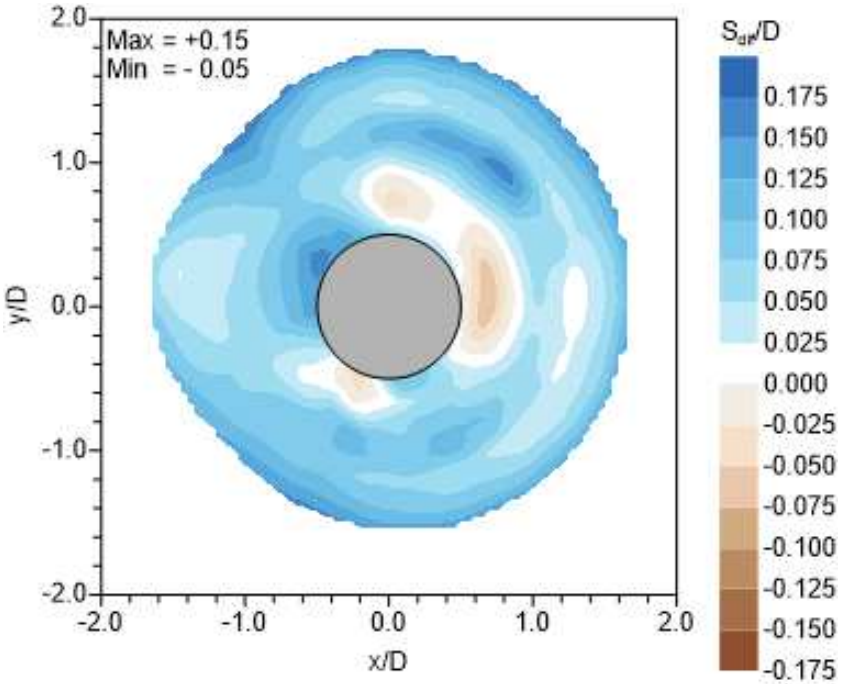

Figure 3.9: Differences in the pile scour estimation between Link (2006) measurements and the numerical data obtained with REEF3D.

Pile scour simulation for unsteady current and oscillatory flow

The results obtained for time series of maximum scour, in (cm), for unsteady current, are presented in Figure 3.10A-E, with A and B being associated with a stepped distribution of discharges, C and D with a triangular distribution of discharges and, finally, E associated with the pulsating flow. In general terms, the numerical results fit well the experimental data, being in agreement both in the value of the maximum scour and geometric distribution of scour.

The result in Figure 3.10A, shows that the maximum scour around the pile has a geometrical agreement with the hydrograph employed to forcing the model. The maximum scour (S_{MAX}) increases if the discharge increase or remains constant. When the discharge begins to decrease, the scour remains constant. These result are comparable with the ones by Oliveto and Hager (2002), Chang et al. (2004), Gjunsburgs et al. (2010), Borghei et al. (2012), and Link et al. (2017), among others.

As can be seen in Figure 3.4A, the hydrograph has two steps before reaching for its maximum and then, in the descent, also makes a step, symmetrical to the second step in the ascent, before stopping. In the ascent of the hydrograph the scour increase for two reasons; one reason is that the scour is increased as the discharge remains constant after reaching a step, because it does not reach its equilibrium scour yet. The other reason is that the scour is increased as the discharge is increasing from one step to the other. When the discharge begins to decrease (descent part of the hydrograph), the scour remains practically constant due to the fact the flow has not been capable to move the sediment into the scour hole.

In Figure 3.10B the scour does not reach an absolute maximum neither in the experiment nor in the simulation final time. This is due to the hydrograph shape, in which the maximum discharge is reached 19 minutes after the test started and then remained constant for another 20 minutes, approximately. The time scale involved is shorter than the required one for a permanent steady flow to reach the equilibrium scour.

The results in Figure 3.10C shows the importance of both the maximum discharge and the time period in which the hydrogram acts, because the bed scour response increases until the discharge reaches its maximum value and remains constant during the whole remaining time of the test. In Figure 3.10D the hydrogram test also showed a constant behavior of the maximum scour, which is reached after the maximum discharge of the time series occurs.

The obtained result for the pulsating flow distribution (Figure 3.10E), indicates two steps in the maximum scour time evolution: the growing phase and the one in which the scour remains constant. At first glance, it is possible to see that the maximum scour increases with the discharge increment until reaching a maximum value around 6 (cm), which is temporally concordant with the first peak of the hydrogram. During the discharge decrement phase, the maximum scour remains constant and increases only when the discharge returns to a crescent phase. According with the obtained results, both experimental and numerical, the maximum scour is expected to be a function of both the maximum discharge of the hydrograph and the time it acts over the bed.

One of the most relevant results found from the numerical model for each hydrograph simulated, is the relationship between the maximum scour and the discharge behavior. In general terms the maximum scour induced by a specific discharge will increment if this discharge remain constant or increase, meanwhile if the discharge decrease, the maximum scour remain constant.

At the end of the pile scour simutation for each hydrograph considered, the maximum scour was located according to Figure 3.11, with azimuthal location of 62° for the hygrograph D and 74° for the hydrograph B.

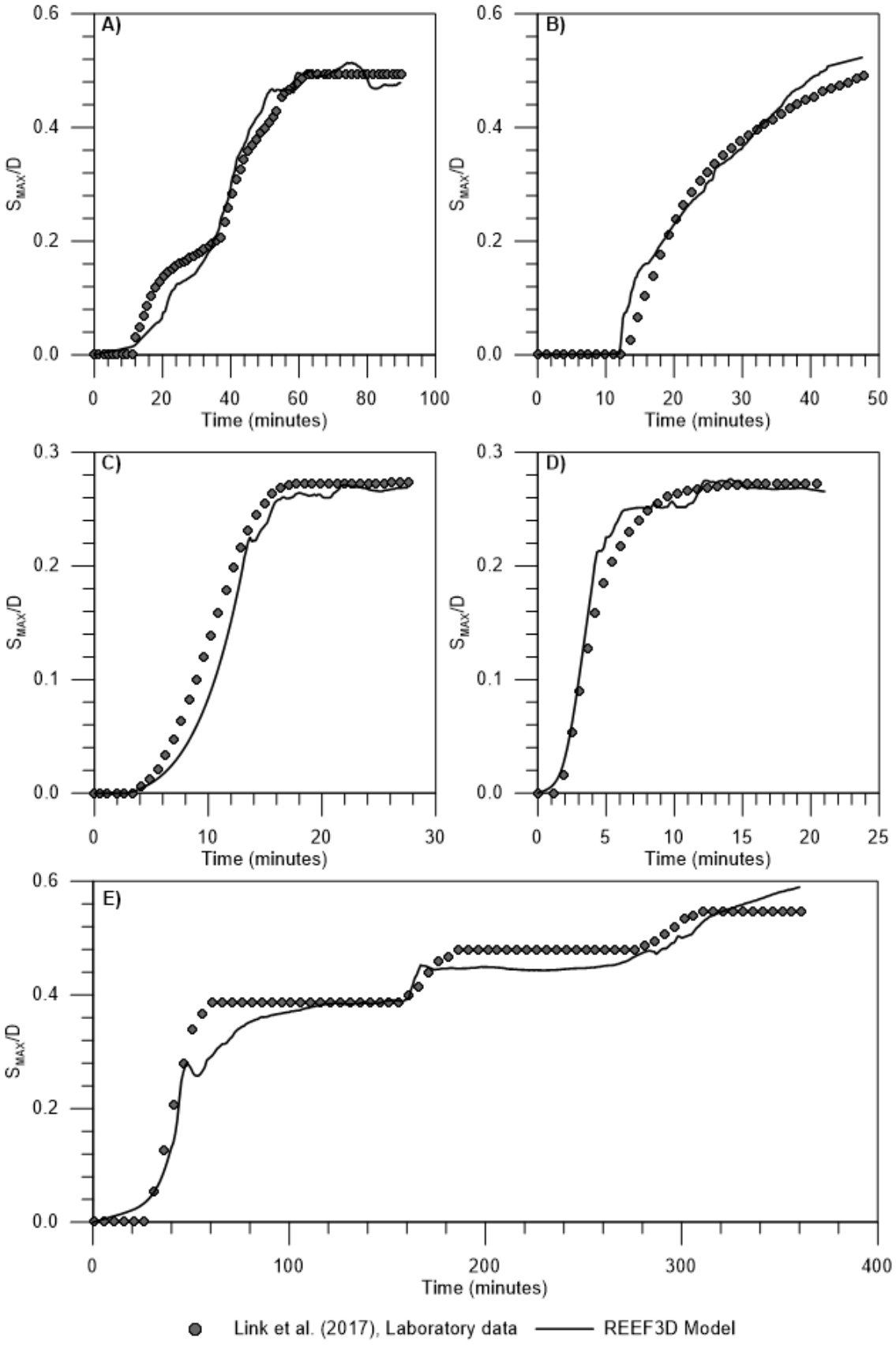

Figure 3.10: Comparison of the results obtained by REEF3D and those reported by Link et al. (2017), for the scour due unsteady flow. a) Scour for hydrograph A, b) Scour for hydrograph B, c) Scour for hydrograph C, d) Scour for hydrograph D and e) Scour for hydrograph E.

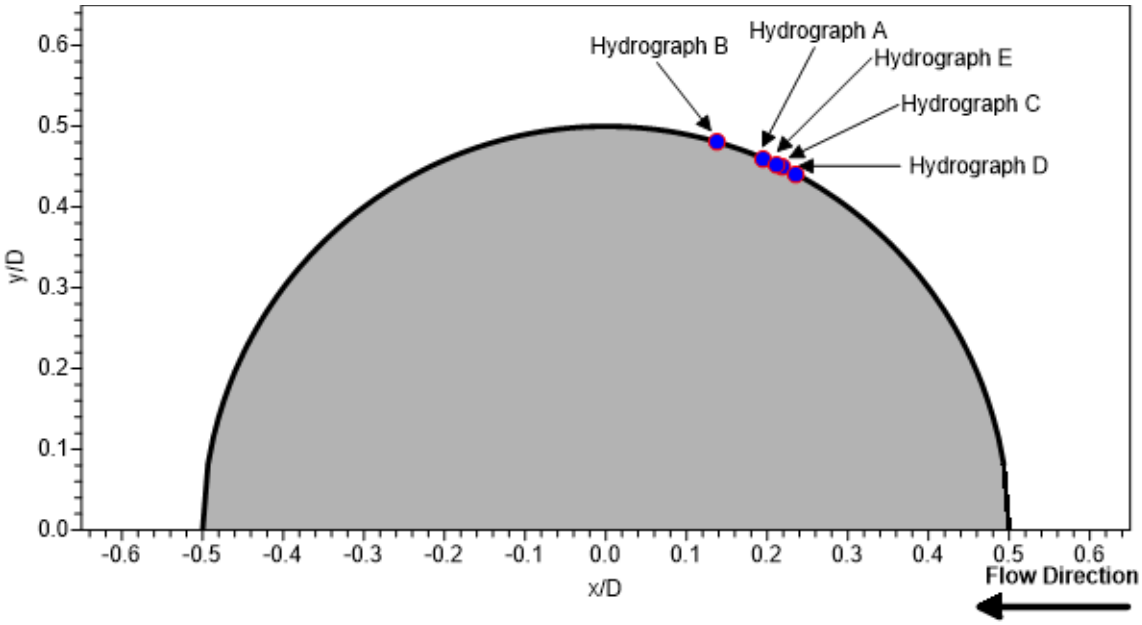

Figure 3.11: Maximum scour location due to unsteady flow at the end of the experiment for each hydrograph simulated in REEF3D.

The results of the numerical simulation for the oscillatory flow showed in Figure 3.12, are presented compiling the information of Sumer et al. (1992), Sumer and Fredsøe (2001) and the empirical relationship of Sumer et al. (1992). The dimensionless maximum scour (S/D) is presented as a function of the Keulegan - Carpenter number (KC), confirming, in every simulated case, a good fit both for the experimental data and the empirical equation.

The dimensionless scour determined by the REEF3D model increase as a function of KC, in agreement with what was expected and previously described by Sumer et al. (1992) and Sumer and Fredsøe (2001), given that higher KC magnitudes imply more powerful horseshoe vortices and higher vortex shedding intensities. When comparing the numerical results with the empirical equation to predict the scour proposed by Sumer et al. (1992), even though the fit is coincident for both, the simulated data tends to underestimate the predicted values.

The obtained data from the numerical simulation were fitted to an exponential function in order to follow Sumer et al. (1992) propossed behavior for KC ≥ 6:

$$\frac{S}{D} = 2.057\,(1 - exp\,[-0.012\,(KC - 6)]) \tag{3.4.29}$$

To construct the previous equation, the shape of the function proposed by Sumer et al. (1992) was kept with the intention of making (3.4.10) directly comparable with the proposed one but with a sole drawback. Sumer et al. (1992) equation indicates that for KC tending to infinity, the maximum dimensionless scour (S/D) finds a limit of 1.3, which is concordant with the steady flow behaviour. Nonetheless, the equation (3.4.10) with the numerical results shows the bound $S/D = 2.057$. This apparent increment in the maximum scour associated with the found fitting equation is due to the validity range, exclusively, since the numerical tests were only representing KC values lesser than 100, being this unable to reflect the behaviour associated with steady flow regime. If the fitting equation obtained by REEF3D is forced, so that the maximum dimensionless scour would converge to a steady flow solution, the following

expression will be:

$$\frac{S}{D} = 1.3\,(1 - exp\,[-0.023\,(KC - 6)]) \tag{3.4.30}$$

When performing the forcing of the maximum dimensionless scour value with the numerical data to be fixed at 1.3, it is practically obtained the same equation presented by Sumer et al. (1992).

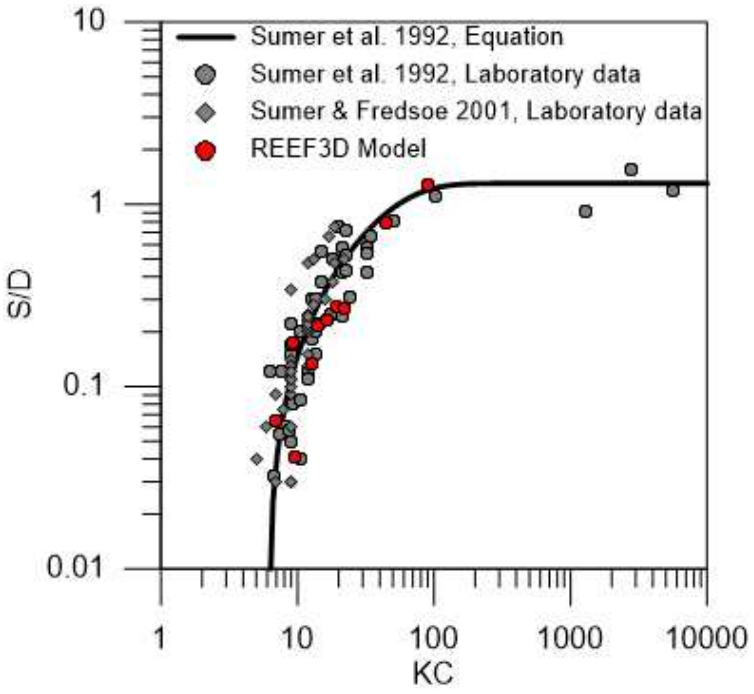

Figure 3.12: Comparison between the dimensionless scour obtained from REEF3D and the results reported by Sumer et al. (1992) and Sumer and Fredsøe (2001).

3.4.5 Discussion

The numerical simulation of the hydrodynamics, has been made on the basis of a mesh that allows to correctly simulate the behavior of the flow around the pile, being used in the vertical both for the case of uniform and impermanent flow, of the order of 15 cells (minimum 12 and maximum 17) it could be considered as a coarse grid to describe the flow. However, there are studies carried out by other authors who have used configurations similar to those used in this study.

Aghaee and Hakimzadeh (2010) carried out a numerical study of the three-dimensional flow field around piers, based on LES and RANS simulations, without considering the scour. In the case of the RANS simulation they use $K - \epsilon$ and 20 cells in the vertical axis. According to their conclusions, the flow predicted by the solution of the RANS equations with $K - \epsilon$ clousure model, is quite similar to the flow observed in their experiment and have a good comparison with LES numerical simulations results as well.

Later, Baranya et al. (2012) perform a numerical study using a three-dimensional numerical simulation using the RANS equations with the turbulent closure model $K - \epsilon$, to evaluate the

flow behavior around two configurations: a single-pile and two piles. For this purpose, a nested grid system proposed by the author is used. To define the vertical grid size, Baranya et al. (2012) perform a sensitivity analysis, which compares experimental results with numerical results considering a scheme with 12 cells and another with 20 cells. From this, it concludes that the use of 12 layers vertically yielded an optimal resolution, since there is no significant change in the flow pattern when employing a finner resolution of 20 layers.

Regarding the flow solved by Baranya et al. (2012), he concludes that the RANS equations with turbulent closure $K-\epsilon$ in the case of single pier, have an adequate adjustment with the laboratory observations in the area upstream of the pile. However, in the donwstream a slight underestimation of the velocities near the bed can be observed.

Similar conditions for numerical simulation (RANS + $K-\epsilon$) were applied by Mohamed (2012), but consider scour at two submerged-emerged tandem cylindrical piers. For the vertical flow definition, they use 14 cells, getting a good comparison of their numerical results with experimental data, when comparing the scour around the piles for different separation distances between piles and both in emerged and submerged conditions of the first pile in the tandem array.

Thanh et al. (2014) concentrates his study on the scour around rectangular pile, solved under a scheme of finite differences of the RANS with turbulent closure model $K-\epsilon$, using a definition in the vertical of 12 cells. He compares his results with experimental data of scour, finding a good relationship between measurements and numerical simulations, both in maximum magnitude and location.

Afzal et al. (2015) apply the numerical model REEF3D with turbulent closure model $K-\omega$, to study in a three-dimensional way the scour around a pile from the action of waves and currents. In the configuration, the authors used 12 vertical cells to describe the hydrodynamics due to currents and 11 cells in the case of the oscillatory flow induced by the waves. Their results when compared with experimental data show a good agreement in the case of currents.

Recently, Hamidi and Siadatmousavi (2018) performed the numerical simulation of the scour and hydrodynamics by applying the RANS with both the turbulent closure $K-\epsilon$, and the $K-\omega$, for different pile arrangements, and comparing their numerical results with experimental ones. From this work it is possible to emphasize that the authors configure the model to describe the vertical one by means of the use of 12 cells, which is comparable with the configuration that the present authors have adopted.

In this way, it can be noticed that our configuration of the numerical model is equivalent to that presented by Aghaee and Hakimzadeh (2010), Baranya et al. (2012), Mohamed (2012), Thanh et al. (2014), Afzal et al. (2015) and Hamidi and Siadatmousavi (2018), so it is expected that the flow around the pile was well simulated.

Bihs et al. (2016) using REEF3D, simulate the flow around a circular pile and also a rectangular abutment due to waves. At first, the general performance of the numerical model was tested, using different grid sizes. In the case of piles exposed to waves, a grid resolution study is carried out by the authors, using 10, 20, 40 and 80 cells in the vertical axis to describe the hydrodynamics. According to their results, a grid with 40 cells in the vertical axis is enough to describe the waves and the hydrodynamics induced by it.

Baykal et al. (2017), as a continuation of the Roulund et al. (2005) research, numerically studied the scour and the backfilling processes around a mono pile. The flow is defining uses a solution of RANS equations with $K-\omega$ as a turbulent closure model. The vertical axis uses 14 cells for the simulated cases with rigid bed and 16 cells for the live-bed simulated cases.

In the wave test simulated in this research, 100 cells were used in the vertical for cases C01 to C08, and 200 cells for cases C09 and C10. If these vertical resolution are compared with the

configuration adopted by Bihs et al. (2016) and Baykal et al. (2017), a better description of the hydrodynamics induced by waves aroud cilindrycal piles can be expected from our numerical simulation.

According to the calibration test, a relaxation coefficient K_r equal to 0.8 was necessary to reproduce adequately the scour. K_r acting as a weighting coefficient of the incipient shear stress, increases the mobility of the sediment in order to improve the comparison among the scour simulations and experimental measurements or field data. From a physical point of view, the relaxation coefficient employed in the numerical model does not directly represent an additional mechanism for sediment transport and/or inter-granular interactions that could favour sediment mobility. Conversely, it allows to regulate the sedimentation dynamics that develops around the pile, a situation that has not been properly described yet in the literature.

The dynamics of the sediment transport near an obstruction to the flow was approached by Hager and Oliveto (2002) and applied by Oliveto and Hager (2002), who assign the incipient motion as a function of the densimentric Froude number. According to Hager and Oliveto (2002) incipient criterion, critical shear stress under the effect of a pile is less than the Shields criterion and based on this, the relaxation coefficient indicated by Bihs (2011), and employed in this numerical simulation, acquires a physical meaning. That is to say, the relaxation coefficient try to reproduce the sediment transport behavior near the pile.

The use of a relaxation coefficient in the calculation of sediment transport under the effect of the pile, allowed to obtain results that were comparable with the experimental data, both for unsteady flow and oscillatory flow. However, at the same time, it constrains considerably the direct applicability of the numerical tool on situations that have not been studied in laboratory or in the field, because there are not a background that would allow calibrating or verifying the magnitude of such factor.

According to Thanh et al. (2014), Wang and Jia (1999) examined the importance of including additional flow effects on sediment transport estimation when the scour phenomenon are included. Wang and Jia (1999) propose empirical functions to alter shear stress in an empirical sediment transport model to account the effects produced by the mean flow, down flow, vortices and turbulence intensity.

Cheng et al. (2018) recognized that the coherent turbulent structures that develop near the bed have an effect on the incipient motion and must be incorporated into the RANS by means of modifications of this.

If the Wang and Jia (1999) and Cheng et al. (2018) studies are taken into account, the use of a relaxation coefficient in the calculation of sediment transport under the effect of the pile are trying to include indirectly all this additional mechanisms of sediment motion, due to physical processes are still not described correctly.

In the unsteady flow case, the obtained results were concordant with the technical discussions previously given by Oliveto and Hager (2002), Chang et al. (2004), Borghei et al. (2012), Gjunsburgs et al. (2010) and Link et al. (2017), among others, detecting two relevant aspects: the maximum discharge magnitude and the time in which this acts.

As a highlighted result in the unsteady current scour computation is that a maximum scour is reached instantly with the maximum discharge and the scour will only increase further if the discharge remains constant or increase, whereas it will stabilize if the discharge decreases. This situation evidences the importance of the timescale in the morphodynamic equilibrium process, since maintaining the maximum discharge constant could be similar to an steady flow, a case which will require prolonged action to reach the maximum scour.

The scour associated with an oscillatory flow has been determined applying the sediments transport equation developed by Meyer-Peter and Müller (1948), although this is for steady

flow. However, its applicability to simulate the sediment transport associated with oscillatory flow (waves) have been based on Ribberink (1998), who proposed a bed load transport equation with similar characteristics of Meyer-Peter and Müller (1948) formula, but increasing their constant parameters to represent the effect of the oscillatory flow.

In this research, Meyer-Peter and Müller (1948) equation was able to represent adequately the expected scour when this was compared with Sumer et al. (1992) results.

3.4.6 Conclusions

The relaxation coefficient of sediment critical shear stress proposed by Bihs (2011), becomes fundamental for the REEF3D numerical model and its selection must be done by the comparison with experimental data, with the purpose of adequately representing the bed response in the surroundings of flow obstructions The relaxation coefficient was 0.8, for steady, unsteady and oscillatory flow and it must be applied in a sub-area contained in the vicinity of the pile and whose width was equal to the channel width, while in the axial axis the distance was twice the diameter of the pile, in both directions, upstream and downstream.

The calibration process of the REEF3D model was made with the comparison of numerical results of other authors (Baykal et al., 2015) and laboratory data (Link, 2006), both under steady flow.

When the relaxation coefficient was applied to unsteady flow and oscillatory flow, the numerical modelled results adjusted correctly to the experimental data. In particular, concerning the obtained results for unsteady flow, the numerical model with the adopted configuration was capable of representing the morphodynamic behaviour of the scour relative to its maximum value, being concordant, both in the temporal development and the prolonged action effects of the maximum discharge of the hydrograph.

The temporal behavior of the pile scour obtained from the numerical simulation was well represented in general terms, being able to reproduce the expected behavior according to the described by several authors according to available literature (Oliveto and Hager, 2002; Chang et al., 2004; Gjunsburgs et al., 2010; Borghei et al., 2012; Link et al., 2017). The numerical scour can overestimate (test A, C and E) or underestimate (test B and D) the experimental data, however the differences are small.

In the oscillatory flow case, the obtained results fitted well the experimental data published by Sumer et al. (1992) and Sumer and Fredsøe (2001), representing the same phenomenon and allowing to adjust well the numerical data to the predictive equations available in the literature.

When the numerical results for the dimensionless pile scour due to oscillatory flow are compiled according to the Keulegan-Carpenter number, they are adjusted in the same form of Sumer et al. (1992). This is an indicator that the numerical model could forecast the pile scour in concordance with the experimental data.

The utilization of Meyer-Peter and Müller (1948) formula, allowed representation of both the sediment transport associated with the unsteady and oscillatory flow, despite that its semi-empirical foundation was based in cases of unidimensional steady flow.

According to the results obtained and the cited studies developed by others, the authors consider it necessary to continue with the study of incipient transport of sediments near piles or other flow obstructions, to define its value or incorporate the obstruction turbulence effects over the sediment motion estimation.

3.5 Article: Numerical study of the hydrodynamics of waves and currents and their effects in pier scouring

This paper was published by the Journal Water on Octuber 28th, 2019, for the special issue Experimental, Numerical and Field Approaches to Scour Research.

The manuscript can be downloaded from https://doi.org/10.3390/w11112256 and can be cited as Quezada et al. (2019). A plain version is included in this section.

3.5.1 Abstract

The scour around cylindrical piles due to codirectional and opposite waves and currents is studied with Reynolds Averaged Navier–Stokes (RANS) equations via REEF3D numeric modeling. First, a calibration process was made through a comparison with the experimental data available in the literature. Subsequently, not only the hydrodynamics, but also the expected scour for a set of scenarios, which were defined by the relative velocity of the current (U_{cw}), were studied numerically. The results obtained show that the hydrodynamics around the pile for codirectional or opposite waves and currents not have significant differences when analyzed in terms of their velocities, vorticities and mean shear stresses, since the currents proved to be more relevant compared to the net flow. The equilibrium scour, estimated by the extrapolation of the numerical data with the equation by Sheppard, enabled us to estimate values close to those described in the literature. From this extrapolation, it was verified that the dimensionless scour would be less when the waves and currents are from opposite directions. The U_{cw} parameter is an indicator used to adequately measure the interactions between the currents and waves under conditions of codirectional flow. Nevertheless, it is recommended to modify this parameter for currents and waves in opposite directions, and an equation is proposed for this case.

3.5.2 Introduction

The hydrodynamics of the coastal environment usually correspond to the result of the interaction of several force, such as waves, tides, and winds, that act at different spatial and temporal scales, thereby modulating circulation. Meanwhile, rivers run mainly due to the gravitational action that moves the waters resulting from snowmelt or rain, which flow into the alluvial channel that transports to the ocean by runoff. The convergence of coastal and fluvial environments is known as an estuary zone, and the resulting currents correspond to a complex interaction between tides, waves, winds, and river flow.

The hydrodynamics of environments where waves and currents interact have been previously studied by various authors both co-directionally (Umeyama, 2005, 2009, 2010) and perpendicularly (Faraci et al., 2011; Lim and Madsen, 2016; Faraci et al., 2018).

The research developed by Umeyama (2005, 2009, 2010), sought to analyze the behavior of Reynolds stress and velocity vertical distributions Umeyama (2005), the changes induced by the combined wave currents over the turbulent flow structures Umeyama (2009), and the surface elevation and particle velocities Umeyama (2010).

In the case of waves orthogonal to currents, the experimental research developed by Faraci et al. (2011), Lim and Madsen (2016) and Faraci et al. (2018) allows us to understand the effects of joint action on the behavior of the resulting velocity of the fluid. For example, Faraci et al. (2011) experimentally demonstrated the joint action of orthogonal waves and currents, which speeds up the evolution process of a sandpit. Lim and Madsen (2016) analyzed, via

an experimental study the effects of the roughness in an experimental study on the velocity distribution in a wave-current interaction. A complete statistical analysis of the near bed velocity behavior due to waves and a current acting perpendicularly was developed by Faraci et al. (2018). They concluded that the probability distribution of near-bed velocity follows a Gaussian distribution in a flow field generated by a current alone. In the presence of waves, the distribution changes and another peak over a Gaussian distribution appears.

However, all the studies in the previous paragraphs do not include any type of obstruction to the flow, which generates additional modifications to the hydrodynamic characteristics of the flow field. It is well known that when placing a circular pile in an environment that has a specific current (that can be produced by waves/tides, river flow, or both), a hydrodynamic modification will be produced around it and, therefore, vortexes will be produced (a horseshoe vortex and vortex shedding), which are the main elements responsible for the scour around the pile.

Through time, different authors have studied pile scour due to a uniform flow. Among these authors it is worth mentioning Hjorth (1975), Melville (1975), Ettema (1980), Chiew and Melville (1987), Melville and Chiew (1999), Oliveto and Hager (2002), Link et al. (2008b), Diab et al. (2010), Link et al. (2019), who focused their interests mainly on the scour around bridge piles. When it comes to scour by waves, the number of studies is limited. On this subject, the authors of this paper consider the contributions of Sumer et al. (1992), Sumer et al. (1997) and Sumer and Fredsøe (2001) to be fundamental to our understanding of multiple hydrodynamic processes responsible for the movement of sediments near the pile.

Experimental studies on the scour around piles under a flow associated with the combined action of waves and currents have been carried out by different authors (Eadie and Herbich, 1986; Kawata and Tsuchiya, 1988; Raaijmakers and Rudolph, 2008; Rudolph et al., 2008; Zanke et al., 2011; Ong et al., 2013; Sumer and Fredsøe, 2001; Qi and Gao, 2014b), who have contributed, through their laboratory tests, to our understanding of the scour phenomenon in this type of environments. The following is a brief bibliographic description.

Eadie and Herbich (1986) studied a physical model with the purpose of evaluating the effects that the combined action of two co-directional forces, waves (random) and currents, have over the scour around cylindric piles. The main results of Eadie and Herbich (1986) indicate that the scour process due to waves and currents together is faster and reaches higher equilibrium compared to currents acting alone. Similar results were determined by Kawata and Tsuchiya (1988), who characterized the scour process for clear-water and live-beds in a similar manner to Eadie and Herbich (1986).

Raaijmakers and Rudolph (2008) studied the temporal dependency of the scour around a pile due to the combined action of waves and currents with the purpose of analyzing the equilibrium scour, the temporal scales needed to reach such depths and the backfilling process. As part of their results, Raaijmakers and Rudolph (2008) propose an equation to determine the scour as a function of time and additionally concluded that the equilibrium scour is of a higher magnitude in cases of currents acting alone compared to the conditions reached for the combined action of waves and currents. The equilibrium scour equation as a function of time, presented by Raaijmakers and Rudolph (2008), was validated through the comparison of field data, as presented by Rudolph et al. (2008).

Zanke et al. (2011), through an analysis of data gathered by other authors, proposed a unified equation to determine the scour depth due to the actions of waves and currents, through the incorporation of a transition function (x_{rel}) defined by the effective scour (x_{eff}). Similarly, Ong et al. (2013) developed a stochastic method by which the maximum equilibrium scour could be determined in piles exposed to long-crested and short-crested nonlinear random

waves plus a current. They validated their approach by comparison with the experimental data provided by Sumer and Fredsøe (2001).

The contribution carried out by Sumer and Fredsøe (2001) to understand the process of scour is significant, since through its dimensional analysis , their model is able to represent the dimensionless scour (S) over the pile diameter (D) as a function of relative flow velocity (U_{cw}), as defined by Equation 3.5.1, where U_c corresponds to the undisturbed current velocity at the transverse distance $z = D/2$ and U_m is the maximum value of the undisturbed orbital velocity at sea bottom just above the wave's boundary layer:

$$U_{cw} = \frac{U_c}{U_c + U_m} \tag{3.5.1}$$

Evidently, the relative flow velocity will have values close to zero when the environment is dominated by waves, but it will approach one if currents are the main flow mechanism.

The main conclusions presented by Sumer and Fredsøe (2001) indicate that in a wave environment, the scour increases significantly in the presence of a current, even if the current is mild. This current, is mainly associated with a strong horseshoe vortex in front of the pile, even in the case of a mild vortex. In addition, the current apparently dominates the pile's scour when $U_{cw} \geq 0.7$; the scour approaches this value due to the current acting alone.

Even though the articles mentioned above have studied the scour around cylindrical piles due to the combined action of waves and currents, they considered forcing to act co-directionally. Qi and Gao (2014b), in their experimental work, studied the scour around cylindrical piles under the combined action of co-directional and opposite waves and currents, for different pile diameters, waves conditions and currents. The main conclusion they reached was that the scour in the combined flows of waves and currents is a nonlinear process, and the time required to reach scour equilibrium is much lower than that required for waves or currents acting independently. Additionally, Qi and Gao (2014b) mentioned that the maximum flow velocity in waves and co-directional currents is much higher than that in waves and currents from opposite directions, thereby affecting the maximum scour magnitude, which is lower in opposite flows.

While there is a number (albeit limited) of experimental articles related to the study of scour caused by combined waves and currents, investigations based on numerical models are even more scarce. It is only possible to find simulations of scour acting separately around piles due to currents or oscillatory flows. A literature review on this subject is available on Quezada et al. (2018).

The application of Reynolds-averaged Navier–Stokes equations (RANS) in simulated environments, in which waves and currents coexist, has been demonstrated by several authors (Teles et al., 2013; Markus et al., 2013; Zhang et al., 2014), who nonetheless fail to include the vertical pile in the flow. Ahmad et al. (2019) recently developed a numerical study based on the REEF3D model in order to study scour on a horizontal pile (pipeline) caused by combined waves and currents. This study is relevant to the research presented in this article, since the same numerical model used by Ahmad et al. (2019) was applied.

Based on the above, the main objective of this article is to study, through numerical models, scour's hydrodynamics around cylindrical piles where waves and currents coexist, both co-directional and opposite to the wave direction as well.

3.5.3 Materials and Methods

Numerical Model: REEF3D

The numerical modelling developed in this research was conducted using the numerical model known as REEF3D (Bihs, 2011; Afzal, 2013), which is a computational fluid dynamic (CFD) tool used to solve Reynolds-averaged Navier–Stokes equations (RANS). This tool is able to simulate hydraulic, coastal, and estuarine phenomena for both compressible and incompressible fluids.

The REEF3D model provides a three-dimensional solution for governing equations composed of Equation 3.5.2, which corresponds to the continuity of an incompressible flow, and Equation 3.5.3, which is the momentum conservation.

$$\frac{\partial u_j}{\partial x_j} = 0 \tag{3.5.2}$$

$$\frac{\partial u_i}{\partial t} + u_j \frac{\partial u_i}{\partial x_j} = -\frac{1}{\rho}\frac{\partial p}{\partial x_i} + \frac{\partial}{\partial x_j}\left((\nu + \nu_t)\frac{\partial u_i}{\partial x_j}\right) + g_i \tag{3.5.3}$$

where $i, j = 1, 2, 3$, u_i is the mean velocity vectorial component, x_i is the spatial vectorial component, t is the time, ρ is the water density, p is the pressure, ν is the kinematic viscosity, ν_t is the kinematic eddy viscosity and g is the gravity.

The turbulence closure model used was the well-known $K - \omega$ (Wilcox, 1994), in which ν_t is defined according to Equation 3.5.4, and both the turbulent kinetic energy (k) and the kinetic energy for the specific turbulent dissipation per unit of turbulence (ω) are determined with a transport equation, according to Equations 3.5.5 and 3.5.6, respectively. The constant values in $K - \omega$ were taken according to $\beta_k = 9/100$, $\alpha = 5/9$, $\beta = 3/40$, $\sigma_\omega = 1/2$, and $\sigma_k = 1$; and P_k is the turbulent production rate defined by Equation 3.5.7.

$$\nu_t = \frac{k}{\omega} \tag{3.5.4}$$

$$\frac{\partial k}{\partial t} + u_j \frac{\partial k}{\partial x_j} = \frac{\partial}{\partial x_j}\left[\left(\nu + \frac{\nu_t}{\sigma_k}\right)\frac{\partial k}{\partial x_j}\right] + P_k - \beta_k k\omega \tag{3.5.5}$$

$$\frac{\partial \omega}{\partial t} + u_j \frac{\partial \omega}{\partial x_j} = \frac{\partial}{\partial x_j}\left[\left(\nu + \frac{\nu_t}{\sigma_\omega}\right)\frac{\partial \omega}{\partial x_j}\right] + \frac{\omega}{k}\alpha P_k - \beta\omega^2 \tag{3.5.6}$$

$$P_k = \nu_t \frac{\partial u_i}{\partial x_j}\left[\frac{\partial u_i}{\partial x_j} + \frac{\partial u_j}{\partial x_i}\right] \tag{3.5.7}$$

To solve the flow around complex structures, the ghost-cell method (Berthelsen, 2004; Tseng and Ferziger, 2003) was applied to impose the boundary conditions when a pile is included in the numerical domain. This approach uses fictional cells that are incorporated in the domain (specifically on the obstacles) and corresponds to a particular case of the immersed boundary method (Leveque and Li, 1994).

The numerical treatment of the governing equations was based on the second order of the Runge–Kutta method for temporal discretization. Meanwhile, the convective terms were solved by the applied weight essentially non-oscillatory (WENO) scheme (Jiang and Shu, 1996). The velocities and pressures were determined under a staggered grid, using the Semi-Implicit Method for Pressure Linked Equations (SIMPLE) (Patankar and Spalding, 1983).

The model configuration to represent waves in the numerical domain was adopted similar to the method presented by Ahmad et al. (2019), using a Dirichlet boundary condition and the second-order Stokes waves theory (Dean and Dalrymple, 1991). We defined the surface elevation (η) and the incident velocity (u, w) according to Equations 3.5.8 and 3.5.9, respectively.

$$\eta\left(x,y,t\right)=\frac{H}{2}cos\vartheta+\frac{H^{2}Kcosh\left(Kh\right)}{16sinh^{3}\left(Kh\right)}\left(2+cosh\left(2Kh\right)\right)cos\vartheta \tag{3.5.8}$$

$$u\left(x,y,t\right)=\frac{\partial\Phi}{\partial x};w\left(x,y,t\right)=-\frac{\partial\Phi}{\partial z} \tag{3.5.9}$$

$$\Phi\left(x,y,t\right)=\frac{Hg}{2\varpi}\frac{cosh\left[K\left(h+z\right)\right]}{cosh\left(2Kh\right)}+\frac{3}{32}H^{2}\varpi\frac{cosh\left[2K\left(h+z\right)\right]}{sinh^{2}\left(2Kh\right)}sin\left(2\vartheta\right) \tag{3.5.10}$$

where H is wave height, K is the wave number, h is the water depth, ϑ is the wave phase, ϖ is the angular frequency, and Φ is the velocity potential.

In order to avoid the wave reflection, active wave absorption (AWA), was used in the outlet according to the method described by Schäffer and Klopman (2000). In this methodology, the waves that reach the outlet cancel out the reflected waves, prescribing the velocity as in Ahmad et al. (2019):

$$u_{0}=-\sqrt{\frac{g}{h}}\eta_{r} \tag{3.5.11}$$

$$\eta_{r}=\eta_{m}-h \tag{3.5.12}$$

where η_r is the reflected wave amplitude and η_m is the actual elevation of the free surface.

Complementary information on the numerical model hydrodynamic configuration is shown in Table 3.6.

Table 3.6: Complementary information for the REEF3D hydrodynamic simulation.

Configuration	Definition
Boundary Condition	Non-slip for velocities
	Non-slip for k, ω and ϵ
	Logarithmic profile for inlet flow
	Fix pressure at inlet
	Zero-gradient outflow
	Active wave absorption at outlet (waves)
Initialization	Potential flow for velocities
	Hydrostatic for pressure

In order to ascertain the sediment transport and changes in the bed, both the bed load and the suspended load were considered, for the morphodynamics evolution, the equation for the conservation of sediment initially proposed by Exner (1925) and later generalized by Paola and Voller (2005), was used.

The bed load sediment transport was computed by using the Meyer-Peter and Müller (1948) formula according to Equation 3.5.13, where q_b^* is the dimensionless bed load, τ^* is the dimensionless shear stress on the bed computed by Equation 3.5.14, τ_c^* is the dimensionless

critical shear stress defined according to the Equation 3.5.15, τ is the bed shear stress, τ_c is the critical bed shear stress, ρ_s the sediment density, and d is the sediment diameter. The real magnitude of the bed load (q_b) can be obtained from Equation 3.5.16.

$$q_b^* = 8(\tau^* - \tau_c^*)^{3/2} \tag{3.5.13}$$

$$\tau^* = \frac{\tau}{(\rho_s - \rho)\, gd} \tag{3.5.14}$$

$$\tau_c^* = \frac{\tau_c}{(\rho_s - \rho)\, gd} \tag{3.5.15}$$

$$q_b^* = \frac{q_b}{\sqrt{\frac{(\rho_s - \rho)\, g}{\rho} d^3}} \tag{3.5.16}$$

The suspended load was computed using the advection diffusion equation shown in Equation 3.5.17, where c is the suspended load concentration, and w_s is the fall velocity of the sediment. To solve Equation 3.5.17 two boundary conditions were applied. The first is the zero vertical flux on the surface and the second is the bed load concentration (c_b) according to Van Rijn (1984b), defined by Equation 3.5.18, where Υ is the relative bed shear stress defined by Equation 3.5.19, and D_* is the particle parameter computed according to Equation 3.5.20.

$$\frac{\partial c}{\partial t} + u_j \frac{\partial c}{\partial x_j} + w_s \frac{\partial c}{\partial z} = \frac{\partial}{\partial x_j}\left(\nu_T \frac{\partial c}{\partial x_j}\right) \tag{3.5.17}$$

$$c_b = 0.015 \frac{d}{a}\left(\frac{\Upsilon^{1.5}}{D_*^{1.3}}\right) \tag{3.5.18}$$

$$\Upsilon = \frac{\tau - \tau_c}{\tau_c} \tag{3.5.19}$$

$$D_* = d\left(\frac{(s-1)\, g}{\nu^2}\right)^{\frac{1}{3}} \tag{3.5.20}$$

In Equation 3.5.18, a is the reference level for computing the suspended load that has been determined according to the methodology proposed by Rouse (1937).

The critical bed shear stress was defined according to Shields (1936) and parameterized according to Yalin (1972), including the slope correction proposed by Dey (2001) and, in addition, applying the incipient transport relaxation factor extensively described by Quezada et al. (2018).

The morpho-dynamic evolution was determined by the sediment volume conservation equation described in Equation 3.5.21, where z_b is the bed elevation, and $q_{b,x}$ and $q_{b,y}$ are the sediment transport for the bed load in the x and y directions, respectively. E is the sediment entrainment rate from the bed load to the suspended-load, and D is the sediment deposition rate from the suspended load onto the bed.

$$\frac{\partial z_b}{\partial t} + \frac{1}{1-n}\left(\frac{\partial q_{b,x}}{\partial x} + \frac{\partial q_{b,y}}{\partial y}\right) + E - D = 0 \tag{3.5.21}$$

The difference between E and D is defined by REEF3D according to Wu et al. (2000). Meanwhile, a more extensive description of the estimation of $q_{b,x}$ and $q_{b,y}$ can be found in Quezada et al. (2018).

In order to develop a numerical study of the present investigation, the model was developed as indicated in Table 3.7, where L is the flume length, W is the width, h_t is the height, and Δx_i is the cell dimension used in the model; N° Cells is the total number of elements comprising the numerical domain, and t_{test} is the simulation time of the numerical model. The W (W1 to W3) and WC series (WC1 to WC3) correspond to a hydrodynamic calibration stage for waves acting alone and waves plus current, respectively, without a pile placed on the flume. Detailed information can be found in Table 3.8.

Series C (C01 to C04) corresponds to a hydrodynamic stage for waves plus current with a pile. Detailed information for each test can be found in Table 3.9. Finally, series E (E01 to E08) corresponds to the simulated cases for hydrodynamic analysis due to the combined action of waves and currents; their detailed information can be found in Table 3.10.

The following sections provide more exstensive information on the simulated scenarios and the data processing used.

Table 3.7: Summary of the REEF3D model configuration applied to each simulated cases.

Case	L (m)	W (m)	h_t (m)	Δx_i (m)	N° Cells	t_{test} (min)
W1	24.00	0.70	1.00	0.01	16,768,400	5.00
W2	24.00	0.70	1.00	0.01	16,768,400	5.00
W3	24.00	0.70	1.00	0.01	16,768,400	5.00
WC1	24.00	0.70	1.00	0.01	16,768,400	5.00
WC2	24.00	0.70	1.00	0.01	16,768,400	5.00
WC3	24.00	0.70	1.00	0.01	16,768,400	5.00
C01	24.00	1.00	1.00	0.01	23,968,400	7.00
C02	24.00	1.00	1.00	0.01	23,968,400	7.00
C03	24.00	1.00	1.00	0.01	23,968,400	7.00
C04	24.00	24.00	1.00	0.01	575,968,400	1.00
E01	24.00	1.00	1.00	0.01	23,968,400	30.00
E02	24.00	1.00	1.00	0.01	23,968,400	30.00
E03	24.00	1.00	1.00	0.01	23,968,400	30.00
E04	24.00	1.00	1.00	0.01	23,968,400	30.00
E05	24.00	1.00	1.00	0.01	23,968,400	30.00
E06	24.00	1.00	1.00	0.01	23,968,400	30.00
E07	24.00	1.00	1.00	0.01	23,968,400	30.00
E08	24.00	1.00	1.00	0.01	23,968,400	30.00

Δx_i is the dimension for the x, y, and z axis, due to the model using regular element definitions.

Hydrodynamics Calibration Test

Prior to executing a numerical simulation of scour due to the combined waves and currents around a circular pile, the process of hydrodynamically calibrating the model REEF3D was conducted by comparing the numerical results with the experimental results obtained by other authors. The calibration process was carried out in two phases. The first phase to verified the numerical model's capacity to represent a flow of waves and currents combined, without the pile in the flume, while the second calibration phase included the presence of a vertical pile in the center of the flume.

In Table 3.8, cases executed in the hydrodynamic calibration process without considering the pile are described. The experimental information for each of the cases was obtained from Umeyama (2010), and these data correspond to the unevenness data for the water surface and the vertical profiles of flow horizontal velocity for different times steps, both for the flow caused only by the actions of waves (case W1 to W3) and by waves and currents (cases WC1 to WC3).

The variables in 3.8 are defined as follows: h is water depth, H is wave height, T is the wave periodic time, and U_c is the undisturbed current velocity defined according to Sumer and Fredsøe (2001).

Table 3.8: Hydrodynamic calibration of waves and currents coexisting without a pile.

Case	h (m)	H (cm)	T (s)	U_c (cm/s)
W1	0.30	1.03	1.00	0.00
W2	0.30	2.34	1.00	0.00
W3	0.30	3.61	1.00	0.00
WC1	0.30	0.91	1.00	8.00
WC2	0.30	2.02	1.00	8.00
WC3	0.30	3.09	1.00	8.00

In order to compare the results obtained by the numerical model and those provided by Umeyama (2010) experimental work, a virtual sensor was established in the middle of the numerical domain, from which the vertical distribution (from the total velocity), and the surface elevation were extracted. The simulation time for all scenarios of the situation without pile (W1 to WC3) was five minutes (300 waves).

Simulated cases for the hydrodynamic calibration of the numerical model, including one pile in a flow due to waves and the combined action of currents, are summarized in 3.9, which considers simulated cases for codirectional (C01 to C03) and perpendicular (C04) waves and currents.

The numerical results obtained by the simulation for cases C01 to C03 (codirectional) contrasted with the experimental data provided by Qi and Gao (2014b), where the flow velocity was the comparison variable. For the case of the perpendicular waves and currents (C04), the experimental information provided by Miles et al. (2017) was used to verify the numerical results, where the contrasted variable was the average vertical profile of the total flow velocity.

Table 3.9: Hydrodynamic calibration of waves and currents coexisting with pile.

Case	h (m)	D (m)	H (cm)	T (s)	U_c (m/s)	Direction
C01	0.50	0.20	2.60	1.40	0.23	Codirectional
C02	0.50	0.20	5.20	1.40	0.23	Codirectional
C03	0.50	0.20	8.50	1.40	0.23	Codirectional
C04	0.50	0.20	4.00	1.25	0.25	Perpendicular

The comparison of the numerical and experimental data obtained by Qi and Gao (2014b) (C01 to C03) was carried out by obtaining the time series of the total velocity in a virtual monitoring station located at the horizontal 20D and 1D relative to the bed. The total time of the simulation was seven minutes (300 waves).

For case C04, the comparison of numerical and experimental data published by Miles

et al. (2017) was conducted via the vertical distribution of the longitudinal velocity averaged in eight points around the pile, which were denominated P1 to P8 and distributed as shown in Figure 3.13. The monitoring stations were located $0.75D$ from the center of the pile, while their angular separation was 45°.

The velocities were nondimensionalized according to the characteristic velocity (C) described in Equation 3.5.22 for all compared cases between the modeled and experimental data (Umeyama, 2010; Qi and Gao, 2014b; Miles et al., 2017).

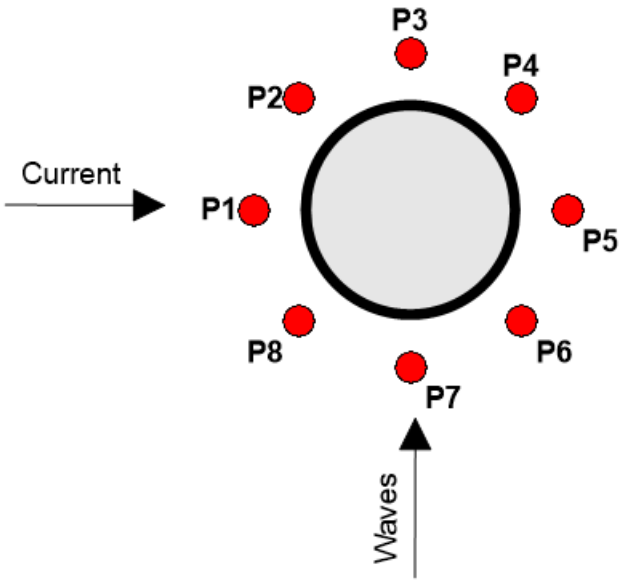

Figure 3.13: Identification of the comparison points of the average velocity profiles obtained from the numerical modeling and those published by Miles et al. (2017).

$$C = \sqrt{gh} \tag{3.5.22}$$

Hydrodynamics Behavior of the Flow around a Cylindrical Pile

To numerically determine the hydrodynamic behavior around a cylindrical pile subjected to the combined action of waves and currents, a set of 8 simulations were developed, as described in Table 3.10. The cases were defined to cover a wide range of waves and current interactions according to the flow relative velocity (U_{cw}) proposed by Sumer and Fredsøe (2001). Thus, we formed scenarios dominated by currents (E01 and E02), waves and currents but with a tendency toward current domination (E03 and E04), waves and currents but with a tendency toward wave domination (E05 and E06), and environments dominated by waves (E07 and E08).

The estimation of the flow relative velocity (U_{cw}) was conducted by considering the maximum value of the undisturbed orbital velocity at the sea bottom just above the wave boundary layer (U_m), according to Equation 3.5.23, while the undisturbed current velocity at the transverse distance $z = D/2$ (U_c) was defined as an edge condition for each of the modeling scenarios. Additionally, the Keulegan-Carpenter number was estimated as indicated in Equation 3.5.24, in order to identify the influence that waves have over maximum scour.

$$U_m = \frac{\pi\, H}{T\, \sinh(Kh)} \tag{3.5.23}$$

$$KC = \frac{U_m\, T}{D} \tag{3.5.24}$$

Table 3.10: Simulated cases for the analysis of hydrodynamics due to the combined action of waves and currents.

Case	h (m)	D (m)	H (m)	T (s)	U_c (m/s)	U_m (m/s)	U_{cw}	KC	Direction
E01	0.50	0.20	0.085	1.40	0.23	0.12	0.65	0.86	Codirectional
E02	0.50	0.20	0.085	1.40	0.23	0.12	0.65	0.86	Opposite
E03	0.50	0.20	0.129	1.40	0.22	0.19	0.54	1.31	Codirectional
E04	0.50	0.20	0.129	1.40	0.22	0.19	0.54	1.31	Opposite
E05	0.50	0.20	0.150	2.00	0.24	0.28	0.47	2.76	Codirectional
E06	0.50	0.20	0.150	2.00	0.24	0.28	0.47	2.76	Opposite
E07	0.50	0.20	0.150	3.00	0.10	0.31	0.25	4.61	Codirectional
E08	0.50	0.20	0.150	3.00	0.10	0.31	0.25	4.61	Opposite

All simulations conducted (E01 to E08) were set to solve the hydrodynamics model within 30 minutes throughout the entire numerical domain, using the potential flow and a hydrostatic distribution of pressures as the initial condition (see Table 3.6).

To analyze the velocities and vortexes associated with the flow, two main vertical planes of the channel were designed. The first of these plains corresponds to the longitudinal axis (flow development) passing through the center of the pile from the beginning of the channel to its end. The second is associated with the axis perpendicular to the channel, as shown in Figure 3.14.

As the first stage of the analysis conducted on the results obtained from the numerical model, the velocity fields along the channel were inspected in order to identify patterns in spatiotemporal flow performance. Subsequently, for each of the planes traced around the cylindrical pile (see Figure 3.14), the vorticity average performance was determined and the associated streamlines were traced to study and analyze the average performance of the horseshoe vortex. Additionally, eight monitoring stations were defined to obtain the vertical distribution of the flow velocity Figure 3.13 indicates the distribution of these stations, which is concordant with the methodological approach of Miles et al. (2017).

Moreover, the amplification of the shear stress (α_τ) around the pile was determined, associated with the average flow conditions and (on a Cartesian plane) based on the numerical domain bed, prior to scour. For such purposes, the proportion of the bed shear stress (τ_0) and the undisturbed bed shear stress (τ_∞) according to Equation 3.5.25 were considered. To determine τ_0 and τ_∞, the shear velocity was computed by the numerical model in the bed's nearest cell for two locations: around the pile ($u_{*T,pile}$) for the calculation of τ_0 and 2 meters downstream of the inlet ($u_{*T,inlet}$) τ_∞.

The relation employed for the bed shear stress estimations corresponds to the conventional hydraulic definition described in Equation 3.5.26 for (τ_0) and Equation 3.5.27 for τ_∞, where $u_{*T,inlet}$ or $u_{*T,pile}$ corresponds to the total bed velocity, determined from the longitudinal and transverse velocity vector magnitude.

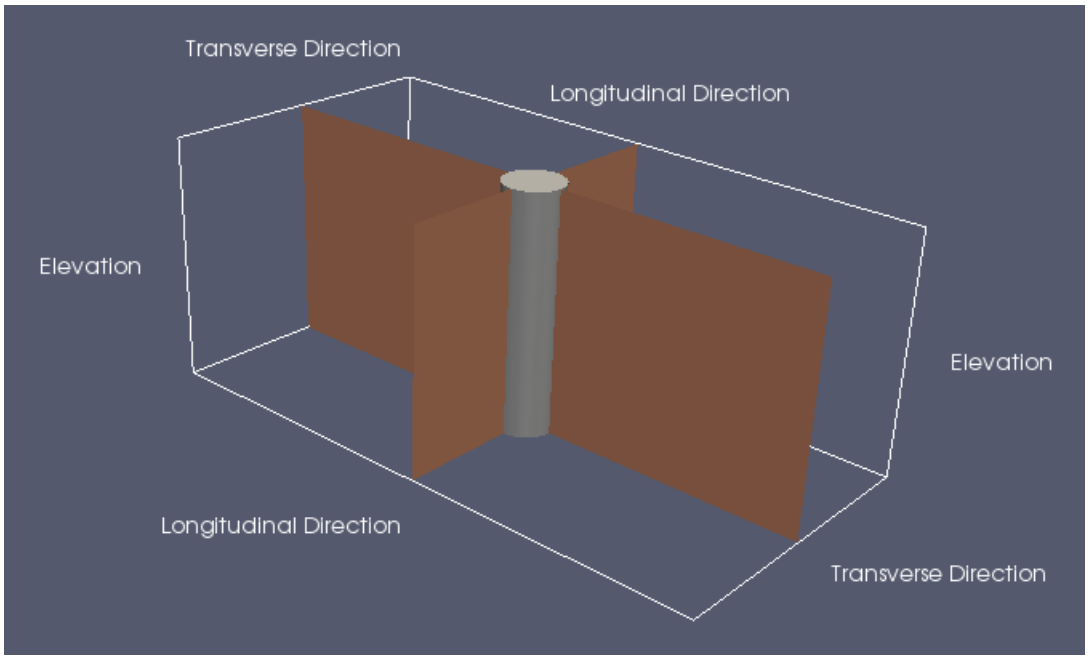

Figure 3.14: Analysis of the hydrodynamic planes around the cylindrical pile.

$$\alpha_\tau = \frac{\mid \tau_0 \mid}{\tau_\infty} \tag{3.5.25}$$

$$\tau_0 = \rho u^2_{*,T,pile} \tag{3.5.26}$$

$$\tau_\infty = \rho u^2_{*,T,inlet} \tag{3.5.27}$$

Scour around a Cylindrycal Pile

Using a simulated scenario for the study of hydrodynamics, the scour around the pile was estimated by considering a bed composed of spherical sediments with diameter of 0.38 mm (d), 2650 Kg/m^3 in density, a 30° angle of repose, and a dimensionless critical shear stress (τ^*_{cr}) equal to 0.036, in order to make the results obtained in this investigation for E01 and E02 comparable to those previously presented by Qi and Gao (2014b).

The scour estimation using the numerical model was activated during the last 25 minutes of the hydrodynamic modelling (S_1), to obtain enough information at the beginning of the simulation for the immobile bed condition and, subsequently, the associated condition for the mobile bed.

The features of the numerical tests conducted on the scour around the modeled cylindrical pile are summarized in Table 3.11. The parameters associated with the incipient transport of sediments for the combined regimen of waves and currents have been estimated according to the methodology extensively described in Soulsby (1997). The fundamental equations for estimating shear stress are described below in summary.

Bed shear stress due to the combined action of waves and currents was estimated according to Equation 3.5.28, where τ_c is shear stress considering only the action of currents, while τ_w corresponds to the shear stress for waves alone. The shear velocity (u_*) was determined based

on a resistance law according to Equation 3.5.31, where U_B is the bulk velocity of the flow due to the current. The wave boundary layer velocity (U_{fm}) is defined in Equation 3.5.32, where f_w is the friction factor, which was determined according to (Fredsøe and Deigaard, 1992, page 25).

$$\tau_{wc} = \tau_c \left[1 + 1.2 \left(\frac{\tau_w}{\tau_c + \tau_w}\right)^{3.2}\right] \tag{3.5.28}$$

$$\tau_c = \rho u_*^2 \tag{3.5.29}$$

$$\tau_w = \frac{1}{2}\rho\, f_w\, U_{fm}^2 \tag{3.5.30}$$

$$\frac{u_*}{U_B} = \frac{1}{7}\left(\frac{d}{h}\right)^{\frac{1}{7}} \tag{3.5.31}$$

$$U_{fm} = \sqrt{\frac{f_w}{2}}\, U_m \tag{3.5.32}$$

The shear stress values associated with currents, waves and the combined action of both were nondimensionalized according to Equation 3.5.14. The results are presented in Table 3.11.

Table 3.11: General characteristics of numerical tests of scour modeling.

Case	τ_c*	τ_w*	$\tau_{wc}*$	$\frac{\tau_{wc}*}{\tau_{cr}*}$	Regimen
E01	0.023	0.003	0.023	0.63	Clear water
E02	0.023	0.003	0.023	0.63	Clear water
E03	0.021	0.005	0.021	0.58	Clear water
E04	0.021	0.005	0.021	0.58	Clear water
E05	0.025	0.008	0.025	0.69	Clear water
E06	0.025	0.008	0.025	0.69	Clear water
E07	0.004	0.008	0.004	0.15	Clear water
E08	0.004	0.008	0.004	0.15	Clear water

Considering that the numerical modeling duration of the scour was 25 minutes and that in this time scale the equilibrium condition was not reached, a projection was made via the equation proposed by Sheppard et al. (2004), which corresponds to a four-parameter exponential function for the extrapolation of the equilibrium scour depth (S_t), which is presented in Equation 3.5.33 where a_i corresponds to the adjustment coefficient i of the equation by Sheppard et al. (2004). This approach was also used by Qi and Gao (2014b), with experimental data.

$$S_t = a_1[1 - exp(-a_2 t)] + a_3[1 - exp(-a_4 t)] \tag{3.5.33}$$

The equilibrium scour was compared with the results presented by Qi and Gao (2014b), Sumer and Fredsøe (2001), Raaijmakers and Rudolph (2008), Sumer et al. (2012), and Mostafa and Agamy (2011) to check whether the numerical results obtained are concordant with the experimental data developed by other authors.

3.5.4 Results

Hydrodynamics Calibration Test

The hydrodynamic calibration process for the numerical model REEF3D is as follows. Figure 3.15 shows the results obtained by numerical modeling and those reported by Umeyama (2010), based on experimental data, for a domain forced by waves and a mixed domain of wave and currents. The comparison variable corresponds to the instant surface elevation (η) nondimensionalized with the wave height (H) as a nondimensional time function ($\frac{t}{T}$), with T as the period. The physical sense of the variable $\frac{\eta}{H}$ corresponds to the fraction of the increase or decrease in the water surface and, evidently, the maximum and minimum fractions are the descriptors of wave asymmetry. The variable $\frac{t}{T}$ corresponds to an indicator of the wave time fraction being simulated.

A comparison between the experimental data for cases where waves are acting alone (W1 to W3, illustrated with circles) and those for waves and currents (WC1 to WC3, illustrated with triangles) are shown in Figure 3.15, boxes 1.1 to 1.3. Here, it can be deduced that a codirectional current modifies the wavelength and amplitude of the wave. The numerical results are found in Figure 3.15, boxes 2.1 to 2.3, both for a flow with waves (blue line) and for waves and currents (red line). Thus, it can be verified that the wavelength and amplitude are modified between both flows, as shown in the experimental data (Figure 3.15, box 1.1 to 1.3). The results of the comparison between the numerical modeling REEF3D and the experimental data provided by Umeyama (2010) are included in boxes 3.1 to 3.3 for waves acting alone, while waves and currents acting together are shown in boxes 4.1 to 4.2.

When analyzing numerical and experimental data associated to waves acting alone (W1 to W3), all model cases were able to adequately reproduce the maximum and minimum wave amplitude, as well as its temporal evolution within a wave time coinciding with the necessary time to reach the peak, the zero crossing time and the time to reach the minimum. Taking into account the difference in the estimation of the crest and trough, for the waves and currents (WC1 to WC3), it can be observed that the numerical model slightly underestimates the experimental data, but at a magnitude of less than one millimeter (around 2% error).

The vertical profiles for the instant velocity associated with each of the simulated cases in the present investigation (which were experimentally registered by Umeyama (2010)) are compared in Figure 3.16 for waves acting alone and in Figure 3.17 for waves and currents combined. Both figures illustrate four instants of time for each simulated case, ordered from left to right and corresponding to $\frac{t}{T} = 0.00$, 0.25, 0.50, 0.75, and 1.00.

The results of the comparison of numerical and experimental data considered in the presence of waves alone (Figure 3.17) reflect a high consistency between vertical and temporal behavior, as the model is capable of adequately representing the flood direction (negative $\frac{u}{C}$) and the ebb direction (positive $\frac{u}{C}$). The experimental and numerical data show equivalent vertical structures for the velocity profile, with a slight increase toward the surface, which is evidenced in a greater proportion when analyzing the case with the highest wave (W3).

Near the bed, the current magnitudes determined based on the numerical model coincide with those determined by experimental means, showing slight differences between the simulated and instrumental data.

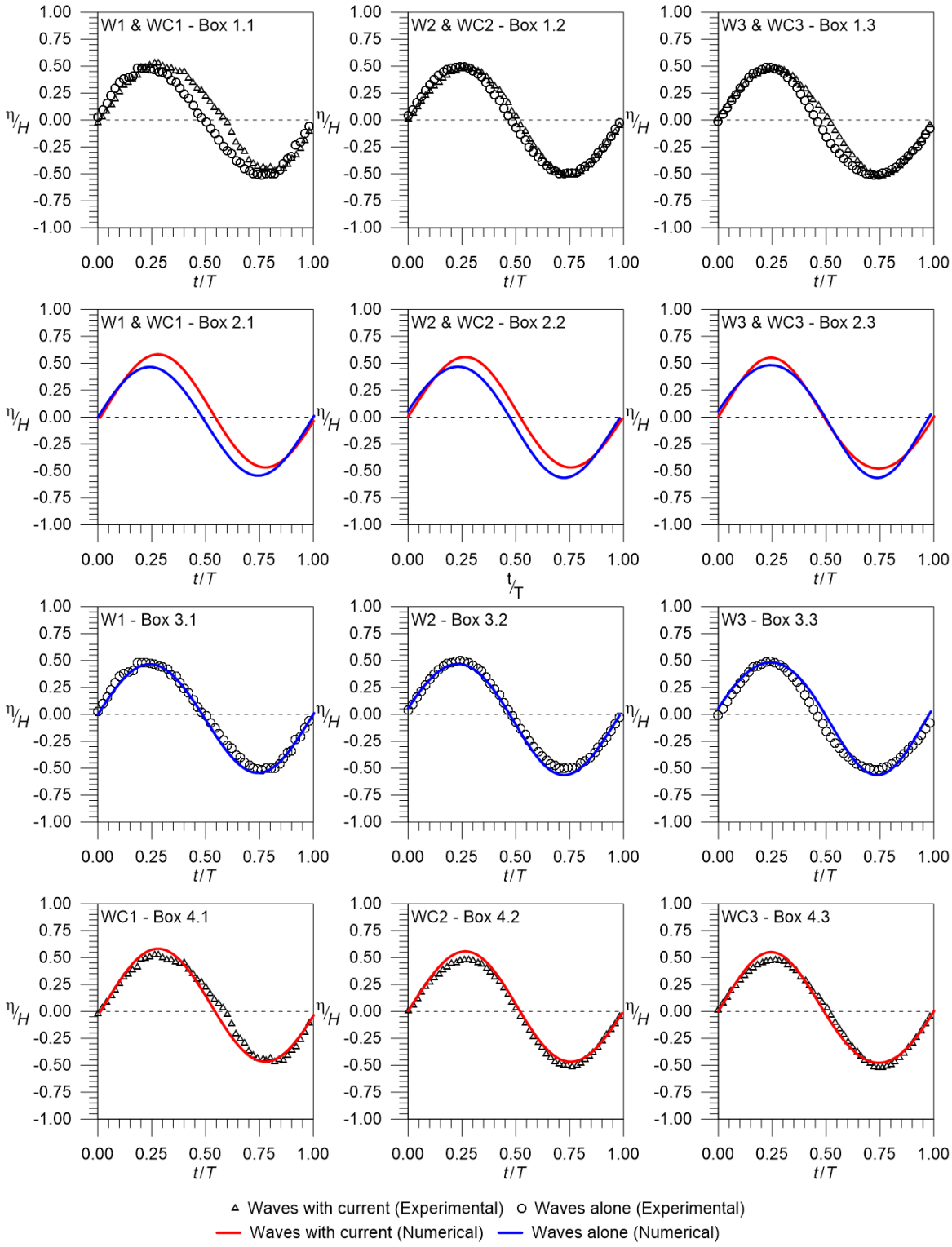

Figure 3.15: Phase-average surface displacements comparison between experimental data (Umeyama, 2010) and numerical results.

The detected differences for $\frac{t}{T} = 0.25$ and 0.75 show a low magnitude. However, the flood and ebb conditions reached different magnitudes described, as follows. For the W1 case, the maximum difference in the nondimensional velocity ($\frac{u}{C}$) obtained by the ebb direction was 0.004 ($\frac{t}{T} = 1.00$), while for the flood direction it was -0.001. For the W2 case, the differences fluctuated between -0.005 and -0.011.

Greater differences between the numerical model and experimental data were found for the W3 case for $\frac{t}{T} = 0.00$, which is produced at the water surface. Meanwhile, near the bed, the greatest difference in $\frac{u}{C}$ was 0.015 for $\frac{t}{T} = 1.00$.

In Figure 3.16, the maximum and minimum velocities are not at 0.25 and 0.75 $\frac{t}{T}$ respectively, because the wave phase effect on the initial condition was adjusted to represent the same oscillatory flow that (Umeyama, 2010) reported in his research.

When incorporating a codirectional current to waves, Figure 3.17 shows that the vertical velocity distribution along the channel only shows the flood direction because the currents control the hydrodynamics. This can be confirmed by calculating the flow relative velocity proposed by Sumer and Fredsøe (2001) (U_{cw}), which offers results equal to 0.84, 0.70, and 0.60, for WC1, WC2, and WC3, respectively.

In general terms, the numerical model adequately captured the behavior of the velocity profile, showing a greater similarity between the currents near the bed and those obtained toward the free surface. Compared to the hydrodynamic scenarios, where only waves were present, the differences found for the dimensionless velocity ($\frac{u}{C}$) have a greater magnitude when the current is incorporated in the centre, reaching 0.010 for WC1, -0.017 for WC2, and -0.037 for WC3.

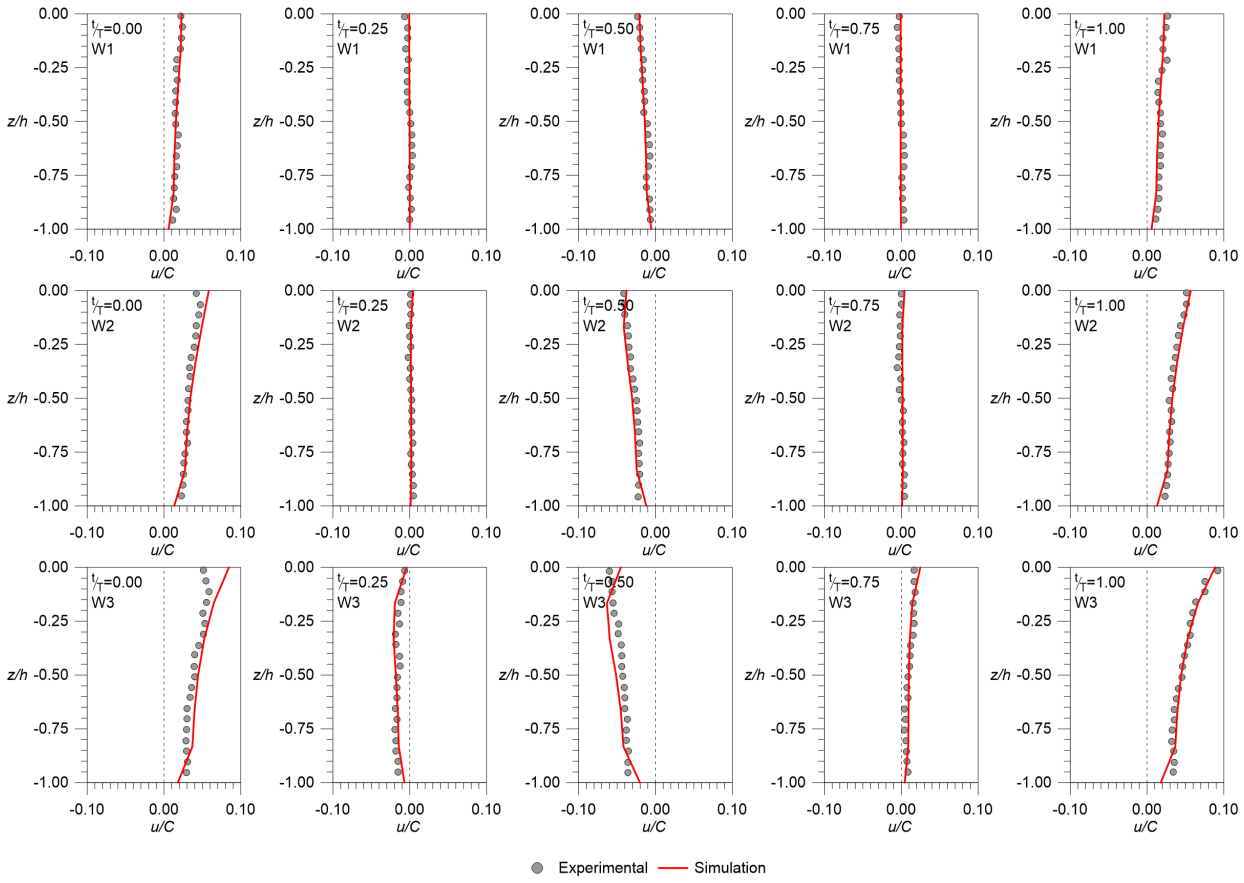

Figure 3.16: Instantaneous horizontal velocity profile comparison between the experimental data (Umeyama, 2010) and numerical results for different time steps, for cases with waves alone.

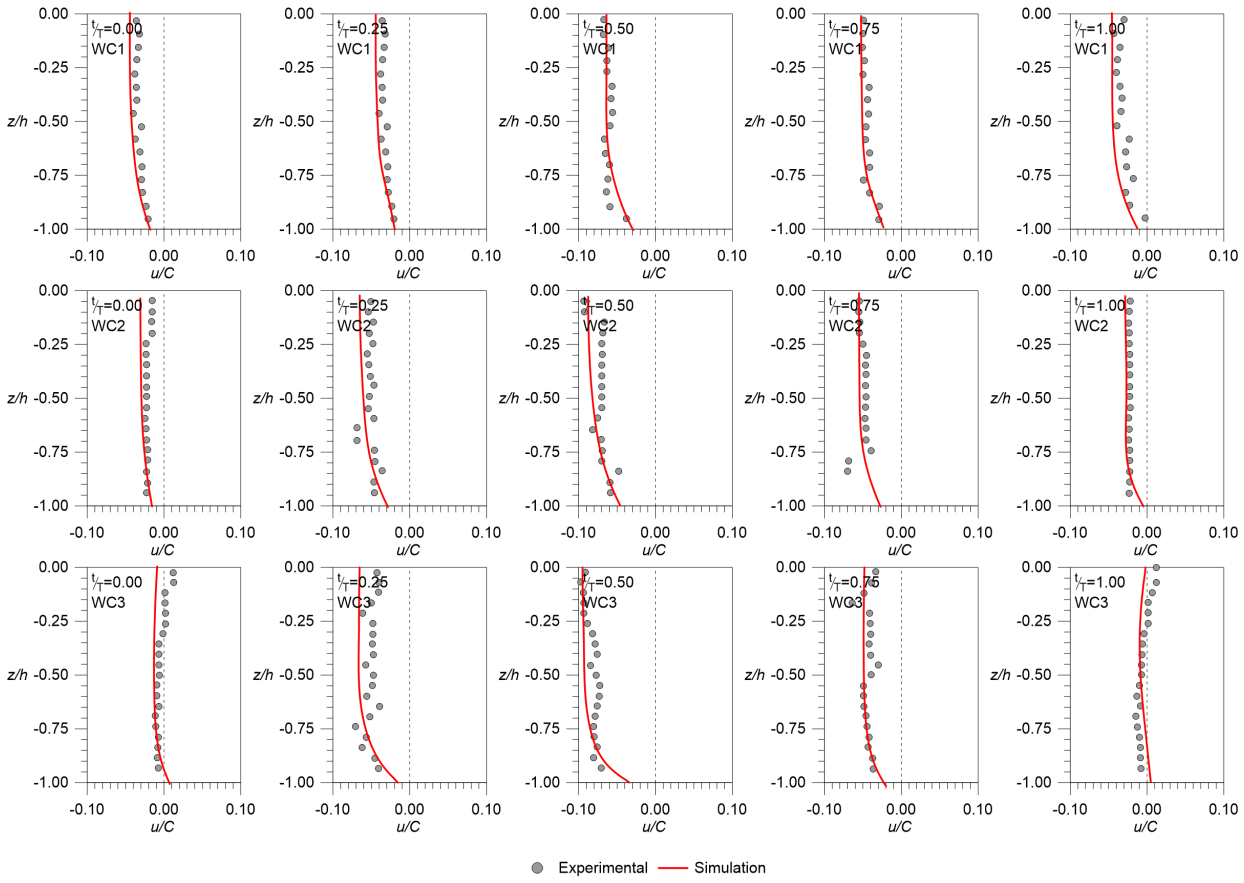

Figure 3.17: Instantaneous horizontal velocity profile comparison between the experimental data (Umeyama, 2010) and numerical results for different time steps, both for waves alone and for current cases.

The previous results correspond to the scenarios of interactions between waves and currents without the incorporation of a circular pile blocking the flow. However, they allow us to confirm that the numerical model is capable of representing the complex hydrodynamics resulting from the combined action of both components (waves and currents). To strengthen this analysis, the results of the model for a circular pile in the flow are shown next.

The results of the comparison of the numerical model with the experimental data obtained from Qi and Gao (2014b) are presented in Figure 3.18, which considers the total flow velocity ($U_c + U_w$) non-dimensionalized with the characteristic velocity (C). Based on this comparison, it was observed that the numerical model was able to represent the dynamic behavior of the combined flow velocity, for the different characteristics of the simulated waves and currents. In test case C01, it can be observed that the numerical model predicted slightly higher velocities in the trough located between $1.00 < \frac{t}{T} < 1.50$, $\frac{U_c+U_w}{C}$ (equal to 0.02). This result, however, was not observed in cases C02 and C03. Hence this case does not correspond to the numerical model configuration.

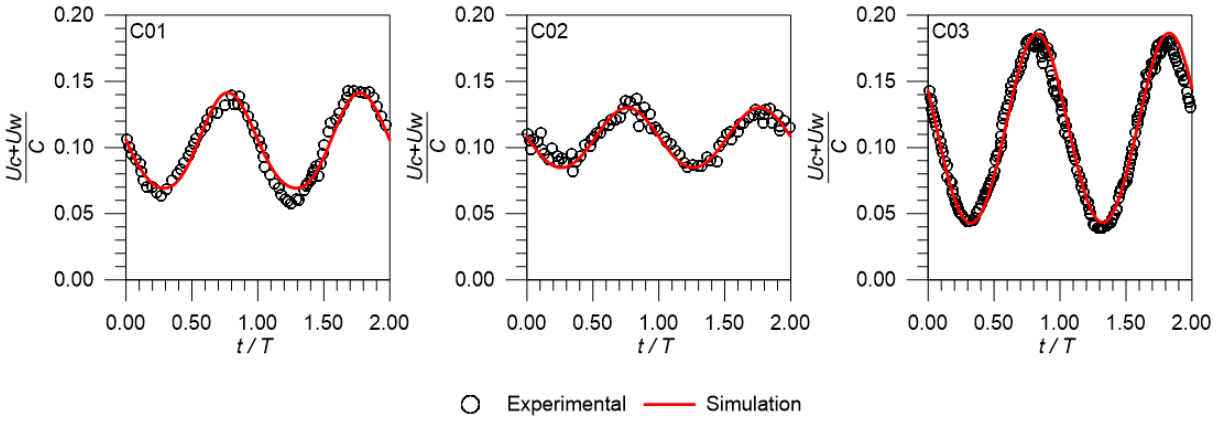

Figure 3.18: Total flow velocity comparison between the experimental data (Qi and Gao, 2014b) and numerical results for waves alone and for current cases in the presence of a cylindrical pile.

It is important to emphasize that the total flow velocity measurements experimentally obtained by Qi and Gao (2014b) were registered upstream from the pile at a distance of $20D$. Ergo, the effects of the opaque structure on the velocities field would not be shown in their behavior. Therefore, this comparison (Figure 3.18) complements that previously shown in Figure 3.15 for the instant surface elevation. Thus, the numerical model is capable of representing the wave and current interactions in a freestream.

The effects on the velocity fields caused by the cylindrical pile in a flow field with waves perpendicular to the currents obtained from the numerical model were compared with data provided by Miles et al. (2017). The results for which waves and currents come from perpendicular directions are shown in Figure 3.19 (associates with case C04). When analyzing monitoring station P1, a high consistency is observed between the velocity profiles modeled (red line) and experimentally obtained data (circles), highlighting that the model is capable of representing the mean velocity near the bed and in the vertical direction as well. Equivalent performance was also verified for P2 and P8, which corresponds to the monitoring stations exposed to the current direction.

In station P4, it is noted that the numerical model may have slight differences in its vertical velocity distributions for elevation range, here $\frac{z}{h}$ is equal to -0.98 to -0.96, which is not clearly presented in the other velocity monitoring stations. This performance detected in station P4 may be caused by the combined wake effect due to currents and waves, since geometrically this location is completely downstream of both forcings (associates with case C04).

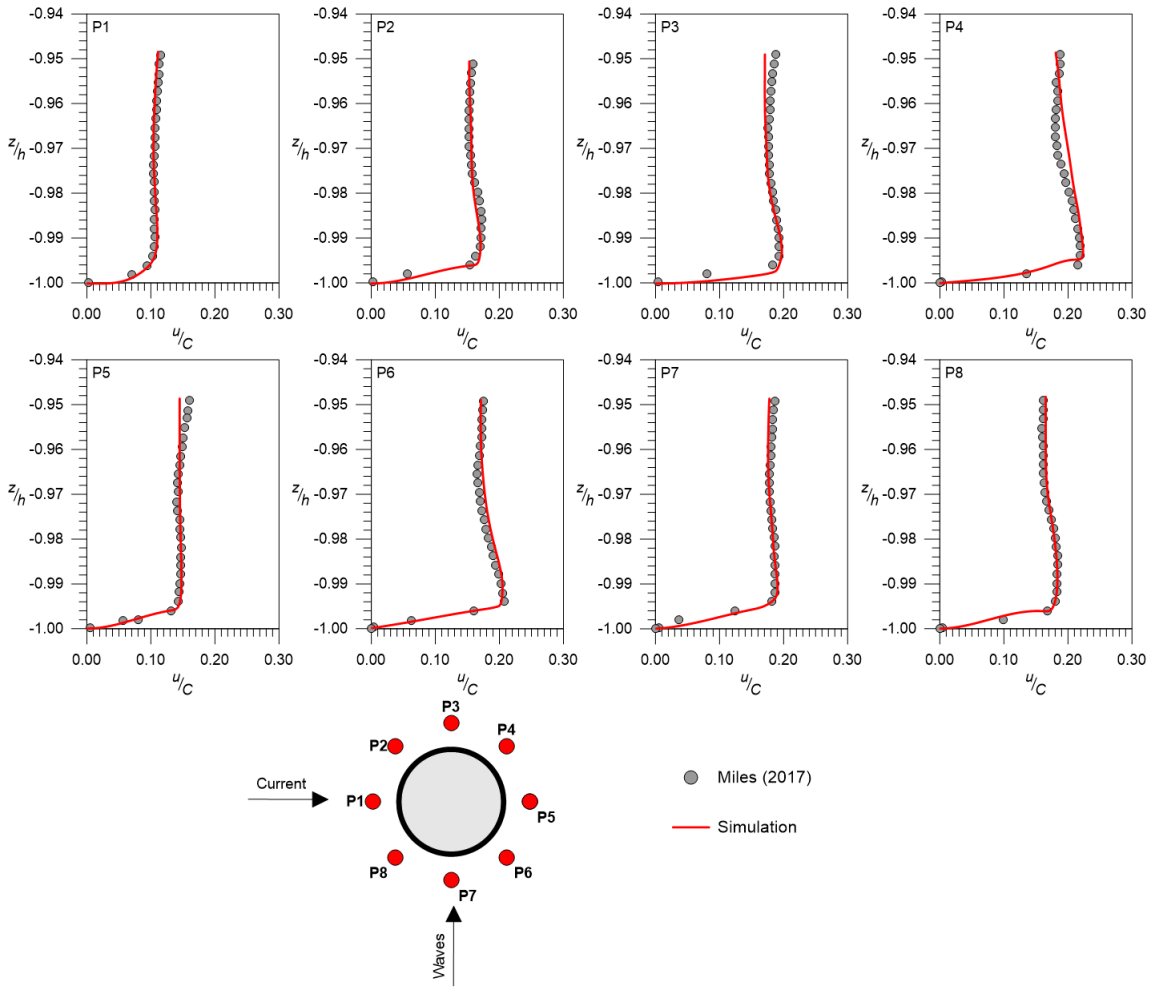

Figure 3.19: Mean velocity profiles comparison between the experimental data (Miles et al., 2017) and numerical results associated with case C04, for waves perpendicular to the current cases in presence of a cylindrical pile.

Hydrodynamics Behavior of the Flow around a Cylindrical Pile

The results obtained for the spatio–temporal evolution of the velocity and vorticity fields for case E07 are illustrated in Figure 3.20. These results consider four instants in time that allow us to visualize the interaction between the flow and the pile. All charted variables have been nondimensionalized by test characteristic scales. For example, the longitudinal and the vertical axes have been made dimensionless with the pile diameter, and, the beginning of the coordinated system has been placed at the center of the pile. The velocities (u and w) have been made dimensionless with the characteristic velocity (C). Vorticity (ω_x, ω_y, and ω_z), on the other hand, was nondimensionalized by the integral temporal scale of the experiment and corresponds to the proportion $\frac{D}{C}$.

In Figure 3.20, in the first instant of time (Time 1 in Figure 3.20), it can be observed that the free surface is on a trough nearby the pile where the longitudinal velocity is mainly an ebb type, which usually form a horseshoe vortex when interacting with the incoming boundary layer. Descending velocities are developed in the vertical axis and near the pile, which may be

associated with the down-flow.

As time progresses and the crest approaches the pile (Time 2 in Figure 3.20), the longitudinal velocity starts to diminish its magnitude (nearing zero), thus reflecting the oscillating effect, since this hydrodynamic behavior is an indicator that both ebb and flow can be present based on the phase of the wave. Contrary to the previous instant, the vertical velocity near the pile shows a positive magnitude, which would not produce down-flow and would consequently modify the horseshoe vortex behavior, as follows.

At time instant 3 (time 3 in Figure 3.20), the wave crest interacts directly with the pile, developing longitudinal velocities mainly oriented downstream the pile, while the vertical component of the velocity is once again oriented toward the bed, thus producing a down-flow. This is maintained for as long as the wave interacts with the pile during the crest phase (time 4 in Figure 3.20), while the longitudinal velocity changes to an ebb direction.

The association of the main component of the vorticity with the cross vorticity ($\frac{\omega_y D}{c}$) is obtained from the vorticity development near the pile and the adjacent bed for the four illustrated instants of time in Figure 3.20. Thus, that the minimum intensities occur under the trough, while in the crest there is a general tendency to maximize these intensities. When the crest is approaching the pile, it is observed that in the bed (upstream), a cross vorticity structure with a positive magnitude approaches the pile, and, conversely, the cross vorticity considerably diminishes its magnitude when the trough moves through the pile. The geometrical characteristics of this cross vorticity structure mainly present a greater longitudinal than vertical development.

The vorticity behavior upstream from the pile (described above) corresponds to the horseshoe vortex, and its intermittence would be conditioned by direction changes of the vertical and longitudinal velocity.

The downstream sector under the pile showed a vorticity behavior ($\frac{\omega_x D}{C}$ and $\frac{\omega_z D}{C}$) with alternate structures (positives and negatives) and a greater development in the vertical axis than in the horizontal axis, compared to the cross vorticity. This spatio–temporal development could be associated with vortex shedding, resulting from structure-fluid interactions.

Based on a general analysis of the information obtained from the numerical modeling (a visual inspection of the results), there are no significant differences in the mean spatio–temporal behavior of the streamlines, vorticities, and velocity field; hence, these element can be broadly described by the specification of one of the eight case simulations, with scenario E01 selected for this effect.

The characteristic results of scenario E01 are presented in Figure 3.21. Unlike Figure 3.20, which illustrates the behavior from the free surface to the bed, in this section, the analysis focused on the bottom to obtain the characteristics of the hydrodynamics that might be responsible for sediments transport and, consequently the scour around the pile.

Figure 3.21 is divided into two main boxes. The upper box illustrates the flow characteristics in the longitudinal profile of the channel, while the lower box illustrates the transverse section. Both have included the streamlines and total vorticity (vector addition, ($\frac{\omega_T D}{C}$), the mean velocity along the channel ($\frac{u}{C}$), the vertical mean velocity ($\frac{w}{C}$), the mean vorticity along the channel ($\frac{\omega_x D}{C}$), the transversal mean vorticity ($\frac{\omega_y D}{C}$), and the vertical mean vorticity ($\frac{\omega_z D}{C}$) in a nondimensionalized manner.

The total vorticity in the longitudinal profile and flow lines reflect the presence of a horseshow vortex as the main structure upstream the pile ($\frac{x}{D} < 0$), this structure approximately centered at $\frac{x}{D}$ = -2.6 and $\frac{z}{D}$ = 0.3. This vorticity system also reflects the average behavior of the flow longitudinal velocity, as in the zone equivalent to the horseshoe vortex location, $\frac{u}{C}$ has negative values that are driven by the vortex counter clockwise rotation. Additionally,

$\frac{w}{C}$ also reflects the horseshoe vortex effects, since negative magnitudes of the vertical velocity (known as the down-flow) can be revealed near the pile. Meanwhile, at a distance lower than $\frac{x}{D}$ = - 2.6, the down-flow becomes positive (mainly driven by the counter clock turn of the vortex).

The pile downstream area ($\frac{x}{D} > 0$) in the mean streamline condition showed a rotational centered structure at around $\frac{x}{D} = 2.4$ and $\frac{z}{D} = 1.6$, which is related to the vortex shedding and could produce alterations in the mean field of the vertical and longitudinal velocities. Longitudinally, near the pile, a flow could be produced toward it, mainly caused by the momentum balance that would be developed at an approximate distance of $\frac{x}{D} = 1.2$. Then, a positive direction of the flow velocity up to a distance of $\frac{x}{D} = 6$ would be present, to subsequently re-adopt a negative velocity; since this behavior is associated with vortex shedding, as stated previously.

Vertical velocities in the downstream area show that, nearby the pile, the flow moves upwards. Meanwhile, an $\frac{x}{D} = 2.7$ distance would make the vertical velocity negative. This and the flow line behavior could be caused by clockwise rotation and related to the formation of vortex shedding.

Analyzing the transverse section of the flow in Figure 3.21, clear that in the mean streamlines, a horseshoe vortex system develops around the pile, with a longitudinal component of mainly positive velocities near the pile. In the case of a vertical component, these velocities would be negative. This means that: a downstream flow component is present once the horseshoe vortex surrounds the pile, and it remains near the bed pushed by the flow vertical velocities.

The presence of structures concordant with the horseshoe vortex around the pile is shown by the transverse vorticity ($\frac{\omega_y D}{C}$). Thus, the vertical development of these structures is limited to an approximately height of $\frac{z}{D} = 0.5$ from the bed. The mean vorticity fields obtained for vertical and longitudinal components are congruent with the classical description of the flow around the cylindrical piles for a permanent flow, which has been widely addressed in the literature (Umeyama, 2005, 2009, 2010; Faraci et al., 2011).

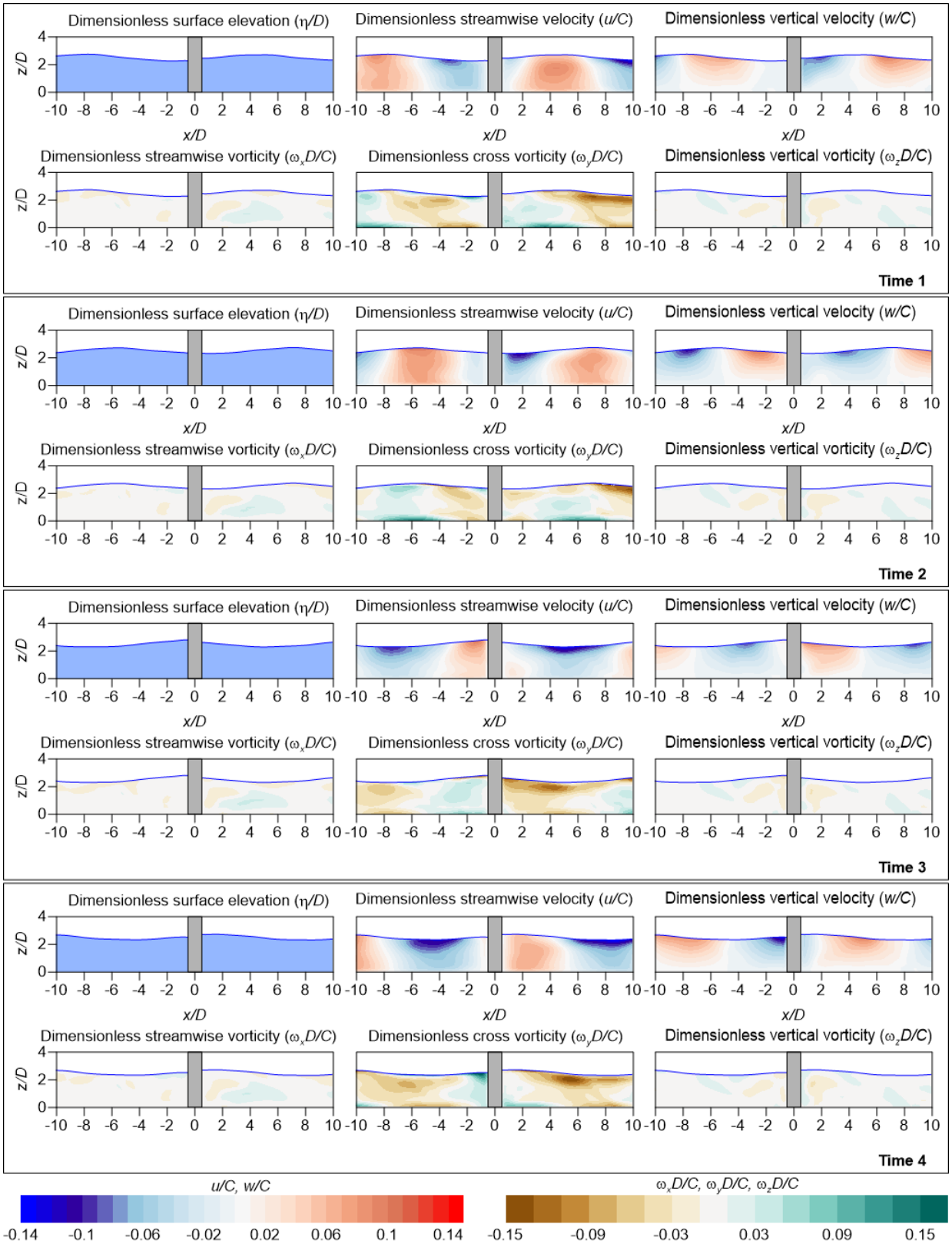

Figure 3.20: Temporal behavior for velocities and vorticities near to the pile, waves and current are coming from the left to the right.

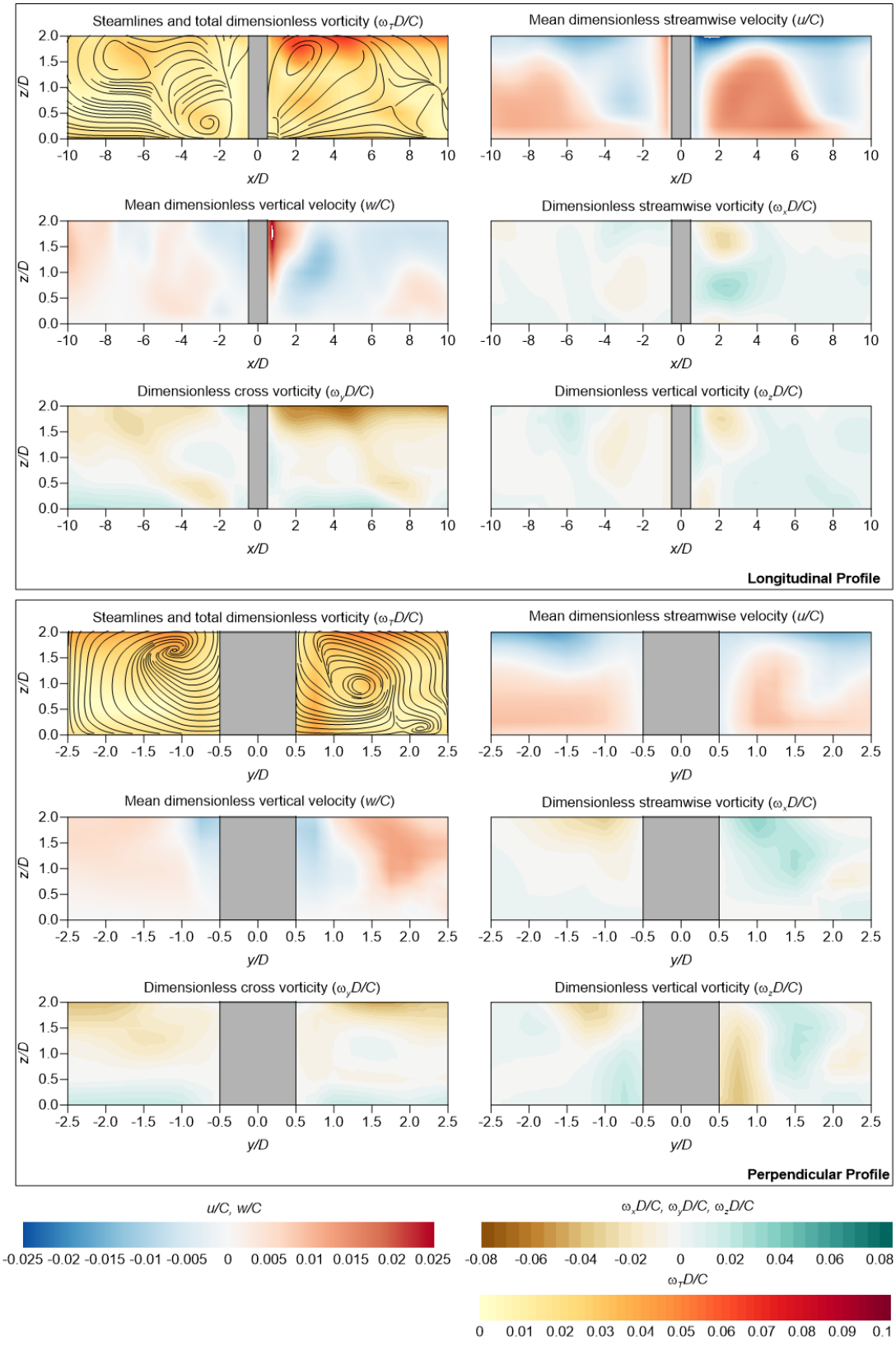

Figure 3.21: General description of the mean velocities and vorticities near the pile for the longitudinal and cross profiles (associated to the scenario E01). Waves and currents are move from the left to the right.

The mean velocity vertical profiles for monitoring stations P1 to P8 are presented in Figure 3.22 for each modeled scenario. From this, it can be observed that the mean characteristics of the codirectional currents and wave velocity profiles are not significantly different under opposite flow conditions in either of the proposed scenarios (those controlled by currents or those controlled by waves).

Clear evidence of this phenomenon is shown in P5 (Figure 3.22), which corresponds to a downward station for codirectional currents and waves and an upstream station for waves in opposite flow scenarios. In each case, the station presented the smallest flow magnitudes, indicating that for all the simulated scenarios of station P5, currents dominate the flow, according to the flow relative velocity (U_{cw}) proposed by Sumer and Fredsøe (2001), this result indicates that a combined regimen is present. This aspect will be further addressed in the analysis of the results.

It is important to note that the currents are symmetrical based on the pile geometrical characteristics (cylinder) and the studied flow. Figure 3.22, shows that the velocity profiles of station pairs P2 with P8; P3 and P7; and P4 and P6 are concordant not only in their magnitudes but also in their vertical axis. Thus, describing only one of the stations associated in a pair is sufficient to understand the flow around the pile. The velocity profiles for both codirectional and opposite cases reached their maximum value in station P3 (P7), mainly due to the contraction of flow lines producing accelerations, thereby increasing the velocities from station P1 towards P3 (P7), followed by a gradual decrease from station P3 (P7) towards P5.

In light of the results described above, and for the simulated scenarios, the hydrodynamics around a pile for combined flow of waves and currents (codirectional and opposite) should behave like a normal flow around a cylinder due to its steady state flow, which is widely described in the literature.

The amplification of the mean shear stresses (α_τ) made dimensionless with an undisturbed bed shear stress around a cylindrical pile is shown in Figure 3.23 for each of the simulated cases, in which the left column shows codirectional currents and waves cases and the right column shows the opposite current and wave cases.

The maximum amplifications of the main bed shear stress were produced in the pile lateral edge and reached magnitudes of 2.5 for codirectional and opposite currents and waves cases. Nevertheless, when waves act on the current in an opposite direction, the amplification zone coverage is reduced (smaller area) compared to the codirectional current and wave cases. As a general trend, the amplification obtained shows that shear stress gradually decreases from hydrodynamic scenarios dominated by currents (E01 and E02) to those dominated by waves (E07 and E08).

Analyzing the results of E01 and E02, the differences found between the spatial distributions of the bed shear stress are not significant when the waves act codirectionally with currents or when they are opposite. No significant movements were noticed in the maximum amplification localization. This means no direct influence of the waves flow or ebb was found for the development of the shear stress in the bottom.

A behavior equivalent to that described for E01 and E02 was identified in E03, E04, E05, and E06, that is, no influence of the waves in the mean bed shear stress distribution was evidenced, even though according to U_{cw} waves domain. In general hydrodynamics, should become more significant when transiting from scenario E01 to E07 and E08. In these last scenarios (E07 and E08), the lowest amplifications of the mean bed shear stress were obtained, which were 1.5.

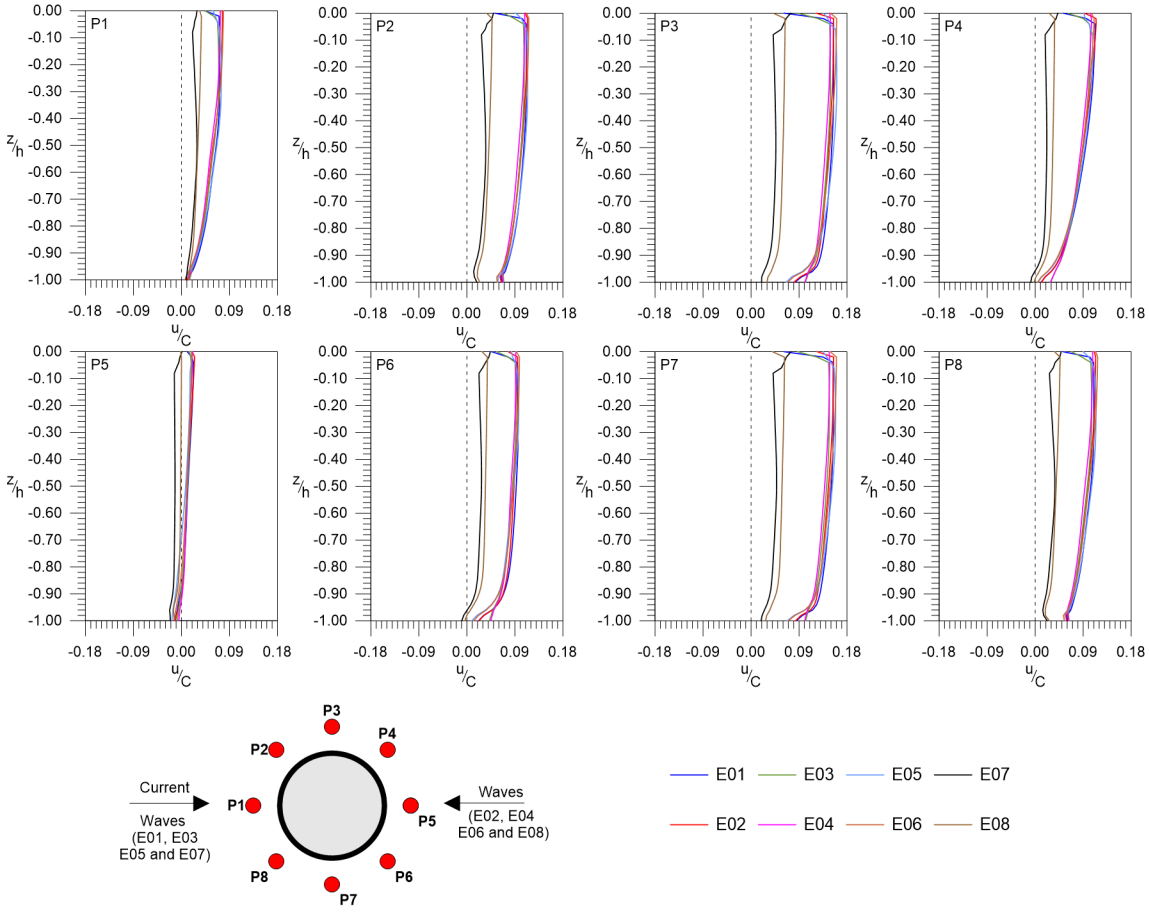

Figure 3.22: Mean streamwise velocity vertical profile for all the simulated cases.

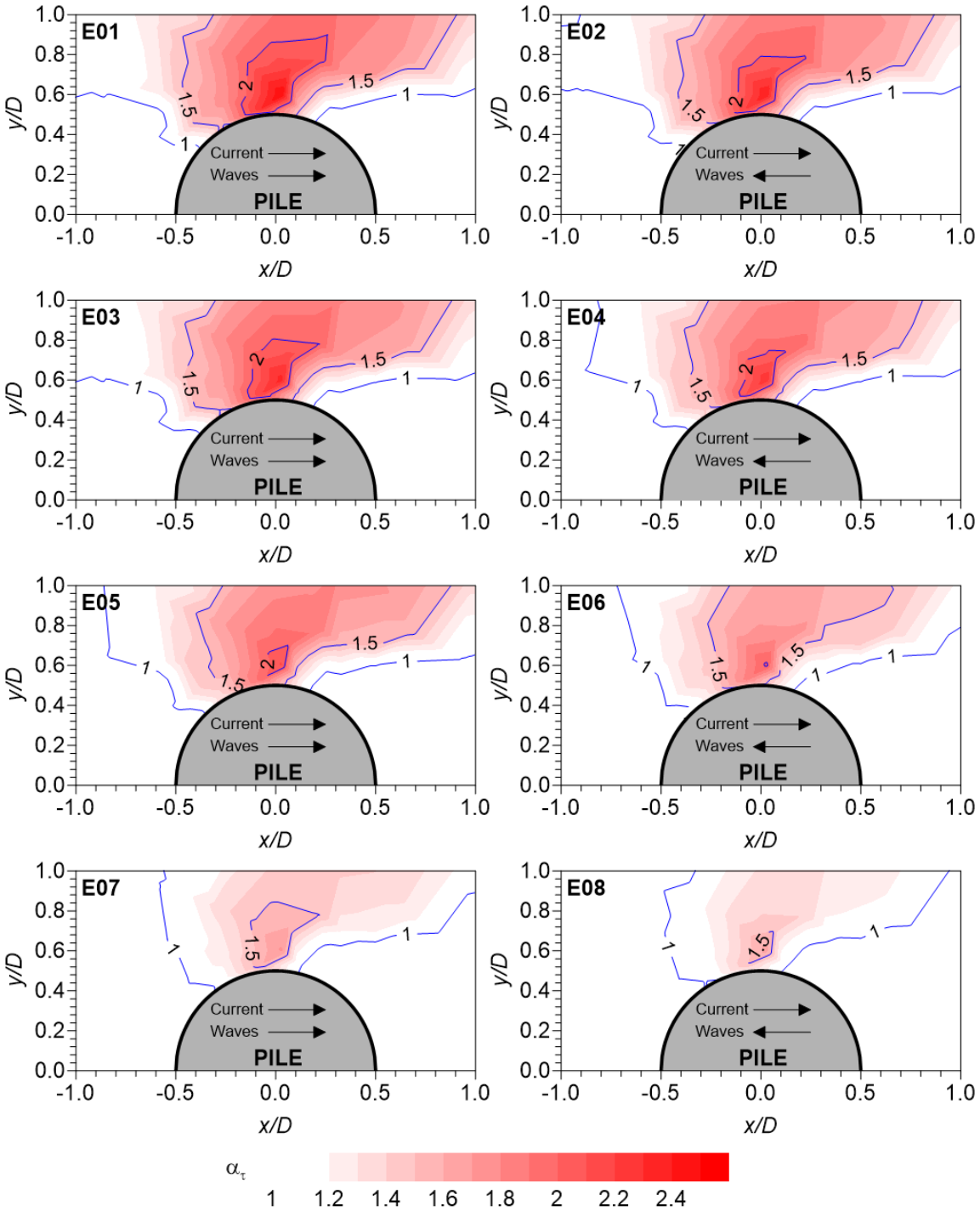

Figure 3.23: Bed shear stress made dimensionless with undisturbed bed shear stress amplification for each simulated case.

Scour around a Cylindrycal Pile

This section presents the analysis results of the scour around the pile. Figure 3.24 presents the dimensionless scour time series ($\frac{S}{D}$) obtained experimentally by Qi and Gao (2014b) and the series resulting from the numerical model, for codirectional (E01) and opposite (E04) waves and currents.

The information for the codirectional flow (E01) illustrated in Figure 3.24 shows a strong agreement between the experimental and simulated data, in its temporal evolution (curve form) and in the magnitude reached by the dimensionless scour. For example, after 10 minutes of simulation the model reached a magnitude of $\frac{S}{D} = 0.173$, and the experimental data reached a magnitude of $\frac{S}{D} = 0.169$ (2.4% of the relative error).

The comparison of numerical data versus experimental data for the dimensionless scour with and opposite flow (E04) illustrated in Figure 3.24 (as the previously described for E01) showed a strong correspondence in both its the temporal evolution and the magnitude reached. For example, within 20 minutes, the experimental data shows the dimensionless scour would be 0.146, while the numerical model showed that the scour would be 0.139 (4.8% of the relative error).

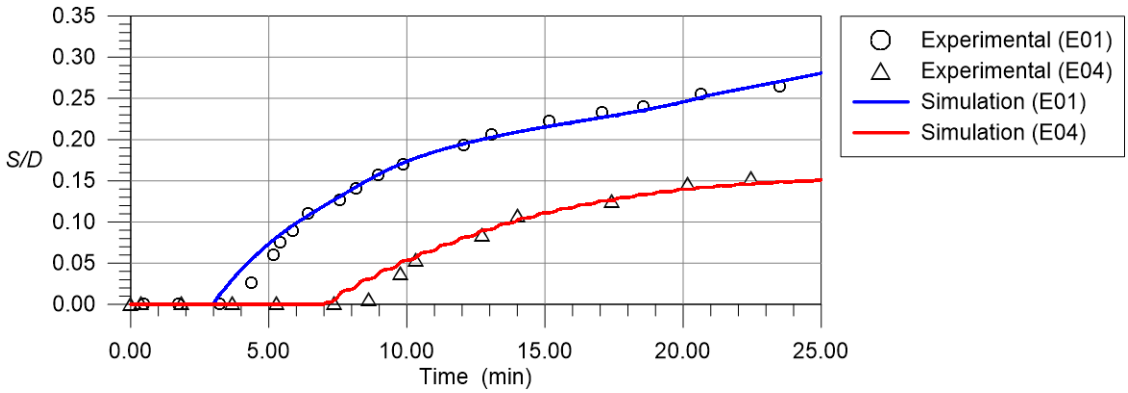

Figure 3.24: Maximum scour development comparison between the experimental data (Qi and Gao, 2014b) and numerical simulation results for cases E01 and E04.

The generality of the results obtained and presented in Figure 3.24 indicates that the scour would be greater when the flow acts codirectional to the waves and currents than in the opposite case. The latter is supported by the results summarized in Table 3.12 column $\frac{S_1}{D}$, which is the dimensionless scour obtained in the last time step of the numerical model. Additionally, Table 6 lists results for the adjustment coefficients of the equilibrium scour equation from Sheppard et al. (2004) (a_1 to a_4), the equilibrium dimensionless scour ($\frac{S_t}{D}$), and the relative scour factor ($\frac{S_t}{S_1}$). A similar method was used by Qi and Gao (2014b) but with experimental data.

The relative scour factors indicated in Table 3.12 were greater in cases where the flow velocity defined at a distance of $z = \frac{D}{2}$ (U_c) was greater. This mean that the scour obtained from the numerical model of a 25 minutes sediment transport and resulting morphodynamics evolution of the bed, is very different from the equilibrium in cases whit greater flow magnitude.

The latter may be associated with major currents acting on the center, producing major scours and subsequently requiring greater action times in order to reach scour equilibrium (Melville and Chiew, 1999). Nonetheless, when magnitudes of the dimensionless equilibrium scour estimated by the equation developed by Sheppard et al. (2004) and based on the data

obtained here for the 25 minutes simulation are compared with the experimental data obtained by third parties, equivalent results and estimates within an acceptable range of experimental variability are obtained, as shown in Figure 3.25.

Table 3.12: Adjustment parameter for equilibrium scour estimate and the results obtained from the numerical simulation.

Case	a_1	a_2	a_3	a_4	$\frac{S_1}{D}$	$\frac{S_t}{D}$	$\frac{S_t}{S_1}$
E01	0.095	0.408	0.423	0.029	0.251	0.518	2.064
E02	0.330	0.078	0.006	1.078	0.161	0.336	2.083
E03	0.330	0.091	0.100	0.091	0.304	0.430	1.414
E04	7.663	0.230	-7.365	0.234	0.151	0.298	1.976
E05	2.553	0.068	-1.878	0.070	0.132	0.675	5.120
E06	0.755	0.002	0.149	0.089	0.110	0.626	5.711
E07	0.020	0.058	0.083	0.070	0.085	0.103	1.213
E08	0.081	0.067	-0.006	0.416	0.060	0.075	1.242

Figure 3.25 presents a comparison between the numerical data obtained in this article (blue circles for codirectional scenarios and red circles for opposite flows), and experimental ones found in the literature (Raaijmakers and Rudolph, 2008; Sumer and Fredsøe, 2001; Qi and Gao, 2014b; Sumer et al., 2012; Mostafa and Agamy, 2011). This graph was formed similarly to that presented by Sumer and Fredsøe (2001), i.e., the dimensionless equilibrium scour as a function of the Keulegan–Carpenter (KC) number for different relative velocity ranges between waves and currents (U_{cw}).

From the general analysis of Figure 3.25, it is observed that, for the range $0.10 < U_{cw} < 0.40$, the data obtained from the numerical model implemented in this article would be close to the data obtained by Raaijmakers and Rudolph (2008) and Sumer et al. (2012) for similar Keulegan–Carpenter numbers (around five) for both the codirectional flow condition and the opposite. This situation repeats in the comparison between ranges $0.40 < U_{cw} < 0.50$ and $0.50 < U_{cw} < 0.80$, meaning that the data obtained from the results projection of the numerical model toward the equilibrium scour based on the equation of Sheppard et al. [54] allows us to gather magnitudes that can be compared with the experimental records obtained by other researchers, for similar hydrodynamic characteristics.

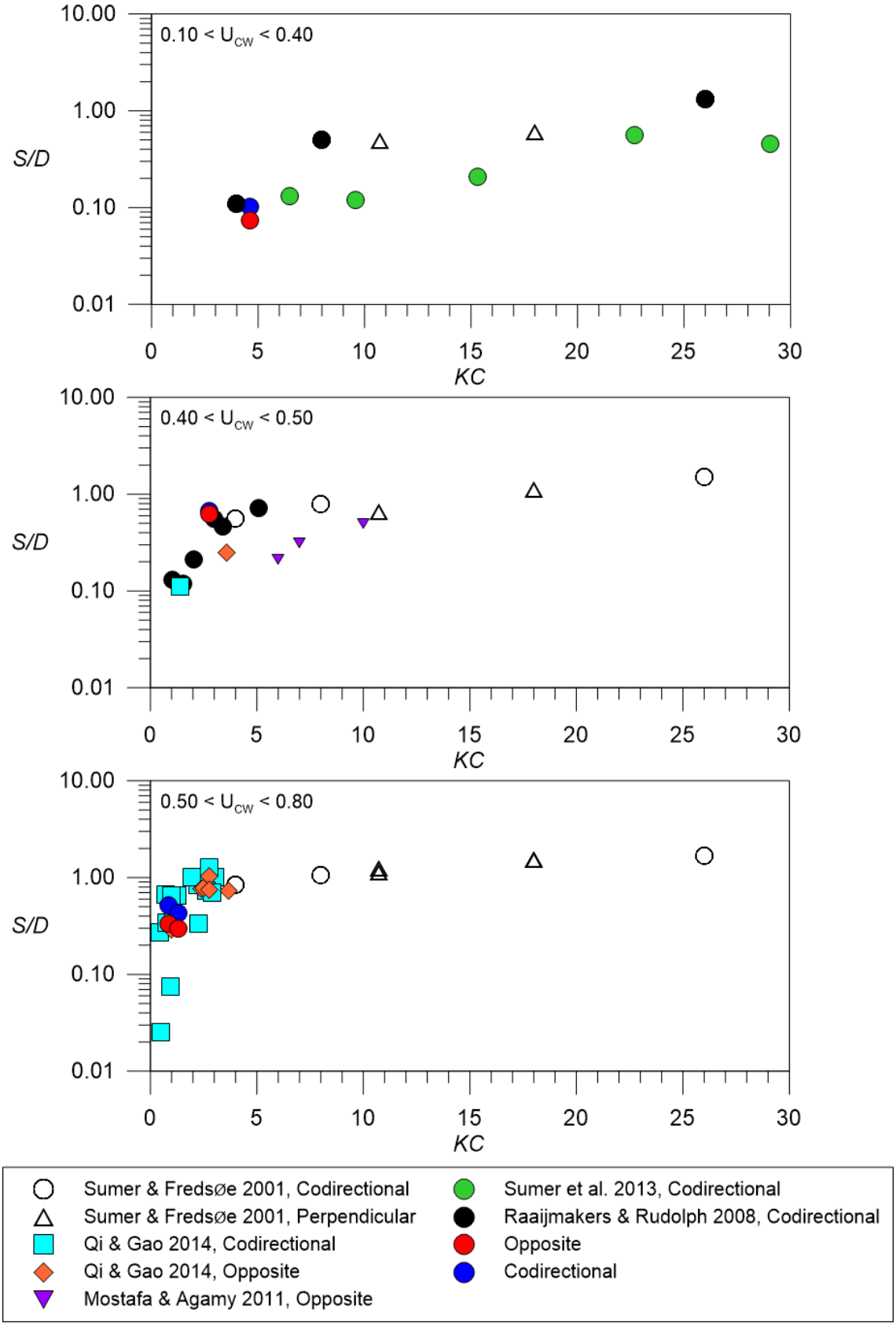

Figure 3.25: The equilibrium scour estimated from numerical data and its comparison with the equilibrium scour obtained by other authors.

3.5.5 Discussion

The experimental data with no scour provided by Umeyama (2010) have been used to compare the numerical results of other authors, such as Zhang et al. (2014) and Ahmad et al. (2019) who used the RANS approach to solve the hydrodynamics of waves and currents acting codirectionally over a grid featuring finite differences with a regular element ($\Delta x = \Delta y = \Delta z$), which correspond to the methodology applied in this investigation.

For the construction of the numerical domain, Zhang et al. (2014) utilized $\Delta x = 0.002$ m to solve the vertical domain in 150 layers, while the configuration applied by the authors of this study considered $\Delta x = 0.01$ m which determines the 30 layers in the vertical direction for the water flow adopted by Umeyama (2010). Despite of the coarser grid used in this research, the results are consistent with the experimental data for the vertical profile of velocities as well as for the instantaneous surface elevation of the water.

In order to model the scour around cylindrical piles, this study used the same element dimension as Ahmad et al. (2019), who proved that the use of an element of 0.01 m is sufficient to estimate the scour under a pipeline (Ahmad et al., 2019). This conclusion was reached by a grid analysis and time convergence study which analyzed the numerical behavior of REEF3D for element sizes of $\Delta x = 0.04$, 0.03, 0.02, 0.01 and 0.005 m.

The results obtained from the eight simulations (scenarios E01 to E08), showed a low variability of the mean velocity profile around the pile (stations P1 to P8), as illustrated in Figure 3.22, although these simulations were constructed to represent both, mixed and current or waves dominated environments, according to the criteria of Sumer and Fredsøe (2001). The results associated with the expected bed shear stresses for each of the eight scenarios (see Table 3.11), show that the effect of the waves on the first six scenarios (E01 to E06) is not significant in the bed dynamics, since the dimensionless shear stress due to waves (τ_w^*) is an order of magnitude less than the dimensionless shear stress due to currents (τ_c^*).

Based on the above, if it is considered that the shear stress is the hydraulic boundary condition to build at vertical profile of flow velocities, and the effect of the current dominates over the waves, it is expected that the first six scenarios present a high similarity for both a co-directional and opposed flow. On the other hand, in the remaining scenarios (E07 and E08), where the dimensionless shear stresses associated to waves and currents are of the same order of magnitude, greater effects on the velocity profile around the pile could be noticed (Figure 3.22), which would indicate that both the co-directional and opposed flow develop differences in the velocity mean behavior.

This difference between the shear stresses and the Sumer and Fredsøe (2001) criteria seems to imply that the use of the dimensionless number called the relative velocity of the current (U_{cw}), does not fully describe the domain of the forcing over the total hydrodynamics, a discussion that is presented in the following paragraphs of this investigation.

From the results obtained, it is possible to verify that the presence of waves in the hydrodynamic behavior for scenarios E01 to E06 was less significant than for scenarios E07 and E08. This can be clearly seen in the mean profile analysis, since when the current dominated, the direction resulting from the flow agreed with the streamwise direction, these results were previously described by Faraci et al. (2011), who, while performing wave and current test acting orthogonally and without the presence of a pile, obtained results comparable to those obtained in this investigation.

The vertical distribution of the mean velocity illustrated in Figure 3.22 is consistent with that described by Lim and Madsen (2016), who mentioned that although the flow field can be mixed (waves and currents acting together and orthogonally), the velocity distribution can

be simply modeled by a uniform return current. The foregoing analysis is also consistent with the results presented by Faraci et al. (2018).

The equation by Sheppard et al. (2004) was applied to estimate the equilibrium scour based on an extrapolation of the numerical model. These results were similar to those obtained experimentally by other authors, which indicates that the methodology applied as well as the configuration adopted by the numerical model are appropriate to describe the phenomenon under study, not only from the perspective of element size but also for the sediment transport equations applied.

An important aspect to highlight is that this investigation has used the relaxation factor previously applied by Quezada et al. (2018), which also allowed the authors to correctly represent the scour for unsteady current and oscillatory flow. According to the results obtained in the current study, this value will also allow us to estimate the scour for uniform and oscillatory flow, not only codirectionally but also opposite. The relaxation coefficient permits in an auxiliary manner effects inherent to the structure of the fluid interaction produced around the pile, thereby improving the estimations of sediment transport and the resulting scour.

Sumer and Fredsøe (2001) propose the relative velocity of the current (U_{cw}) as a dimensionless number relevant for the description of the scour due to codirectional or perpendicular waves and currents. This is defined in Equation 3.5.1, where the current magnitude (U_C) is estimated at a height of $\frac{D}{2}$ from the bed, while the velocity of the wave is considered as the maximum value of the undisturbed orbital velocity at the bottom, just above the wave boundary layer (U_m). By this dimensionless definition, Sumer and Fredsøe (2001) established that values of U_{cw} higher than 0.7 indicate that the current dominates in the center, while waves have a significant effect when U_{cw} is close to zero (cases waves alone) and less than 0.4.

This dimensionless number considers that U_C and U_m are added, independently of the direction of incidence of the currents and waves. In this respect, Sumer and Fredsøe (2001) consider a single value of U_{cw} for codirectional and perpendicular flow, if U_C and U_m are the same in magnitude but different in direction.

The above, according the authors of this paper, would not be appropriate as a general indicator of wave and current interaction, nor would their effects on the scour for cases in which the forcings are not codirectional, since when both flows face in the opposite direction, the wave would propagate with greater difficulty and modify the net velocity of the channel, such that the current present in the center would correspond to the residual value of both forcings.

Soulsby (1997) and Van Rijn (1993b) indicates that current wave interactions must be treated in terms of the net current produced between the two forcing agents, which corresponds to an algebraic sum that is usually treated according to Equation 3.5.34, where ϖ is the angular frequency, U_B is the bulk velocity of the flow due to the current, K is the wave number, ϑ' is the angle between current and wave direction ($\vartheta' = 0$ for codirectional, and $\vartheta' = 180°$ for opposing), g is the gravity and h is the water depth:

$$\varpi - U_B \; K \cos\left(\vartheta'\right) = \sqrt{gK \tanh\left(Kh\right)} \tag{3.5.34}$$

The left term of Equation 3.5.34 correspond to the net velocity (defined according the relative velocity between the current and waves). Meanwhile, the right term corresponds to the dispersion relationship of the waves.

From Equation 3.5.34 it can be seen that in cases of co-directional or opposite waves, the $\cos(\vartheta')$ changes its sign and therefore, the system net velocity is the sum or subtraction of both forcings. Therefore, defining a dimensionless number that summarizes the wave and

current interaction, must include a differentiation when the action is codirectional or when it is counter current.

An approximation to the description of scour due to opposite and codirectional currents and waves was conducted by Qi and Gao (2014a) who, using experimental data, obtained by the same authors in previous works (Qi and Gao, 2014b) and by third parties as well (Sumer and Fredsøe, 2001; Sumer et al., 2013), propose the use of the Froude number (F_{ra}) defined in Equation 3.5.35), as a function of absolute velocity (U_a, defined by Equation 3.5.36) and the pile diameter.

$$F_{ra} = \frac{U_a}{\sqrt{gD}} \tag{3.5.35}$$

$$U_a = U_c + \frac{2}{\pi} U_m \tag{3.5.36}$$

From this analysis Qi and Gao (2014a) proposed a formula fitted to the experimental data for a dimensionless scour ($\frac{S}{D}$) which is presented in Equation 3.5.37 and is valid for the range $0.1 < F_{ra} < 1.1$ and $0.4 < KC < 2.6$.

$$\log\left(\frac{S}{D}\right) = -0.8 \ \exp\left(\frac{0.14}{F_{ra}}\right) + 1.11 \tag{3.5.37}$$

A comparison of the numerical results gathered in this paper, the experimental data and the equation proposed by Qi and Gao (2014a) are shown in Figure 3.26.

In Figure 3.26, it is observed that the information available in the literature (experimental) and that generated in this study (numerical) are adequately concordant with the equation proposed by Qi and Gao (2014a), and such a description may be enough to collect information on the equilibrium scour around a dimensionless number that represents its behavior.

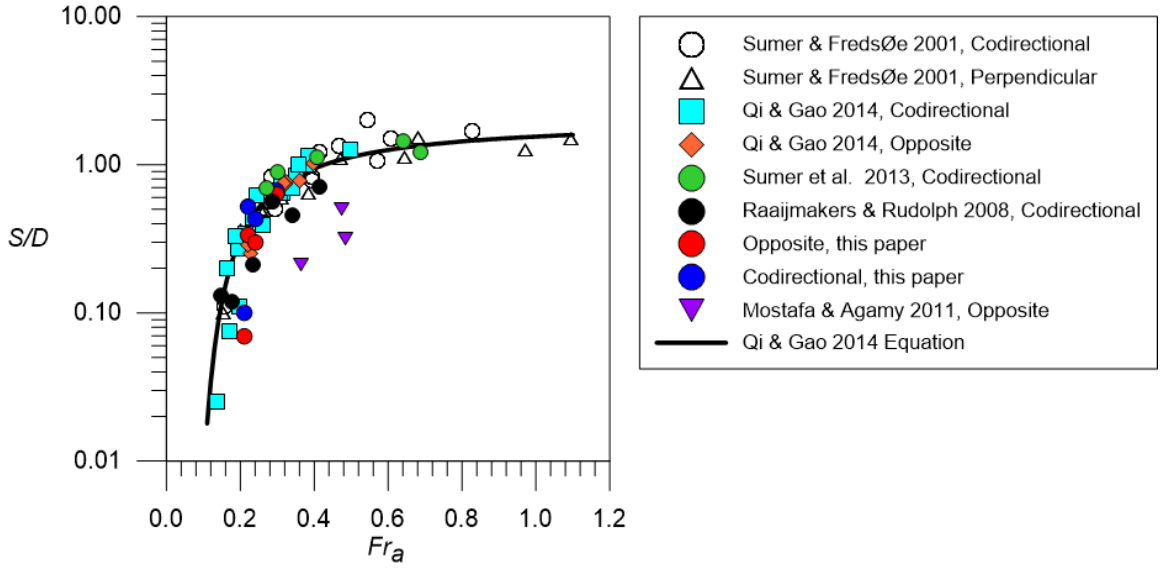

Figure 3.26: Equilibrium scour distribution according to absolute Froude number proposed by Qi and Gao (2014a).

Notwithstanding the above, Qi and Gao (2014a), as well as Sumer and Fredsøe [26], consider current and wave actions added equally if they act in a codirectional or opposite manner,

which, in general, is not consistent with a residual flow estimation that would be generated by the interaction. The foregoing disagrees with the results by SSoulsby (1997) and Van Rijn (1993b), who indicate that the sum of the forcing agents must be algebraic, respecting the angle between current and wave direction. Although the arguments are contradictory, both proposals (Qi and Gao, 2014a; Sumer and Fredsøe, 2001) compile reasonably well the scour information regardless of the direction. This should be analyzed in greater detail as proposed below.

Thus, the Froude number may be rewritten according to Equation 3.5.39 if the absolute velocity defined by Qi and Gao (2014a) is considered, albeit modified according to Equation 3.5.38, which is a proposal of the authors of this paper, and where C_φ is a coefficient to describe the flow direction, and where $C_\varphi = 1$ describes codirectional flows and C_φ = -1 describe opposite flows.

$$U'_a = U_c + \frac{2}{\pi} U_m \, C_\varphi \tag{3.5.38}$$

$$F'_{ra} = \frac{U'_a}{\sqrt{gD}} \tag{3.5.39}$$

C_φ was included in order to incorporate the recommendations of Soulsby (1997) and Van Rijn (1993b), in order to consider the effects of waves and currents directionality acting together on the pile.

Considering this proposal and collecting scour data (experimental and numerical from this paper), Figure 3.27 is obtained. The blue circles indicate codirectional cases and red circles indicate opposite flow cases. Two trends are found in two areas of the figure. The first trend corresponds to codirectional data, which are still represented by the equation proposed by Qi and Gao (2014a). Nevertheless, the opposite flow cases are to the left of the codirectional data and apparently adjust to an equation different than that proposed by Qi and Gao (2014a), which, according to the available data set (experimental and numerical data from this paper) correspond to Equation 3.5.39).

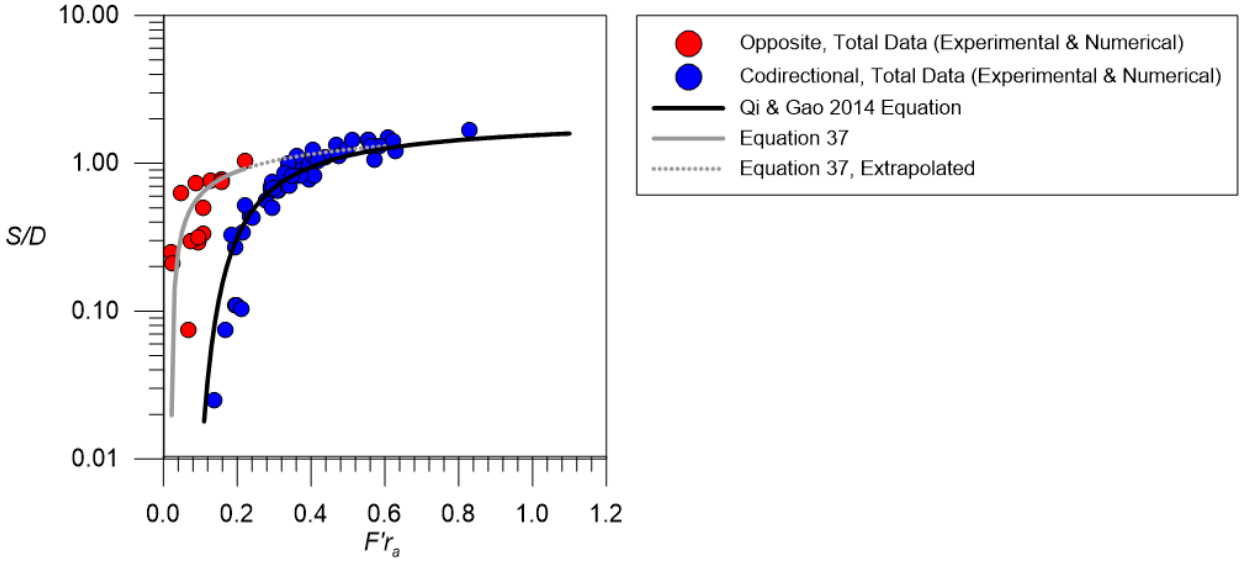

Figure 3.27: Equilibrium scour distribution according to the absolute Froude number (F'_{ra}) proposed in this research.

$$\frac{S}{D} = 0.39\ ln\left(F'_{ra}\right) + 1.51 \tag{3.5.40}$$

Equation 3.5.40 seems to agree with the solution proposed by Qi and Gao (2014a) for high values of the Froude number. However, such behavior may be verified by adding new experimental and/or numerical antecedents, which enable us to complement equilibrium scour data in a combined domain of currents and waves acting in opposite directions.

3.5.6 Conclusions

A comparison of the results obtained numerically in this research with experimental data from other authors, show that CFD REEF3D adequately models a hydrodynamic field in a combined domain of waves and currents, correctly depicting both the instantaneous water surface and velocities developed by the flow of a freestream and also the flow in the presence of a pile.

The average hydrodynamics determined for each of the simulated scenarios showed that in 6 (E01 to E06) out of 8 cases, currents were the main flow mechanism over the waves, despite the relative velocity of current (U_{cw}) proposed by Sumer and Fredsøe (2001), which indicate a combined flow regime. This was clearly reflected in the velocity profiles traced in points P1 to P8, where it could be verified that codirectional and opposite flow cases converge to the same vertical distributions of velocity.

The equilibrium scour estimated by the projection of the numerical data with the equation by Sheppard et al. (2004), enabled us to estimate values close to those described in the literature and to use the numerical model effectively to solve a time scale lower than the equilibrium. From this projection, it was verified that the dimensionless scour would be less when waves and currents come from opposite directions.

The U_{cw} parameter is an indicator that adequately measures the interactions between of currents and waves under the condition of codirectional flow. However, it is recommended to modify this parameter for currents and waves from opposite directions, since it does not properly account for the interaction of both forcings. For such purposes, it is recommended to use the modified Froude number (F'_{ra}) proposed in this paper.

Chapter 4

Conclusions

4.1 General conclusions

The sediment transport study in regions of the flow obstructed by a pile was conducted through both numerical modeling and experimental work, drawing several conclusions which are described below.

Chronologically, a numerical model was developed first and presented in Quezada et al. (2018). This enabled to identify the need to incorporate a relaxation coefficient in the numerical model in order to properly estimate scour from experimental data. This relaxation coefficient consisted of a virtual reduction in the critical shear stress of sediments, that is, increasing the mobility in the condition of the currents that act on the grains of the bed.

According to the results presented by Quezada et al. (2018), with the relaxation coefficient applied to the critical shear stress of the sediments, the scour may be properly represented in the steady flow, unsteady flow and oscillatory flow. Additionally, in Quezada et al. (2019), considering the same relaxation coefficient, it was shown that scour in circular piles due to waves and currents that acts combining both the codirectional and opposite direction, was also adequately represented by the numerical model.

The latter leads to the conclusion that the use of the relaxation coefficient improves the representation of sediment transport around the areas of flow obstruction, and consequently, the scour estimation. This is valid when the Reynolds Averaged Navier Stokes Equations are used to determine the hydrodynamics, regardless the flow type to be solved.

According to our results, this need could be due to the inability of the RANS equation to determine the turbulent fluctuations of the velocity (since it only solve the turbulence in averaged terms), because according to the experimental work conducted in this investigation, the turbulent structures of the flow, are responsible for the incipient motion of the sediment in front of a circular pile.

Experimental work showed that the main turbulent structures of the flow in front of a circular pile are: down-flow (as the main mode), the horseshoe vortex (as the second mode) and the secondary vortices system (as the third mode), being the first two responsible for the incipient transport, and even when RANS are able to represent them in average terms (Roulund et al., 2005; Baykal et al., 2015), turbulent fluctuations in time are those who start sediment movement. Some research works attempt to incorporate this turbulent structures into RANS (Cheng et al., 2018).

Based on the results that have been presented throughout the thesis, the relaxation coefficient and the ability to simplify the process of scour around circular piles, allows the use of RANS in engineering problems, without the need to simulate in detail the hydrodynamics of

small vortices and thus employ computational resources more efficiently.

Although numerical and experimental evidence developed in this investigation, links turbulent coherent structures with incipient transport of sediments upstream the pile, it is necessary to develop complementary experimental work in order to obtain an equation for the incipient motion and bed load, which it allows to describe the physics of the problem and not only simulate it through a relaxation coefficient. The latter corresponds to new lines of investigation in the understanding of the scour process around circular piles.

4.2 About the coherent turbulent structures and incipient motion

Using velocity fields registered with the PIV technique, average behavior of the velocity profiles, the turbulent flow structures and the characteristics of the incipient transport in the vicinity of the pile were analyzed.

The average velocity profiles determined from the experimental data indicated that, when the incipient transport is reached, the average magnitude of the velocity near the bottom is not equal to zero. This situation is due to the intensification of turbulent fluctuations and would be responsible for moving the sediments in front of the pile.

Through the analysis of Proper Orthogonal Decomposition, it was possible to characterize the behavior of the turbulent structures in front of the pile and classify them into the different types of flows and vorticities that occur. The hydrodynamic mechanism with the higher energy corresponds to the down-flow and the incoming boundary layer (Φ_1), followed by the primary horseshoe vortex (Φ_2) and the secondary vorticity system (Φ_3).

Analysis of the incipient sediment transport showed that the temporal evolution of the turbulent structure associated with mode 1 (Φ_1) and mode 2 (Φ_2), corresponding to the down-flow/incoming boundary layer and the primary horseshoe vortex, respectively, match significantly with the events of sediment motions registered for the I01, I02 and I03 tests, as evidenced by the high values of the cross-corelation of $C_1 + C_2$ with the incipient motion events.

Quadrant analysis of turbulent fluctuations showed that ejection, sweeps and outward interaction mechanisms account for 80% of the fraction of events in which incipient transport occurs. The results were consistent with the analysis of the turbulent modes in the incipient transport, so that it can be concluded that both the down-flow/incoming boundary layer and the primary horseshoe vortex, are the hydrodynamic mechanisms responsible for incipient motion in front of the pile.

4.3 About the numerical simulation of scour due to unsteady and oscillatory flow

The relaxation coefficient of sediment critical shear stress proposed by Bihs (2011) becomes essential for the REEF3D numerical model and its selection must be made by the comparison with experimental data, in order to adequately represent the bed response in the surroundings of flow obstructions. The relaxation coefficient was 0.8, for steady, unsteady and oscillatory flow and sjould be applied in a sub-area contained in the vicinity of the pile and whose width was equal to the channel width, while in the axial axis the distance was twice the diameter of the pile, in both directions, upstream and downstream.

The REEF3D model calibration process of the was performed with comparison of numerical results from other authors (Baykal et al., 2015) and laboratory data (Link, 2006), both under steady flow.

When the relaxation coefficient was applied to unsteady flow and oscillatory flow, the numerical modeled results were correctly adjusted to the experimental data. In particular, concerning the obtained results for unsteady flow, the numerical model with the configuration adopted was able to represent the morphodynamic behavior of the scour relative to its maximum value, being concordant, both in the temporal development and the prolonged action effects of the maximum discharge of the hydrograph.

The temporal behavior of the pile scour obtained from the numerical simulation was well represented in general terms, being able to reproduce the expected behavior as described described by several authors according to the available literature (Oliveto and Hager, 2002; Chang et al., 2004; Gjunsburgs et al., 2010; Borghei et al., 2012; Link et al., 2017). The numerical scour may overestimate (test A, C and E) or underestimate (test B and D) the experimental data, however the differences are small.

In the oscillatory flow case, the results obtained were well ajusted to the experimental data published by Sumer et al. (1992) and Sumer and Fredsøe (2001), which represent the same phenomenon and allow them to adjust well the numerical data to the predictive equations available in the literature.

When the numerical results for the dimensionless pile scour due to oscillatory flow are compiled according to the Keulegan-Carpenter number, they are adjusted in the same way as Sumer et al. (1992). This is an indicator that the numerical model could forecast the pile scour in concordance with the experimental data.

The utilization of Meyer-Peter and Müller (1948) formula, allowed the representation of the sediment transport associated with both the unsteady and oscillatory flow, despite that its semi-empirical foundation is based in cases of unidimensional steady flow.

According to the results obtained and the studies cited, we consider it necessary to continue with the study of incipient transport of sediments near piles or other flow obstructions, to define its value or incorporate the obstruction turbulence effects on the sediment motion estimation.

4.4 About the numerical simulation of scour due to waves and currents

A comparison of the results obtained numerically in this research with experimental data from other authors show that CFD REEF3D adequately models a hydrodynamic field in a combined domain of waves and currents, correctly representing both the instantaneous water surface and velocities developed by the flow of a freestream and also the flow in the presence of a pile.

The average hydrodynamics determined for each of the simulated scenarios showed that in 6 (E01 to E06) out of 8 cases, currents instead of waves were the main flow mechanism, despite the relative velocity of current (U_{cw}) proposed by Sumer and Fredsøe (2001), indicates a combined flow regime. This was clearly reflected in the velocity profiles traced around the pile, where was possible to verify that cases of codirectional and opposite flow converge to the same vertical velocity distributions.

The equilibrium scour estimated by the projection of the numerical data with the equation by Sheppard et al. (2004), enabled us to estimate values close to those described in the literature and use the numerical model effectively to solve a smaller time scale than equilibrium.

From this projection, it was verified that the dimensionless scour would be less when the waves and currents come from opposite directions.

The U_{cw} parameter is an indicator that adequately measures the interactions between currents and waves under the condition of co-directional flow. However, it is recommended to modify this parameter for currents and waves from opposite directions, since it does not properly account for the interaction of both forcings. For such purposes, it is recommended to use the modified Froude number (F'_{ra}) proposed in this document.

Bibliography

Afzal, M. S. (2013). 3d Numerical modelling of sediment transport under current and waves. Master's thesis, NorwegianUniversity of Science and Technology, Trondheim, Norway.

Afzal, M. S., Bihs, H., Kamath, A., and Arntsen, Ø. A. (2015). Three-dimensional numerical modeling of pier scour under current and waves using level-set method. *Journal of Offshore Mechanics and Arctic Engineering*, 137(3):032001.

Aghaee, Y. and Hakimzadeh, H. (2010). Three dimensional numerical modeling of flow around bridge piers using les and rans. *River Flow, Dittrich, Koll, Aberle & Geisenhainer (eds)*, pages 211–218.

Ahmad, N., Bihs, H., Kamath, A., and Arntsen, Ø. A. (2015). Three-dimensional cfd modeling of wave scour around side-by-side and triangular arrangement of piles with REEF3D. *Procedia Engineering*, 116:683–690.

Ahmad, N., Bihs, H., Myrhaug, D., Kamath, A., and Arntsen, i. A. (2019). Numerical modelling of pipeline scour under the combined action of waves and current with free-surface capturing. *Coastal Engineering*, 148:19–35.

Ahmed, F. and Rajaratnam, N. (1998). Flow around bridge piers. *Journal of Hydraulic Engineering*, 124(3):288–300.

Airy, G. B. (1841). Tides and waves. *Encyc. Metrop.*, 192:241–396.

Ali, K. H. and Karim, O. (2002). Simulation of flow around piers. *Journal of Hydraulic Research*, 40(2):161–174.

Altomare, C., Crespo, A. J., Domínguez, J. M., Gómez-Gesteira, M., Suzuki, T., and Verwaest, T. (2015). Applicability of smoothed particle hydrodynamics for estimation of sea wave impact on coastal structures. *Coastal Engineering*, 96:1–12.

Apsilidis, N., Diplas, P., Dancey, C. L., and Bouratsis, P. (2015). Time-resolved flow dynamics and reynolds number effects at a wall–cylinder junction. *Journal of Fluid Mechanics*, 776:475–511.

Apsilidis, N., Diplas, P., Dancey, C. L., and Bouratsis, P. (2016). Effects of wall roughness on turbulent junction flow characteristics. *Experiments in Fluids*, 57(1):12.

Ataie-Ashtiani, B. and Aslani-Kordkandi, A. (2013). Flow field around single and tandem piers. *Flow, turbulence and combustion*, 90(3):471–490.

Bagnold, R. A. and Taylor, G. (1946). Motion of waves in shallow water. interaction between waves and sand bottoms. In *Proceedings of the Royal Society of London A: Mathematical, Physical and Engineering Sciences*, volume 187, pages 1–18. The Royal Society.

Baker, C. (1979). The laminar horseshoe vortex. *Journal of fluid mechanics*, 95(02):347–367.

Baker, C. (1980). The turbulent horseshoe vortex. *Journal of Wind Engineering and Industrial Aerodynamics*, 6(1-2):9–23.

Baldwin, B. S. and Barth, T. J. (1990). *A one-equation turbulence transport model for high Reynolds number wall-bounded flows*. National Aeronautics and Space Administration, Ames Research Center.

Baranya, S., Olsen, N., Stoesser, T., and Sturm, T. (2012). Three-dimensional rans modeling of flow around circular piers using nested grids. *Engineering Applications of Computational Fluid Mechanics*, 6(4):648–662.

Bardina, J., Ferziger, J. H., and Reynolds, W. (1980). Improved subgrid-scale models for large-eddy simulation. In *American Institute of Aeronautics and Astronautics, Fluid and Plasma Dynamics Conference, 13th, Snowmass, Colo., July 14-16, 1980, 10 p.*, volume 1.

Bassi, F. and Rebay, S. (1997). A high-order accurate discontinuous finite element method for the numerical solution of the compressible navier–stokes equations. *Journal of computational physics*, 131(2):267–279.

Batchelor, G. (1997). *An introduction to fluid dynamics*. Cambridge University Press.

Baykal, C., Sumer, B. M., Fuhrman, D. R., Jacobsen, N. G., and Fredsøe, J. (2015). Numerical investigation of flow and scour around a vertical circular cylinder. *Philosophical Transactions of the Royal Society of London A: Mathematical, Physical and Engineering Sciences*, 373(2033):20140104.

Baykal, C., Sumer, B. M., Fuhrman, D. R., Jacobsen, N. G., and Fredsøe, J. (2017). Numerical simulation of scour and backfilling processes around a circular pile in waves. *Coastal Engineering*, 122:87–107.

Beheshti, A. and Ataie-Ashtiani, B. (2008). Analysis of threshold and incipient conditions for sediment movement. *Coastal Engineering*, 55(5):423–430.

Berger, M. and Aftosmis, M. (1998). Aspects (and aspect ratios) of cartesian mesh methods. In *Sixteenth International Conference on Numerical Methods in Fluid Dynamics*, pages 1–12. Springer.

Berthelsen, P. A. (2004). A decomposed immersed interface method for variable coefficient elliptic equations with non-smooth and discontinuous solutions. *Journal of Computational Physics*, 197(1):364–386.

Berthelsen, P. A. and Faltinsen, O. M. (2008). A local directional ghost cell approach for incompressible viscous flow problems with irregular boundaries. *Journal of computational physics*, 227(9):4354–4397.

Bihs, H. (2011). *Three-dimensional numerical modeling of local scouring in open channel flow*. PhD Thesis, Norwegian University of Science and Technology, Trondheim, Norway.

Bihs, H., Chella, M. A., Kamath, A., and Arntsen, Ø. A. (2017). Numerical investigation of focused waves and their interaction with a vertical cylinder using reef3d. *Journal of Offshore Mechanics and Arctic Engineering*, 139(4):041101.

Bihs, H., Kamath, A., Chella, M. A., Aggarwal, A., and Arntsen, Ø. A. (2016). A new level set numerical wave tank with improved density interpolation for complex wave hydrodynamics. *Computers & Fluids*, 140:191–208.

Bonnefille, R. (1963). Essais de synthèse des lois de début d'entraînement des sédiments sous l'action d'un courant en régime continu. *Bull. du Centre de Rech. et d'ess. de Chatou*, 5:17–22.

Borghei, S. M., Kabiri-Samani, A., and Banihashem, S. A. (2012). Influence of unsteady flow hydrograph shape on local scouring around bridge pier. In *Proceedings of the Institution of Civil Engineers-Water Management*, volume 165, pages 473–480. Thomas Telford Ltd.

Bourgoin, M., Qureshi, N. M., Baudet, C., Cartellier, A., and Gagne, C. (2011). Turbulent transport of finite sized material particles. In *Journal of Physics: Conference Series*, volume 318, page 012005. IOP Publishing.

Brahms, A. (1757). *Anfangsgründe der Deich-und Wasserbaukunst*, volume 1.

Breusers, H., Nicollet, G., and Shen, H. (1977). Local scour around cylindrical piers. *Journal of Hydraulic Research*, 15(3):211–252.

Brevis, W., García-Villalba, M., and Niño, Y. (2014). Experimental and large eddy simulation study of the flow developed by a sequence of lateral obstacles. *Environmental Fluid Mechanics*, 14(4):873–893.

Brørs, B. (1999). Numerical modeling of flow and scour at pipelines. *Journal of hydraulic Engineering*, 125(5):511–523.

Brown, D. L., Cortez, R., and Minion, M. L. (2001). Accurate projection methods for the incompressible navier–stokes equations. *Journal of computational physics*, 168(2):464–499.

Burkow, M. (2010). Numerische simulation stromungsbedingten sedimenttransports und der entstehenden gerinnebettformen. Master's thesis, Mathematisch-Naturwissenschaftlichen Fakultat der Rheinischen Friedrich-Wilhelms-Universitat Bonn, Bonn, Germany.

Capote, J., Alvear, D., Abreu, O., Lázaro, M., and Espina, P. (2008). Influencia del modelo de turbulencia y del refinamiento de la discretización espacial en la exactitud de las simulaciones computacionales de incendios.

Castillo, C. and Link, O. (2015). Un modelo para análisis de la socavación alrededor de cepas circulares de puente durante crecidas fluviales. *Sociedad Chilena de Ingeniería Hidráulica, XXII Congreso Chileno de Ingeniería Hidráulica*.

Celik, A. O., Diplas, P., Dancey, C. L., and Valyrakis, M. (2010). Impulse and particle dislodgement under turbulent flow conditions. *Physics of Fluids*, 22(4):046601.

Chang, W., Constantinescu, G., Tsai, W., and Lien, H. (2011). Coherent structure dynamics and sediment erosion mechanisms around an in-stream rectangular cylinder at low and moderate angles of attack. *Water Resources Research*, 47(12).

Chang, W.-Y., Lai, J.-S., and Yen, C.-L. (2004). Evolution of scour depth at circular bridge piers. *Journal of Hydraulic Engineering*, 130(9):905–913.

Chau, K. and Jiang, Y. (2001). 3d numerical model for pearl river estuary. *Journal of Hydraulic Engineering*, 127(1):72–82.

Chau, K. and Jiang, Y. (2004). A three-dimensional pollutant transport model in orthogonal curvilinear and sigma coordinate system for pearl river estuary. *International Journal of Environment and Pollution*, 21(2):188–198.

Chen, H., Patel, V., and Ju, S. (1990). Solutions of reynolds-averaged Navier-Stokes equations for three-dimensional incompressible flows. *Journal of Computational Physics*, 88(2):305–336.

Chen, Q., Qi, M., Zhong, Q., and Li, D. (2017). Experimental study on the multimodal dynamics of the turbulent horseshoe vortex system around a circular cylinder. *Physics of Fluids*, 29(1):015106.

Chen, Q., Yang, Z., and Wu, H. (2019). Evolution of turbulent horseshoe vortex system in front of a vertical circular cylinder in open channel. *Water*, 11(10):2079.

Cheng, Z., Koken, M., and Constantinescu, G. (2018). Approximate methodology to account for effects of coherent structures on sediment entrainment in rans simulations with a movable bed and applications to pier scour. *Advances in Water Resources*, 120:65–82.

Chiew, Y. M. and Melville, B. W. (1987). Local scour around bridge piers. *Journal of Hydraulic Research*, 25(1):15–26.

Chorin, A. J. (1968). Numerical solution of the Navier-Stokes equations. *Mathematics of computation*, 22(104):745–762.

Clarke, D. K., Hassan, H., and Salas, M. (1986). Euler calculations for multielement airfoils using cartesian grids. *AIAA journal*, 24(3):353–358.

da Vinci, L. (1958). *Del Moto e Misura Dell'Aqua (English translation)*. Nabu Press, Charleston SC, United States.

Dalrymple, R. and Rogers, B. (2006). Numerical modeling of water waves with the sph method. *Coastal engineering*, 53(2):141–147.

Dargahi, B. (1987). Flow field and local scouring around a cylinder. *Bulletin No 137, Royal Institute of Technology, Hydraulic Laboratory, Kungliga Tekniska Hogskolan, Sweden*.

Dargahi, B. (1989). The turbulent flow field around a circular cylinder. *Experiments in Fluids*, 8(1):1–12.

Dargahi, B. (1990). Controlling mechanism of local scouring. *Journal of Hydraulic Engineering*, 116(10):1197–1214.

Das, S., Das, R., and Mazumdar, A. (2013). Circulation characteristics of horseshoe vortex in scour region around circular piers. *Water Science and Engineering*, 6(1):59–77.

Davies, A. (1985). Field observations of the threshold of sediment motion by wave action. *Sedimentology*, 32(5):685–704.

Davies, D. R., Wilson, C. R., and Kramer, S. C. (2011). Fluidity: A fully unstructured anisotropic adaptive mesh computational modeling framework for geodynamics. *Geochemistry, Geophysics, Geosystems*, 12(6).

Dean, R. G. and Dalrymple, R. A. (1991). *Water wave mechanics for engineers and scientists*, volume 2. World Scientific Publishing Company.

Devenport, W. J. and Simpson, R. L. (1990). Time-depeiident and time-averaged turbulence structure near the nose of a wing-body junction. *Journal of Fluid Mechanics*, 210:23–55.

Dey, S. (2001). Experimental studies on incipient motion of sediment particles on generalized sloping fluvial beds. *Journal of Sediment Research*, 16(3):391–398.

Dey, S., Bose, S. K., and Sastry, G. L. (1995). Clear water scour at circular piers: a model. *Journal of Hydraulic Engineering*, 121(12):869–876.

Dey, S. and Papanicolaou, A. (2008). Sediment threshold under stream flow: A state-of-the-art review. *KSCE Journal of Civil Engineering*, 12(1):45–60.

Dey, S. and Raikar, R. V. (2007). Characteristics of horseshoe vortex in developing scour holes at piers. *Journal of Hydraulic Engineering*, 133(4):399–413.

DeZeeuw, D. and Powell, K. G. (1993). An adaptively refined cartesian mesh solver for the euler equations. *Journal of Computational Physics*, 104(1):56–68.

Diab, R., Link, O., and Zanke, U. (2010). Geometry of developing and equilibrium scour holes at bridge piers in gravel. *Canadian Journal of Civil Engineering*, 37(4):544–552.

Diplas, P., Dancey, C. L., Celik, A. O., Valyrakis, M., Greer, K., and Akar, T. (2008). The role of impulse on the initiation of particle movement under turbulent flow conditions. *Science*, 322(5902):717–720.

Doolan, C. (2010). Large eddy simulation of the near wake of a circular cylinder at sub-critical reynolds number. *Engineering Applications of Computational Fluid Mechanics*, 4(4):496–510.

Dou, G. (1974). Similarity theory and its application to the design of total sediment transport model. *Research Bulletin of Nanjing Hydraulic Research Institute*.

Dou, X. S. and Jones, J. S. (2000). A new sediment transport formula for local scour prediction. *Joint Conference on Water Resources Engineering and Water Resources Planning and Management, Minneapolis*.

Du Buat, P. L. G. (1816). *Principes d'hydraulique et de pyrodynamique, verifies par un grand nombre d'experiences faites par ordre du gouvernement; ouvrage en trois volumes. Par M. Dubuat,... Tome premier [-troisieme]*, volume 1.

Durbin, P. (1995). Separated flow computations with the k-epsilon-v-squared model. *AIAA journal*, 33(4):659–664.

Durbin, P. A. and Reif, B. P. (2011). *Statistical theory and modeling for turbulent flows*. John Wiley & Sons.

Eadie, R. W. and Herbich, J. B. (1986). Scour About a Single, Cylindrical Pile Due to Combined Random Waves and a Current. *20th International Conference on Coastal Engineering*, pages 1858–1870.

Engelund, F. and Fredsøe, J. (1976). A sediment transport model for straight alluvial channels. *Nordic Hydrology*, 7(5):293–306.

Enright, D., Fedkiw, R., Ferziger, J., and Mitchell, I. (2002). A hybrid particle level set method for improved interface capturing. *Journal of Computational physics*, 183(1):83–116.

Escauriaza, C. and Sotiropoulos, F. (2011a). Initial stages of erosion and bed form development in a turbulent flow around a cylindrical pier. *Journal of Geophysical Research: Earth Surface*, 116(F3).

Escauriaza, C. and Sotiropoulos, F. (2011b). Lagrangian model of bed-load transport in turbulent junction flows. *Journal of Fluid Mechanics*, 666:36–76.

Escauriaza, C. and Sotiropoulos, F. (2011c). Reynolds number effects on the coherent dynamics of the turbulent horseshoe vortex system. *Flow, turbulence and combustion*, 86(2):231–262.

Ettema, R. (1976). *Influence of bed material gradation on local scour*, volume 124 of *Department of Civil Engineering: Report*. University of Auckland, School of Engineering.

Ettema, R. (1980). *Scour at bridge piers*. PhD Thesis, Department of Civil Engineering, University of Auckland, Auckland, New Zeland.

Ettema, R., Kirkil, G., and Muste, M. (2006). Similitude of large-scale turbulence in experiments on local scour at cylinders. *Journal of Hydraulic Engineering*, 132(1):33–40.

Exner, F. M. (1925). Uber die wechselwirkung zwischen wasser und geschiebe in flüssen. *Akad. Wiss. Wien Math. Naturwiss. Klasse*, 134(2a):165–204.

Faraci, C., Foti, E., Marini, A., and Scandura, P. (2011). Waves plus currents crossing at a right angle: Sandpit case. *Journal of Waterway, Port, Coastal, and Ocean Engineering*, 138(5):339–361.

Faraci, C., Scandura, P., Musumeci, R. E., and Foti, E. (2018). Waves plus currents crossing at a right angle: near-bed velocity statistics. *Journal of Hydraulic Research*, 56(4):464–481.

Fornberg, B. (1977). A numerical study of 2-d turbulence. *Journal of Computational Physics*, 25(1):1–31.

Fourtakas, G. and Rogers, B. (2016). Modelling multi-phase liquid-sediment scour and resuspension induced by rapid flows using smoothed particle hydrodynamics (sph) accelerated with a graphics processing unit (gpu). *Advances in Water Resources*, 92:186–199.

Fredsøe, J. and Deigaard, R. (1992). *Mechanics of Coastal Sediment Transport. Advanced Series on Ocean Engineering, Volume 3. Hackensack*. New Jersey: World Scientific.

Gal-Chen, T. and Somerville, R. C. (1975). Numerical solution of the navier-stokes equations with topography. *Journal of Computational Physics*, 17(3):276–310.

García, M. H. (1996). *Hidrodinámica ambiental*. Colección Ciencia y Técnica. Universidad Nacional del Litoral, Buenos Aires, Argentina.

Gingold, R. A. and Monaghan, J. J. (1977). Smoothed particle hydrodynamics: theory and application to non-spherical stars. *Monthly notices of the royal astronomical society*, 181(3):375–389.

Gjunsburgs, B., Jaudzems, G., and Govša, J. (2010). Hydrograph shape impact on the scour development with time at engineering structures in river flow. *Construction Science*, 11:6–12.

Golub, G. H. and Reinsch, C. (1970). Singular value decomposition and least squares solutions. *Numerische mathematik*, 14(5):403–420.

Graf, W. and Yulistiyanto, B. (1998). Experiments on flow around a cylinder; the velocity and vorticity fields. *Journal of Hydraulic Research*, 36(4):637–654.

Grass, A. J. (1970). Initial instability of fine bed sand. *Journal of the Hydraulics Division*, 96(3):619–632.

Greifzu, F., Kratzsch, C., Forgber, T., Lindner, F., and Schwarze, R. (2016). Assessment of particle-tracking models for dispersed particle-laden flows implemented in openfoam and ansys fluent. *Engineering Applications of Computational Fluid Mechanics*, 10(1):30–43.

Guan, D., Chiew, Y.-M., Wei, M., and Hsieh, S.-C. (2018). Characterization of horseshoe vortex in a developing scour hole at a cylindrical bridge pier. *International Journal of Sediment Research*, In Press.

Guyon, E., Hulin, J.-P., Petit, L., and Mitescu, C. D. (2001). *Physical hydrodynamics*. Oxford university press.

Hager, W. and Del Giudice, G. (2000). Discussion to movable bed roughness in alluvial channels. *J. Hydraul. Eng*, 127(7):627–628.

Hager, W. H. and Oliveto, G. (2002). Shields' entrainment criterion in bridge hydraulics. *Journal of Hydraulic Engineering*, 128(5):538–542.

Hamidi, A. and Siadatmousavi, S. M. (2018). Numerical simulation of scour and flow field for different arrangements of two piers using SSIIM model. *Ain Shams Engineering Journal*, 9(4):2415–2426.

Hamill, L. (1998). *Bridge hydraulics*. CRC Press.

Haque, M. N., Katsuchi, H., Yamada, H., and Nishio, M. (2016). Flow field analysis of a pentagonal-shaped bridge deck by unsteady rans. *Engineering Applications of Computational Fluid Mechanics*, 10(1):1–16.

Higham, J. and Brevis, W. (2018). Modification of the modal characteristics of a square cylinder wake obstructed by a multi-scale array of obstacles. *Experimental Thermal and Fluid Science*, 90:212–219.

Higham, J., Brevis, W., and Keylock, C. (2018). Implications of the selection of a particular modal decomposition technique for the analysis of shallow flows. *Journal of Hydraulic Research*, 56:1–10.

Hirt, C. and Cook, J. (1972). Calculating three-dimensional flows around structures and over rough terrain. *Journal of Computational Physics*, 10(2):324–340.

Hirt, C. W. and Nichols, B. D. (1981). Volume of fluid (vof) method for the dynamics of free boundaries. *Journal of computational physics*, 39(1):201–225.

Hjorth, P. (1975). *Studies on the nature of local scour*. Inst. för Teknisk Vattenresurslära, Lunds Tekniska Högskola, Lunds Univ.

Hoffman, J., Jansson, J., and Johnson, C. (2016). New theory of flight. *Journal of Mathematical Fluid Mechanics*, 18(2):219–241.

Hokpunna, A. and Manhart, M. (2010). Compact fourth-order finite volume method for numerical solutions of navier–stokes equations on staggered grids. *Journal of Computational Physics*, 229(20):7545–7570.

Hongwu, T., Wang, H., Liang, D., Lv, S., and Yan, L. (2013). Incipient motion of sediment in the presence of emergent rigid vegetation. *Journal of hydro-environment research*, 7(3):202–208.

Issa, R. I. (1986). Solution of the implicitly discretised fluid flow equations by operator-splitting. *Journal of computational physics*, 62(1):40–65.

Jacobs, C. T., Goldin, T. J., Collins, G. S., Piggott, M. D., Kramer, S. C., Melosh, H. J., Wilson, C. R., and Allison, P. A. (2015). An improved quantitative measure of the tendency for volcanic ash plumes to form in water: implications for the deposition of marine ash beds. *Journal of Volcanology and Geothermal Research*, 290:114–124.

Jacobsen, N. G., Fuhrman, D. R., and Fredsøe, J. (2012). A wave generation toolbox for the open-source cfd library: Openfoam®. *International Journal for Numerical Methods in Fluids*, 70(9):1073–1088.

Jiang, G.-S. and Shu, C.-W. (1996). Efficient implementation of weighted ENO schemes. *Journal of computational physics*, 126(1):202–228.

Kaftori, D., Hetsroni, G., and Banerjee, S. (1995). Particle behavior in the turbulent boundary layer. i. motion, deposition, and entrainment. *Physics of Fluids*, 7(5):1095–1106.

Kamath, A., Alagan Chella, M., Bihs, H., and Arntsen, Ø. A. (2015). Evaluating wave forces on groups of three and nine cylinders using a 3d numerical wave tank. *Engineering Applications of Computational Fluid Mechanics*, 9(1):343–354.

Kang, S., Lightbody, A., Hill, C., and Sotiropoulos, F. (2011). High-resolution numerical simulation of turbulence in natural waterways. *Advances in Water Resources*, 34(1):98–113.

Kato, M. (1993). The modelling of turbulent flow around stationary and vibrating square cylinders. *Turbulent Shear Flow*, 1:10–4.

Kawata, Y. and Tsuchiya, Y. (1988). Local Scour around Cylindrical Piles Due to Waves and Currents Combined. *21st International Conference on Coastal Engineering*, pages 1310–1322.

Keshavarzi, A., Melville, B., and Ball, J. (2014). Three-dimensional analysis of coherent turbulent flow structure around a single circular bridge pier. *Environmental Fluid Mechanics*, 14(4):821–847.

Keshavarzy, A. and Ball, J. (1999). An application of image processing in the study of sediment motion. *Journal of Hydraulic Research*, 37(4):559–576.

Keutner, C. (1932). Stromungsvorgange an strompfeilern von verschiedenen grundrissformen und ihre einwirkung auf die flussohle. *Die Bautechnik*, 10(12):161–170.

Kirkil, G. and Constantinescu, G. (2015). Effects of cylinder reynolds number on the turbulent horseshoe vortex system and near wake of a surface-mounted circular cylinder. *Physics of Fluids*, 27(7):075102.

Kirkil, G., Constantinescu, G., and Ettema, R. (2005). The horseshoe vortex system around a circular bridge pier on a flat bed. In *XXXIst International Association Hydraulic Research Congress, Seoul, Korea.*, pages 1–10.

Kirkil, G., Constantinescu, S., and Ettema, R. (2008). Coherent structures in the flow field around a circular cylinder with scour hole. *Journal of Hydraulic Engineering*, 134(5):572–587.

Kobayashi, T. (1992). Three-dimensional analysis of the flow around a vertical cylinder on a scoured seabed. *Coastal Engineering Proceedings*, 3(99):3482–3495.

Kobayashi, T. and Oda, K. (1994). Experimental study on developing process of local scour around a vertical cylinder. *Coastal Engineering Proceedings*, 1(24):1284–1297.

Kolmogorov, A. N. (1941). The local structure of turbulence in incompressible viscous fluid for very large reynolds numbers. In *Dokl. Akad. Nauk SSSR*, volume 30, pages 299–303.

Komar, P. D. and Miller, M. C. (1973). The threshold of sediment movement under oscillatory water waves. *Journal of Sedimentary Research*, 43(4):1101–1110.

Komar, P. D. and Miller, M. C. (1975). On the comparison between the threshold of sediment motion under waves and unidirectional currents with a discussion of the practical evaluation of the threshold: Reply. *Journal of Sedimentary Research*, 45(1):362–367.

Korteweg, D. J. and De Vries, G. (1895). On the change of form of long waves advancing in a rectangular canal, and on a new type of long stationary waves. *The London, Edinburgh, and Dublin Philosophical Magazine and Journal of Science*, 39(240):422–443.

Kothyari, U. C., Garde, R. C. J., and Ranga Raju, K. G. (1992). Temporal variation of scour around circular bridge piers. *Journal of Hydraulic Engineering*, 118(8):1091–1106.

Kramer, H. (1935). Sand mixtures and sand movement in fluvial model. *Transactions of the American Society of Civil Engineers*, 100(1):798–838.

Krieg, R. and Hailfinger, G. (1980). Transient, three-dimensional potential flow problems and dynamic response of the surrounding structures. part i: Description of the fluid dynamics by a singularity method (computer code sing). *Journal of Computational Physics*, 34(2):139–163.

Kundu, P. K., Dowling, D. R., Tryggvason, G., and Cohen, I. M. (2015). Fluid mechanics.

Landau, L. D. and Lifshits, E. M. (1959). *Fluid mechanics, by LD Landau and EM Lifshitz*, volume 11. Pergamon Press Oxford, UK.

Launder, B., Reece, G. J., and Rodi, W. (1975). Progress in the development of a reynolds-stress turbulence closure. *Journal of fluid mechanics*, 68(03):537–566.

Launder, B. and Sharma, B. (1974). Application of the energy-dissipation model of turbulence to the calculation of flow near a spinning disc. *Letters in heat and mass transfer*, 1(2):131–137.

Launder, B. E. and Spalding, D. B. (1974). The numerical computation of turbulent flows. *Computer methods in applied mechanics and engineering*, 3(2):269–289.

Laursen, E. M. and Toch, A. (1956). *Scour around bridge piers and abutments*, volume 4. Iowa Highway Research Board Ames, Iowa.

Le Mehaute, B. (1976). *An introduction to hydrodynamics and water waves*. Springer Science & Business Media.

Lee, S. O. and Hong, S. H. (2019). Turbulence characteristics before and after scour upstream of a scaled-down bridge pier model. *Water*, 11(9):1900–1914.

Leveque, R. J. and Li, Z. (1994). The immersed interface method for elliptic equations with discontinuous coefficients and singular sources. *SIAM Journal on Numerical Analysis*, 31(4):1019–1044.

Leveque, R. J. and Li, Z. (1997). Immersed interface methods for stokes flow with elastic boundaries or surface tension. *SIAM Journal on Scientific Computing*, 18(3):709–735.

Li, J., Qi, M., Fuhrman, D. R., and Chen, Q. (2018). Influence of turbulent horseshoe vortex and associated bed shear stress on sediment transport in front of a cylinder. *Experimental Thermal and Fluid Science*, 97:444–457.

Li, Z. and Lai, M.-C. (2001). The immersed interface method for the navier–stokes equations with singular forces. *Journal of Computational Physics*, 171(2):822–842.

Lim, K. Y. and Madsen, O. S. (2016). An experimental study on near-orthogonal wave–current interaction over smooth and uniform fixed roughness beds. *Coastal Engineering*, 116:258–274.

Link, O. (2006). *Untersuchung der Kolkung an einem schlanken zylindrischen Pfeiler in sandigem Boden*. Inst. für Wasserbau u. Wasserwirtschaft.

Link, O., Castillo, C., Pizarro, A., Rojas, A., Ettmer, B., Escauriaza, C., and Manfreda, S. (2017). A model of bridge pier scour during flood waves. *Journal of Hydraulic Research*, 55(3):310–323.

Link, O., Gobert, C., Manhart, M., and Zanke, U. (2008a). Effect of the horseshoe vortex system on the geometry of a developing scour hole at a cylinder. In *4th International Conference on Scour and Erosion, Tokyo*, pages 162–168.

Link, O., González, C., Maldonado, M., and Escauriaza, C. (2012). Coherent structure dynamics and sediment particle motion around a cylindrical pier in developing scour holes. *Acta Geophysica*, 60(6):1689–1719.

Link, O., Henríquez, S., and Ettmer, B. (2019). Physical scale modelling of scour around bridge piers. *Journal of Hydraulic Research*, 57(2):227–237.

Link, O., Pfleger, F., and Zanke, U. (2008b). Characteristics of developing scour-holes at a sand-embedded cylinder. *International Journal of Sediment Research*, 23(3):258–266.

Liu, X. and García, M. H. (2006). Numerical simulation of local scour with free surface and automatic mesh deformation. In *Proceedings of World Environmental and Water Resource Congress. Omaha, NE.*

Liu, X. and García, M. H. (2008). Three-dimensional numerical model with free water surface and mesh deformation for local sediment scour. *Journal of Waterway, Port, Coastal, and Ocean Engineering*, 134(4):203–217.

Lucci, F., Ferrante, A., and Elghobashi, S. (2011). Is stokes number an appropriate indicator for turbulence modulation by particles of taylor-length-scale size? *Physics of Fluids*, 23(2):025101.

Lumley, J. L. (1967). The structure of inhomogeneous turbulent flows. *Atmospheric turbulence and radio wave propagation. ed. AM Yaglom, VI Tatarsky*, pages 166–177.

Maday, Y. and Rønquist, E. M. (2002). A reduced-basis element method. *Journal of scientific computing*, 17(1-4):447–459.

Manohar, M. (1955). Mechanics of bottom sediment movement due to wave action. Technical report, DTIC Document.

Markus, D., Hojjat, M., Wüchner, R., and Bletzinger, K.-U. (2013). A CFD approach to modeling wave-current interaction. *International Journal of Offshore and Polar Engineering*, 23(01):29–32.

Marrone, S., Colagrossi, A., Antuono, M., Colicchio, G., and Graziani, G. (2013). An accurate sph modeling of viscous flows around bodies at low and moderate reynolds numbers. *Journal of Computational Physics*, 245:456–475.

Mayer, S., Garapon, A., and Sørensen, L. S. (1998). A fractional step method for unsteady free-surface flow with applications to non-linear wave dynamics. *International Journal for Numerical Methods in Fluids*, 28(2):293–315.

Melville, B. W. (1975). *Local scour at bridge sites.* PhD Thesis, University of Auckland, School of Engineering, Auckland, New Zeland.

Melville, B. W. (2008). The physics of local scour at bridge piers. In *Fourth International Conference on Scour and Erosion*, pages 28–38.

Melville, B. W. and Chiew, Y.-M. (1999). Time scale for local scour at bridge piers. *Journal of Hydraulic Engineering*, 125(1):59–65.

Melville, B. W. and Coleman, S. E. (2000). *Bridge scour.* Water Resources Publication.

Menter, F. R. (1994). Two-equation eddy-viscosity turbulence models for engineering applications. *AIAA journal*, 32(8):1598–1605.

Meruane, C., Tamburrino, A., Niño, Y., and De la Fuente, A. (2015). Ecuaciones continuas de dos fases para la modelación del transporte incipiente de sedimentos. *SOSociedad Chilena de Ingeniería Hidráulica, XXII Congreso Chileno de Ingeniería Hidráulica.*

Meyer-Peter, E. and Müller, R. (1948). Formulas for bed-load transport. In *IAHSR 2nd meeting, Stockholm, appendix 2*. IAHR.

Mia, M. F. and Nago, H. (2003). Design method of time-dependent local scour at circular bridge pier. *Journal of Hydraulic Engineering*, 129(6):420–427.

Mia, M. F. and Nago, H. (2004). Closure to "design method of time-dependent local scour at circular bridge pier" by md. faruque mia and hiroshi nago. *Journal of Hydraulic Engineering*, 130(12):1213–1213.

Miles, J., Martin, T., and Goddard, L. (2017). Current and wave effects around windfarm monopile foundations. *Coastal Engineering*, 121:167–178.

Mingmin, H. and Qiwei, H. (1982). Stochastic model of incipient sediment motion. *Journal of the Hydraulics Division*, 108(2):211–224.

Mohamed, H. I. (2012). Numerical simulation of flow and local scour at two submerged emergent tandem cylindrical piers. *Journal of Engineering Sciences*, 41(1):1–19.

Moore, B. (1981). Principal component analysis in linear systems: Controllability, observability, and model reduction. *IEEE transactions on automatic control*, 26(1):17–32.

Mostafa, Y. E. and Agamy, A. F. (2011). Scour around single pile and pile groups subjected to waves and currents. *International Journal of Engineering Science and Technology, IJEST*, 3(11):8160–8178.

Munk, W. H. (1949). The solitary wave theory and its application to surf problems. *Annals of the New York Academy of Sciences*, 51(1):376–424.

Muzzammil, M. and Gangadhariah, T. (2003). The mean characteristics of horseshoe vortex at a cylindrical pier. *Journal of Hydraulic Research*, 41(3):285–297.

Nagy, H. and Watanabe, K. (2000). Critical shear stress in vegetated open channel. volume 1. Proceeding of 12th Congress of APD-IAHR.

Naheer, E. (1978). Incipient motion of arbitrary shape particles under solitary waves. *Coastal Engineering*, 2:277–296.

Nakayama, P. and Romero, N. (1971). Numerical method for almost three-dimensional incompressible fluid flow and a simple internal obstacle treatment. *Journal of Computational Physics*, 8(2):230–240.

Navier, C. (1823). Memoire sur les lois du mouvement des fluides. *Memoires de l'Academie Royale des Sciences de l'Institut de France*, 6:389–440.

Nelson, J. M., Shreve, R. L., McLean, S. R., and Drake, T. G. (1995). Role of near-bed turbulence structure in bed load transport and bed form mechanics. *Water resources research*, 31(8):2071–2086.

Niño, Y. and García, M. (1996). Experiments on particle—turbulence interactions in the near–wall region of an open channel flow: implications for sediment transport. *Journal of Fluid Mechanics*, 326:285–319.

Nichols, B. and Hirt, C. (1973). Calculating three-dimensional free surface flows in the vicinity of submerged and exposed structures. *Journal of Computational Physics*, 12(2):234–246.

Niño, Y. (2013). Flow and transport equations in surface water. *CI71Q-CI6111 Hidrodinámica Ambiental*, pages 1–16.

Oishi, Y., Piggott, M. D., Maeda, T., Kramer, S. C., Collins, G. S., Tsushima, H., and Furumura, T. (2013). Three-dimensional tsunami propagation simulations using an unstructured mesh finite element model. *Journal of Geophysical Research: Solid Earth*, 118(6):2998–3018.

Oliveto, G. and Hager, W. H. (2002). Temporal evolution of clear-water pier and abutment scour. *Journal of Hydraulic Engineering*, 128(9):811–820.

Olsen, N. R. and Kjellesvig, H. M. (1998). Three-dimensional numerical flow modeling for estimation of maximum local scour depth. *Journal of Hydraulic Research*, 36(4):579–590.

Olsen, N. R. and Melaaen, M. C. (1993). Three-dimensional calculation of scour around cylinders. *Journal of Hydraulic Engineering*, 119(9):1048–1054.

Ong, M. C., Myrhaug, D., and Hesten, P. (2013). Scour around vertical piles due to long-crested and short-crested nonlinear random waves plus a current. *Coastal Engineering*, 73:106–114.

Osher, S. and Sethian, J. A. (1988). Fronts propagating with curvature-dependent speed: algorithms based on hamilton-jacobi formulations. *Journal of computational physics*, 79(1):12–49.

Özkan, F., Wenka, A., Hansjosten, E., Pfeifer, P., and Kraushaar-Czarnetzki, B. (2016). Numerical investigation of interfacial mass transfer in two phase flows using the vof method. *Engineering Applications of Computational Fluid Mechanics*, 10(1):100–110.

Paik, J., Escauriaza, C., and Sotiropoulos, F. (2007). On the bimodal dynamics of the turbulent horseshoe vortex system in a wing-body junction. *Physics of Fluids*, 19(4):045107.

Paola, C. and Voller, V. (2005). A generalized exner equation for sediment mass balance. *Journal of Geophysical Research: Earth Surface*, 110(F4).

Patankar, S. V. and Spalding, D. B. (1972). A calculation procedure for heat, mass and momentum transfer in three-dimensional parabolic flows. *International journal of heat and mass transfer*, 15(10):1787–1806.

Patankar, S. V. and Spalding, D. B. (1983). A calculation procedure for heat, mass and momentum transfer in three-dimensional parabolic flows. In *Numerical Prediction of Flow, Heat Transfer, Turbulence and Combustion*, pages 54–73. Elsevier.

Peskin, C. (1972). Flow patterns around heart valves: A digital computer method for solving the equations of motion (ph. d. thesis). *Bronx, NY: Albert Einstein College of Medicine*.

Pope, S. B. (2000). *Turbulent Flows*. Cambridge University Press.

Popovac, M. and Hanjalic, K. (2007). Compound wall treatment for rans computation of complex turbulent flows and heat transfer. *Flow, turbulence and combustion*, 78(2):177–202.

Posey, C. (1949). Why bridges fail in floods. *Civil Engineering*, 19:42.

Pracht, W. E. (1975). Calculating three-dimensional fluid flows at all speeds with an eulerian-lagrangian computing mesh. *Journal of computational physics*, 17(2):132–159.

Qi, W. and Gao, F. (2014a). Equilibrium scour depth at offshore monopile foundation in combined waves and current. *Science China Technological Sciences*, 57(5):1030–1039.

Qi, W.-G. and Gao, F.-P. (2014b). Physical modeling of local scour development around a large-diameter monopile in combined waves and current. *Coastal Engineering*, 83:72–81.

Quarteroni, A. and Rozza, G. (2007). Numerical solution of parametrized navier–stokes equations by reduced basis methods. *Numerical Methods for Partial Differential Equations*, 23(4):923–948.

Quezada, M., Tamburrino, A., and Niño, Y. (2018). Numerical simulation of scour around circular piles due to unsteady currents and oscillatory flows. *Engineering Applications of Computational Fluid Mechanics*, 12(1):354–374.

Quezada, M., Tamburrino, A., and Niño, Y. (2019). Numerical study of the hydrodynamics of waves and currents and their effects in pier scouring. *Water*, 11(11):354–374.

Raaijmakers, T. and Rudolph, D. (2008). Time-dependent scour development under combined current and waves conditions-laboratory experiments with online monitoring technique. In *4th International Conference on Scour and Erosion, ICSE, Tokyo*, pages 152–161.

Reiner, M. (1964). The deborah number. *Physics today*, 17(1):62.

Reynolds, O. (1895). On the dynamical theory of incompressible viscous fluids and the determination of the criterion. *Philosophical Transactions of the Royal Society of London. A*, 186:123–164.

Ribberink, J. S. (1998). Bed-load transport for steady flows and unsteady oscillatory flows. *Coastal Engineering*, 34(1):59–82.

Rodi, W. (1980). *Turbulence models and their application in hydraulics - A state of the art review*. Research supported by the Deutsche Forschungsgemeinschaft. Delft, International Association for Hydraulic Research.

Roper, A., Schneider, V., and Shen, H. (1967). Analytical approach to local scour. In *Proceedings of the 12th IAHR Congress, Ft. Collins*, volume 3, pages 151–161.

Roshko, A. (1961). Experiments on the flow past a circular cylinder at very high reynolds number. *Journal of Fluid Mechanics*, 10(3):345–356.

Roulund, A., Sumer, B. M., Fredsøe, J., and Michelsen, J. (2005). Numerical and experimental investigation of flow and scour around a circular pile. *Journal of Fluid Mechanics*, 534:351–401.

Rouse, H. (1937). Modern conceptions of the mechanics of fluid turbulence. *Trans ASCE*, 102:463–505.

Rudolph, D., Raaijmakers, T., and Stam, C.-J. (2008). Time-dependent scour development under combined current and wave conditions–hindcast of field measurements. In *4th International Conference on Scour and Erosion, ICSE, Tokyo*, volume 4, pages 340–347.

Saghatchi, R., Ghazanfarian, J., and Gorji-Bandpy, M. (2014). Numerical simulation of water-entry and sedimentation of an elliptic cylinder using smoothed-particle hydrodynamics method. *Journal of Offshore Mechanics and Arctic Engineering*, 136(3):031801.

Sarker, M. A. (1998). Flow measurement around scoured bridge piers using acoustic-doppler velocimeter (adv). *Flow measurement and instrumentation*, 9(4):217–227.

Saud, M. (2013). 3d numerical modelling of sediment transport under current and waves. *Coastal and Marine Enginwweing and Management, Norwegian University of Science and Technology, Msc-Thesis*, page 110.

Schäffer, H. A. and Klopman, G. (2000). Review of multidirectional active wave absorption methods. *Journal of waterway, port, coastal, and ocean engineering*, 126(2):88–97.

Schanderl, W., Jenssen, U., Strobl, C., and Manhart, M. (2017). The structure and budget of turbulent kinetic energy in front of a wall-mounted cylinder. *Journal of Fluid Mechanics*, 827:285–321.

Schanderl, W. and Manhart, M. (2016). Reliability of wall shear stress estimations of the flow around a wall-mounted cylinder. *Computers & Fluids*, 128:16–29.

Sheppard, D. M., Odeh, M., and Glasser, T. (2004). Large scale clear-water local pier scour experiments. *Journal of Hydraulic Engineering*, 130(10):957–963.

Shields, A. (1936). Anwendung der aehnlichkeitsmechanik und der turbulenzforschung auf die geschiebebewegung. Technical report, Preussischen Versuchsanstalt für Wasserbau.

Silvester, R. and Mogridge, G. R. (1970). Reach of waves to the bed of the continental shelf. *Coastal Engineering Proceedings*, 1(12).

Simpson, R. L. (2001). Junction flows. *Annual review of fluid mechanics*, 33(1):415–443.

Smagorinsky, J. (1963). General circulation experiments with the primitive equations: I. the basic experiment*. *Monthly weather review*, 91(3):99–164.

Smith, B. L. (1988). A general numerical procedure for the treatment of moving interfaces in implicit continuous eulerian (ice) hydrodynamics. *Journal of Computational Physics*, 77(2):384–424.

Soulsby, R. (1997). *Dynamics of marine sands: a manual for practical applications*. Thomas Telford.

Spalart, P. R. and Allmaras, S. R. (1992). A one-equation turbulence model for aerodynamic flows. In *30th aerospace sciences meeting and exhibit*, pages 439–456. AIAA.

Stokes, S. G. G. (1845). *On the Friction of Fluids in Motion and the Equilibrium and Motion of Elastic Solids*. JW Parker, Pitt Press.

Sumer, B., Christiansen, N., and Fredsøe, J. (1993). Influence of cross section on wave scour around piles. *Journal of waterway, port, coastal, and ocean engineering*, 119(5):477–495.

Sumer, B. M., Christiansen, N., and Fredsøe, J. (1997). The horseshoe vortex and vortex shedding around a vertical wall-mounted cylinder exposed to waves. *Journal of Fluid Mechanics*, 332:41–70.

Sumer, B. M., Chua, L. H., Cheng, N.-S., and Fredsøe, J. (2003). Influence of turbulence on bed load sediment transport. *Journal of Hydraulic Engineering*, 129(8):585–596.

Sumer, B. M. and Fredsøe, J. (2001). Scour around pile in combined waves and current. *Journal of Hydraulic Engineering*, 127(5):403–411.

Sumer, B. M. and Fredsøe, J. (2006). *Hydrodynamics around cylindrical strucures*, volume 26. World scientific.

Sumer, B. M. and Fredsøe, J. (1997). *Hydrodynamics around cylindrical structures*. Number 12. World Scientific.

Sumer, B. M. and Fredsøe, J. (2001). Wave scour around a large vertical circular cylinder. *Journal of waterway, port, coastal, and ocean engineering*, 127(3):125–134.

Sumer, B. M. and Fredsøe, J. (2002). *The mechanics of scour in the marine environment*. World Scientific.

Sumer, B. M., Fredsøe, J., and Christiansen, N. (1992). Scour around vertical pile in waves. *Journal of waterway, port, coastal, and ocean engineering*, 118(1):15–31.

Sumer, B. M., Petersen, T. U., Locatelli, L., Fredsøe, J., Musumeci, R. E., and Foti, E. (2012). Backfilling of a scour hole around a pile in waves and current. *Journal of Waterway, Port, Coastal, and Ocean Engineering*, 139(1):9–23.

Sumer, B. M., Petersen, T. U., Locatelli, L., Fredsøe, J., Musumeci, R. E., and Foti, E. (2013). Backfilling of a scour hole around a pile in waves and current. *Journal of Waterway, Port, Coastal, and Ocean Engineering*, 139(1):9–23.

Sumer, M. B. (2007). Mathematical modelling of scour: A review. *Journal of Hydraulic Research*, 45(6):723–735.

Taira, K., Brunton, S. L., Dawson, S. T., Rowley, C. W., Colonius, T., McKeon, B. J., Schmidt, O. T., Gordeyev, S., Theofilis, V., and Ukeiley, L. S. (2017). Modal analysis of fluid flows: An overview. *AIAA Journal*, pages 4013–4041.

Teles, M. J., Pires-Silva, A. A., and Benoit, M. (2013). Numerical modelling of wave current interactions at a local scale. *Ocean Modelling*, 68:72–87.

Tennekes, H. and Lumley, J. L. (1972). *A first course in turbulence*. MIT press.

Thames, F. C., Thompson, J. F., Mastin, C. W., and Walker, R. L. (1977). Numerical solutions for viscous and potential flow about arbitrary two-dimensional bodies using body-fitted coordinate systems. *Journal of Computational Physics*, 24(3):245–273.

Thanh, N. V., Chung, D. H., and Nghien, T. D. (2014). Prediction of the local scour at the bridge square pier using a 3D numerical model. *Open Journal of Applied Sciences*, 4(02):34.

Thielicke, W. (2014). *The flapping flight of birds: Analysis and application*. PhD thesis, Department of Ocean Ecosystems, University of Groningen.

Thielicke, W. and Stamhuis, E. (2014a). Pivlab–towards user-friendly, affordable and accurate digital particle image velocimetry in matlab. *Journal of Open Research Software*, 2(1).

Thielicke, W. and Stamhuis, E. (2014b). Pivlab-time-resolved digital particle image velocimetry tool for matlab (version: 1.35). *Journal of Open Research Software*, 2(1):e30.

Tison, L. (1940). Erosion autour de piles de ponts en riviere. In *Annales des Travaux Publics de Belgique*, volume 41, pages 813–817.

Trewhela, T., Ihle, C., and Tamburrino, A. (2014). Numerical simulations of comminution slurries over complex topographies: Putting together cfd and pipeline integrity. *Minerals Engineering*, 63:139–148.

Tritton, D. (1959). Experiments on the flow past a circular cylinder at low reynolds numbers. *Journal of Fluid Mechanics*, 6(4):547–567.

Tseng, Y.-H. and Ferziger, J. H. (2003). A ghost-cell immersed boundary method for flow in complex geometry. *Journal of computational physics*, 192(2):593–623.

Tucker, P. G. (2012). *Computation of unsteady internal flows: fundamental methods with case studies*. Springer Science & Business Media.

Ulloa, H. N., Winters, K. B., de la Fuente, A., and Niño, Y. (2015). Degeneration of internal kelvin waves in a continuous two-layer stratification. *Journal of Fluid Mechanics*, 777:68–96.

Umeyama, M. (2005). Reynolds stresses and velocity distributions in a wave-current coexisting environment. *Journal of waterway, port, coastal, and ocean engineering*, 131(5):203–212.

Umeyama, M. (2009). Changes in turbulent flow structure under combined wave-current motions. *Journal of waterway, port, coastal, and ocean engineering*, 135(5):213–227.

Umeyama, M. (2010). Coupled PIV and PTV measurements of particle velocities and trajectories for surface waves following a steady current. *Journal of Waterway, Port, Coastal, and Ocean Engineering*, 137(2):85–94.

Unger, J. and Hager, W. H. (2007). Down-flow and horseshoe vortex characteristics of sediment embedded bridge piers. *Experiments in Fluids*, 42(1):1–19.

Unverdi, S. O. and Tryggvason, G. (1992). A front-tracking method for viscous, incompressible, multi-fluid flows. *Journal of computational physics*, 100(1):25–37.

Van Rijn, L. C. (1984a). Sediment transport, part i: bed load transport. *Journal of hydraulic engineering*, 110(10):1431–1456.

Van Rijn, L. C. (1984b). Sediment transport, Part II: Suspend load transport. *Journal of hydraulic engineering*, 110(11):1613–1641.

Van Rijn, L. C. (1993a). *Handbook sediment transport by currents and waves*. Delft Hydraulics.

Van Rijn, L. C. (1993b). *Principles of sediment transport in rivers, estuaries and coastal seas*, volume 1006. Aqua publications Amsterdam.

Vollmer, S. and Kleinhans, M. G. (2007). Predicting incipient motion, including the effect of turbulent pressure fluctuations in the bed. *Water Resources Research*, 43(5).

Wang, H., Tang, H., Yuan, S., Lv, S., and Zhao, X. (2014). An experimental study of the incipient bed shear stress partition in mobile bed channels filled with emergent rigid vegetation. *Science China Technological Sciences*, 57(6):1165–1174.

Wang, S. and Jia, Y. (1999). Computational simulations of local scour at bridge crossings–capabilities and limitations. In *International Water Resources Conference on "Water Resources into the New Millennium: Past Accomplishments and New Challenges" ASCE, Seattle*, pages 8–12.

Watanabe, K., Nagy, H., and Noguchi, H. (2002). Flow structure and bed-load transport in vegetation flow. In *Advances in Hydraulics and Water Engineering: Volumes I & II*, pages 214–218. World Scientific.

Westerweel, J. and Scarano, F. (2005). Universal outlier detection for piv data. *Experiments in fluids*, 39(6):1096–1100.

Whitehouse, R. (1998). *Scour at marine structures: A manual for practical applications*. Thomas Telford.

Wilcox, D. C. (1988). Reassessment of the scale-determining equation for advanced turbulence models. *AIAA journal*, 26(11):1299–1310.

Wilcox, D. C. (1994). *Turbulence modeling for CFD*. DCW industries La Canada, CA.

Wilcox, D. C. et al. (1998). *Turbulence modeling for CFD*, volume 2. DCW industries La Canada, CA.

Wu, C. and Chau, K. (2006). Mathematical model of water quality rehabilitation with rainwater utilization: a case study at Haigang. *International Journal of Environment and Pollution*, 28(3-4):534–545.

Wu, F.-C. and Chou, Y.-J. (2003). Rolling and lifting probabilities for sediment entrainment. *Journal of Hydraulic Engineering*, 129(2):110–119.

Wu, W., Rodi, W., and Wenka, T. (2000). 3d numerical modeling of flow and sediment transport in open channels. *Journal of hydraulic engineering*, 126(1):4–15.

Xie, J. and Jin, Y.-C. (2016). Parameter determination for the cross rheology equation and its application to modeling non-newtonian flows using the wc-mps method. *Engineering Applications of Computational Fluid Mechanics*, 10(1):111–129.

Yalin, M. S. (1972). Mechanics of sediment transport. *New York - Pergamon Press*.

Yuhi, M., Ishida, B., and Umeda, S. (2000). A numerical study of three-dimensional flow fields around a vertical cylinder mounted on a bed. *Coastal Structures Proceedings*, 2:783–792.

Zanke, U. C., Hsu, T.-W., Roland, A., Link, O., and Diab, R. (2011). Equilibrium scour depths around piles in noncohesive sediments under currents and waves. *Coastal Engineering*, 58(10):986–991.

Zhang, J.-S., Zhang, Y., Jeng, D.-S., Liu, P.-F., and Zhang, C. (2014). Numerical simulation of wave–current interaction using a RANS solver. *Ocean Engineering*, 75:157–164.

Zhang, Q. (2014). A fourth-order approximate projection method for the incompressible Navier–Stokes equations on locally-refined periodic domains. *Applied Numerical Mathematics*, 77:16–30.